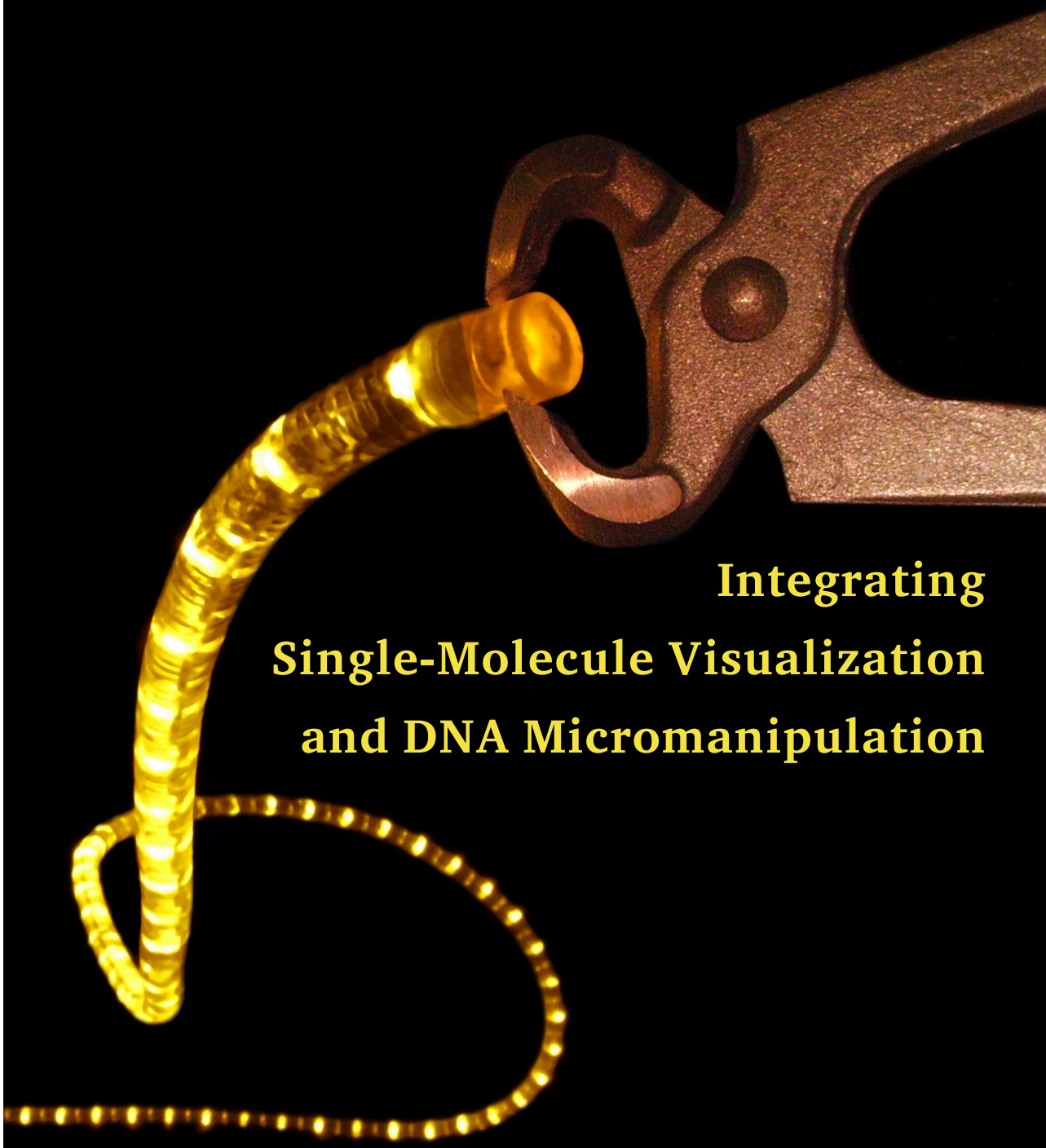

Integrating Single-Molecule Visualization and DNA Micromanipulation

Joost van Mameren – Schotvanger

Integrating single-molecule visualization and DNA micromanipulation

This thesis was reviewed by:

prof.dr. Herbert van Amerongen	Wageningen University
prof.dr. Roel van Driel	University of Amsterdam
dr. John T.M. Kennis	VU University, Amsterdam
prof.dr. Stephen C. Kowalczykowski	University of California, Davis, CA
dr.ir. John van Noort	Leiden University
prof.dr. Mark C. Williams	Northeastern University, Boston, MA

ISBN: 978-90-8659-225-8.

Printed in the Netherlands by PrintPartners Ipskamp, Enschede, www.ppi.nl.
A digital version of this thesis can be obtained at www.ubvu.vu.nl/dissertations.

This work is part of the research programme of the 'Stichting voor Fundamenteel Onderzoek der Materie (FOM)', which is financially supported by the 'Nederlandse Organisatie voor Wetenschappelijk Onderzoek (NWO)'. The research was performed in the section 'Physics of Complex Systems' at the Vrije Universiteit, Amsterdam.

vrije Universiteit *amsterdam*

VRIJE UNIVERSITEIT

Integrating single-molecule visualization and DNA micromanipulation

ACADEMISCH PROEFSCHRIFT

ter verkrijging van de graad Doctor aan
de Vrije Universiteit Amsterdam,
op gezag van de rector magnificus
prof.dr. L.M. Bouter,
in het openbaar te verdedigen
ten overstaan van de promotiecommissie
van de faculteit der Exacte Wetenschappen
op donderdag 26 juni 2008 om 10.45 uur
in de aula van de universiteit,
De Boelelaan 1105

door

Joost van Mameren – Schotvanger

geboren te Alkmaar

promotor:	prof.dr. F.C. MacKintosh
copromotoren:	dr.ir. E.J.G. Peterman
	dr.ir. G.J.L. Wuite

Table of contents

1 General introduction

1.1 Biophysics: physical approaches to biology

The experimental research described in this thesis is best categorized with the buzz-phrase *single-molecule biophysics*. Now what exactly *is* biophysics? As often with such compound words, its two constituents 'bio' and 'physics' actually hint in the right direction: biophysics is the study of biological systems with approaches borrowed from physics. Cutting some corners: biophysics shares with physics the 'bottom-up' approach to scientific research. This implies that biophysicists have the tendency to study a stripped, bare-bone system, adding complexity along the road. Many biologists, on the other hand, learn a lot from taking a complete biological system (like a cell), modifying a component, and registering the changes in behavior. Of course, the distinction is not as crisp as it is put here, yet the example gives an idea.

The distinction is more clearly seen when considering the types of questions that are asked by either biologists or biophysicists and, connected to that, the techniques they use. Biophysicists, like 'real' physicists, think in physical terms such as energies, forces, rates, etc. In an attempt to make this statement somewhat quantitative, I have counted[1] the number of occurrences of these three exemplary words in a widely used, excellent introductory textbook on biophysics by Philip Nelson [1]. Indeed, the 1277, 717 and 212 times the above three words occur in this book, respectively, stand in sharp contrast to the usage of typical (molecular-) biology terminology, such as 'mutants', 'gels', or 'phenotype' (9, 4, and 3 times, respectively). This implies that the questions studied by physicists are often those that biologists do not even think about considering, and vice versa.

[1] The word count was actually performed by Adobe Reader® in a preprint student version of the book.

Although biophysics is certainly not a new scientific field—physical approaches to biological questions have been successful for many decades, if not centuries (depending on definitions of 'physical')—the relatively recent advent of microscopic *single-molecule* techniques in the early nineties has sparked an explosive growth of the field. Such techniques, as the name suggests, are aimed at studying the system of interest by one molecule at the time. This has the generally appreciated advantage of avoiding the registration of only the *averaged* behavior of a huge collection of molecules (hence the term 'bulk techniques'), which may or may not display intrinsic heterogeneity. For one thing, studying single molecules avoids the requirement for synchronization of the system, which bulk techniques often require in order to bring all components into the same initial (bio)chemical reaction state. Such synchronization is unfortunately often difficult, if not impossible, in practice. Another advantage of many single-molecule approaches is that they allow for the physical *manipulation* of the system under study—pushing, pulling, bending, twisting or winding it to see how its properties change. This latter advantage explains why so many physicists have joined the field of biophysics over the past decades: they can use their 'native language', while studying fascinating, largely open questions in biology. Fortunately, the application of these techniques yields more than just keeping physicists off the streets. Many enigmas about how proteins do their enzymatic job in maintaining life in all its forms have been resolved just with such techniques.

Since this thesis is explicitly not a textbook about biophysics, this first chapter is mainly aimed at briefly introducing the biological systems (section 1.2) and the biophysical techniques (section 1.3) used in the following chapters of this thesis. As it plays a role in almost all subsequent chapters, the methodology related to the biophysical technique called *optical tweezers* is explained in some more detail. The chapter ends with a short description of the subsequent chapters of this thesis.

1.2 Introducing DNA

1.2.1 Cells, DNA, proteins

The functional building block of living organisms is the cell. A cell is a closed compartment separated by the outside world through a membrane, and ranges in size from one up to typically ∼100 micrometer (with some extreme outliers: neuronal cells extend all the way from the brain to the corresponding sensory spot, which can be a body length away). The simplest organisms are composed of a single cell, whereas complex vertebrates like humans are composed of countless numbers of cells, many of them dedicated to perform certain specialized tasks. As a functional unit, however,

a cell contains all ingredients to 'be alive', that is, to reproduce and grow, to respond to external stimuli, etc.[2]. An absolute requirement for this is the availability of all *information* needed for life functions. In all organisms, this information is stored in a long, polymeric molecule called deoxyribonucleic acid (DNA). DNA is composed of 'nucleotides', each comprising a base, a sugar, and one or more phosphate groups. The bases (and with that, the nucleotides) come in four flavors: adenine, guanine, thymine, and cytosine, abbreviated to A, G, T and C. Every biological species is genetically unique by the sequence in which the nucleotides are placed on the organism's DNA. Even within a species, individual organisms have a unique genetic sequence, which is in higher organisms inherited as a mixture from both parents. Already thousands of nucleotides constitute the DNA of the simplest viruses, whereas human DNA is composed of as many as three billion. Sections of DNA called *genes* contain the code that represents the primary structure of *proteins*, the 'work horses' of life. The building blocks of proteins are *amino acids*. Three consecutive nucleotides from the four-letter DNA alphabet encode one out of 20 possible amino acids. The sequence of nucleotides directly determines the sequence of amino acids in a protein, called the primary protein structure. The differentiated chemistry of the 20 amino acids defines how the linear amino-acid polymer folds into a well-defined 3D structure.

Proteins make up about 50% of the dry weight of biological matter, and play a central role in almost all biological processes. Their sizes range from 50 to over 2000 amino acids. Proteins serve very diverse cellular functions. Specific proteins called *enzymes* catalyze particular (bio)chemical reactions, increasing the corresponding reaction rates sometimes a millionfold or more. Some proteins are responsible for the regulated transport of chemicals through the organism. So-called 'motor proteins' are able to convert chemical energy into mechanical energy, doing physical work. The actual production of proteins from the DNA code is performed largely by a string of proteins itself, through an intricate sequence of reactions—including the *transcription* from DNA to *RNA* (ribonucleic acid) and the subsequent *translation* from RNA to amino acid strings. Similarly, the accurate replication of a cell's DNA, required to provide the two daughter cells with identical copies of the genetic material upon cell division, leans on the coordinated enzymatic activity of a large number of proteins.

1.2.2 Structure of DNA

As described above, DNA is composed of a linear string of nucleotides. Comprising a base (either of the aforementioned A, G, C and T), a sugar, and one or more

[2]The definition of 'life' is tricky subject, that I will not burn my hands on further. See, for example, Wikipedia: `http://en.wikipedia.org/wiki/Life`.

phosphate groups, the nucleotides form a covalently linked polymer through a sugar–phosphate 'backbone'. In the cell, DNA is stored as a 'duplex', i.e., as two strands of DNA together: double-stranded DNA. As was elucidated by James Watson and Francis Crick in the fifties [2] (based on X-ray crystallographic data taken by Rosalind Franklin), these strands are held together by specific bonds between pairs of bases. Importantly, not all combinations of base pairs are allowed: adenine (A) only pairs with thymine (T); guanine (G) only with cytosine (C). A–T base pairs are held together by two *hydrogen bonds* (relatively weak intermolecular bonds caused by the sharing of a hydrogen atom); G–C bases pair through three such hydrogen bonds and are thus a bit stronger. This specific base pairing of complementary bases, postulated by Watson and Crick, is the very feature that underlies the mechanism by which DNA is replicated—only noted as a sideline in their 1953 Nature article [2]. Due to the relatively low stability of the hydrogen bonds that hold the two strands together, they can be reversibly separated ('melted'), e.g., enzymatically by proteins called *helicases*, or by increased temperature. During replication, the base pairs locally separate to allow reading off of the 4-letter code, using the two native strands as a template for the newly synthesized DNA. Also for protein synthesis, the two strands transiently melt to be read off. In addition, the application of mechanical tension on the DNA can similarly lead to reversible DNA melting, as will be the subject of Chapter 9 (see

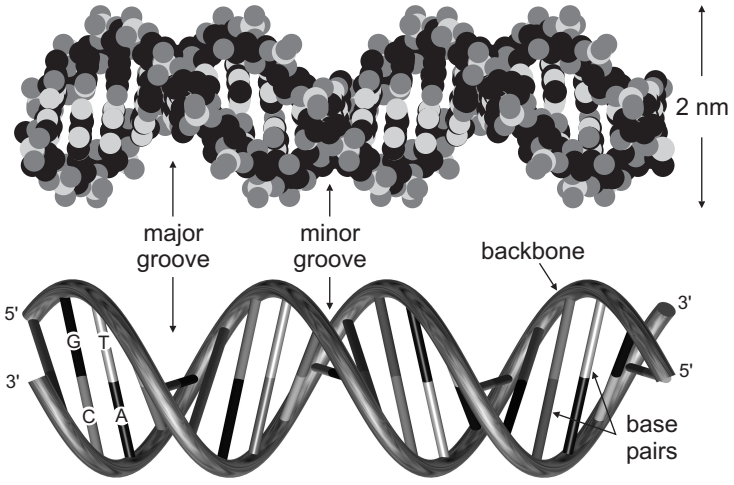

Figure 1.1 – DNA structure. Double-stranded DNA represented as a space-filling (top) and a schematic (bottom) model. The helix axis runs horizontally. The base pairing planes are approximately vertical; two specific base pairs are indicated. The major and minor grooves are clearly seen. The outer diameter of the DNA helix is about 2 nm.

also section 1.2.3).

The three-dimensional structure of double-stranded DNA is the famous double helix depicted in Figure 1.1. The two strands are wound around each other; the helix repeats itself roughly every 10 base pairs (bp), corresponding to 3.4 nm. The diameter of the double-stranded polymer is roughly 2 nm. The double helix gives rise to two structural features called the major and the minor groove, clearly depicted in Figure 1.1. The base pairs are formed in the direction perpendicular to the helix axis. Importantly, the chemical nature of the phosphate backbone imposes directionality on the two strands, which run in opposite directions. Because of the chemistry of the sugar structure, their ends are referred to as either 3' or 5'.

As eluded to above, numerous proteins are required for replication of DNA as well as protein synthesis based on the DNA code. In addition to these crucial processes, a plethora of proteins is required for 'DNA maintenance' processes, e.g.:

- DNA compaction to fit the long polymer into the relatively small cell (or cell nucleus) by proteins called *histones* and the like;
- DNA protection against viral infection—in bacteria obtained through so-called *restriction enzymes*, reappearing in Chapter 4;
- repair of damaged DNA—a topic which is introduced in section 1.2.4 and which reappears in Chapters 7 and 8.

Apart from these different proteins binding and acting on DNA, many other ligands show some level of binding affinity for DNA. Part of this binding is induced by DNA having negative electrostatic charge, inducing attraction by positive ions. One specific class of molecules binding to double-stranded DNA is formed by molecules that sandwich themselves in between consecutive base pairs, a process called *intercalation*. Due to the mechanical distortion caused by such intercalating ligands, such ligands are often carcinogenic. A number of *fluorescent dyes* (see section 1.3.1) bind specifically to dsDNA by intercalation. We will employ these dyes in Chapters 9 and 10 to visualize the DNA during single-molecule manipulation experiments.

1.2.3 DNA as a rubber band: DNA elasticity

DNA is a so-called *semi-flexible* polymer. This means that it has a finite intrinsic stiffness and thus resists sharp bending. From a physical point of view, the elasticity of DNA therefore influences its dynamics in an interesting manner. Biologically speaking, the elasticity of DNA affects a wide variety of cellular processes, including protein-induced DNA bending, twisting or looping. On a larger scale, the compaction of DNA is bounded by its elastic properties.

For these reasons, the advent of techniques to mechanically manipulate single (bio)molecules (discussed in section 1.3) has sparked large efforts to precisely study the elastic properties of DNA. Since the first single-molecule stretching experiments were performed [3], many reports on the stretchability of double-stranded DNA (ds-DNA) have appeared and the available data are relatively well understood. When pulled on from both ends, the elastic behavior of DNA goes through several phases, as seen in the *force-extension curve* of Figure 1.2.

When the DNA is slack (i.e., when the DNA ends are much closer together than the DNA *contour length*), still a finite force has to be exerted in order to fix its ends. This finite force is of *entropic* nature: due to the continuous bombardment by solvent molecules, the DNA actually 'wants to' attain as many conformations as possible. Keeping the DNA at a fixed end-to-end distance, one precludes a tremendous number of conformations, lowering the entropy of the DNA. The further one pulls, the more conformational states are precluded, and hence the higher this entropic force is. When the DNA is (almost) pulled taut, one actually starts to increase the length of the DNA contour by stretching the DNA backbone. This stretching occurs linearly with extension, as for a 'Hookean' spring. This regime is called the *enthalpic* regime.

The entropic regime can be mathematically described by the so-called *worm-like chain* model (WLC) [4]. To also include the enthalpic regime, the *extensible* WLC model was put forward [5,6]:

$$F = \frac{k_B T}{L_p}\left[\frac{1}{4}\left(1 - \frac{L}{L_0} + \frac{F}{S}\right)^{-2} - \frac{1}{4} + \frac{L}{L_0} - \frac{F}{S}\right], \tag{1.1}$$

with F the force, L the end-to-end distance (or extension) of the DNA with contour length L_0 (16.4 μm for λ-phage DNA used here, see vertical dashed line in Figure 1.2). The parameter L_p is the DNA's *persistence length*, a temperature-dependent measure for the bending rigidity ($\sim$ 50 nm); S represents the DNA *stretch modulus* (1000–1500 pN [6]). The Boltzmann constant k_B times the absolute temperature T represent

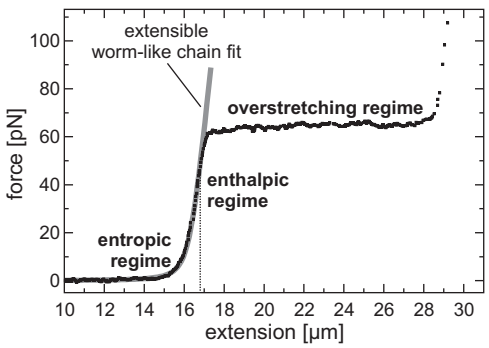

Figure 1.2 – Typical force-extension curve of double-stranded DNA. As the DNA is pulled to larger extensions, it undergoes several phases of distinct elastic behavior. The gray line is a fit to the worm-like chain model; see text for details.

the thermal energy. Figure 1.2 shows a fit of the elasticity data to the extensible WLC model (gray line).

A remarkable feature is observed at a force of ∼65 pN: without the requirement of additional force, the DNA lengthens by almost a factor two. This characteristic *phase transition*, first reported in 1996 by two groups in the same issue of Science [7, 8], is called the *overstretching transition*. This transition reproducibly occurs at the same pulling force, and is found to be reversible. When the DNA is extended beyond ∼170% of its contour length, the transition is complete and a steep increase in force is observed. Much debate exists in the literature about the structural nature of the transition. In Chapter 9, I present experimental data that should settle this debate. The intricate force-extension graph of Figure 1.2 underscores that DNA is certainly not 'just another semi-flexible polymer'.

1.2.4 DNA repair by homologous recombination

Although the biochemical reactions involved in, for example, DNA replication are in general very reliable and have some level of built-in error-checking, there is a significant potential for these reactions to get stalled and yield mechanically distorted DNA. Moreover, besides these native biochemical reactions, the DNA is also constantly exposed to hazardous external influences like ionizing radiation or reactive chemical agents. As a worst-case result of these invasive reactions, both strands of the DNA can get cleaved, resulting in 'double-stranded breaks' (DSBs). The trouble can be increased if the ends are consecutively rejoined in an incorrect manner. The resulting irreversible mutations to the genetic code are one of the sources for diseases such as cancer.

In order to maintain the integrity of the genome while performing all biologically crucial reactions, all organisms have dedicated protein machinery that actively scans for distortions and damaged sites on the DNA. Once such a site is found, other enzymes are recruited to catalyze biochemical reactions to repair the damage. Different types of damages often have their own sets of enzymes involved in the repair. For the repair of double-stranded breaks, two strategies exist. The simplest solution is to bluntly stick back together the two loose ends, referred to as *(non-homologous) end-joining*. This approach is relatively prone to DNA mutations, for instance due to some nucleotides having detached from the broken ends in the damaging process. A second, more reliable DNA repair pathway, called *homologous recombination*, repairs double stranded breaks by using the genetic code of a *homologous* (same sequence) segment of DNA as a template. This way, the break is repaired reliably without introducing mutations. The main reaction steps of this intricate biochemical reaction,

involving a large number of different proteins, are indicated in Figure 1.3.

The central process of the homologous recombination reaction is the search for the homologous template DNA, buried somewhere within a tremendous excess of non-homologous DNA. Once found, the single-stranded broken end is exchanged with the homologous strand in the double-stranded template DNA ('strand invasion and exchange'). Then, the actual repair process can start by copying the template DNA sequence starting from the broken end ('polymerase activity'). The resulting products of this re-annealing reaction are two intertwined DNA molecules. Other helper proteins then resolve this topologically complicated intermediate to finally yield two homologous, intact DNA molecules. To catalyze the homology search, dedicated *recombinase* proteins form a filament around the broken, single-stranded ends of the DNA. This so-called *nucleoprotein filament* is the active species in the search process. In prokaryotic organisms (bacteria), the protein *RecA* is responsible for this filament formation and homology search; in eukaryotic (higher) organisms, the protein in action is *RAD51*. How exactly the search for a homologous template takes place within

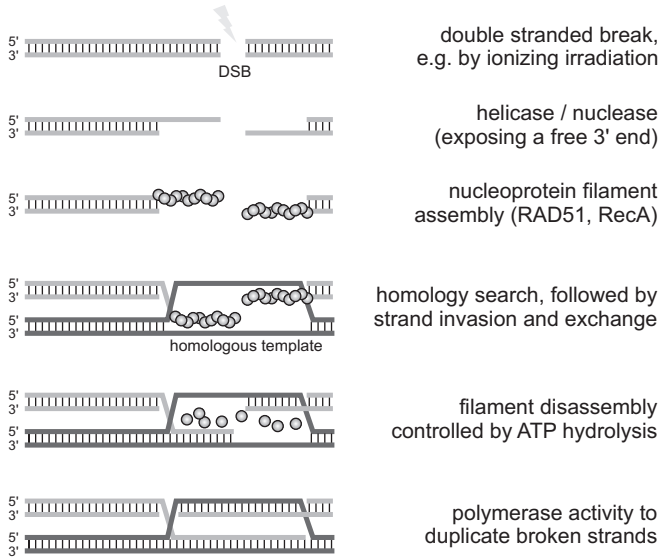

Figure 1.3 – Schematic of the homologous recombination DSB-repair reaction. The repair goes through different reaction steps. The central step is the recognition of a homologous DNA template, catalyzed by nucleoprotein filaments formed around the broken DNA. After the polymerase reaction step (bottom), other proteins finish the reaction by resolving the crossed-over structure to yield two intact dsDNA molecules (not shown).

the abundance of non-homologous DNA is largely unknown. This question resembles that of how individual proteins targeted for a specific DNA sequence perform their search.

In Chapter 7, the effects of the nucleoprotein filament formed by RAD51 on the elasticity of the DNA are studied. Chapter 8 reports on how the disassembly step of these nucleoprotein filaments is controlled by the hydrolysis of *adenosine triphosphate* (ATP), the generic 'fuel molecule' of nature. In addition, the effect of mechanical tension in the DNA on this process is elucidated. The biological importance of this disassembly step lies in the fact that homologous recombination cannot proceed unhampered with the bulky filament still bound. These results were exclusively obtained using a unique combination of single-molecule techniques. Since many mechanistic questions about the complex homologous recombination pathway are still open, the subject is currently widely studied by many research groups around the world. The combined efforts of molecular biologists, geneticists, biochemists, and biophysicists will without doubt help elucidate many of the unanswered questions.

1.3 Biophysical techniques in this thesis

In this section, I will briefly introduce the biophysical techniques that are used in the following chapters for the study of DNA-protein interactions, DNA structure, and DNA dynamics. Since optical tweezers play a crucial role in almost all chapters, I will describe this technique in some more detail (see section 1.3.3). Many of the techniques described here have become standard techniques in today's biophysical and, in part, biological research.

1.3.1 Fluorescence microscopy

Optical microscopy, despite its proven power, is intrinsically limited with respect to its *resolution*[3]: the theoretical maximum resolution is on the order of the wavelength of the illuminating light (typically 300–700 nm). This means that optical microscopy cannot resolve structures to the finest details: DNA, with its 2-nm diameter, is invisible under the microscope if we do not work a bit harder. One of the tricks often played is to switch to *fluorescence microscopy*. Fluorescence is the emission of light by a molecule, caused by the preceding absorption of light of *shorter* wavelength. This red-shift of the fluorescent light (called 'Stokes shift') is caused by partial loss of

[3]Resolution can be defined as: 'how far apart do two entities have to be under the microscope to allow resolving them as separate'.

the excitation energy by collisions with solvent molecules. The Stokes shift can be exploited to selectively collect only the emitted fluorescence, spectrally blocking out the exciting light.

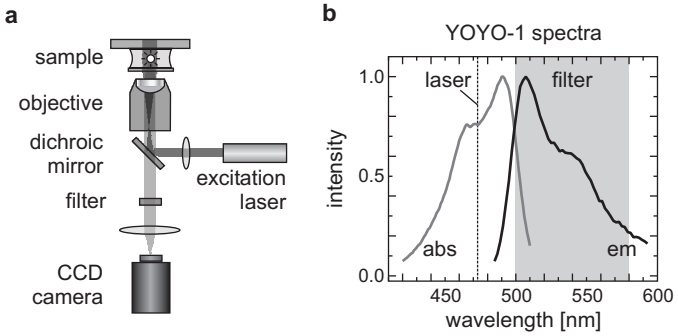

Figure 1.4 – Fluorescence microscopy [**a**] Core components of an epi-fluorescence microscope. A dichroic mirror couples the excitation light (here from a laser) into the microscope objective. The objective collects the backwards emitted fluorescence light emitted specifically by fluorescent molecules in the sample. The emission filter blocks all but the fluorescence light, which is recorded on a sensitive CCD camera or other detector. [**b**] Absorption (gray) and emission (black) spectrum of the DNA-specific chemical dye YOYO-1®. Also indicated are the spectral characteristics of our 473-nm laser line and our band-pass emission filter 'hq540/80m-2p' (shaded area).

Fluorescence detection is often combined with microscopic observation. A typical configuration for such fluorescence microscopy is shown in Figure 1.4a. To avoid spectral overlap, the excitation light source is filtered by a narrow width bandpass *excitation* filter. When using a laser as the excitation source, this is not necessary due to its narrow wavelength range. A special 'dichroic' mirror, reflective for only this wavelength and transparent for other, couples the light into a microscope objective. In the sample, fluorescent molecules absorb the excitation light, and subsequently re-emit fluorescence light with a red-shifted spectrum in all directions. In *epi-fluorescence* mode (indicated in Figure 1.4a), the objective collects the 'backwards' emitted fluorescence light, for which the dichroic mirror is transparent. A second bandpass filter, the emission filter, is used to filter out the remaining excitation light. The fluorescence is imaged onto a camera (or other detector).

If the investigated specimen does not fluoresce naturally, a fluorescent dye can be chemically attached to it. As an example, Figure 1.4b shows the absorption and emission spectra of the DNA-specific dye YOYO-1®, used in Chapters 9 and 10 for visualization of DNA. A dye or dye-labeled molecule essentially acts like a microscopic

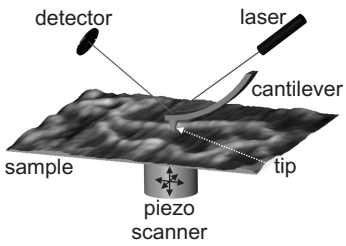

Figure 1.5 – Schematic representation of a scanning force microscope. With a piezo scanner, the sample is brought in contact to a sharp tip on a bendable cantilever. The deflection of the cantilever is recorded using a laser. By scanning the tip across the surface, the topography of the surface can be mapped with sub-nanometer resolution. (Figure courtesy of Maarten Noom.)

light-bulb, switched on with the excitation light. The optical resolution of the microscope is then only limiting the minimum distance between two such dyes to be resolved as two separate entities; fluorescence can be emitted by dyes that are much smaller than the optical resolution and that thus would otherwise be invisible in an optical microscope.

Although the fluorescence intensity of an individual fluorescent dye is very faint, nowadays detection instrumentation is sufficiently sensitive to pick up this light. Such single-molecule fluorescence detection is often used in biophysics to, for example, track individual proteins or DNA molecules in real-time. Fluorescence microscopy suffers from one major limitation: fluorescent dyes only have a finite lifetime, after which the dye is chemically destroyed or *(photo)bleached*. This limits the total number of emitted photons to typically 10^5–10^6 per dye molecule [9]. In Chapter 6, the feasibility of the coincident application of (single-molecule) fluorescence and optical tweezers (introduced below), and the additional bleaching due to the presence of the powerful trapping laser are investigated. On the other hand, photobleaching can also be exploited: it may provide an excellent fingerprint of single-molecule fluorescence, as demonstrated in Chapter 8.

1.3.2 Scanning force microscopy

With a *scanning force microscope* (SFM), invented in 1986 by Binnig, Quate and Gerber [10], one can defeat the finite imaging resolution of optical microscopy in a radically different manner. The basic principle of the SFM is depicted in Figure 1.5. A sample is attached to a flat surface, which is brought into contact with a very sharp tip on a bendable cantilever. When the tip touches the sample, the cantilever bends, which can be sensitively detected as a deflection of a laser reflected off the cantilever. By scanning the tip across the sample, a topographical or height map of the sample can be constructed. Due to the precision that can be achieved with nowadays piezo scanners, this map can be made with sub-nanometer resolution. Although the

term scanning force *microscope* is actually a misnomer—the SFM rather 'feels' than 'sees'—the technique has been used to generate high-resolution images of (among others) many biological samples. Moreover, this imaging can be performed both in air or in a buffered solution. The latter allows for observing biological samples in a close-to-natural environment.

Another application of SFM is to use the tip to very locally apply mechanical forces to a sample. This has been used in our lab to measure the local elastic properties of individual microtubules [11] and viruses [12].

Using SFM, DNA molecules can be routinely visualized. In Chapter 3, a method is introduced which is used to measure the bending angle that certain DNA-binding proteins impose on the local DNA structure. This technique is based on the quantitative analysis of high-resolution SFM images of protein–DNA complexes, like shown in Figure 3.1 on page 42.

1.3.3 Optical tweezers

Most of the chapters of this thesis are based on experiments using *optical tweezers* which, as the name suggests, are a means to manipulate objects with light. With the technique, microscopically small objects can be held and steered. At the same time, the forces exerted on the trapped objects can be accurately measured. The basic physical principle underlying optical tweezers is the radiation pressure, exerted by light when colliding with matter. For macroscopic objects, the radiation pressure exerted by typical light sources is orders of magnitude too small to have any measurable effect: we do not feel the light power of the sun pushing us away. However, for objects of microscopic dimensions ($<$100 μm) radiation pressure can have considerable effects, as was first observed by Ashkin in 1970 for micron-sized latex spheres and a focused argon laser with a few mW power [13]. He found that the spheres were attracted towards the center of the laser beam. When tightly *focusing* the laser beam, using for example a microscope objective as a lens, the focus can be used to trap small objects in three dimensions [14, 15]: one speaks of an 'optical trap' or, more figuratively, of 'optical tweezers'.

Over the past decades, optical tweezers have found many applications in the field of biophysics [16–18]. Optical tweezers have been used extensively not only to manipulate biomolecules, but also to accurately measure the minute forces (on the order of a *piconewton* or 0.000000000001 N) involved. Most often, the biomolecules of interest are not trapped themselves directly, but are manipulated through micrometer-sized beads. In most experiments described in this thesis, DNA molecules are manipulated by suspending them between two optically trapped beads. This section will

introduce the physics of optical trapping, the detection of forces and some techniques to generate multiple optical traps.

Physics of optical trapping

The correct physical description of optical trapping depends on the size of the trapped object. One speaks of the 'ray-optics' regime when the object's dimension d is much larger than the wavelength of the trapping light: $d \gg \lambda$. In this case, diffraction effects can be neglected and the trapping forces of the light can be understood in terms of geometric or ray optics. The regime where $d \ll \lambda$ is called the Rayleigh regime. In this case, the trapped particles can be treated as point dipoles, as the electromagnetic field is constant on the scale of the particle. Obviously, if the laser is not focused, the particle will be propelled away due to the forward radiation pressure caused by light scattering. In the Rayleigh regime, this scattering force is given by

$$\mathbf{F}_s = n_1 \frac{\langle \mathbf{S} \rangle \sigma}{c}, \tag{1.2}$$

where n_1 is the index of refraction of the surrounding medium (mostly water with $n_1 = 1.33$), c the speed of light, $\langle \mathbf{S} \rangle$ the time-averaged 'Poynting vector' of the electromagnetic wave (a measure for the intensity) and $\sigma = \sigma(d, \lambda, n_2/n_1)$ the scattering cross section of a Rayleigh particle of diameter d and refractive index n_2. For a non-uniform laser beam profile, the 'gradient force' is the force that attracts the particle uphill the intensity gradient. In general, a Gaussian laser beam is used, holding the particle in its center. In the Rayleigh regime, the gradient force is the Lorentz force acting on the dipole induced by the electromagnetic wave:

$$\mathbf{F}_g = \frac{\alpha}{2} \boldsymbol{\nabla} \langle E^2 \rangle, \tag{1.3}$$

where E is the electric field and $\alpha = \alpha(d^3, n_2/n_1)$ the polarizability of the object.

In the ray-optics regime, the trapping force can be understood in terms of refraction of light rays between media with different indices of refraction [13–15]. Figure 1.6 qualitatively depicts the origin of the trapping forces in this regime. The lateral gradient restoring force (Figure 1.6a) can be understood as follows. If rays p_1 and p_2 have different intensity, the momentum changes of these rays (Δp_1 and Δp_2, respectively) differ in magnitude, causing a net reaction force on the refracting medium in the direction of highest intensity. The x–projection of this force, Δp_x, tends to counteract a displacement from the laser beam axis, pulling the particle to the center of beam.

The axial gradient force is similarly caused by momentum transfer upon refraction, resulting in a restoring force towards the focus, as in Figure 1.6b. The scattering

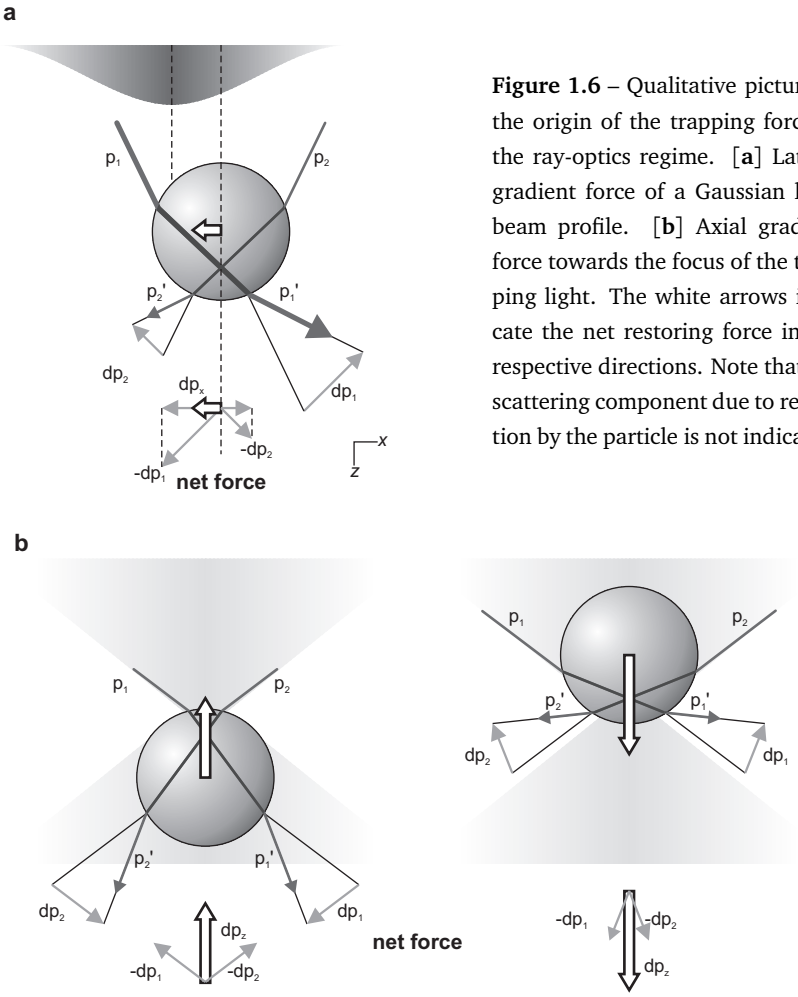

Figure 1.6 – Qualitative picture of the origin of the trapping force in the ray-optics regime. [**a**] Lateral gradient force of a Gaussian laser beam profile. [**b**] Axial gradient force towards the focus of the trapping light. The white arrows indicate the net restoring force in the respective directions. Note that the scattering component due to reflection by the particle is not indicated.

force would cause the object to be propelled out of the focus (along the positive z–direction). The object is stably trapped only if the scattering force along the positive z–direction is compensated by the gradient force along the negative z–direction. To achieve this, a tight focus is needed, with a significant fraction of the incident light coming in from large angles.

The maximum incidence angle $\theta_{\max}$ is determined by the 'numerical aperture' (NA) of the microscope objective used to focus the laser beam. This is a measure for the solid angle over which the objective lens can gather light, defined as:

$$\mathrm{NA} = n_3 \sin\theta_{\max}, \tag{1.4}$$

where n_3 is the refractive index of the immersion medium (i.e., the medium between

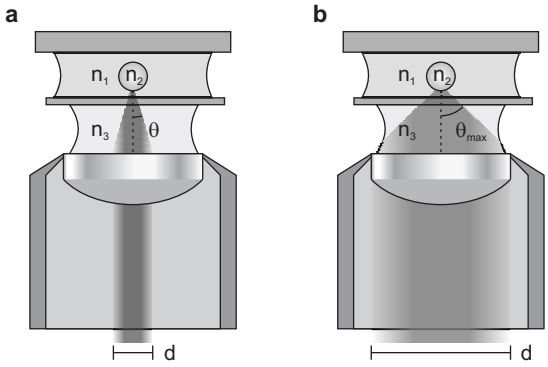

Figure 1.7 – Objective NA and overfilling. [**a**] When the trapping laser does not (over)fill the back aperture of the objective, the highest-angle rays are smaller than θ_{max} and thus the high NA is not fully exploited. [**b**] The scattering force is more efficiently gi counteracted by an expanded beam. The parameters used in Eq. 1.4 are depicted.

the sample and the objective lens) and θ_{max} is one-half the angular aperture (see Figure 1.7). The value of n_3 varies between 1.0 for air and ≈ 1.5 for most immersion oils. For oil-immersion objectives, the NA can be as high as 1.4, corresponding to a total 'acceptance angle' of the objective of about 130°. To obtain a stable, three-dimensional optical trap, the laser beam entering the objective has to be expanded to fill or overfill the back aperture of the objective. This way, one provides sufficient convergent, high-angle rays to counteract the scattering force.

The maximum forces exerted by the trap can be enhanced by increasing the laser power, or by optimizing the quality of the focal spot of the laser and the refraction of the laser by the trapped particle. The laser power can only be increased up to a certain limit, above which more laser light would lead to heating or photodamage of the optics or the examined system (often delicate biomaterials) [19]. Therefore, care must be taken to optimize the quality of the focal spot of the trapping laser. The difference in refractive index of the trapped object n_2 compared to that of the surrounding medium n_1 determines how strongly the incident rays are refracted and, consequently, how strong the trapping force is. The required balance between gradient and scattering forces yields an optimal refractive index of $n_2 = 1.69$ [16]. One often uses silica (glass) particles (n_2=1.37–1.47) or polystyrene particles ($n_2 = 1.57$). The trapping forces that can be obtained for polystyrene particles are thus higher—provided the trapping laser is sufficiently expanded to counteract the scattering force.

When using an oil-immersion objective, the refractive index of the immersion oil matches both that of the objective lens and that of the glass of the sample. Therefore,

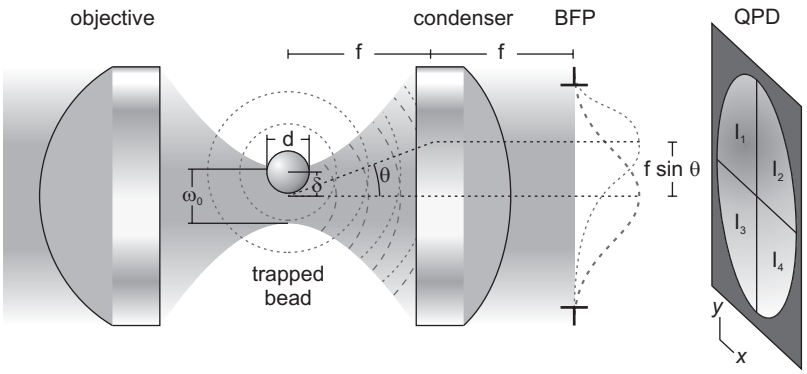

Figure 1.8 – Back-focal-plane interferometry. Configuration for the detection of lateral displacement of a trapped sphere from the trap center. The condenser's back focal plane (BFP) is imaged onto a quadrant photodiode (QPD). Reading out the differential signals $(I_1+I_3)-(I_2+I_4)$ and $(I_1+I_2)-(I_3+I_4)$ (both normalized by the total intensity), displacement signals for x and y are obtained, respectively.

the maximum NA can be achieved with oil-immersion objectives. However, due to the refractive index mismatch between the sample glass and the water of the sample itself, spherical aberrations deteriorate the quality of the laser focus when the distance of the focus to the sample surface increases [20]. To allow equally stable trapping at any distance to the surface, water-immersion objectives can be used. Despite the higher costs and the fact that the NA is somewhat compromised (typically NA=1.2 for water-immersion objectives), the ability to move away from the sample surface without lowering the trap quality can be a good reason to use water-immersion objectives, as was done in most experiments described in this thesis.

Force calibration and detection

It is often hard or even impossible to theoretically predict the force exerted by the trapping laser beam from first principles. However, it is possible to use the trapping light that is scattered by the object to get an accurate measure for external forces (i.e., other than the trapping force) acting upon the trapped object. These external forces tend to push or pull the object from the center of the trap. The refractive object, in turn, acts like a little lens and refracts the rays passing through it. Gittes and Schmidt [21] have modeled the far-field interference of the outgoing laser light with the scattered light from the trapped particle. This model describes the intensity shifts due to the lateral (i.e., off-axis) displacement of the particle. The illuminating and scattered light is collimated by a condenser lens of focal length f. If the right

trap steering scheme is used (see below), the intensity distribution in the back focal plane (BFP) of the condenser lens does not change when moving the optical trap around in the sample; the distribution is only affected by motion of the trapped object with respect to the laser focus. When imaging the light distribution in the BFP onto a position-sensitive detector, such as a *quadrant photodiode* (QPD: a light sensitive diode which is divided into four equal segments), displacements of the particle in the trap can be measured. Figure 1.8 shows the configuration for the detection of the lateral displacement from the trap center. This scheme for detection of displacements of a trapped object or the external forces acting on them is known as *back-focal-plane interferometry* [21].

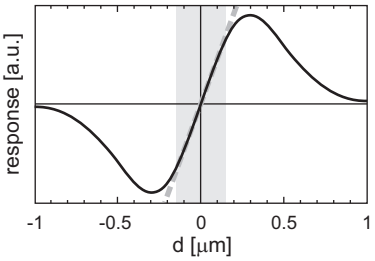

Figure 1.9 – S-shaped detector response.

The expected detector response upon a displacement δ of a micrometer-sized bead with diameter d from the center of a beam of 'focal waist diameter' ω_0 has been calculated [21]. This S-shaped response is plotted in Figure 1.9 for a sphere diameter $d = 0.5\,\mu\text{m}$ and a focal beam waist $\omega_0 = 0.53\,\mu\text{m}$, which is the value for an NA-1.3 objective and an unexpanded beam of 1.0 mm diameter. As seen in the figure, for small displacements ($|\delta| \lesssim 0.15\,\mu\text{m}$), the response is approximately linear (dashed line and shaded area). The slope of the linear range scales with the sphere diameter as d^3, but its width is hardly affected by this parameter. Chapter 2 introduces and describes a calibration technique that directly measures this S-shaped detector response for a trapped bead by rapidly scanning the laser across the sphere.

If a force of known magnitude and direction is applied to the trapped bead (preferably within the linear range) and one observes the response of the QPD signals, one can calibrate the detector to physically relevant units of displacement or force. For instance, one can move the sample in which the trapped bead is suspended with constant velocity with respect to the position of the trap. The bead will be pulled out of the trap along with the sample motion due to the viscous drag of the fluid on the bead: for a fluid of viscosity η flowing with velocity v along a bead of diameter d, the force on the bead is

$$F = 3\pi\eta d v = \gamma v, \tag{1.5}$$

where γ is the drag coefficient.

Another, more accurate calibration procedure is to make use of the *Brownian* motion of the bead, caused by the continuous and random bombardment by solvent

molecules[4]. For a freely diffusing bead, the variance of the spatial coordinate x after a time t will be [23]:

$$\mathrm{Var}(x) = \left\langle x^2(t) - \langle x(t)\rangle^2 \right\rangle = \frac{2k_\mathrm{B}T}{\gamma} t = 2Dt, \tag{1.6}$$

with D the diffusion constant and $k_\mathrm{B}T$ the available thermal energy. The Brownian force is also known as the thermal force.

The diffusive Brownian motion exerted by a particle in a viscous liquid (for which inertia does not play a role), is theoretically described by the 'Langevin' equation of motion. A bead that is held in an optical trap will feel both the thermal forces and a restoring optical force, confining its motion to within the laser focus. Assuming the confining force to be linear in the displacement with a proportionality constant κ (i.e., a *harmonic* trap), the Langevin equation for the bead becomes [23]:

$$F(t) = \gamma \frac{dx}{dt} + \kappa x. \tag{1.7}$$

$F(t)$ represents the random thermal force, which averages to zero over time. The *power spectrum* or *power spectral density* of $F(t)$, $S_F(f)$, contains the contribution to $F(t)$ of motions with different frequencies. For idealized Brownian motion this is 'white noise', i.e., the power spectrum is constant [24]:

$$S_F(f) = |\mathscr{F}^2(f)| = 4\gamma k_\mathrm{B}T, \tag{1.8}$$

where $\mathscr{F}(f)$ is the Fourier transform of $F(t)$. Calculating the Fourier transform of Eq. 1.7—writing $\xi(f)$ as the Fourier transform for $x(t)$—and taking the modulus on both sides, the power spectrum of the displacement fluctuations is found to have a *Lorentzian* shape [24]):

$$S_x(f) = |\xi^2(f)| = \frac{k_\mathrm{B}T}{\gamma\pi^2\left(f_c^2 + f^2\right)}. \tag{1.9}$$

Here, $f_c \equiv \kappa/2\pi\gamma$ is introduced as a characteristic *corner frequency* of the trap: at frequencies $f \ll f_c$, the power spectrum is roughly constant, $S(f) = S_0 = 4\gamma k_\mathrm{B}T/\kappa^2$; at $f \gg f_c$, it falls off like $1/f^2$. The high-frequency behavior is characteristic of free diffusion, indicating that at short time scales the particle does not 'feel' the confinement of the trap. Two typical power spectra taken in traps of different stiffness are shown in Figure 1.10.

Once the values for S_0 and f_c are measured from fitting the observed displacement power spectrum of a trapped particle (see Figure 1.10), these numbers can be used

[4]The original 1828 article by Robert Brown is a wonderful read for those interested in how science was conducted before the twentieth century [22].

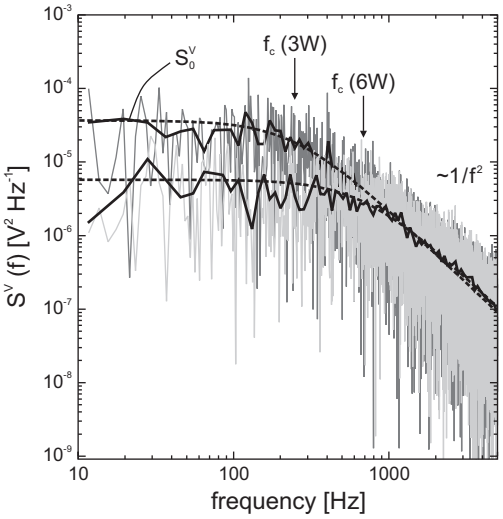

Figure 1.10 – Power spectra. A 1-μm diameter polystyrene bead is held in a trap, while the displacement signals are sampled at a 195-kHz rate. The graph shows power spectra of this displacement signal at 3 W (dark gray) and 6 W (light gray) laser power, respectively. Both the downward shift of the low-frequency plateau S_0 and the upward shift of the corner frequency f_c (arrows, from 250 Hz to 650 Hz, measured from a Lorentzian fit) for the stiffer 6W-trap are clearly seen.

to find the trap stiffness κ:

$$\kappa = \frac{2k_BT}{\pi S_0 f_c} \qquad \text{or} \qquad \kappa = 2\pi\gamma f_c. \tag{1.10}$$

The stiffness κ has units [N/m] like a mechanical spring. It is important to note that in practice, the detector reads *uncalibrated* displacement fluctuations $x(t)$ (i.e., as some voltage rather than as a displacement in nanometers). Nevertheless, the Stokes formula for the viscous drag coefficient on a spherical bead ($\gamma = 3\pi\eta d$), which gives γ from first principles, can be used to calibrate the response R[m/V] of the detector, provided the bead diameter and solvent viscosity are known:

$$R[\text{m/V}] = \left[\frac{k_BT}{\pi^2\gamma S_0^V f_c^2}\right]^{1/2} \overset{25^\circ\text{C}}{=} \left[\frac{5.0\cdot 10^{-20}\text{m}^3\ \text{s}^{-1}}{S_0^V f_c^2 d}\right]^{1/2}, \tag{1.11}$$

where a 25°C-temperature and the corresponding value for the viscosity of water have been substituted. The quantity S_0^V is the low-frequency limit of the uncalibrated power spectrum (in volts). To calibrate the data to forces, the displacement response R should simply be multiplied by the trap stiffness κ, to match $F = \kappa x$.

The largest advantage of the new calibration technique introduced in Chapter 2 (see above) is that an accurate calibration can be obtained, even when *a priori* no knowledge of particle diameter, solvent viscosity or both is available.

Trap steering and generation of multiple traps

In most experiments described in this thesis, DNA was manipulated by pulling on opposite ends with two independently steerable optical traps. For the generation and controlled manipulation of multiple optical traps, several schemes are available. The most widely used scheme is to separate the light from a single laser source into two orthogonally polarized beams using a polarizing beam splitter. The two beams can then be independently steered in the sample. The way this is mostly done in the experiments described here, is by laterally moving the first lens in a telescope system [25]. As shown in Figure 1.11a, this beam-steering scheme is compatible with the force detection described before, as the intensity distribution in the BFP of the objective (which is 'conjugate' to the BFP of the condenser, see Figure 1.8) is not altered when the beam is moved. Rather, the angle under which the light enters the objective is changed, generating a lateral translation of the focus in the sample. To this end, the second telescope lens should be placed such that the intensity distribution in the plane of the first telescope lens is imaged onto the BFP of the objective [25]. Figure 1.11a shows how this telescope can be combined with beam expansion required for (over)filling the objective aperture, by choosing a stronger first lens. Additionally, by changing the distance between the telescope lenses, the focal depth of the trap can be controlled, as is done in Chapter 4.

This polarization-splitting approach to generate and detect two fully steerable op-

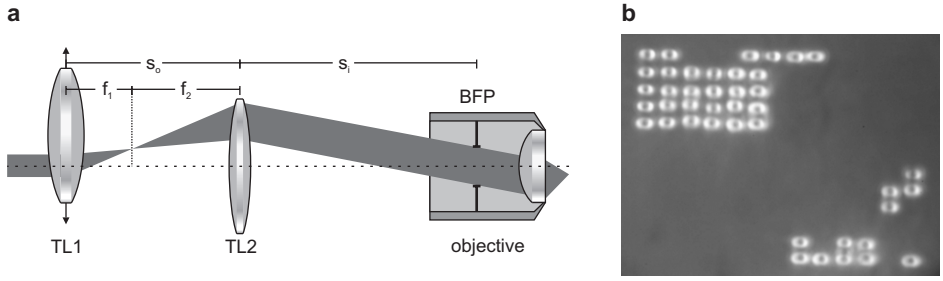

Figure 1.11 – Steering of optical traps. [**a**] Telescope configuration for trap steering. The second telescope lens images the plane of the first onto the back focal plane (BFP) of the objective: $1/s_i = 1/f_2 - 1/(f_1 + f_2)$. Lateral movement of the first telescope lens causes the incident collimated laser beam to enter the BFP under an angle. The laser focus in the sample thereby displaces laterally. When splitting a single laser source into two orthogonal polarization components, two independent thus steerable traps can be realized. [**b**] Time-shared optical trapping using AODs demonstrated by playing the smallest game of *Tetris* ever with 42 beads in a microscope.

tical traps is used in most chapters of this thesis. For faster control of the trap position than achievable using the telescope, one can use *acousto-optic deflectors* or AODs. AODs are crystals in which an ultrasonic (often radio-frequency) acoustic wave is generated, which is used to diffract the incident laser light. Tuning the acoustic frequency leads to a change in the diffraction angle. The extremely fast beam steering that can be obtained using AODs can also be exploited to generate multiple, multiplexed or *time-shared* optical traps: the laser is scanned across different positions fast enough that at every scanned position a bead can be stably trapped. An illustrative example demonstrating this principle is shown in Figure 1.11b: 42 beads are simultaneously trapped and computer-steered to play the smallest game of *Tetris* ever. A more academic use of such time-shared optical trapping is described in Chapter 4, where four traps are used to manipulate two DNA molecules by both ends simultaneously.

1.3.4 Microfluidics

To ascertain well-controlled experimental conditions in single-molecule experiments, it is often useful—if not required—to implement a way to bring the biochemical 'ingredients' together under the microscope. The use of *microfluidics* allows for a fine control over this process by fluid flow of tiny volumes of the solutions used. In most of

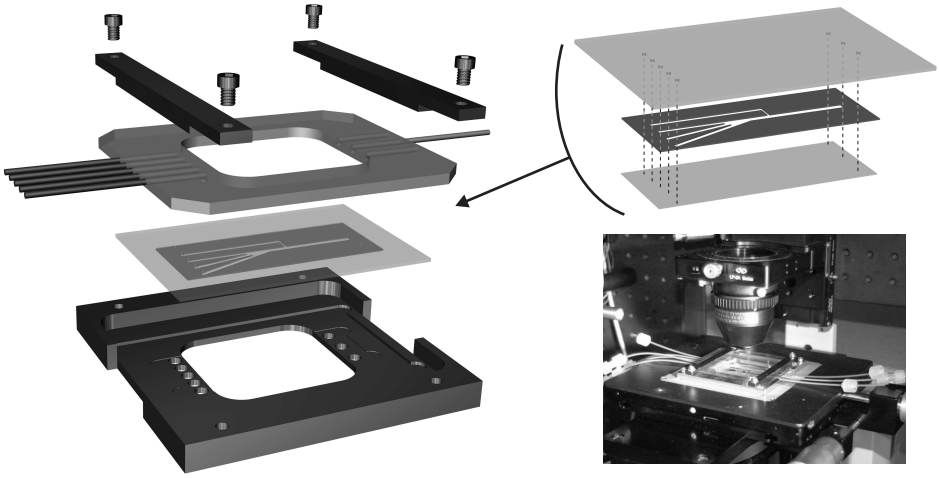

Figure 1.12 – Construction of the microfluidic flow cell. The heart of the flow cell consists of a channel pattern manually cut out of parafilm (shown on the top right). The solutions in these channels do not mix when merged, since the flow is highly laminar. The figure shows a photograph of the assembly mounted on the microscope stage. The flow cell is described in more detail in section 4.5.5 on page 67.

the experiments described in this thesis, this was obtained using a self-designed and -built flow cell, featuring an adjustable number of laminar channels, flowing parallel to each other, as depicted in Figure 1.12. The pattern of channels is manually cut out of a parafilm spacer, sandwiched between a microscope slide and a cover slip as shown. The input channels merge into a large main channel, yet do not mix because of the laminarity of the flow. This allows for rapid exchange of buffer conditions of optically trapped beads or trap-suspended DNA molecules simply by moving the microscope stage orthogonal to the flow direction into a different buffer flow. Apart from enhanced user convenience (an easily underestimated design consideration!), such fast buffer exchange enables one to trigger (bio)chemical reactions in real time during single-molecule observation, as shown and exploited in Chapter 8. Using the flow cell, a typical experiment is preceded by the following preparatory steps: [1] optical trapping of one or more beads, [2] 'catching' of a DNA molecule (or two; see Chapter 4) by moving the traps and waiting for a flow-stretched DNA connecting between the beads, [3] integrity testing of the captured DNA force-extension analysis (section 1.2.3), [4] conduction of the actual experiment—e.g., study protein binding to the DNA. Examples of such experimental protocols are graphically depicted in Figure 4.2 on page 55 and Figure 8.1a on page 107. Such experiments would be extremely tricky, if not impossible, without the features of a microfluidic flow cell.

1.3.5 Combining single-molecule techniques

As the title of this thesis suggests, my research has to a large extent been aimed at the successful application of multiple of the single-molecule techniques introduced in this section simultaneously. The main reason for pursuing such an integrated approach is that the possibility of synchronous controlled manipulation and visualization of DNA and/or DNA-binding proteins is expected to reveal novel insights, remaining concealed by the application of either technique alone. Nonetheless, such combined approaches have been performed relatively few times up till now, primarily due to the technical challenges.

Chapter 5 reviews the development of such integrated approaches over the past decade. The subsequent chapters describe the biophysical results of my combined optical-tweezers, fluorescence and microfluidics experiments, showing how this 'visual-biophysics' approach may have added value over employing either one of the techniques.

1.4 Outline of this thesis

This thesis is organized as follows.

Chapter 2 introduces a new technique to calibrate the displacements of trapped beads held by optical tweezers. Unlike the power spectrum analysis approach described in section 1.3.3, this new approach does not require any *a priori* knowledge about the diameter of the bead or the viscosity of the sample it is immersed in. The calibration is performed by very rapidly scanning the laser across the trapped bead using AODs (section 1.3.3), such that the bead does not follow. The response can be directly recorded and calibrated.

Chapter 3 describes a method to measure the bending angles induced by specific DNA-binding proteins. Several techniques have been reported to perform such measurements, many of which are based on high-resolution imaging such as scanning force microscopy (introduced in section 1.3.2). For the most commonly used approach, tangent angles are simply drawn on SFM images of protein–DNA complexes to measure the induced bending angle. This approach suffers from disadvantages such as 'operator bias'. The technique introduced in this chapter relies on quantitatively comparing histograms of the distance between end points of DNA molecules in SFM images to simulations of such molecules. The results are compared to existing techniques.

In **Chapter 4**, optical tweezers are used to study DNA–protein interactions. The rapid scanning of optical traps with AODs as used in Chapter 2 is now employed to generate multiple time-shared optical traps (section 1.3.3). This allows for the simultaneous manipulation of two DNA molecules, which can be wound around each other. By dragging one molecule along the other, the wound loop acts as a probe for proteins that are bound to the 'scanned' DNA. The tightness of the loop is shown to control whether proteins remain bound or are wiped off. This novel DNA micro-manipulation assay serves as a demonstration of what can be achieved with the simultaneous control over two DNA molecules, instead of a single one.

In **Chapter 5**, the development of integrated single-molecule approaches to both visualize and manipulate DNA molecules will be reviewed. Various techniques of increasing technological complexity are discussed, as well as several examples of successful applications.

Chapter 6 discusses the feasibility of combining the techniques of optical tweezers with that of sensitive or even single-molecule fluorescence microscopy: the main topic of this thesis. The sensitivity of the latter relies on the selective detection of a minute fluorescence signal from a sample excited with substantial light powers. The addition of an even more powerful trapping laser augments the technical challenge. In this chapter, we show that the major challenge of combining these two techniques is posed by the enhanced *photobleaching* (see section 1.3.1) of the dye molecules due to the presence of the high-power trapping laser. The photophysical mechanism of this effect is revealed, as well as experimental measures to reduce it.

In **Chapter 7**, we show how a combined optical-tweezers and fluorescence approach can have added value over the application of either of the two. We dissect the elasticity of DNA molecules coated inhomogeneously with RAD51, a key protein in eukaryotic homologous recombination (see section 1.2.4). The heterogeneity in the elastic behavior of uncoated, continuously coated and partially coated segments can be assessed thanks to the synchronized approach; a method involving only optical tweezers would have been 'blind' for this inhomogeneous coating. We show that uncoated segments behave exactly like 'naked' DNA, as expected, yet that RAD51-coated segments do not participate in the stretching at all.

Chapter 8 studies in depth how these RAD51 nucleoproteins disassemble from DNA upon triggering ATP hydrolysis. The use of our microfluidic flow cell (section 1.3.4) enables us to do this triggering well-controlled and swiftly. Filament disassembly is shown to be slowed down by applying tension to the DNA. Moreover, by calibrating our fluorescence intensity, we are able to count RAD51 proteins during disassembly. Doing so, we reveal that RAD51 filaments fall apart in bursts. We unite our observations in a concise model for filament disassembly, and discuss the similarity of the mechanism with other biopolymeric systems. The biological importance of this disassembly step is that homologous recombination cannot proceed unhampered with the bulky filament still bound. Moreover, the interplay with proteins that aid this reaction step *in vivo* can now be studied in a similar fashion.

In **Chapter 9** we apply our integrated assay to elucidate the so-called *overstretching transition* of DNA, where at tensions of $\sim$65 pN, the DNA gains almost a factor of two in length (see section 1.2.3). However, the nature of the structural change underlying this transition has been subject to debate. We observe the binding of ligands that are specific for either double-stranded or single-stranded DNA: the fluorescent dye YOYO, and fluorescently labeled single-stranded binding proteins (SSB), respec-

tively. This way, we are able to unequivocally deduce that the DNA actually melts, i.e., strand-separates. Moreover, we observe that the melting transition is actually much more cooperative than anticipated by analogy with thermal melting (i.e., heating of the DNA to melt the strands).

Chapter 10 describes the technically challenging experiment of combining single-molecule DNA manipulation with *polarized* fluorescence microscopy. By labeling the DNA again with YOYO, which binds in a specific orientation to the DNA by intercalation (see section 1.2.2), we are able to study the gradual alignment of these dyes by slowly pulling on the DNA. This study allows for the direct and controlled study of DNA conformational dynamics under tensions up to and even beyond the overstretching transition studied in Chapter 9.

2

Calibrating bead displacements in optical tweezers using acousto-optic deflectors

Abstract — Displacements of optically trapped particles are often recorded using back-focal-plane interferometry. In order to calibrate the detector signals to displacements of the trapped object, several approaches are available. One often relies either on scanning a fixed bead across the waist of the laser beam, or on analyzing the power spectrum of movements of the trapped bead.

Here, we introduce an alternative method to perform this calibration. The method consists of very rapidly scanning the laser beam across the solvent-immersed, trapped bead using acousto-optic deflectors while recording the detector signals. It does not require any knowledge of solvent viscosity and bead diameter, and works in all types of samples—viscous or visco-elastic. Moreover, it is performed with the same bead as that used in the actual experiment. This represents marked advantages over established methods.

This chapter has been published in *Review of Scientific Instruments* [26].

2.1 Introduction

The optical trap [14] has become an important and versatile tool in biophysics [17, 27]. In many experiments trapped beads serve as handles for proteins, cytoskeletal filaments or DNA [28–33]. In other applications trapped particles are immersed in polymer networks to perform (micro)rheology, or are used to manipulate cells [34–36]. The displacement of a bead in a trap is a measure of the forces working on it, and can report on the viscous and elastic properties of what is attached to the bead or surrounds it [37,38]. Bead movement is often detected using back-focal-plane (BFP) interferometry [21,25]. In this method, the intensity distribution of the trapping laser in the BFP of the condenser used to collect the laser light downstream from the trap is imaged on a quadrant photodiode (QPD). With the bead close to the trap center, the normalized difference signals from the quadrants depend linearly on the lateral displacement of the bead in the plane normal to the optical axis [21].

In order to relate the voltage output of the detector electronics to displacements and forces, the detector has to be calibrated accurately and the trap stiffness has to be determined. A widely used method to measure the detector calibration factor consists of moving a fixed bead over a known distance across the laser beam waist, while recording the signals from the QPD [25,39–41]. Apart from the advantage of it being a direct measurement, this method also has several disadvantages: (i) calibration cannot be performed with the same bead or at the same position in the sample as the actual experiment, the latter being especially important when the focus gets distorted with increasing distance from the surface due to spherical aberration [20,42]; (ii) it is critical, but difficult in practice, to position the fixed calibration bead correctly with respect to the laser in x–, y– and z–direction; and (iii) the proximity of the cover slip could influence the measured response.

One can also determine the calibration factor from the power spectral density (PSD) of the Brownian motion of a bead confined by the trap in a viscous fluid [16, 43]. If bead diameter, fluid viscosity and temperature are known, the PSD of Brownian motion is exactly predictable and hence can be used to calibrate the measured displacements of the bead in the trap. Although this method is less direct than the one described above, it has the advantage that the same bead can be used for calibration and experiment if one works in a purely viscous medium, and that one can calibrate at the very position in the sample where the experiment takes place. However, this method depends on the precise knowledge of the bead diameter, temperature and the local viscous-drag coefficient. The latter is often not well known when trapping near a surface, or when heating of the solvent by the laser changes temperature and viscosity [19].

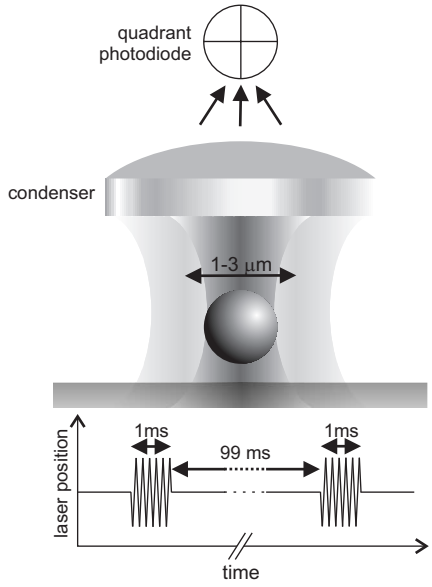

Figure 2.1 – Schematic sketch of the detector calibration method. The trapping laser is periodically scanned across the bead for short periods of time ($\sim$ 1 ms) over known distances ($\sim$1–3 μm), while a quadrant photodiode (QPD) detects the response to the position change relative to the bead.

We have developed a new method to determine detector calibration factors directly and irrespective of the type of sample. Using acousto-optic deflectors (AODs), we scan the trapping laser rapidly across the bead, such that the bead cannot follow the trap (see Figure 2.1). After a few oscillation periods, the laser is held stationary for a fixed time to force the bead to remain trapped in the potential minimum before the next burst of oscillations initiates. A pair of orthogonal AODs allows us to calibrate the detector response in two directions, normal to the optical axis. This method is related to the first method described above, but by moving the laser instead of the bead, the calibration can be directly integrated into most experiments. This avoids problems of bead polydispersity, location of the trap in the sample or the bead in the trap. Furthermore, knowledge of exact bead diameter or local viscosity is not required. The latter can be useful in, for example, trapping experiments in visco-elastic media [38].

Our calibration approach is different from the one introduced recently by Lang *et al*. [44], in which AODs were used to move the bead with the trapping laser while measuring the detector response with a second, weaker detection laser. That method will not work when the bead cannot be freely moved in the sample, in for instance

dense visco-elastic media or with beads attached to cells. An AOD-based laser scanning scheme has also been used to create a line trap [45]. In the specific case of a line trap, the position of a trapped bead along the scanning direction can be measured directly.

Here, we compare our method to that using the power spectrum. We verified that the results of our method do not depend on the details of the laser scanning. We also show that the calibration factor strongly depends on the distance of the bead to the surface when a refractive index mismatch at the surface distorts the shape and size of the focus due to spherical aberration. This effect is directly related to the decrease of trap stiffness due to spherical aberration, when using an oil-immersion objective [20, 39–41, 46, 47].

2.2 Results

To validate our method, we first compared it with the power spectrum calibration method. In Figure 2.2 we show the distribution of values found from repeated measurements with both methods on the same bead. We see excellent quantitative agreement between both methods (both methods: 136 ± 4 nm/V). Hence, the reproducibility of our method (as for the PS method) is $\sim 3\%$.

We tested the sensitivity of the calibration factor found with the AOD method to experimental parameters chosen in the procedure. In all tests a 0.9 μm silica bead was trapped 10 μm above the surface. Two effects caused by bead motion during the scans could bias the results: (i) the beads are dragged along with the moving trap to some extent, and (ii) the bead diffuses during the scans. The distance over which the bead follows the passing laser trap is expected to be proportional to laser power and to the time over which the force acts in each sweep. This, in turn, is determined by frequency and amplitude of the sweeps. We checked for this effect by varying laser power such

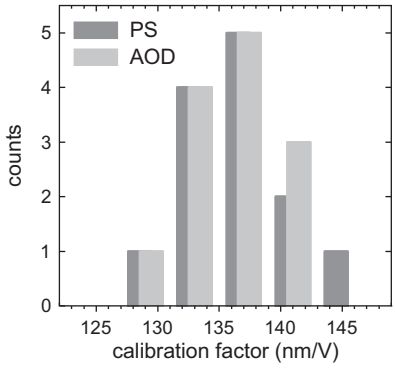

Figure 2.2 – Comparison of calibration methods. Distribution of calibration values found from repeated measurements on the same individual bead with both the power spectrum (PS) and AOD calibration methods. Both methods give a detector calibration factor of 136 ± 4 nm/V.

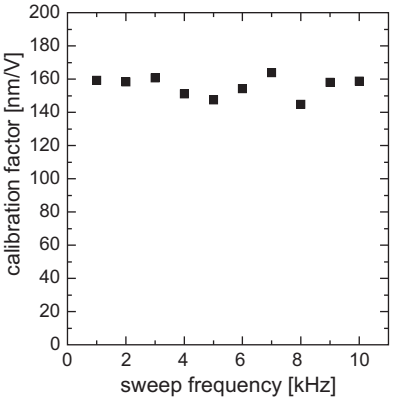

Figure 2.3 – Sweep-frequency dependence. Dependence of the calibration factor on the sweep carrier frequency measured with 0.9 μm silica beads at 10 μm to the surface. The corner frequency of the trap was 300 Hz. Each data point represents an average value derived from 20 bursts of 1 ms (see section 2.4).

that the corner frequency (a measure for the trap stiffness, see section 2.4) ranged between 300 Hz and the full sweep frequency of (in this case) 1 kHz. We confirmed that the calibration factor was independent of laser power in this range (data not shown). Furthermore, we observed that the calibration factor was independent of the sweep frequency with which we scanned the laser across the bead in the range from 500 Hz to 10 kHz (see Figure 2.3). We used sweep amplitudes of 1.5 μm and a corner frequency of 300 Hz. In a frequency regime well below the corner frequency the bead will follow the trap. Frequencies higher than 10 kHz yield insufficient data points in the linear response region due to the finite sampling frequency of 195 kHz. We observed that for amplitudes of the laser sweep larger than the bead diameter, the data becomes less reproducible, presumably because of periods of free diffusion when the trap has moved beyond the bead.

The duration of the burst of oscillations determines how far the bead can diffuse out of the original trap center during the burst. Diffusion in the direction parallel to the sweep direction is unimpeded by the laser, but does not affect the measured response as long as the distance diffused remains small compared to the linear range of the response. The latter should indeed be the case since diffusion gives a displacement of typically 50 nm in 1 ms, while the linear range of the trap (taken here as the region where the response deviates less than 5% from a straight line, see vertical dashed lines in Figure 2.8b) extends to $\sim$ 150 nm. Diffusion in the other two directions is counteracted by the oscillating trap, but less strongly than by the stationary trap. Therefore it leads to a systematic decrease of the response (resulting in an increase of the detector calibration factor). To test if our experiments suffer from this effect, we varied the duration of the burst and the amplitude of the sweep, with fixed laser power and sweep frequency, and we evaluated consecutive sweeps within the bursts separately. A slight dependence on the time elapsed since the start of the burst

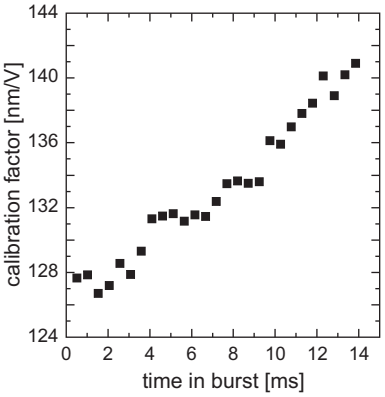

Figure 2.4 – Dependence of the calibration factor on time elapsed since the start of a burst. The calibration factor was determined for consecutive blocks of four sweeps across a 0.9 μm silica bead at a distance of 10 μm to the surface. Each data point shown here is an average over the respective 4-sweep segments from 10 consecutive bursts of 14 ms. The sweep frequency was 5 kHz and the trap corner frequency was 300 Hz.

could be observed within bursts longer than 1 ms (see Figure 2.4). This result sets an upper limit of approximately 1–2 ms for the burst duration. It is thus better to average over a large number of short bursts than a small number of long bursts. For all other data in this study the burst length was 1 ms or shorter.

Figure 2.5 shows the focusing depth dependence of the calibration factor for the water- and oil-immersion objectives. The calibration factor found for the 60× water immersion objective was approximately constant over a large range of distances to the surface. The influence of spherical aberration on the calibration factor when using the 100× oil-immersion objective is evident in Figure 2.5: the detector sensitivity decreased by 30% over a range of 30 μm.

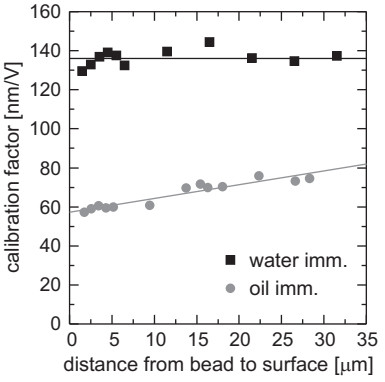

Figure 2.5 – Depth dependence of calibration. Dependence of the calibration factor on the depth in the sample using the 60× water-immersion (squares) and the 100× oil-immersion objective (circles), for 0.9 μm silica beads. The corner frequency of the trap was 300 Hz, and the scanning frequency was 5 kHz. Every data point represents an average value derived from 20 bursts of 1 ms.

2.3 Discussion

Optical trapping combined with force and displacement detection has been developed from a qualitative and initially inaccurate tool to a rather precise one over recent years [43]. Accuracy of better than 5% or even 1% is of course not always needed, and a variety of convenient methods give calibration accuracies of 20–40%. These methods are often indirect, meaning that a few beads are tested as representative for a whole batch, that the solvent in which the calibration is done may not be the same as the one in the actual experiment, or that the method requires known input parameters such as solvent viscosity, temperature, or bead diameter. If such accuracy is not good enough to, for example, precisely measure the force exerted by a molecular motor or to measure thermal fluctuations in techniques such as microrheology [37, 38], the most prominent sources of error have to be avoided. The method described here does this in a convenient way. The calibration factor for each individual bead used in experiments can be determined. Moreover, both the position of the bead within the laser focus and its location in the sample chamber are the same as during the experiments. As an example of the importance of this we showed the expected and observed depth dependence of the calibration factor due to spherical aberrations when using an oil-immersion objective. Our method is robust because it does not depend on details of the laser scanning. At the same time it is rapid (typically less than a second measuring time) and independent of further experimental parameters such as viscosity, temperature or bead diameter, which can cause uncertainties in other in-solution calibration methods.

2.4 Experimental methods

2.4.1 Experimental setup

The experiments were performed in a custom-built inverted microscope as depicted in Figure 2.6. A Nd:YVO_4 laser (1064 nm 10W cw, Millennia IR, Spectra Physics, Mountain View, CA), directed through a Faraday isolator (IO-3-λ-VHP, Optics For Research, Caldwell, NJ) and expanded by a beam expander (2–8×, Linos Photonics GmbH, Göttingen, Germany), was used for trapping. A 1:1 telescope system was implemented for coarse beam steering in the sample [16]. Two orthogonal AODs (DTD 276HD6, IntraAction, Bellwood, IL) were placed just in front of this telescope. The first-order deflected beam in both directions was then coupled via a dichroic mirror (1020dclp, Chroma Tech Corp., Rockingham, VT) into a 60× water-immersion objective (Plan Apo 60×, NA = 1.20 WI, Nikon), or alternatively, for depth dependence experiments,

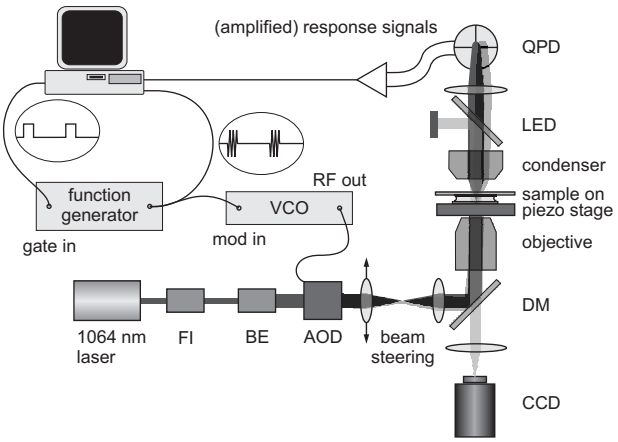

Figure 2.6 – Experimental setup. The 1064 nm laser beam, directed through a Faraday isolator (FI) and a beam expander (BE), can be deflected in two directions by a set of acousto-optic deflectors (AODs). The radio frequency (RF) input signal for the AOD crystal is generated by a voltage-controlled oscillator (VCO). The modulation signal for the VCO is a triangular wave generated by a function generator, gated in turn by a TTL signal from a computer. The laser beam is coupled via a dichroic mirror (DM) into either a 60× water-immersion or a 100× oil-immersion objective which focuses the laser into the sample. The transmitted light through the sample is then collected by a condenser, the back focal plane of which is imaged onto a quadrant photodiode (QPD) with an additional lens. Signals from the QPD and the modulation signal from the function generator are recorded by a computer. The sample can be moved in three dimensions using a piezo stage. A blue LED illuminates the sample, the image of which is collected by a CCD camera.

into a 100× oil-immersion objective (Plan Fluor 100×, NA = 1.3, Nikon). Here, we characterized this calibration method in one of the two scanning directions available with our AODs, yet the method can be readily extended to 2D calibration of the detector response. For displacement detection, the intensity profile in the back-focal plane of the condenser (Achromat Aplanat, NA = 1.4, Nikon) was imaged onto a QPD (YAG444-4A, Perkin Elmer, Vaudreuil, Canada) [21]. We used this special purpose p-type, silicon QPD, operated at a reverse bias voltage of 100 V, to avoid suppression of high-frequency signals [48].

For fine control of the sample surface with respect to the trap, a piezo stage (P-517.3CL Physik Instrumente, Karlsruhe/Palmbach, Germany) and a digital piezo controller (E-710.4CL, Physik Instrumente) were used.

To rapidly steer the laser trap using the AODs, we used a voltage-controlled oscil-

lator (VCO, model AA.DRF.40, AA Opto-Electronics, St. Remy les Chevreuse, France) as the source for the RF signal that drives the AODs (see Figure 2.6). The gated, triangular wave output of a function generator (LFG-1310, Leader, Cypress, CA) was used as input for the VCO, as detailed in the next section. The gate signal for the function generator was computer-controlled using a PC interface board (NI PCI-6221, National Instruments, Austin, TX).

The displacement of the trap in the sample chamber as a function of the input voltage on the VCO was characterized using a continuous 5 kHz square wave as input for the VCO to generate two (time-shared) optical traps. Two beads were held in these traps and their microscope image was digitized using a frame grabber board (IMAQ PCI-1409, National Instruments). With a LabVIEW program employing template-directed pattern matching we measured the distance between the two trapped beads as a function of the peak-to-peak voltage of the input signal. Figure 2.7 shows the trap displacement as a function of the input voltage on the VCO when using the 60× water-immersion objective. The relation is linear, as expected, and its slope independent of the distance to the surface. The same measurement was performed with the 100× oil-immersion objective. Also in this case the slope did not depend on the distance to the surface. The ratio of the slopes found with the oil- and water-immersion objectives is consistent with the magnification factors of the two objectives.

2.4.2 Experimental procedures

Beads (silica, 0.906 μm diameter, Kisker, Steinfurt, Germany) were diluted in deionized water to a final concentration of $2.5 \cdot 10^{-5}$ % (w/v) and infused into a sample chamber made from a cover slip and a microscope slide glued together with two narrow strips of double-stick tape. Except when noted otherwise, all measurements were

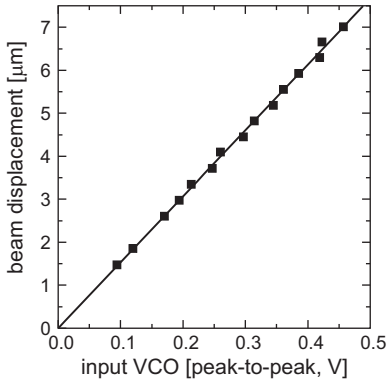

Figure 2.7 – VCO calibration. Dependence of the displacement of the trap in the sample on the input modulation voltage to the VCO (5 kHz square wave from a function generator). The distance between the beads in the two time-shared traps is plotted as a function of VCO square wave amplitude. A straight line fit is shown (fit parameters: $y = (15.3 \pm 0.2)\, x + 0.0 \pm 0.1$).

performed at 10 μm distance from the surface, a position at which the viscous drag coefficient for beads of this size is hardly influenced by the surface. The x, y and total intensity signals of the QPD, as well as the input signal of the VCO, which can be related to the position of the optical trap, were recorded for 3 seconds at a sampling rate of 195 kHz using a data acquisition board (AD16 module on a ChicoPlus PCI board, Innovative Integration, Simi Valley, CA).

The triangular-wave input signal of the VCO was gated on for about 1 ms within a total cycle of 100 ms. During this 1 ms period the laser was swept at an oscillation frequency of 5 kHz across the bead 12 times (6 full periods), after which the trap remained stationary for 99 ms. In most experiments, the corner frequency of the trap $f_(c)$ (which is a measure for the trap stiffness $\kappa = 2\pi\gamma f_c$, with γ the viscous drag coefficient) was 300 Hz. With each data set, we also performed the same routine without a trapped bead, i.e., we recorded QPD signals immediately after releasing the bead from the trap in order to detect the small, but reproducible bead-independent signal on the QPD produced by the AOD sweep itself, which was then used to correct the data with bead. We have found the slope of this signal to be independent of most experimental parameters; hence, it needs to be characterized only once to allow offline correction. To exclude effects of polydispersity in the bead diameter, we used the same bead for a complete data series in successive measurements, recapturing the bead after recording the background signal.

As explained in the section 2.1, the detector calibration factor can also be determined from the amplitude of the power spectral density of the Brownian motion of the bead in the trap [16, 43]. To compare our measurements to the power-spectrum-based detector calibration, the Brownian motion of the same bead was also recorded without moving the trapping laser for 3 seconds at a sampling rate of 195 kHz.

2.4.3 Data analysis

Using a custom-written LabVIEW program, typically 60 to 120 sweeps of the laser across the bead were automatically extracted from the data. The response signal was then scatter-plotted against the VCO driving signal to yield (a part of) the typical S-shaped detector response curve (Figure 2.8a) [21]. Except when single sweeps were analyzed, an average response curve was calculated by binning and averaging the raw data into 15–20 equidistant points along the displacement axis, followed by spline interpolating to 200 points (Figure 2.8a). The bead-independent signal was extracted from the data without bead in the same way, and could be fitted with a straight line (Figure 2.8a). The slope of the background signal did not vary significantly from day to day and from sample to sample, with an average background

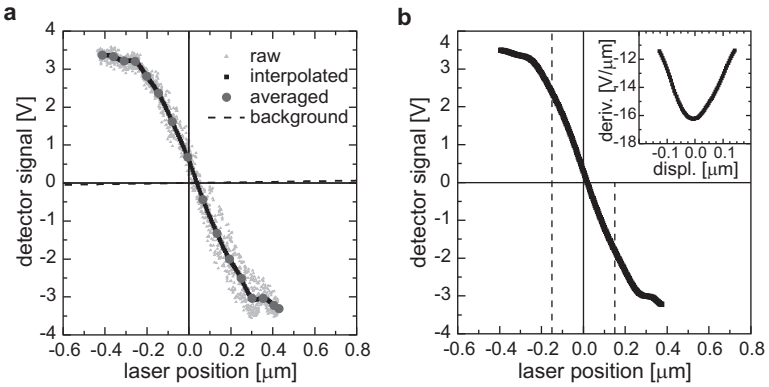

Figure 2.8 – Data analysis. [**a**] Example of scatter plotted raw data of the detector response for a 0.9 μm silica bead at 10 μm from the surface. The amplitude of the laser scan across the bead was ∼0.4 μm; the frequency of scanning was 5 kHz. The corner frequency of the trap was 300 Hz. This particular example contains the data of 19 bursts of 0.4 ms (∼ 60 scans). Besides the raw data, the averaged and interpolated data are also shown. The dashed line represents the reproducible background signal obtained by scanning the laser without a bead. [**b**] The interpolated data obtained in panel a was corrected for the slope of the background signal (dashed straight line in panel a to give the detector signal. The derivative of this signal is shown in the inset. The maximal negative slope gives (the inverse of) the calibration factor, which in this case was found to be $6.16 \cdot 10^{-8}$ m/V. The vertical dashed lines indicate the linear region where the detector response deviates less than 5% from a straight line fit to the data.

slope of 11.4 ± 1.6 mV/μm (s.d., $n = 40$). The magnitude of the slope is significantly smaller than the real response signal (∼ 1000×). The detector response curves are corrected for the background signal using this line fit (Figure 2.8b). The maximal (absolute) slope should occur in the response curve when the center of the trap passes through the center of the bead. The detector calibration factor in m/V (for small displacements) is obtained as the reciprocal of this maximal slope which in magnitude corresponds to the minimum of the derivative shown in the inset in Figure 2.8a.

To independently extract the distance calibration factor from the power spectral density data, we used a LabVIEW program that calculates analytically an uncalibrated diffusion coefficient D from the Brownian displacement signal of the bead in the trap [43]. We then find the calibration factor by comparing the uncalibrated D with the expected D for a bead in physical units $D = k_B T/\gamma$, with γ the Stokes viscous drag coefficient [24, 49].

2.5 Acknowledgments

This work is part of the research programme of the 'Stichting voor Fundamenteel Onderzoek der Materie' (FOM), which is financially supported by the 'Nederlandse Organisatie voor Wetenschappelijk Onderzoek' (NWO).

3

Analysis of scanning force microscopy images of protein-induced DNA bending using simulations

Abstract — Bending of DNA is a feature essential to the function of many DNA binding proteins. Bending angles can be estimated with a variety of techniques, but most directly from images obtained using scanning force microscopy. Direct measurement of the bending angle using a tangent method often produces angles that deviate significantly from values obtained using other techniques. Here, we describe the application of scanning force microscopy in combination with simulations of DNA as a means to estimate protein-induced bending angles in a reliable and unbiased fashion. In this manner, we were able to obtain accurate estimates for the bending angles induced by NFI, Oct-1, XPC-HR23B and IHF.

This chapter has been published in *Nucleic Acids Research* [50].

3.1 Introduction

DNA bending proteins play important roles in a wide range of biological processes. Locally, bending of DNA is used to promote functional contacts between proteins or between protein and DNA, for instance in the regulation of transcription or DNA replication [51, 52]. At the level of global organization of bacterial chromosomal DNA, bending is important as a means of DNA compaction [53–55].

Various techniques are available for the measurement of protein-induced DNA bending angles. Estimates can be obtained from gel retardation experiments [56], DNA circularization experiments [57], co-crystal structures [58–60] and Förster Resonance Energy Transfer (FRET) [61–64]. A limitation of these techniques is that the value obtained is usually an ensemble average and that possible sub-populations cannot be observed. Using scanning force microscopy (SFM), DNA bending can be directly evaluated in single complexes [65, 66]. The shape of the distribution provides insight into the nature of the bend. For instance, different well-defined conformations would be reflected in a multi-modal distribution and flexibility of the bend would be reflected in the width of the distribution. Usually, these measurements are done by placing tangent vectors from the site of the bend after visual inspection. The outcome of this tangent method is not well defined, since the apparent bend depends on the image resolution, which in turn has an upper bound set by tip convolution effects [67]. The outcome is also operator dependent [67], primarily since the approach taken in drawing tangents is not uniquely defined. As a consequence, bending angles thus estimated tend to deviate from values obtained using other techniques [68–70].

A method to avoid this has been proposed by Rivetti and co-workers. Their method, based on the worm-like chain model for semi-flexible polymers [71, 72], describes the effect of local bends on the end-to-end distance (EED) of the polymer [67]. They derived an expression for the bend angle as a function of contour length, persistence length and the mean squared EED (msEED). This has been applied to DNA containing regions of high curvature or intrinsic flexibility [67, 73] and to the analysis of protein-induced DNA bending [74]. Since only the msEED value of a population of molecules is used in Rivetti's approach (hereafter msEED approach), information contained in the shape of the EED distribution (which displays a characteristic shoulder at short EED) is disregarded. One of the potential advantages of a method which makes use of the shape of the distribution is the early detection of deposition anomalies, otherwise concealed by using an average value. An alternative approach to estimate DNA bending angles, exploiting these advantages, could then be to fit experimental data to a mathematical expression for these distributions. However, only analytical expressions that do not take into account any induced bending at a defined site have

been reported to date [75] and even these are not suited for fitting purposes due to their mathematical complexity.

In order to obtain information about bend angles in a controlled and well-defined manner using the shape of the EED distribution, we introduce an alternative method inspired by the work of Rivetti *et al.* [67, 74], yet not employing analytical solutions. Instead, we use simulations of large numbers of DNA molecules with varying bending parameters, to obtain EED distributions that indeed display the aforementioned asymmetry. We employ these distributions to fit experimentally obtained EED histograms for the DNA bending proteins and protein complexes Nuclear Factor I (NFI), Octamer-binding transcription factor 1 (Oct-1), xeroderma pigmentosum group C complexed to human Rad23B (XPC-HR23B), and Integration Host Factor (IHF), thereby taking into account the distributions of EED values acquired from SFM images. Using this procedure, we estimate in a reliable and unbiased fashion bending angles induced by these proteins. This new method enables one to extend the analysis of DNA bending to cases in which one is forced to use mixed populations of bent/unbent DNA. Furthermore, bending configurations which are inaccessible to analytical approaches, such as flexible bends or multiple bends per DNA molecule, can be easily addressed.

3.2 Results and discussion

3.2.1 Visualization of protein–DNA complexes

Our analysis of protein-induced DNA bending comprised the structural effects of the binding of four different proteins, IHF, Oct-1, NFI and XPC-HR23B, to their respective specific sites. For the estimation of the NFI and Oct-1 induced bend we analyzed the end-to-end distance of NFI–DNA and Oct-1–DNA complexes formed at the Ad5 wt origin and two mutant Ad5 origins by SFM. The DNA bending by these proteins has been previously analyzed from SFM images using the tangent method [69, 76–78] and/or with biochemical techniques [56, 57, 79]. In this case, the relatively large size of NFI and Oct-1 allows the complexes to be easily distinguished from bare DNA molecules and therefore the data for the bare DNA and the complexes can be plotted as separate histograms. In a similar fashion, we determined the end-to-end distance of complexes between XPC-HR23B and a DNA fragment containing a defined damage at a known position [78]. Finally, we tested our approach on IHF–DNA complexes for which (due to the small size of IHF) it is often not clear by simple visual inspection that protein is bound. In order to estimate the IHF-induced bend in DNA we imaged IHF–DNA complexes by SFM (Figure 3.1a) and determined the end-to-end distance of a mixed population of bare DNA and IHF–DNA complexes. In this case, all data were simul-

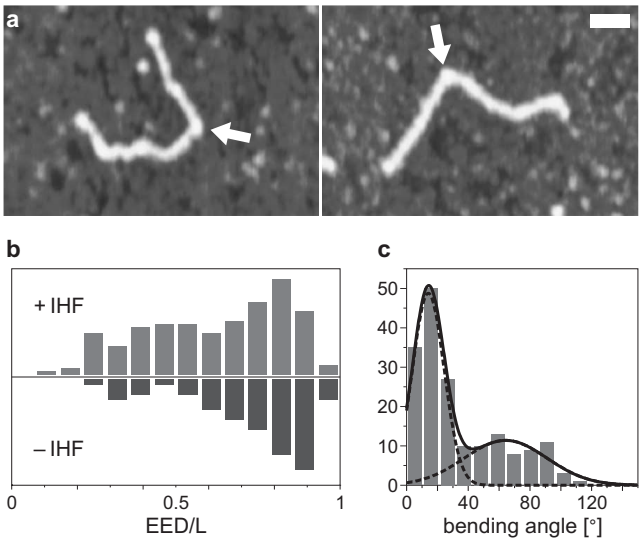

Figure 3.1 – SFM data of IHF–DNA complexes. [**a**] Typical IHF–DNA complexes imaged as described in the section 3.3. The protein-induced bend is indicated by the arrows. Due to its size, the IHF protein cannot be unambiguously identified in the images, demonstrating the need for an analytical approach using other than visual characteristics. The scale bar is 50 nm. Grayscale represents height ranging from 0 nm (darkest) to 2 nm (brightest). [**b**] Distributions of EED values normalized by contour lengths L of IHF–DNA complexes (top) and bare DNA molecules (bottom), demonstrating the effect of DNA bending. [**c**] Histogram of bending angles estimated using tangents from IHF–DNA complexes. The bimodal distribution shows that not all DNA molecules have IHF bound; by fitting to a double gaussian distribution we estimate that about 50% of the imaged molecules have IHF bound.

taneously plotted in a histogram, displaying a higher abundance of molecules with low end-to-end distance than in control experiments with bare DNA (Figure 3.1b, top and bottom, respectively). The shoulder at low end-to-end distances must therefore be attributed to IHF–DNA complexes.

3.2.2 Simulations

In order to predict the end-to-end distance (EED) distributions for DNA molecules equilibrated in two-dimensional space (as opposed to being projected from their three-dimensional conformation [80]), we simulated DNA molecules as worm-like chains and constructed histograms of EED values. DNA molecules were simulated as a collection of segments, using custom-written LabVIEW software (National In-

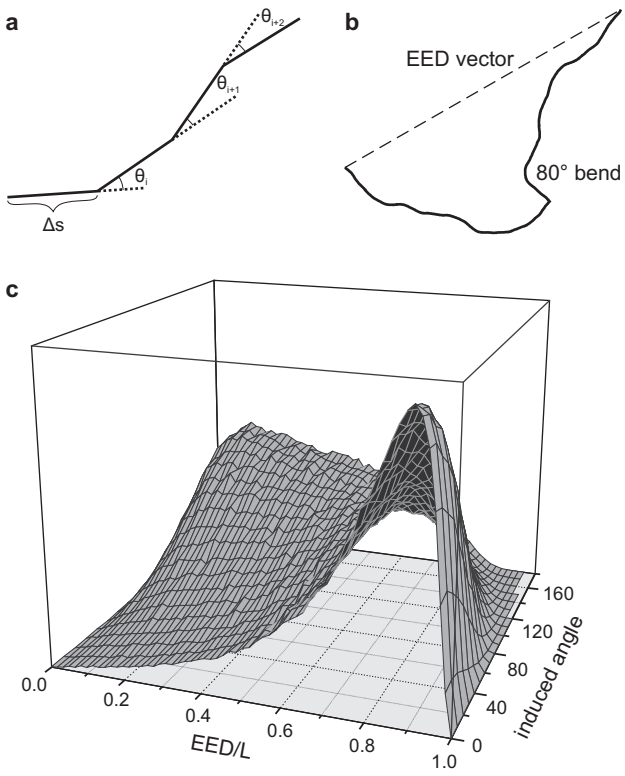

Figure 3.2 – Simulation of DNA molecules equilibrated on a surface. [**a**] Definition of the polymer parameters in Eq. 3.1. [**b**] Simulated molecule with a contour length $L = 4P$ and an 80° bend at 50% of its contour length; the dashed line indicates the end-to-end vector. [**c**] Normalized EED histograms for such molecules with angles ranging from 0 to 160°. Each histogram is based on 100,000 simulated molecules.

struments). The planar angles between consecutive segments (see Figure 3.2a) were drawn from a Gaussian distribution [81], the width of which is directly proportional to the persistence length P:

$$\left\langle (\Delta\theta)^2 \right\rangle = \frac{k_B T \Delta s}{\kappa} = \frac{\Delta s}{P}, \tag{3.1}$$

where Δs is the length of a segment, κ is the bending modulus and $k_B T$ the available thermal energy. The Gaussian shape of the angle distribution ensures the chain to be worm-like (whereas a uniform distribution would yield freely-jointed chains). This was independently confirmed by calculation of the persistence length for thus obtained chains from its defining equation,

$$\langle \cos(\Delta\theta(s)) \rangle = \exp(-s/2P), \tag{3.2}$$

which indeed reproduced the persistence length that was imposed in the simulation. In all simulations, the molecules consisted of 1000 segments, rendering a single segment to be shorter than a base pair. Increasing the number of segments did not influence the simulations.

An additional, fixed bend was introduced at a given segment, generating a polymer chain like that shown in Figure 3.2b. For each simulated molecule, the value of the EED is stored as a fraction of its contour length, L. We generated histograms of EED/L values of 100,000 simulated molecules for many combinations of parameters (persistence length, bending angle, bending location along DNA). Results for $L = 4P$ polymers with induced angles ranging from 0 to 160° are shown in Figure 3.2c. Since the equilibration of linear DNA on a surface almost always leads to non-overlapping molecules, we included self-avoidance in our simulations simply by rejecting self-crossing chains from the histograms. We found only very small deviations exclusively at high bending angles, rendering this computationally expensive procedure unnecessary.

The EED distributions obtained from our experiments were fitted to simulated histograms using a least-squares minimization procedure. Using this method, a value for the induced bending angle and its statistical uncertainty is obtained, as described in the section 3.3. The fitting procedure is performed easily using only EED and L data, which are in turn extracted from SFM images in a straightforward manner.

To validate this approach, we generated images from over 200 simulated molecules with 0°, 50° and 120° angles, which strongly resembled the experimentally obtained images after a Gaussian convolution (to mimic tip convolution effects). We then subjected these images to the same analytical procedure, while keeping the simulation parameters hidden to the operator to eliminate biased analysis. The results are shown in Figure 3.3. From the histograms and the corresponding fit results, we conclude that the procedure successfully reproduces the input parameters.

3.2.3 Estimation of the DNA bending angle

The bending angles extracted from our SFM-imaged protein–DNA complexes using the method described above are shown in Table 3.1. In most cases the measured EED distributions of the bare DNA and the protein–DNA complexes could be well fit to the distributions obtained from our simulations, yielding reliable estimates of the bend angle (Figures 3.4, 3.5, 3.6 and 3.7). One data set (NFI–DNA complexes) appeared to be shifted to anomalously low end-to-end distances (Figure 3.5b). As a consequence, it could not be well fit to any simulated histogram and a bending angle could therefore not be determined unambiguously. A possible explanation is

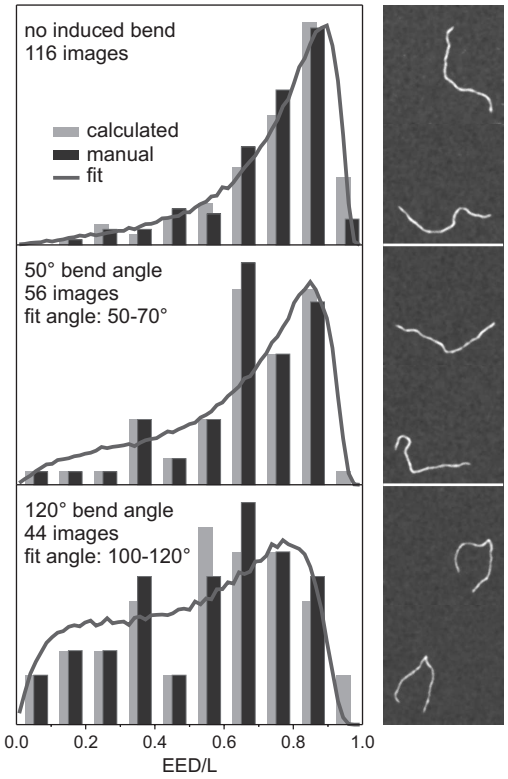

Figure 3.3 – Consistency of manual tracking of molecules and simulation-based analysis. Simulated molecules were digitized onto a grid and convolved with a gaussian kernel resulting in the images on the right. Their contour lengths L and EEDs are manually traced and shown as 'manual' in the histograms. The numbers extracted directly from the simulations yield the histograms indicated with 'calculated'. No significant deviations are observed, validating the manual tracing approach. Next, we subjected these data to the fitting procedure described in the text. From the 0° data set we obtain a persistence length of $L/4$, exactly as imposed in the simulation. The data sets with 50° and 120° induced bending angles yield the angle ranges indicated in their respective histograms, confirming the validity of the procedure.

that the NFI–DNA complexes had not fully equilibrated in two dimensions, but rather had a configuration resembling that of DNA molecules trapped from solution [80]. Alternatively, a systematic overestimation of the contour length would explain the shifted appearance of this histogram. Indeed, the average value for the contour length for this particular data set was about 20 nm longer than expected from the number of base pairs.

Table 3.1 – DNA bending angles for several protein–DNA complexes obtained using different methods.

	Simulations	msEED	Tangent	Gel retardation or DNA cyclization	X-ray
NFI	N.D.	46°	60±19° [76]	-	-
NFI – 4 G/C	20 ± 20°	20°	33 ± 14° [76]	-	-
NFI – 6 G/C	20 ± 20°	N.D.[1]	37 ± 17° [76]	-	-
Oct -1	40 ± 20°	41°	42 ± 12° [77]	37° [79]	-
Oct-1 – 4 G/C	40 ± 20°	29°	39 ± 15° [82]	-	-
XPC-HR23B	50 ± 10°	54°	39 ± 24° [78]	-	-
IHF	110 ± 20°	N.D.	64 ± 20° (*ibid.*) 50 ± 27° [70] 123° [69]	140° [56] 120 – 180° [57]	160° [60]

[1] No value could be calculated for this data set using the msEED method, which in this case implies a bending angle close to zero.

In the case of IHF (Figure 3.7), the protein often cannot be distinguished in the SFM images. We have therefore fitted the IHF-EED data to simulated bent-DNA histograms augmented in an adjustable ratio with an unbent-DNA histogram, to accommodate for a fraction of DNA molecules with no IHF bound. The best fit was obtained assuming that about 50% of the DNA molecules had IHF bound. As a control, we applied a tangent method to the images. The bimodal distribution of bending angles that we found (Figure 3.1c), elegantly confirms that about 50% of the DNA molecules has IHF bound and has been bent (64 ± 20°).

In order to relate to the values estimated using our simulations, Table 3.1 also displays values of bending angles obtained using Rivetti's msEED method (where possible), the tangent method, and biochemical methods. The bending angles obtained using the simulations are in good agreement with values obtained by the msEED method and biochemical techniques. Using biochemical techniques and X-ray crystallography, the bending angle induced by IHF had been estimated between 120° and 180° [56, 57, 60, 63, 84]. Similarly, using gel retardation and circularization experiments a bending angle of 37° had been determined for Oct-1 [79]. Note that the msEED approach cannot be applied to the mixed population of bent/unbent molecules in the case of IHF. The agreement between the various methods provides another validation for our approach. There are, however, clear deviations among SFM based measurements of the IHF-induced bending angle. The bending angles for this strongly bending protein are underestimated by the tangent method compared

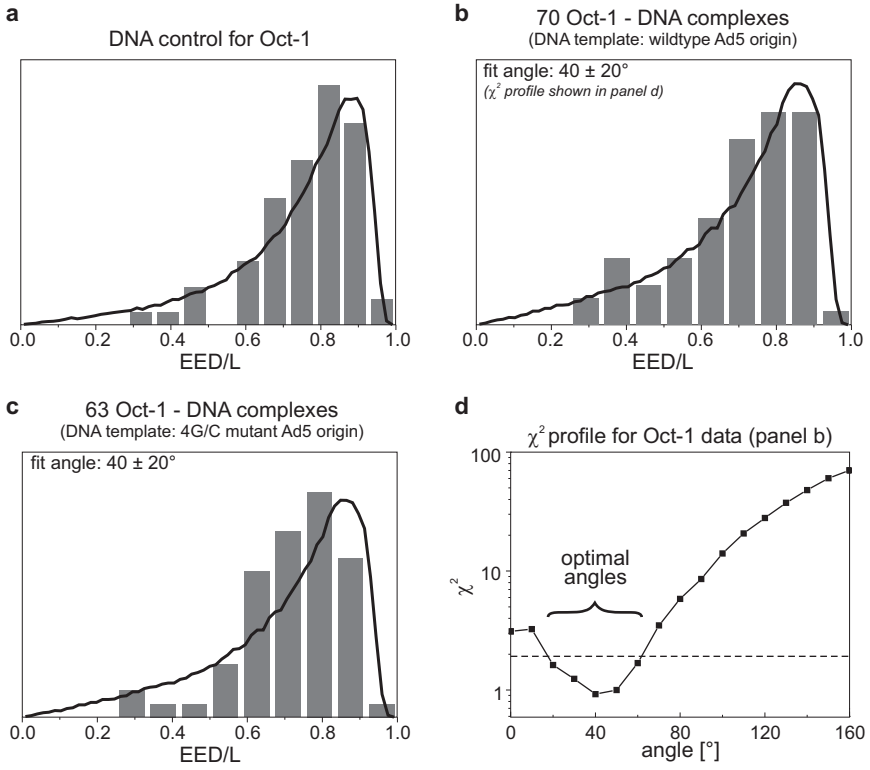

Figure 3.4 – Oct-1 EED histogram analysis. Histograms and fits of experimentally obtained values for EED normalized by contour lengths L of [**a**] a bare DNA control and [**b-c**] Oct-1–DNA complexes. [**d**] χ^2 profile for the data set in panel b. The intersections with the dashed line at $\chi^2_{\min}+1$ indicate the uncertainty in the angle determination [83].

to the two EED-based analysis methods[1]. These IHF results suggest that the tangent method leads to underestimation when the DNA is strongly bent. This is probably due to the limited resolution and the consequent difficulty of accurately choosing a proper tangent vector at the site of the bend. Our method is based on the estimation of a bending angle from intrinsic properties of the polymer. This type of estimate is not affected by operator bias, nor by tip convolution effects resulting in difficulties determining the tangents. The method can therefore, in principle, equally well be applied to DNA with low and high degrees of protein-induced bending. However, in the case

[1]An apparent exception to this tendency is the value reported by Seong *et al.* [69]. However, this is probably due to their deposition procedure, which projects the DNA molecules in its 3D conformation onto the surface. This procedure probably exaggerates the induced angle, thus effectively compensating for the underestimation of large bend angles that seems to be associated with the tangent method.

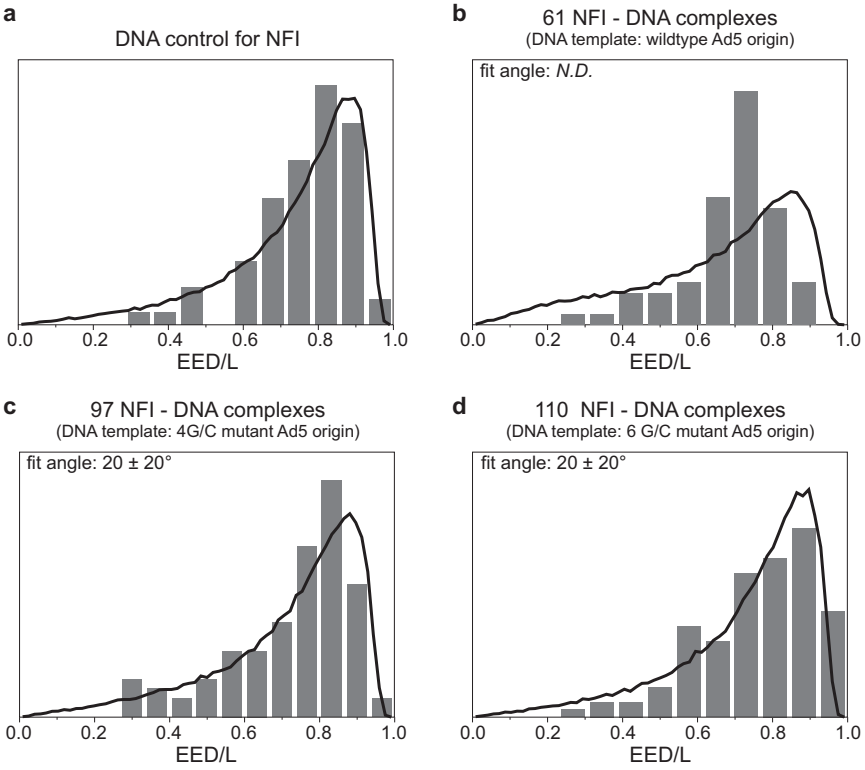

Figure 3.5 – NFI EED histogram analysis. Histograms and fits of experimentally obtained values for EED normalized by contour lengths L of [**a**] a bare DNA control and [**b-d**] NFI–DNA complexes. The data in panel b clearly cannot be fit using the simulated histograms, presumably due to ill complex equilibration on the mica surface.

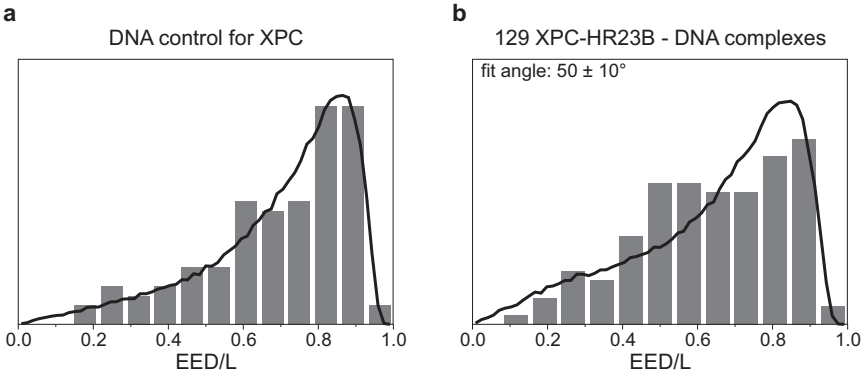

Figure 3.6 – XPC-HR23B EED histogram analysis. Histograms and fits of experimentally obtained values for EED normalized by contour lengths L of [**a**] a bare DNA control and [**b**] XPC-HR23B–DNA complexes.

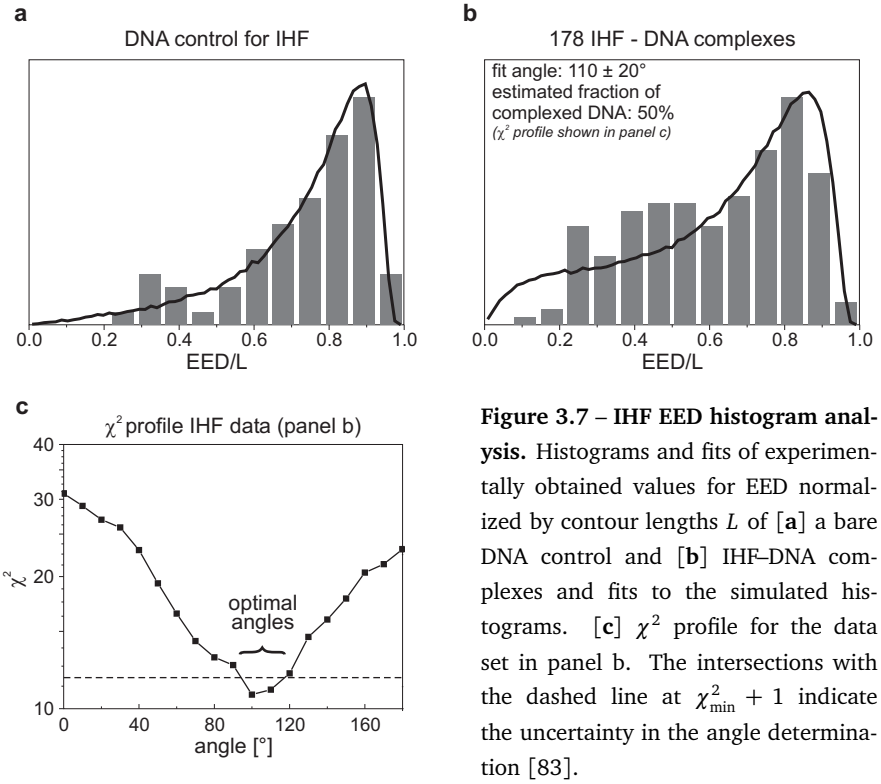

Figure 3.7 – IHF EED histogram analysis. Histograms and fits of experimentally obtained values for EED normalized by contour lengths L of [**a**] a bare DNA control and [**b**] IHF–DNA complexes and fits to the simulated histograms. [**c**] χ^2 profile for the data set in panel b. The intersections with the dashed line at $\chi^2_{\min} + 1$ indicate the uncertainty in the angle determination [83].

of low bend angles the end-to-end distributions change only marginally with respect to those of unbent DNA. Therefore, accurate determination of low degrees of bending requires a distribution with reduced statistical noise (implying the need for more data), such that the data can be more unequivocally fit. We wish to emphasize that, although the relatively large reported uncertainty of bending angles might suggest the simulation-based analysis to be less accurate, error margins reported in studies based on a tangent method often do not take systematic errors like those listed above into account.

A number of marked advantages of our present method become apparent when compared to the other methods. Firstly, our method shares with the msEED method improved reliability of bend angle estimates due to its robustness and immunity for SFM tip convolution effects, to which the tangent method is sensitive. Moreover, they both significantly reduce the time required for the actual analysis, which potentially allows for much better statistics. Secondly, using our distribution-based method, irregular distributions as seen for NFI on the wildtype Ad5 origin (Figure 3.5b) can be immediately disregarded, whereas the msEED and tangent methods yield a poten-

tially unreliable value (Table 3.1). If the data cannot be fit with the simulations like in the case of NFI–DNA (Figure 3.5b), the DNA may have been ill equilibrated in 2D on the surface. Improper equilibration strongly decreases the reliability of bending angle analysis using the tangent method. Equilibration is key to reliable application of the msEED and simulation-based approaches. Hence, besides being a tool to analyze DNA bending angles, our method can also be used to assess the 'quality' of the deposition of the DNA on the mica. Secondly, the present method does not require a visible feature at the site of bending, as exemplified by the case of IHF–DNA complexes. This property also extends the applicability to the analysis of DNA deformations such as those induced by particular sequences or chemical adducts. Another advantage of the simulation-based approach is that it can in principle be adapted for more complex situations. For instance, one could consider (protein-induced) bends that are variable rather than fixed (i.e., hinges) or multiple bends per molecule, whether or not at a defined site. These situations are virtually inaccessible to analytical approaches like the msEED method, yet readily implemented in our simulations.

3.3 Experimental methods

3.3.1 Sample preparation

A linear DNA fragment containing the IHF-site exactly at its centre was obtained by PCR from the vector pGP160 [85] using primer I (5'–GGCGTTATCCCATTTGCTCCA CAGTGCCTCACGATCATAATCATGG–3') and II (5'–CGTCCAGCTCACTACCCGGGCG-TTTTTCTTCAGGTAATGC–3'). Primer II was biotinylated at the 5' end such that the resulting PCR product has a biotin at one of its ends. This primer was also designed such as to give rise to a unique *Sma*I site in the PCR product, which after digestion gives rise to a DNA molecule of 1075 bp. The biotinylated DNA (1-4 pmol) was immobilized on streptavidin-coated paramagnetic beads. After washing the DNA on the beads as described elsewhere [86], the beads were resuspended in 10 µl BI (50 mM HEPES (pH 7.6), 60 mM KCl, 15 mM NaCl, 10 mM $MgCl_2$). 2 pmol IHF was added and the reaction mixture was incubated at 37° C for 30 minutes. After removal of the liquid (to take away excess IHF) the beads were resuspended in 5 µL BI containing 2 units of *Sma*I (New England Biolabs, Beverly, MA) and incubated for 1 hour. 2 µL of the solution containing the IHF–DNA complexes was subsequently diluted 20× into DB (2.5 mM HEPES (pH 7.6), 1.25 mM KCl, 5 mM $MgCl_2$). 12 µL of this mixture was subsequently deposited onto mica. After 1 min. the mica disc was gently rinsed with HPLC water and blown dry with argon.

NFI–, Oct-1– and XPC-HR23B–DNA complexes were prepared as described else-

where [76–78]. The lengths of the respective DNA molecules were 711 bp (NFI and Oct-1) and 769 bp (XPC-HR23B).

3.3.2 Scanning force microscopy

Images of IHF–DNA complexes were acquired on a Nanotec microscope operating in tapping mode in air, with NanoDevices Metrology Probes. Images of NFI-, Oct-1 and XPC-HR23B–DNA complexes were acquired on a Nanoscope IIIa (Digital Instruments, Santa Barbara, CA) operating in tapping mode in air with silicon nanotips™ (Nanoprobe). The size of the DNA fragments used was in the range optimal for detecting changes in EED (roughly from 200 – 500 nm, or 600 – 1500 bp), as derived from the dependence of the mean-squared EED on an induced bend [67].

3.3.3 SFM image analysis

DNA molecules were selected for analysis after visually determining the absence of overlaps with itself or others, as well as for the presence of bound protein (if its size permits). To measure the contour length and EED, DNA molecules were manually traced using Image SXM v. 1.69 (Steve Barrett, Surface Science Research Centre, University of Liverpool, UK). End points were chosen as being at the centre of the semi-circle at the ends of the DNA molecule. Contour length and EED values used for further quantitative analysis were the average of ten repeated measurements.

The thus measured contour lengths of the respective DNA fragments were 352 nm (IHF), 233 nm (NFI and Oct-1), and 259 nm (XPC-HR23B), which results in a rise per bp of 0.33 nm, well in agreement with that of B-form DNA [2]. By comparing the contour lengths of bare and complexed DNA, we assured that the contour length of the DNA is not significantly affected by binding of the protein.

EED values were normalized by dividing the measured EED by the measured contour length of each individual molecule/complex. In the case of IHF–DNA complexes, bending angles were also estimated using the tangent method halfway each molecule's contour.

3.3.4 Fitting procedure

The end-to-end distributions obtained from our experiments were fitted using least-squares minimization to simulated histograms as follows. We first fitted the EED/L data from images of naked DNA controls to the simulated histograms for zero bending angle, to obtain the appropriate persistence lengths for these DNA templates and to ensure that they correspond with literature values. We then fitted the data from DNA

bound by IHF, NFI, Oct-1, and XPC-HR23B to the simulated histograms corresponding to that persistence length, yielding a fit value for the induced bending angle.

In order to perform least-squares minimization in a statistically sound way, we used an expression for χ^2 (the mean-squared error) that is explicitly applicable to data that are, like our histograms, governed by Poisson instead of Gaussian statistics [87]:

$$\chi^2_{\text{Poisson}} = 2\sum_{i=1}^{N} f(x_i,\alpha) - n_i + n_i \log n_i / f(x_i,\alpha),$$

where N is the number of histogram bins, n_i the number of counts in bin i and $f(x_i,\alpha)$ the simulated value for parameters α. To obtain the statistical uncertainty in the best-fit bending angle, we locate the intersections of the χ^2 profile with the minimum $\chi^2_{\text{min}} + 1$ [83] (see Figures 3.4d and 3.7).

Software download

The software written for our simulation-based analysis of bending angles is available for download from `http://www.nat.vu.nl/compl/bendinganalysis`. It has been successfully applied to the study of the DNA-bending angle of *Sulfolobus solfataricus*' LrpB [88], and, for estimation of the persistence length, to the study of nanotube structures self-assembled by α-lactalbumin [89].

3.4 Acknowledgments

Nora Goosen (Leiden University) is kindly acknowledged for the donation of IHF and the vector pGP160. We thank Fred MacKintosh, Bram van den Broek and Wim Sterrenburg (Vrije Universiteit) for useful discussions. This work was financially supported by an ALW-NWO Open competition grant, a grant within the FOM Biomolecular Physics program and an NWO Vernieuwingsimpuls.

4

Visualizing single DNA-bound proteins using DNA as a scanning probe

Abstract — Many biological processes involve enzymes moving along DNA. Such motion might be impeded by DNA-bound proteins or supercoils. Current techniques are incapable of directly measuring forces such 'roadblocks' might impose. We have constructed a setup with four independently movable optical traps, enabling us to manipulate two DNA molecules held between beads. By tightly wrapping one DNA around the other, we create a probe that can be scanned along the contour of the second DNA. Here we show that friction between the two polymers remains below 1 pN. Upon encountering DNA-bound proteins substantial friction forces are measured, allowing for accurate localization of protein positions. Furthermore, we show that these proteins remain associated at low probe tensions but can be driven off using forces that exceed 20 pN. Finally, the orientational control of two DNA molecules opens a wide range of experiments on proteins interacting with multiple DNA regions.

This chapter has been published in *Nature Methods* [90].

4.1 Introduction

Experiments with single DNA molecules have revealed many intrinsic properties of DNA and associated proteins. In these experiments, the precise control of a single DNA molecule allows studying properties of, and interactions between DNA and proteins difficult to assess in conventional biochemical experiments. However, biological processes that require the involvement of multiple DNA tracts are still hard to explore with single DNA molecule experiments. For instance, various DNA recombination proteins [91–93], restriction endonucleases [94] and bridging nucleoid-associated proteins [95] interact simultaneously with two separate DNA regions. The relative angle between, and tensions on such regions cannot be controlled when handling a single DNA molecule. Here we describe a method which allows us to manipulate two DNA molecules independently. This technique enables us to study proteins interacting with multiple DNA binding sites [96]. To demonstrate the capabilities of this technique, we utilize the two DNA molecules in a novel scanning probe technique to detect and manipulate DNA-bound proteins. Many biological processes on DNA involve either ATP-driven or 1D-diffusive motion along the DNA contour [97–99]. Bound proteins or DNA supercoils might act as roadblocks [100], impeding such motion. With this new scanning technique, one DNA molecule is wrapped around the other molecule (Figure 4.1) and then employed as a mechanical probe to scan along the contour of the first DNA molecule. With this scanning mode, we apply forces on single DNA-bound proteins in a direction along the DNA contour. Consequently, we are capable of directly exploring removal of these roadblocks similar to when they are encountered *in vivo* by motor proteins translocating along the DNA contour.

4.2 Results

We have designed and built an optical-tweezers instrument that enables the manipulation of two DNA molecules in three dimensions simultaneously and independently. This is done by trapping micron-sized polystyrene beads attached to the ends of the DNA molecules. As schematically depicted in Figure 4.8 on page 64, four optical traps are generated by first splitting a laser beam in two orthogonally polarized beams. One of these beams generates a continuous trap; the other beam is time-shared over three trap positions using acousto-optic deflectors (see Chapter 2). Forces acting on the bead in the continuous trap can be detected with sub-picoNewton resolution using back-focal-plane interferometry [21, 25]. In order to attach DNA between the four beads held in the optical traps, we designed and constructed a flow chamber with multiple laminar flows of solution running parallel to each other [101] (see section 4.5 for

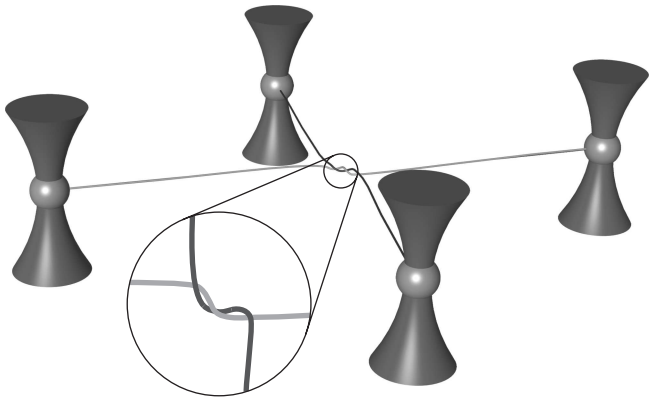

Figure 4.1 – Dual DNA manipulation assay. Two λ-DNA molecules are suspended between four optically trapped polystyrene beads and wound around each other.

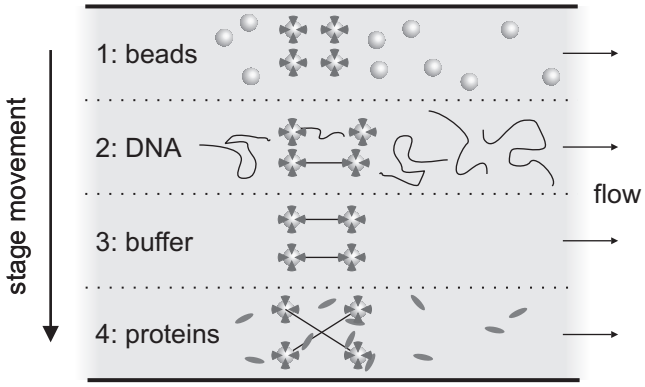

Figure 4.2 – Laminar flow cell. The dual-DNA experiment is conducted in a multi-channel flow cell exhibiting non-mixing laminar flows: 1, bead channel: four beads are trapped with optical traps. 2, DNA channel: two λ-DNA molecules are caught between the beads. 3, buffer channel: here, a number of DNA windings is imposed. 4, protein channel: the DNA is incubated in protein solution. Scanning can be performed either in the protein or buffer channel.

details). By moving the chamber relative to the optical traps, the four trapped beads can be moved into different solutions. In this way, the ends of two DNA molecules can be attached to the four beads (Figure 4.2). After catching two λ-DNA molecules, they are moved into a channel containing only buffer. Using force-extension analysis we ensure that every pair of beads holds only one DNA molecule (Figure 4.3). The four traps can be freely moved with respect to each other in the sample plane, giving us full control over the relative orientation of the two DNA molecules as well as the tension on both molecules. In addition, moving the continuous trap in the third dimension enables us to wind one DNA molecule around the other.

4.2.1 Using DNA as a scanning probe

In order to scan one DNA duplex (the scanned DNA) using the second one as probe (the probing DNA), we positioned the beads such that the two DNA molecules are in a crossed configuration. Next, the probing DNA is wrapped around the scanned DNA one or multiple time(s), creating a loop (Figure 4.1). We stretch both DNA molecules to a pre-set tension, (typically 5–20 pN) to tighten the DNA loop. For a circular DNA

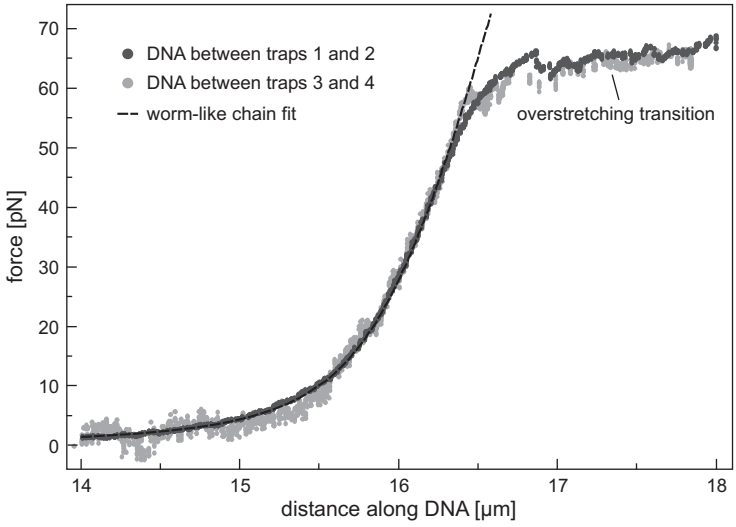

Figure 4.3 – Force-extension analysis of two DNA molecules. Two force-extension curves of two λ-DNA molecules, taken simultaneously. The scanned DNA molecule is suspended between two beads, one in the continuous trap and one in a time-shared trap. The probing DNA is suspended between two beads caught in time-shared traps and a separate detection laser is used for detection on one of these beads. The black trace shows the worm-like chain behavior with which the DNA can be modeled.

loop, the diameter D depends on the tension S and the persistence length P as $D \approx \sqrt{2Pk_BT/S}$ [102], approximately 5–10 nm for the tensions mentioned above. This is an upper limit of the actual probe size, since in our experiments the DNA loop does not have a circular, but a twisted or supercoil-like structure (Figure 4.1). By moving both beads that hold the probing DNA (beads 3 and 4 in Figure 4.4a) simultaneously

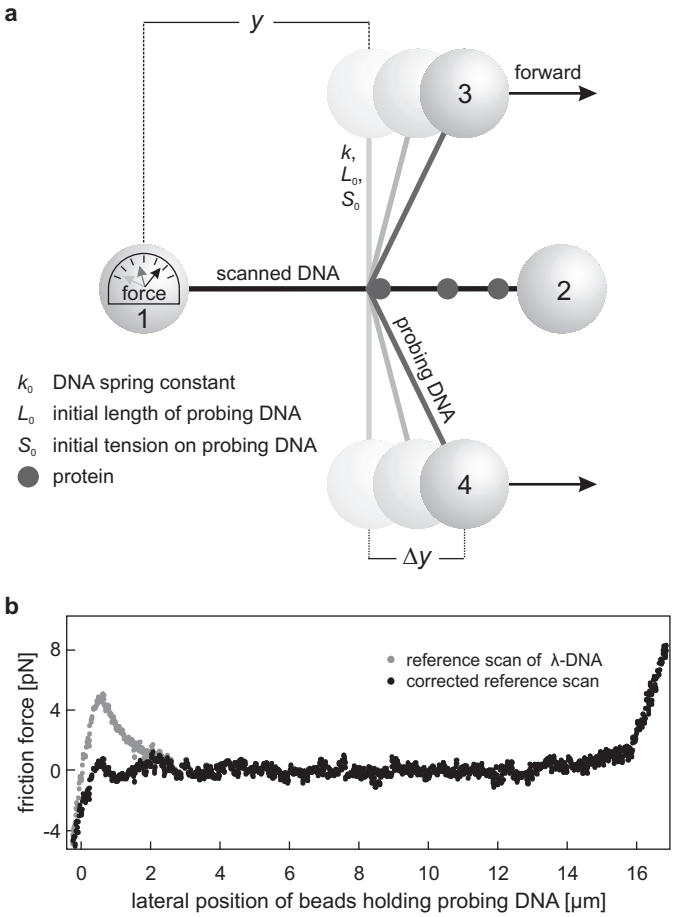

Figure 4.4 – DNA scanning scheme and reference scan. [**a**] To detect DNA-bound proteins, the probing DNA (held between beads 3 and 4) is moved along the scanned DNA. Upon encountering a protein bound to the scanned DNA, the measured force on bead 1 scales with distance y. [**b**] Typical scanning trace of λ-DNA without proteins (gray) using a probing force of 10 pN. The black trace shows the same data, corrected for interference between time-shared traps holding beads 3 and 4 and the continuous trap holding bead 1 (see Figure 4.10 and section 4.5.4).

parallel to the scanned DNA, we utilize the DNA loop to probe the contour of the scanned DNA (Figure 4.4a). If this DNA loop stalls due to an obstacle or friction on the scanned DNA, we measure an increase in force on the bead in the continuous trap.

Figure 4.4b displays a typical scanning trace of λ-DNA in the presence of 5 mM Ca^{2+}. The feature visible on the left side of the measured reference scan (gray) in Figure 4.4b is due to the collinear alignment of the time-shared optical traps 3 and 4 with the (continuous) trap 1, used for force detection [26]. In the black trace and all subsequent traces this is corrected for (see Figure 4.10 and section 4.5.4 for details). The left edge of a scanning trace is marked by the probing DNA pushing against bead 1, resulting in a negative force. Similarly, at the right edge of the trace, the probing DNA pushes against bead 2 resulting in a positive force measured at bead 1. The difference in slopes originates from additional stretching of the scanned DNA.

Notably, the friction force between the tightly pulled DNA loop and the scanned DNA remains well below 1 pN (standard deviation (s.d.) of friction signal: 0.3 pN around the base line). Similar results were obtained when scanning in the presence of only 150 mM Na^{+} and no divalent salts (s.d.: 0.2 pN) and even in DNA condensing conditions [103], 200 μm spermine^{4+}, (s.d.: 0.4 pN). Scans at various speeds (∼200–2000 bp/s) and with various tensions on both DNA molecules, with single and multiple DNA windings yielded similar results as well. Thus, even though in DNA condensing conditions the repulsion between the negatively charged DNA molecules is practically neutralized, very little frictional interaction is present when the two tightly wrapped DNA molecules are moved past each other.

To further demonstrate the localization and manipulation capabilities of our technique, we incubated the scanned λ-DNA with Type IIP restriction enzymes in non-cleaving conditions. These restriction enzymes bind specifically to their recognition sequence. Because the locations of these recognition sequences are known, these enzymes function as a convenient site-specific marker in these experiments. Figure 4.5a displays three consecutive scans in forward and backward directions along the same λ-DNA molecule with *Eco*RI restriction enzymes associated to it. In these traces, force peaks are measured at four locations that match with the expected specific target sites of *Eco*RI, immediately revealing the orientation of the DNA. Besides peaks at these specific sites, we occasionally observe additional (smaller) peaks at other locations. Presumably this is a signature of non-specific or non-cognate binding of *Eco*RI to sites that are similar (e.g., 1 base pair mismatch) to the specific binding sequence—over 250 of such sites are present on λ-DNA. At every bound protein that is encountered by the DNA probe the measured force on bead 1 increases with similar inclination, after which it 'snaps back' to a zero friction force. The distribution of measured peak forces for both non-specific and specific events from the scan displayed in Figure 4.5b shows

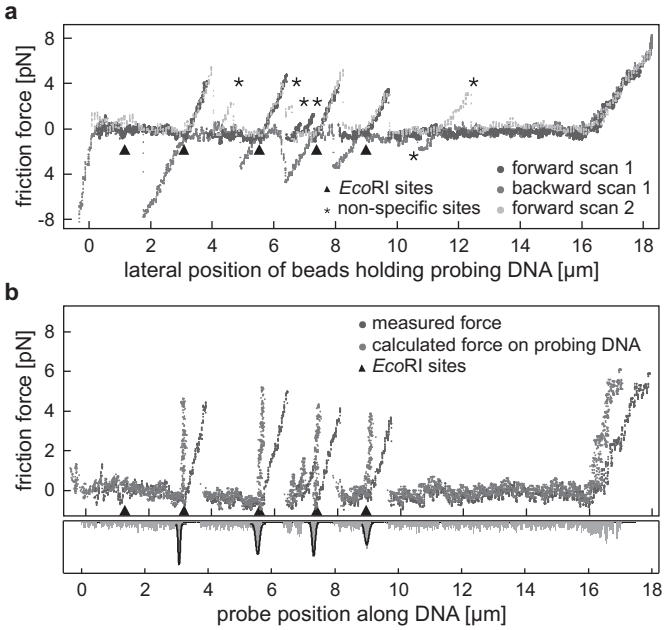

Figure 4.5 – Detection of individual DNA-bound restriction enzymes. [**a**] Three consecutive scans along λ-DNA in forward and backward directions, with 0.1 units/l (∼1 nM) *Eco*RI restriction enzyme bound to the DNA using a probe tension of 10 pN. An additional friction force is measured when the probing DNA loop stalls behind DNA-bound *Eco*RI proteins (sites indicated with black triangles). Less substantial peaks presumably indicate non-specific scanned DNA–*Eco*RI interactions (indicated with black asterisks). The x–axis depicts the location of the beads holding the probing DNA. [**b**] During each event, the traveled distance by the probing DNA y, can be corrected by modeling the lateral stretching of the probing DNA and the bead displacement out of the optical traps (see the Appendix on page 69). Corrected data of the probing DNA scanning loop (light gray), calculated from the *Eco*RI forward scan (dark gray). The x-axis now depicts the location of the scanning loop. At four peaks the distribution is fit with Gaussians (lower graph) to determine the location of specifically bound proteins with ∼120 bp resolution.

that forces measured at non-specific sites, 2 ± 1 pN (n = 7, s.e.m.) with a typical duration of 3 ± 1 s, are substantially lower than at specific sites, 5 ± 1 pN (n = 11, s.e.m.) with a duration of 7 ± 2 s. This implies that the nature of the events is different. The fact that peak forces at non-specific sites are lower may indicate that the probe triggers such a protein to dissociate, whereas a specifically bound protein may either dissociate (yet at a higher peak force) or stay bound with the probe slipping

over it. Below we demonstrate that for low probe tensions the latter is the case.

4.2.2 Resolution and accuracy

To determine the accuracy and resolution of our scanning technique, we corrected our data to compensate for lateral stretching of the scanning DNA molecule and bead displacement out of the optical traps (see Appendix on page 69). Figure 4.5b displays the thus corrected force-distance trace for the first *Eco*RI forward scan in Figure 4.5a, where the x–axis now represents the actual position of the probing loop and the force increases vertically at every encountered protein. The accuracy of localization of the DNA-bound proteins is assessed by evaluating a dwell time histogram of the corrected data (Figure 4.5b lower graph). From the standard deviations of Gaussian fits to the observed peaks, we determine the spatial resolution to be ∼120 bp. Comparison with the known locations of the specific binding sequences on λ-DNA yields a relative position accuracy of ∼50 bp. In Figure 4.6 we focus on a part of the DNA that contains four *Eco*RV restriction sites, three of which can be unambiguously distinguished. The fourth site cannot be distinguished since it is only separated 35 bp from the adjacent site, demonstrating the finite resolution of the technique.

The (un)binding of DNA-associated proteins can be probed with a repetition rate equal to the scan time, typically 100 seconds for the complete λ-DNA at a scanning speed of 500 bp/s. The temporal resolution can be greatly improved by scanning only part of the DNA or by increasing the scanning speed. However, high scanning speeds will result in larger loading rates acting on the enzyme-DNA bond, possibly activating dissociation [104]. Moreover, the stretch correction fails where the DNA elasticity starts to deviate from the worm-like chain (WLC), at ∼50 pN total force. Finally, the nature of the DNA itself sets an upper limit to the force that can be applied since at

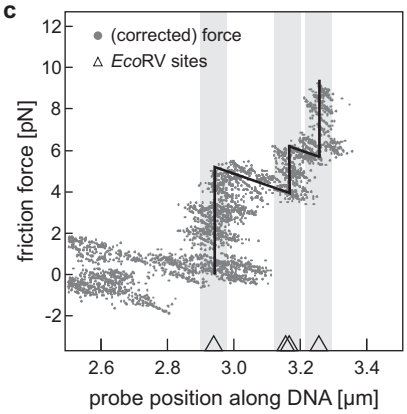

Figure 4.6 – Resolution of protein localization. Detail of a scan along a λ-DNA molecule incubated with *Eco*RV restriction enzymes using a probe tension of 25 pN. The scan shows the presence of three proteins on the DNA whereas there are four known binding sites, demonstrating the resolution of the method. The gray boxes indicate the spatial resolution of the localization. The dark line is drawn to guide the eye.

65 pN the DNA double helix starts to overstretch [7], making it difficult to interpret the signal.

4.2.3 Detection efficiency

We determined the detection efficiency using Type IIP restriction enzymes that have well-known (and well-separated) locations of their binding sites on λ–DNA. This allows for distinguishing false positives (i.e., the probe sticking at locations where no protein is bound) from specifically bound proteins. We did not observe such events when scanning DNA in the absence of proteins. Since it is known that restriction enzymes can bind DNA in a non-specific manner [105], we do not regard events in the presence of proteins at non-specific sites as false positives.

On λ-DNA there are five recognition sites for *Eco*RI whereas in Figure 4.5a we detect four specifically bound proteins. The fact that we neither detect a protein at this particular location in the second and third scan (while the other four are consequently detected) makes it unlikely that there is actually a protein bound at this location. When we repeatedly scan other constructs we observe similar results and therefore we argue that hardly any proteins are missed with this method. Apparently, the absence of proteins at specific binding locations is limited by the biochemical binding probability of proteins [106] or local irregularities on the DNA.

4.2.4 (Non-)destructive imaging

Do the specifically bound proteins stay bound when the scanning loop encounters them or are they pulled off their binding site and subsequently replaced by others present in the surrounding solution? To examine this, we first 'loaded' the DNA construct with *Sbf*I restriction enzyme (under conditions where generally the protein stays bound for ∼1 hr [107]) by briefly moving it into a flow channel containing the proteins. We then moved the DNA into a channel with identical buffer conditions but without proteins to ensure that no more proteins could bind to the DNA. Hereafter, we scanned the DNA repeatedly at a probe tension of ∼10 pN. Figure 4.7a shows the friction force of a part of a λ–DNA molecule with a protein bound to the single *Sbf*I-site that is present in this region, which is scanned three times in succession. The scans show that the *Sbf*I stays bound, demonstrating that the protein binding is undisturbed by the DNA scanning. Apparently, the DNA loop that exerts lateral force on the bound protein slips over it when some critical force is reached (in this case ∼10–20 pN).

Increasing the tension on the probing DNA results in a tighter DNA loop, potentially preventing it from slipping over the protein. When this probe tension is

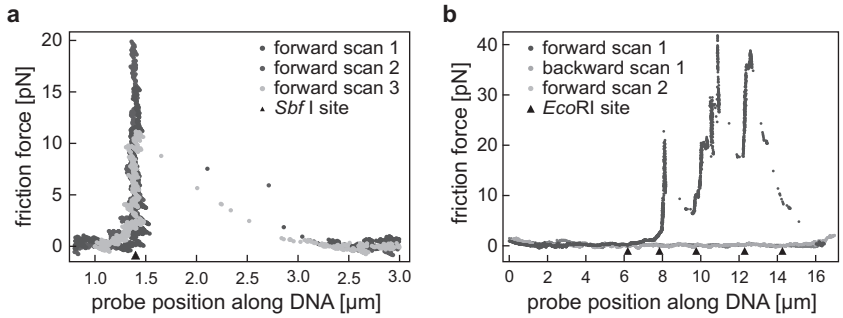

Figure 4.7 – (Non-)destructive imaging. [**a**] Three consecutive scans (in forward direction and corrected for lateral stretching of the probing DNA) acquired in a buffer solution without proteins, after loading of the DNA construct with *Sbf*I. All detected proteins stay bound when scanned with a low probe tension (5-10 pN). [**b**] Destructive imaging. A larger tension on the probing DNA (35-40 pN) yields a smaller loop-size. Consecutive traces show that this results in a DNA molecule with no proteins associated to it. The two peaks right after the third specific site are attributed to non-specifically bound proteins, briefly interacting (∼3 s) with the scanning probe before dissociating.

increased to 25–40 pN, the observed force peaks are significantly higher: 20–40 pN (Figure 4.7b). In subsequent scans no more force peaks appear, indicating that proteins are indeed pushed off by the application of high lateral forces.

4.3 Discussion

An alternative technique capable of manipulating multiple DNA molecules is to attach two DNA molecules between a surface and a single paramagnetic bead manipulated by magnetic tweezers [108]. By rotating the magnetic bead, the DNA molecules are wound around each other. Unlike our approach, this technique yields very limited control over the relative orientation of the DNA molecules and lacks the ability to exert different forces on them.

An established scanning probe technique is scanning force microscopy (SFM). With SFM, deviations of a scanning tip are used to generate a topographic image [10]. DNA can be visualized and associated proteins may be observed [109] and manipulated [110]. In contrast to SFM experiments, the technique introduced here is performed far away from any (charged) surfaces that potentially affect protein-DNA interactions [111, 112]. Additionally, we exert and measure forces on the proteins *in the direction* of the DNA contour, as is also expected for a roadblock encounter *in vivo*.

Recently, the development of a technique combining a scanning probe and opti-

cal tweezers was reported [113]. A micropipette is used as a probe to scan along the contour of a DNA molecule suspended between optical tweezers. The technique, however, has not yet been shown to allow detection of proteins bound to DNA. Since the micropipette scans the DNA on one side only and does not enclose it, as in our case, it might miss bound proteins due to the finite torsional compliance of the DNA. Finally, a technique in which mechanical separation of the two strands of the DNA double helix provides information about the location of associated proteins and binding strengths has been described [114]. Contrary to our capability to visualize individual DNA-associated proteins repeatedly without affecting the binding, unzipping the double helix leads to destruction of the protein recognition site.

4.4 Outlook

We have described the design and application of a dual DNA manipulation technique. The realization of four movable optical traps in combination with the laminar flow system provides a powerful means to study biological processes governed by proteins interacting with multiple DNA sites [86, 94, 115, 116]. The involvement of multiple DNA-binding domains complicates studying their interactions with conventional single-molecule approaches. With our dual-DNA manipulation technique, such interactions can now be explored in detail [96]. The scanning probe technique introduced here, where DNA itself is utilized as a scanning probe, illustrating the topological freedom this dual DNA assay offers.

4.5 Experimental methods

4.5.1 DNA and proteins

To allow specific binding to streptavidin-coated beads (1.87 μm diameter, Spherotech Inc., IL), we biotinylated λ-phage dsDNA (Roche) at both ends on opposite strands. To this end, we incubated the DNA for 30 min at 37° C with 80 mM biotin-14-dATP and biotin-14-dCTP (Invitrogen), 100 mM dGTP and dTTP (Sigma-Aldrich) and Klenow DNA Polymerase exo$^-$ (Fermentas) to fill in the 5'-overhangs. Excess nucleotides were removed with Microcon YM-10 filters (Millipore) in 10 mM Tris-HCl (pH 7.7). *Eco*RI and *Sbf*I were purchased from New England Biolabs (Ipswich, MA) and used without further purification. We recovered *Eco*RV from ammonium sulfate precipitates, dialyzed it into (10% (v/v) glycerol, 20 mM Tris-HCl (pH 7.5), 1 M NaCl, 10 mM 2-mercaptoethanol, 1 mM EDTA and filtered it through 0.2 μm syringe filters. Aliquots (59 μm) were flash-frozen and stored at −80 ° C. We performed all protein scanning

experiments in 10 mM Tris-HCl (pH 7.5), 100 mM NaCl, 5 mM $CaCl_2$ and 1 mM DTT, with protein concentrations of ∼1–5 nM.

4.5.2 Experimental setup

We performed the experiments using a custom-built inverted microscope as shown in Figure 4.8. To generate the optical traps we used a Nd:YVO_4 laser (1064 nm 10W cw, Millennia IR, Spectra Physics, Mountain View, CA), isolated against back-reflections by a Faraday isolator (IO-3-λ-VHP, Optics For Research, Caldwell, NJ) and expanded by a beam expander (2–8×, Linos Photonics GmbH, Göttingen, Germany). We split this laser beam into two beams by a polarizing beam splitter cube (PBS-1064, CVI, Albuquerque, NM). In both beam paths, we implemented a 1:1 telescope system ($f = 150$ mm) allowing beam steering in the sample [16]. In one path (which we refer to as the 'continuous' path), the first telescope lens could be displaced laterally using two computer-controlled actuators (T–LA28, Zaber Technologies Inc., Richmond, British Columbia, Canada). In the other 'time-shared' path, we placed two orthogonal acousto-optic deflectors (AODs, DTD 276HD6, IntraAction, Bellwood, IL) directly in front of the telescope. We then coupled the first-order deflected beam via a dichroic mirror (1020dclp, Chroma Tech Corp., Rockingham, VT) into a 60× water-immersion

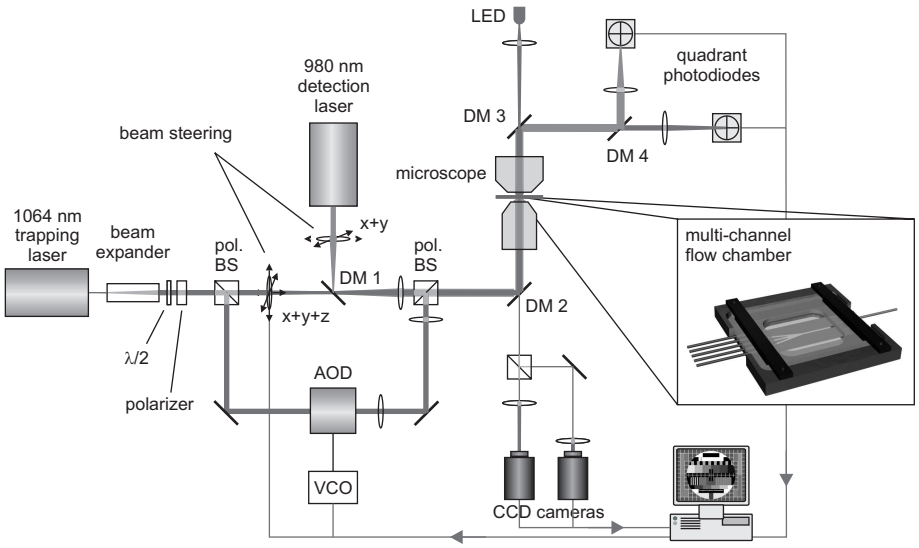

Figure 4.8 – Schematic representation of the experimental setup. The inset shows an impression of the multi-channel flow cell. See section 4.5 for details.

objective (Plan Apochromat 60, NA = 1.2, Nikon) to form the other laser traps.

A third computer-controlled actuator moves the first telescope lens in the continuous path along the propagation direction of the laser light, thereby changing the depth of the laser focus with respect to the traps from the time-shared path. Doing so, we can wind two DNA molecules around one another.

For displacement detection of the continuous trap, we imaged the intensity profile in the back focal plane of the condenser (Achromat/Aplanat, NA = 1.4, Nikon) onto a quadrant photodiode (QPD, SPOT-9DMI, UDT Sensors, Hawthorne, CA) [21]. We likewise measured displacements in one of the AOD-generated traps using a separate (low-power, non-trapping) detection laser (980 nm IQ2C140/6018, Power Technology Inc.), overlaid on the trap and imaged onto a separate QPD. To generate multiple traps, the AODs were driven by voltage-controlled oscillators (VCOs) (DE-272H Deflector Driver, IntraAction, Bellwood, IL) as RF synthesizers (see below). A bright-field image of the trapped beads, illuminated by a blue LED (LXHL-NB98 Luxeon Star/O, LumiLeds) was imaged onto a CCD camera (902B, Watec).

4.5.3 Quadruple trap implementation

We used AODs to generate three independent, time-shared traps by modulating the VCOs that synthesize the RF signal with analog voltages generated by a multifunction data acquisition PC board (NI PCI-6221, National Instruments, Austin, TX), similar to the approach used in Chapter 2. Using two orthogonally placed AODs, traps can be generated and steered in both directions in the sample plane. The DC-offset of the voltage that is input to the VCO determines the frequency deviation of the synthesized RF signals (typically 27 MHz) that drive the AODs. Therefore, VCO-input signals consisting of repeated patterns with a number of DC levels yield a corresponding number of successively scanned, independent laser deviations (see Figure 4.9) and thus trap positions in the sample.

4.5.4 Correction of interference between traps

At the beginning of a scan, when time-shared traps 3 and 4 are in a collinear geometry with trap 1 (see Figure 4.4), the rapid time-sharing between traps 3 and 4 causes interference on the signal detected from the optical trap holding bead 1, as seen in the scan without DNA (black trace in Figure 4.10a). The deviation of the DNA scan from this reference trace is caused by the probing DNA, pulling on bead 1 when the three traps align. [**b**] The same scan (with DNA) corrected for this interference effect by subtracting the scan without DNA. The deviation from zero force is now exclusively

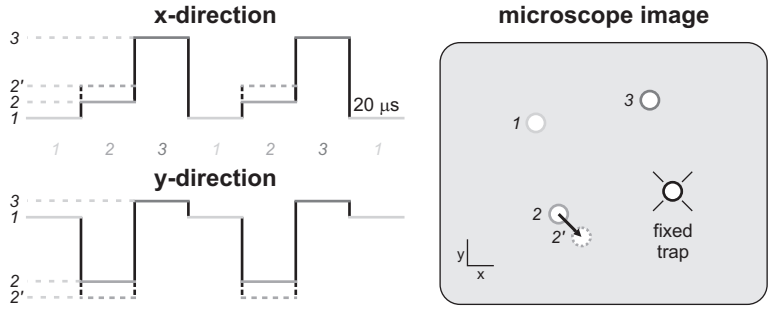

Figure 4.9 – Input signal for time-shared trap generation and corresponding trap position. Example of multi-level square-wave voltage signal serving as input for the VCOs. The DC-offset of the voltage that is input to the VCO determines the frequency deviation of the synthesized RF signals that drive the AODs. Altering one of the DC levels, for instance level 2→ 2'), changes the position of one of the traps in the sample. These levels were output at a typical refresh rate of 20 kHz. Since this rate greatly exceeds the cut-off frequencies of the (suppressed) Brownian motion (∼1.5 kHz) that the beads undergo in the traps, the beads are trapped stably enough to allow for DNA stretching up to and beyond the overstretching plateau at 65 pN (see Figure 4.3).

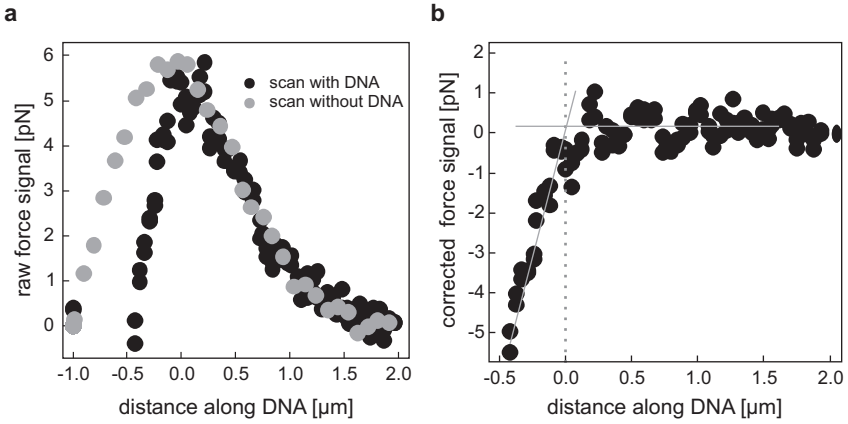

Figure 4.10 – Correction of interference between traps. [**a**] Scan with and without DNA present between the beads. [**b**] The same scan (with DNA) corrected for the interference between collinear traps in panel a by subtracting the scan without DNA. See section 4.5.4 for details.

due to the probing DNA pulling on bead 1 (see also Figure 4.4b. This correction allows for marking the beginning of the scanned DNA.

4.5.5 Microfluidic flow cell

To enable swift exchange of buffers and to have fine control over the process of catching the DNA molecules between beads, we used a custom-built microfluidic flow chamber (Figures 4.2 and 4.8). The central part of this flow chamber consists of four channels cut manually out of a spacer (Parafilm), as depicted in Figure 4.2, sandwiched between a 24×60 mm #1 cover slip and a $50 \times 75 \times 1$ mm microscope slide. The slide contains 1-mm holes which connect to the input channels. By cutting a pattern with merging channels, a region exists in the flow chamber where juxtaposed buffers exhibit laminar flow. At the locus of the experiment in the flow chamber the channels are well-separated, facilitating rigorous sub-second buffer exchange by simply translating the microscope stage in a direction perpendicular to the flow (vertical arrow in Figure 4.2). A custom-made, sealed pressure chamber holds a reservoir for different solutions (containing beads, DNA, restriction enzymes or buffer). Contents of each channel are input to the channels through PEEK™ tubing (Upchurch Scientific Inc., Oak Harbor, WA) and can be altered using selection valves (V-241, Upchurch Scientific Inc.). We control the flow speed through adjustment of the air pressure in the pressure chamber, thereby pushing the buffers through the flow chamber [42]. Fine control of pressure is attained by using solenoid valves (ES-2T-6, Clippard Europe S.A., Louvain-la-Neuve-Sud, Belgium) to in- or decrease the pressure, while monitoring the pressure using a differential pressure meter (CTE8005GY0, Sensortechnics GmbH, Puchheim, Germany). This approach yields smoother flow (transitions) than when using a stepper motor syringe pump [33]. Typical working flow speeds are on the order of 100 μm/s, achieved at 50–100 mbar overpressure. To diminish any effects of flow on the measured force, we turned off the buffer flow during actual measurements. To ensure that the solution in which the experiments are performed remain uncontaminated, the measurements are typically done in a channel before it merges with the others in the laminar flow chamber.

4.5.6 Data acquisition and analysis

For two traps, we recorded bead displacements within the traps in x and y directions using two quadrant photodiodes and a data acquisition board (AD16 module on a ChicoPlus PCI board, max. sampling rate 195 kHz, Innovative Integration, Simi Valley, CA) [21, 26]. We calibrated voltages to forces using power spectrum analysis [21]. For concurrent force and extension recordings of the captured DNA molecules, we

measured the distances between pairs of beads on-line using pattern matching on a digitized microscope image (IMAQ PCI-1409 and NI-Vision software, National Instruments).

4.6 Acknowledgments

We thank E. J. G. Peterman and R. T. Dame for useful discussions. We acknowledge D. A. Hiller and J. J. Perona for the kind gift of *Eco*RV. This research was supported by the Netherlands Organization for Scientific Research (NWO) through an NWO-Vernieuwingsimpuls grant, a FOM-projectruimte grant and a grant from ALW-NWO.

Appendix: Derivation of lateral spring constant of the probing DNA

The slope in the increasing force signal measured upon the encounter with a bound protein is most likely due to the lateral stretching of the probing DNA. We calculated the position of the scanning loop along the scanned DNA based on the force and measured positions of beads 3 and 4, and corrected the traces for this effect. The probing DNA has initial contour length L_0 and initial tension S_0. The loop in the probing DNA is deflected by a distance y. This causes the tension on it to increase to S and stretch to length L. These parameters relate to their initial values by:

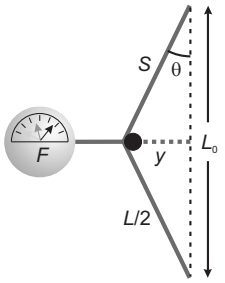

Figure 4.11 – Diagram introducing the variables used in the scan correction model.

$$\begin{aligned} L &= \sqrt{L_0^2 + 4y^2}, \\ S &= S_0 + k\left(L - L_0\right), \end{aligned} \tag{4.1}$$

where k is the intrinsic spring constant of the DNA. To correct for the position of the probe, the deflection y as a function of force F, we need to calculate the effective spring constant of the probing DNA perpendicular to its axis. The applied force can be described by (see Figure 4.11):

$$F = 2S\sin\theta = \frac{4Sy}{L}. \tag{4.2}$$

This means the perpendicular spring constant $k_\perp$ can be modeled by

$$k_\perp = \frac{F}{y} = \frac{4S}{L}. \tag{4.3}$$

If we assume that the deflection y of the probing DNA is much less than the length L_0 of the probing DNA, Eq. 4.1 can be approximated as:

$$\begin{aligned} L &\approx L_0 + \frac{2y^2}{L_0}, \\ S &\approx S_0 + \frac{2ky^2}{L_0}. \end{aligned} \tag{4.4}$$

The perpendicular spring constant (Eq. 4.3) now becomes:

$$k_{\perp} = \frac{4S}{L} \approx \frac{4S_0 + 8ky^2/L_0}{L_0 + 2y^2/L_0} \approx \frac{4}{L_0}\left[S_0 + \frac{2ky^2}{L_0}\right]. \tag{4.5}$$

The intrinsic spring constant of the probing DNA can be estimated by approximating the behavior of DNA with the worm-like chain model [4,5]:

$$F = \frac{k_B T}{P}\left[\frac{1}{4\left(1 - x/L_0\right)^2} + \frac{x}{L_0} - \frac{1}{4}\right], \tag{4.6}$$

where F is the applied force, P the persistence length, x the end-to-end distance, $k_B T$ the thermal energy and L_0 the contour length. The intrinsic spring constant k_{DNA} can now be determined as [42]:

$$k_{DNA} = \left.\frac{\partial F}{\partial x}\right|_{x \approx L} = \frac{4F^{3/2}}{L_0}\sqrt{\frac{P}{k_B T}}. \tag{4.7}$$

Inserting Eq. 4.7 into Eq. 4.5, where the force F is equal to tension S, yields:

$$k_{\perp} \approx \frac{4}{L_0}\left[S_0 + \frac{8S^{3/2}y^2}{L_0^2}\sqrt{\frac{P}{k_B T}}\right]. \tag{4.8}$$

Now the relation between the measured force F and the inferred deflection y is:

$$F \approx \frac{4y}{L_0}\left[S_0 + \frac{8S^{3/2}y^2}{L_0^2}\sqrt{\frac{P}{k_B T}}\right]. \tag{4.9}$$

This allows for determining y as a function of F, which is used to correct the force traces for lateral stretching of the probing DNA.

5

‘See me, feel me’: Methods to concurrently visualize and manipulate single DNA molecules and associated proteins

Abstract — Direct visualization of DNA and proteins allows researchers to investigate DNA–protein interaction with great detail. Much progress has been made in this area as a result of increasingly sensitive single-molecule fluorescence techniques. At the same time, methods that control the conformation of DNA molecules have been improving constantly. The combination of both techniques has appealed to researchers ever since single-molecule measurements have become possible and indeed first implementations of such combined approaches have proven useful in the study of several DNA-binding proteins in real-time. Here, we describe the technical state-of-the-art of various integrated manipulation-and-visualization methods. We first discuss methods that allow only little control over the DNA conformation, such as DNA combing. We then describe DNA flow-stretching approaches that allow more control, and end with the full control on position and extension obtained by manipulating DNA with optical tweezers. The advantages and limitations of the various techniques are discussed, as well as several examples of applications to biophysical or biochemical questions. We conclude with an outlook describing potential future technical developments in combining fluorescence microscopy with DNA micromanipulation technology.

5.1 Introduction

The most powerful and convincing approach to decipher protein-DNA interactions is to directly observe proteins binding to DNA under well-controlled conditions. To achieve this, scientists have developed ever more powerful methods and instrumentation. In most of these approaches, the DNA is manipulated in some way, while the DNA and/or proteins binding to it are observed with fluorescence microscopy. Fluorescence microscopy has become so sensitive that single fluorophores can be detected and interrogated routinely. Single-molecule fluorescence microscopy on DNA and DNA-binding proteins has been successfully applied to many biologically relevant systems [117]. In most of these experiments, short DNA fragments are used, either free in solution or attached to a surface. In organisms, however, DNA molecules are in general very long, flexible and dynamic. In order to observe the interaction of a protein with such more natural DNA substrates, fluorescent observation of the protein (or DNA) is not enough: the shape and position of the DNA has to be well-controlled. Over the years, many methods for manipulating single DNA molecules have been developed. Approaches such as magnetic and optical tweezers and flow stretching have led to a remarkable understanding of the complex mechanical properties of DNA. Furthermore, these methods have been applied to study the actions of proteins interacting with the DNA, indirectly by measuring changes in the physical properties of the DNA strand (length, stiffness, elasticity) [18]. Such indirect detection has proven to be powerful, but in many cases the actual location and potential multimerization state of the proteins on the DNA are crucial to understand their functioning. Moreover, having mechanical cues backed up by simultaneous direct (fluorescent) observation of proteins interacting with DNA strengthens the quality of the data: both signatures have to match, providing an intrinsic experimental control: *seeing is believing*. These considerations have led researchers to combine (single-molecule) fluorescence microscopy with DNA manipulation tools. In this review we will discuss this development, from relatively simple (but powerful) methods that allow limited control of the DNA up to sophisticated instruments with high degrees of control of the DNA and capabilities of high-resolution detection and localization of DNA-bound proteins.

5.2 Molecular combing

5.2.1 Technique description

One of the least complicated techniques to manipulate single DNA molecules for visualization with fluorescence microscopy is molecular combing. In molecular comb-

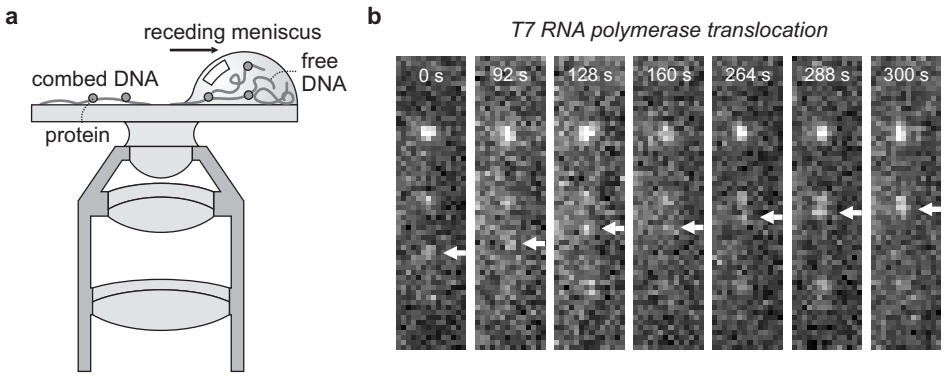

Figure 5.1 – Immobilizing DNA on a surface by combing. [**a**] Cartoon of the combing procedure. DNA can be stretched and immobilized using hydrophobic silanized glass surfaces and a receding air-water interface. After rehydration of the sample the DNA stays firmly attached to the glass slide. Combing can also be achieved using fluid flow which results in lower stretching forces. [**b**] Kim and Larson visualized in real time the motion of T7 RNAP along combed DNA strands [118]. The directional movement of the T7 RNAP elongation complex along a DNA molecule is observed using the incorporation of fluorescent UTP into RNA strand. Adapted by permission of Oxford University Press from Ref. [118].

ing, DNA molecules are (non-)specifically attached to a solid surface, extended and aligned by various means. The first report of molecular combing was by Bensimon *et al.* [119]. They stretched long pieces of DNA (50 kbp up to 1 Mbp) on hydrophobic silanized glass surfaces using a receding air-water interface (Figure 5.1a). Surface tension extends the DNA and results in stretched DNA. In this way, DNA is irreversibly stuck to the surface and rehydration of the sample does not result in detachment of the DNA. The non-specific attachment of the DNA to the surface is probably the result of hydrophobic interaction with parts of the double-stranded DNA that have frayed and thus expose hydrophobic single-stranded DNA pieces. This combing procedure has found powerful uses in mapping and analyzing complete genomes with fluorescent *in situ* hybridization (FISH)—see for more details the review of Lebofsky and Bensimon [120]. Its major drawback is, however, that it overstretches the DNA (i.e., the DNA is longer than its contour length) [7] because of the high surface tension at the air-water interface ($\sim$0.5 nN) [121]. This major structural change most probably interferes with DNA–protein interaction.

In an elegant solution to this problem, Gueroui *et al.* [122] lowered the surface tension by addition of a monolayer of the fatty alcohol 1-dodecanol at the air-water interface. This resulted in combed DNA extended to its contour length. The low

solubility of 1-decanol in water (∼1 ppm) results in a negligibly low effect on the properties of the DNA molecules in solution. Another solution is to use fluid flow in a flow cell to stretch the DNA. Although this approach requires more sophisticated instrumentation, it provides much more control on the degree of DNA extension [123].

By using a different treatment of the surfaces, the extent and nature of the interactions of the DNA with the surface can be altered. On hydrophobic silanized surfaces DNA is stuck along its full length with a very high density of attachment points. When the glass is coated with hydrophobic polymers such as polymethylmetacrylate (PMMA), polydimethyl-siloxane (PDMS) or polystyrene, the combed DNA only attaches in a few places to the surface [122, 123]. When the pH is lowered to a value of 6 during combing, the tethering can be restricted to only the extremities of the DNA [123]. The use of biotin labels on the DNA ends in combination with biotin binding glass (for example coated with streptavidin) provides another means to ensure that DNA only sticks with its end to the surface [118]. When the DNA is only attached to the glass at a few positions and not overstretched, combing is an excellent means to study interactions between the DNA and DNA-binding proteins.

In molecular combing, DNA is often visualized with intercalating dyes such as YOYO-1 [119]. YOYO-1 lengthens and stiffens the DNA, which can actually help to stretch the DNA to full length [124]. On the other hand, structural modification of DNA by YOYO-1 might interfere with DNA-binding proteins and therefore other means of visualization have been developed, in most cases involving specific end-labeling of the DNA. Crut *et al.*, for instance, used quantum dots to discern the ends of combed DNA [125], while Chan *et al.* generated fluorescent end-labels using PCR with Cy3- and Cy5-labeled primers [124]. The latter study demonstrated that it is possible to use a mixture of Cy5-labeled nucleotides and unlabeled nucleotides in the PCR to lightly stain an entire DNA molecule [124], albeit constrained to a DNA length of ∼25 kb due to PCR limitations. For fluorescence imaging of combed DNA wide-field, epi-illuminated fluorescence microscopy is often used, using CCD cameras as detector. Alternatively, with the combed DNA attached to a glass-water interface, total internal reflection fluorescence (TIRF) microscopy can be used [126].

5.2.2 Applications

A good example of the combination of combed DNA and TIRF microscopy for the study of protein-DNA interactions is the work of Kim and Larson, who visualized in real time the diffusive motion of immunolabeled T7 RNA polymerase (RNAP) along DNA [118]. They combed λ-phage DNA by flow, thus avoiding overstretching of the DNA, and attached it to a hydrophobic surface, resulting in multiple anchor points

along the backbone. They did not observe any hindrance of RNAP's diffusive motion by the anchor points. RNAP was localized by fitting the fluorescence intensity profiles with 2D-Gaussians [127] with an accuracy of 60 nm (standard error). They determined RNAP's diffusion coefficient to be $1.2 \pm 1.0 \cdot 10^{-9}\,\mathrm{cm}^2/\mathrm{s}$ ($3.6 \cdot 10^7\,\mathrm{bp}^2/\mathrm{s}$) from the mean square displacement along the contour. They showed that the large spread in the diffusion constants is not due to the uncertainty of protein localization but to a surprising, intrinsic variability of individual RNAPs. This conclusion could only be reached because this approach allows the observation of individual proteins moving along DNA. Next, the researchers visualized RNAP binding, initiation and transcription. In the latter experiment, they used fluorescently labeled nucleotides that are incorporated in the nascent RNA produced during transcription (Figure 5.1b). During transcription, however, the moving RNAP halts at the location where the DNA is anchored to the surface and transcription stalls. The authors estimated the tension on the DNA from the rates of transcription they observed. This indirect way of determining the force requires the assumption that only force alters the transcription rate and that surface proximity or non-uniform NTP concentrations do not alter the rate. A more direct way of controlling the force on the DNA would be preferable.

5.3 Surface-tethered DNA extended in flow

5.3.1 Technique description

In order to improve the control over the tension on the DNA, other approaches than combing have been taken. A particularly straightforward one is the attachment of a DNA to a surface with one end and stretching it with shear flow (Figure 5.2a). For attachment, DNA (in most cases the 48502-bp double-stranded DNA from λ-phage, with a contour length of about 16.5 μm) is biotinylated on one end by hybridizing one of its single-stranded overhangs to a short complementary strand modified with biotins. This biotinylated λ-DNA can then be attached to a surface coated with streptavidin or other biotin-binding protein. Entropic forces will keep the DNA in a relatively compact, random coil. However, these forces can be overcome by applying a shear flow with flow rates of the order tens of ml/hr [129, 130]. The drag force working on a DNA stretched in this way decreases along the length of the DNA, in the direction of the free end. This force can be made homogeneous along the DNA by attaching a micron-sized bead to the free end. The drag force the bead experiences significantly exceeds the drag on the DNA and will therefore be the major source of tension experienced by the DNA [131, 132]. A shear flow can be created by pumping a buffer solution through a flow cell using a syringe pump. Flow cells

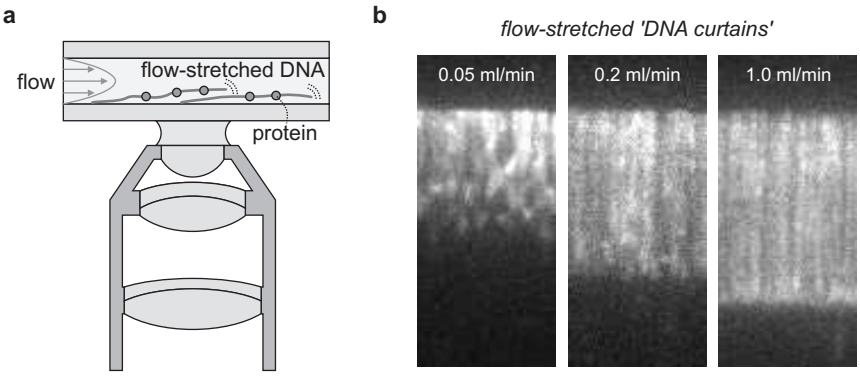

Figure 5.2 – Stretching of surface-tethered DNA using continuous flow. [**a**] Schematic of the assay. DNA is attached to the glass surface with one end. To overcome the entropic forces that keep the DNA compact a continuous solvent flow is applied, extending the DNA. Visualization of DNA or associated proteins can be realized using fluorescence microscopy. [**b**] Application of this assay to YOYO-stained λ-DNA [128], demonstrating how DNA stretching and extension depends on the flow rates. It furthermore highlights ability of this approach to allow the simultaneous observation of many DNA molecules in one field of view. Adapted with permission from Ref. [128]. Copyright 2006 American Chemical Society.

are commercially available (e.g., Integrated Biodiagnostics) or can be custom-made using (soft) lithography or by gluing two glass plates on a patterned spacer (like parafilm or adhesive tape) [90]. In such flow chambers, the flow follows a parabolic Poiseuille velocity profile, with zero velocity at the surface. This depth-dependent velocity profile complicates determination of the local shear the DNA experiences. It has been estimated that a surface-tethered λ-DNA that is extended to 80% of its contour length is on average 0.2 μm away from the surface and experiences a flow velocity of 100 μm/s [129]. As an alternative to the use of flow to stretch DNA, the use of magnets in combination with magnetic beads has been reported [3]. Wide-field fluorescence imaging can be readily combined with these DNA-stretching approaches. A key advantage of the proximity of the surface is that TIRF microscopy can be applied to reduce background fluorescence. It should, however, be realized that the distance from the surface is not constant in time and along the DNA. This results in fluctuations in fluorescence intensity since the excitation intensity in the evanescent wave used in TIRF illumination decays exponentially with the distance from the interface, with a decay constant of typically 100-150 nm. The proximity of the surface, however, can also be problematic due to undesired interactions with the DNA or DNA-binding proteins. To reduce these effects, the glass surface can be coated

with poly(ethylene)glycol (PEG) [129], or supported lipid bilayers [128]. Like DNA combing, the surface-tethered DNA stretching approach has one key advantage over other DNA manipulation methods: it can be performed using many DNA molecules in parallel, which can be simultaneously observed in one field of view, e.g., to produce flow-stretchable 'DNA curtains' (Figure 5.2b) [128].

5.3.2 Applications

This flow-stretching approach has been applied to study fluorescently labeled proteins diffusing along DNA. Xie and coworkers have investigated how individual base-excision DNA-repair proteins (human oxoguanine DNA glycolase 1, hOgg1) find damaged bases by fast diffusion along the DNA. They studied the pH, salt and flow dependence of the diffusive interaction and concluded that hOgg1, at near-physiological pH and salt concentrations, binds to the DNA for on average 0.025 s while sliding along it with a diffusion constant of $5 \cdot 10^6$ bp^2/s, leading to a mean sliding length of 440 bp. The surface-tethered DNA flow-stretching approach was also used to study recombinase RAD51-diffusion along double-stranded DNA [133]. The authors proposed that the diffusing complexes are multimers of RAD51 forming a ring around the DNA, since the complexes remained bound for many minutes while diffusing over substantial distances along λ-DNA. The reported diffusion constants range from 10^4-10^6 bp^2/s. In their experiment, diffusion also appeared to take place when the flow was switched off after attaching the DNA with both ends to the surface (i.e., combing the DNA). In other studies [134, 135], the formation and ATP-hydrolysis-dependent disassembly of RAD51 nucleoprotein filaments, which do not move along the DNA were visualized. Subsequent incubation with RAD51 labeled with different dyes yielded 'harlequin' filaments, indicating that RAD51-filaments nucleate on multiple sites on the DNA [134]. A related approach was taken to study the ejection of DNA by bacteriophage T5 [136] and λ [137]. In these studies, the phages were non-specifically attached to the glass surface of a flow chamber. DNA ejection was triggered by addition of the *E. coli* outer membrane proteins that serve as receptor for the phages. Ejected DNA was stretched in a buffer flow and visualized by addition of the intercalating dye YO-PRO-1. DNA ejection could thus be followed and quantified in real time. The T5 DNA was shown to be ejected in a stepwise manner, pausing at the five specific nicks on T5's genome [136]. A maximum genome [136]. A maximum ejection rate of 75 kbp/s was observed. In the case of phage λ [137], the genome was ejected in a continuous manner in about 1.5 s, with a maximum speed of 60 kbp/s.

5.4 DNA flow-stretched from an optically trapped bead

5.4.1 Technique description

In order to reduce the complications of the nearby surface (unwanted DNA and protein interactions and the Poiseuille flow profile), an approach where the DNA is tethered to an optically trapped microsphere and extended in a flow away from the surface of the flow chamber can be used (Figure 5.3a). In this approach, the DNA is attached with similar chemistry to a polystyrene or silica sphere with a diameter of typically a micrometer. Such a sphere can be optically trapped in the focus of an intense near-infrared laser beam [17, 18]. The physical origin of optical trapping is the transfer of momentum from photons refracted or reflected by the sphere to the sphere itself. In the geometry of the tight focus of a laser beam generated by a high numerical aperture objective, the momenta of many photons add up leading to a 3-dimensional 'potential well', keeping the sphere in place [27]. Although the high intensity of this trapping laser may lead to enhanced photobleaching [139] (see Chapter 6), selective fluorescence detection of dyes very close to or even in the laser focus has been proven

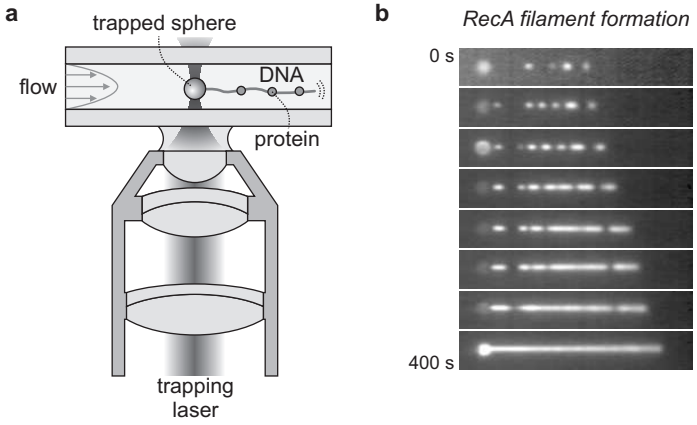

Figure 5.3 – Stretching of DNA held with one side in an optical trap using continuous flow. [**a**] Schematic of the assay. DNA is attached to a bead with one end, the bead is held in an optical trap. To overcome the entropic forces that keep the DNA compact a continuous solvent flow is applied extending the DNA. DNA or associated proteins can be visualized using fluorescence microscopy. [**b**] Application of this assay to the formation of RecA filaments [138]. λ-DNA is incubated with fluorescent RecA and filament formation is monitored by fluorescence. Note the increase of the length of the DNA due to RecA binding. Adapted by permission from Macmillan Publishers Ltd: Nature [138], copyright 2006.

to be possible [139–142].

5.4.2 Applications

Chu and coworkers have used this assay extensively to study the mechanical properties of DNA as a prototypical semi-flexible polymer [143–145]. In order to visualize the DNA they used intercalating dyes and wide-field fluorescence imaging. They did not drive the buffer flow required for extending the DNA with a pump, but rather moved the whole sample chamber with respect to the optical trap. This allowed them to overcome two shortcomings of stretching in buffer flow: in general it is difficult (1) to get a stable flow and (2) to quickly change the flow rate. Movement of the sample, however, can only be performed over a limited range and thus for a limited time. Using this approach, they visualized and measured the relaxation of stretched DNA after abrupt release of the shear force. They found that the relaxation rate depends on the length of the DNA and can be described by a distribution of decay times with sharp peaks, ranging from a tenth of a second to tens of seconds, in agreement with theoretical predictions [143]. In a subsequent publication [145] they studied the extension and dynamics of the DNA exposed to different drag velocities. They found that for DNA stretched in flow, the interaction of the DNA with the solvent is not constant along the chain, i.e., the DNA is not 'free draining'. This finding illustrates that extending DNA in a flow without a bead being attached to the free end results in a complicated profile of forces acting along the DNA chain and, as a consequence, to non-uniform extension.

An extensive series of fluorescence experiments on RecBCD using optically trapped, flow-stretched DNA has been performed by the Kowalczykowski group [146–149]. RecBCD is a highly processive DNA helicase and nuclease, among others involved in homologous repair. They have directly visualized DNA unwinding by RecBCD by making use of the property of intercalating dyes to bind to double-stranded DNA and not to single-stranded DNA. They demonstrated that RecBCD unwinds DNA at a rate of 100-1000 bp/s over lengths of tens of thousands of bases [146]. In a next study using the same intercalating-dye approach, they showed that when the helicase encounters a specific sequence ('χ') it pauses for several seconds and subsequently proceeds unwinding the DNA at a substantially lower velocity. This observation raised the question how the two motor subunits of RecBCD, RecB and RecD, work together. They showed, by attaching a fluorescent bead to the RecD subunit, that after χ recognition, the whole complex stays intact and that RecD does not fall off [147], as was hypothesized before. Later they measured the activity of RecBCD with a mutation in the RecD domain abolishing RecD's helicase activity [148]. This mutant unwound

DNA at an equal velocity before and after χ recognition. On the basis of this and their previous results they could propose a detailed model of how the two motor domains in RecBCD work together. The Kowalczykowski group has also used a similar assay to study the formation of RecA nucleoprotein filaments on single-stranded DNA (Figure 5.3b) [138]. They directly visualized the nucleation of fluorescently labeled RecA recombinases and demonstrated that 4-5 subunits are necessary for a stable nucleus; after formation of a stable nucleus the filaments elongate on both ends at a rate of several nanometers per second.

5.5 DNA tethered between two optically trapped beads

5.5.1 Technique description

As discussed before, the inhomogeneous force distribution along flow-stretched DNA may pose problems to a quantitative analysis. Moreover, the approach requires the continuous application of flow: when flow is switched off, the DNA swiftly relaxes to a globular shape [143] (see also Figure 5.2b). This continuous flow precludes the application of such techniques to the study of many dynamic DNA–protein interactions, including the direct visualization of the diffusional target search of site-specific proteins along an extended DNA molecule. For the aforementioned hOgg1 system, this continuous flow apparently did not impose a preferential direction [129], yet for the sliding of RAD51 multimers, the diffusion on a one-side tethered DNA was governed by flow [133]. Such drawbacks in flow-controlled experiments can be overcome by attaching the DNA from both ends, as in the molecular combing experiments. However, increased control is obtained because the DNA is manipulated from both ends by optical tweezers (Figure 5.4a) (alternatively, the DNA can be manipulated using an optical trap on one end and a micropipette [42]). In that case, control over the distance between the traps allows for fine adjustment of the extension of and the tension in the DNA. Another advantage of this method is that no special surface treatments of the microscope slides are required to specifically attach the DNA and at the same time block the binding of unwanted species. Most importantly, optical trapping permits accurate measurement of the forces applied to the DNA with a range of different optical detection methods (see [17] and references therein). This simultaneous fine control over the DNA tension and the quantitative detection of this tension enables one to directly probe the effect of force on biochemical or biophysical processes, such as the binding, locomotion or release of DNA binding enzymes, at the same time visualized using fluorescence.

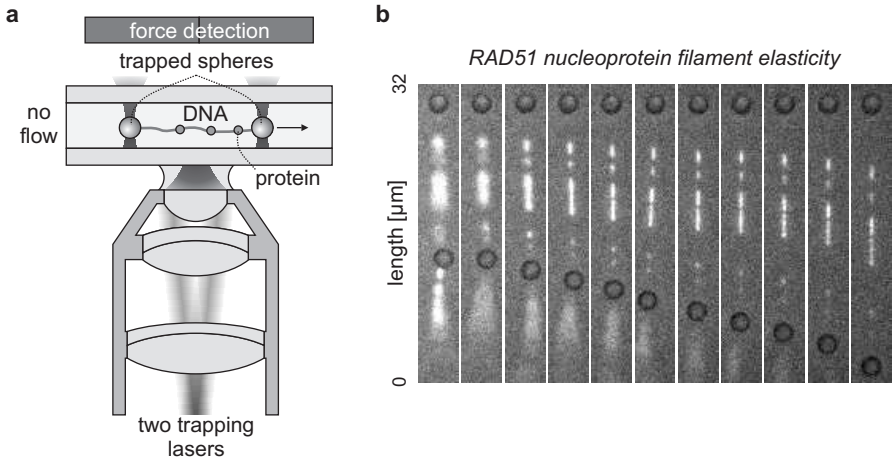

Figure 5.4 – Enhanced control using two force-measuring optical traps. [**a**] Schematic of the dual-trap assay. Two traps can be generated from a single laser source by splitting into two orthogonal polarizations, which may be independently steered in the sample. After suspending a single DNA molecule in between two trapped beads, the DNA can be manipulated without the application of force. In addition, optical tweezers can be employed to quantitatively detect the forces exerted on the DNA. The fluorescence from DNA-staining dyes or fluorescently labeled DNA-binding proteins can be detected using a CCD camera. [**b**] The assay from panel a employed in our study of the elasticity of RAD51 nucleoprotein filaments formed on double-stranded DNA [93]. By increasing the distance between the traps, tension can be applied to the DNA in a controlled manner. The increasing suppression of thermally excited diffusion of the DNA is readily observed.

5.5.2 Applications

In a first application of such dual-beam optical tweezers featuring DNA visualization, Chu and coworkers extended their aforementioned flow-stretched DNA control to observe the conformational dynamics of a DNA molecule stained with YOYO-1 without flow [150]. This allowed for an expansion of the polymer's dynamics in linearly independent normal modes after video analysis. Doing so, they observed that higher-order fluctuations are suppressed when the DNA is extended, as expected from polymer dynamics theory. For these experiments, direct measurement of forces was not implemented and the extension of the DNA was used as a control parameter instead. Arai *et al.* used a similar system to illustrate the versatility of simultaneous single-molecule observation and manipulation, by tying a knot in individual DNA molecules and comparing them to actin filaments [102]. To suppress Brownian fluctuations,

they performed this tricky single-molecule gymnastics in a high-viscosity solvent. By simultaneously measuring forces, they used this approach to investigate the dependence of the knot diameter on tension. Since the DNA knots were wrapped around (unlabeled) actin filaments in solution, the tension in the knot could not be increased enough to break the DNA.

The Yanagida group has been able to track individual *E. coli* RNA polymerase enzymes interacting with a DNA molecule suspended between two traps [151]. To visualize the Cy3-labeled RNA polymerase, they used TIRF microscopy. For efficient TIRF excitation, they used cover slips with pedestals. The beads used to trap the DNA were held, using the tweezers, in the depressions facing the pedestals. In this way, the DNA could be kept at a distance of about 100 nm from the pedestal quartz surface, allowing for efficient TIRF excitation. The pedestals were chemically etched into the cover slip, and had been used in a similar experiment assaying the mechano-chemistry of individual myosins on a suspended actin track [152]. Due to the enhanced enzyme affinity for the two asymmetrically positioned promoter sites along the DNA, the authors could readily determine the orientation of the captured DNA based on their knowledge of the promoter positions. Doing so, they showed that association and dissociation rates of RNA polymerase are different for GC-rich and for AT-rich regions. Moreover, they were able to observe polymerases undergoing linear diffusion along the DNA ('sliding'), which had been anticipated for decades but at the time lacked solid and direct observation. Finally, decreased enzyme affinity for DNA was reported under higher tensions. Similar effects of tension on enzymatic activity have been reported for many different systems, including DNA polymerase and restriction enzymes [31, 33]. This TIRF approach is complicated by intensity fluctuations (due to movement of the DNA with respect to the interface) and the requirement to etch the cover slips. Wide-field epi-illuminated fluorescence microscopy would not suffer from these drawbacks.

The lab of Greve has used polarized fluorescence detection to get an estimate for the orientation of absorption dipole moments of intercalated YOYO dyes [153]. They immobilized DNA between an optically trapped bead and one held in a micropipette. Here, the fluorescence detection was used mostly as a control in a range of experiments mainly focusing on the physics of YOYO intercalation and of DNA-binding by RecA. The use of a water-immersion objective allows for stable trapping even at a significant distance of the captured DNA from the glass surfaces of the sample chamber [20, 42], which reduces background fluorescence without the need for any surface blocking. Remarkably, these promising first experiments combining dual-tweezers and fluorescence microscopy in the late nineties have, to our knowledge, led to only a limited number of follow-up reports.

Recently, our group has demonstrated the feasibility of simultaneously performing controlled force-extension measurements and sensitive fluorescence detection in widefield epi-fluorescence mode. We applied this to the study of RAD51 filament mechanics on double-stranded DNA [93] (see Chapter 7). By carrying out these experiments on partly RAD51-coated DNA molecules, we were able to dissect the inhomogeneous elasticity of the DNA into uncoated, partly coated and fully coated segments (Figure 5.4b). Only the uncoated or partly coated segments showed the well-known overstretching transition [7]; fully coated segments, in which the DNA is held in a 150%-extended configuration, could not be stretched further. Such dissection could only be performed using a combination of manipulation and visualization techniques.

5.6 Outlook

The methods and applications presented here highlight the potential of combinations of DNA manipulation techniques with fluorescence imaging. Over the years, approaches have evolved from relatively straightforward ones, allowing only limited control over the DNA with respect to location and tension (such as combing and flow stretching), to more advanced ones, allowing full control over these parameters using dual optical tweezers. It is to be expected that in particular the combination of dual optical tweezers and fluorescence microscopy will be further developed, allowing for more sophisticated DNA manipulation schemes, for instance, involving force feedback [154], or the simultaneous trapping of two DNA strands [90]. At the same time, we and others are adding more advanced fluorescence methods to the tweezers, such as superresolution methods [155], FRET [140, 141], and polarization measurements [153] (see also Chapter 10). Moreover, single-molecule sensitivity on tweezers-suspended DNA in an epi-fluorescence configuration (instead of TIRF, as discussed here; see also Chapter 8) will allow for single-enzyme tracking in a relatively straightforward manner. It is to be expected that soon combinations of fluorescence imaging and magnetic tweezers [27, 156, 157] will be reported, allowing simultaneously the visualization of and control over the DNA torsion, i.e., the degree of supercoiling. The strength of these combined imaging and manipulation approaches is such that we expect to be only at the beginning of a technical development that will have great impact on the field of protein-DNA interactions in the coming years.

6

Enhanced photobleaching in combined optical trapping and single-molecule fluorescence microscopy

Abstract — To obtain high-resolution information on position or conformation of a molecule and at the same time apply forces to it, one can combine optical trapping with single-molecule fluorescence microscopy. The technical challenge in such an experiment is to discriminate a minute fluorescence signal from the much larger background signals caused by the trap and the fluorescence excitation laser light. We show here that this is feasible even when the fluorophore is directly attached to the trapped particle, by using optimized optical filters. We found, however, that the photostability of the fluorophores we tested suffered from the presence of the additional laser light used for trapping. We found that bleaching rates increased linearly both with the intensity of the trapping laser and the intensity of the fluorescence excitation light. Photobleaching rates were unaffected by the presence or absence of oxygen, but were significantly diminished in the presence of antioxidants. Our results indicate that the enhanced photobleaching is caused by the absorption of a visible photon followed by the excited-state absorption of a near-infrared photon. The higher excited singlet states generated in this way readily form non-fluorescent dye cations. We found that different dyes suffer to a different extent from the excited-state absorption, with Cy3 being most and tetramethylrhodamine least affected.

This chapter has been published in *Journal of Physical Chemistry B* [139].

6.1 Introduction

Over the last decade single-molecule techniques, such as single-molecule fluorescence spectroscopy [158, 159] and optical trapping or optical tweezers [16, 27, 160], have become important and successful tools in biology, chemistry and physics. Optical tweezers can be used to 3-dimensionally trap micrometer-sized particles near the focus of a laser beam, using laser powers of up to one Watt. In general, near-infrared lasers that are not resonant with electronic transitions of the molecules present in the sample are used in order to reduce photo damage caused by the high light intensities (up to 100 MW cm^{-2}) [161]. In single-molecule fluorescence microscopy, individual fluorophores are excited with laser light and the resulting fluorescence is measured with a fluorescence microscope. In general, excitation intensities on the order of hundreds of W cm^{-2} are applied, generating fluorescence intensities on the order fW (assuming a typical emission rate of 10000 photons per second). An important limitation of the organic dyes used in single-molecule fluorescence experiments is photodamage, which limits the total number of emitted photons to typically 10^5–10^6 [9]. A well-known cause of photodamage is oxidation of the dye by singlet oxygen. Singlet oxygen can be formed by sensitization of ground-state triplet oxygen present in the sample by dye in the triplet state [162]. Under typical illumination conditions the triplet state of most dyes is substantially populated. This source of photodamage can be reduced significantly by decreasing the oxygen concentration using deoxygenation or oxygen scavengers such as the glucose oxidase/catalase system [163]. In fluorescence experiments using 2-photon excitation, excited states are generated with high light intensities (most often femto- or picosecond laser pulses with peak intensities of order 100 GW cm^{-2} [164]) of half the photon energy needed for excitation of the dye molecules. It has been shown that the photobleaching rate under these excitation conditions is proportional to the third power of the excitation intensity, indicating that it is a process caused by three photons [165]. This bleaching behavior was explained by a mechanism not involving triplet states, but higher excited singlet states. These states are populated by 3-photon excitation of the fluorophores and couple, in polar solvents like water, efficiently to ionized states involving a solvated electron and a non-fluorescent dye cation [166]. Schwille and coworkers have shown that the efficiency of this photobleaching channel can be reduced substantially by addition of antioxidants such as ascorbic acid to the sample at concentrations of 1 mM and higher [167]. The idea is that these reducing agents recover the fluorescence signal by donating an electron to a bleached dye cation. A similar recovery effect of electron donors has recently been observed on the on–off blinking of the fluorescence from quantum dots [168]. This blinking phenomenon is due to ejection of an electron out

of the core of the dot leading to a dark state and subsequent recombination leading to recovery of the fluorescence signal. It was shown that electron donors such as dithiothreitol and β-mercaptoethanol substantially reduce the off-times [168].

In recent years there have been several attempts to apply single-molecule fluorescence spectroscopy and optical tweezers simultaneously in order to obtain detailed information on conformation and location using fluorescence, while at the same time manipulating the molecules with the optical tweezers. In one study two optical traps were used to extend a DNA molecule while the location of a single RNA-polymerase molecule moving along the DNA searching for promoter sites was measured with fluorescence [151]. In another experiment the same researchers held an actin filament between two traps and measured single fluorescent ATP turnovers by a myosin motor bound to the actin [152]. In both studies, the traps and the area from which fluorescence was detected were separated by several microns, which avoided potential problems caused by the high intensity of the trapping lasers, such as larger background signals and enhanced photobleaching. In a more recent study, the distance between trap and fluorescent molecules was smaller—only several hundred nanometers, on the order of the trap diameter [140]. A short length of double-stranded DNA was unzipped using an optical trap while at the same time the separation of the two single strands of DNA was measured with fluorescence. In this study it was demonstrated that detection of fluorescence from a single fluorophore close to an optical trap is feasible when the proper optical filters and excitation methods are used. There were indications that enhanced photobleaching in the presence of the intense trapping beam could be a problem in such experiments [140].

Here, we investigate photobleaching of fluorophores in combined fluorescence and optical tweezers experiments when the dye molecules are located directly in the center of the trap. In these experiments two laser beams are present, a relatively weak one for fluorescence excitation, resonant with the optical transition, and another non-resonant one for optical trapping, with an intensity 5 to 6 orders of magnitude higher. It should be noted that the wavelength of the trapping beam is similar to what is generally used in 2-photon excitation of the fluorophore, but the intensity is 3 to 4 orders of magnitude lower. In the present study we investigate whether enhanced photobleaching indeed occurs in combined trapping and fluorescence experiments, we quantify the effect, we examine under what experimental conditions it occurs and whether measures can be taken to reduce it. We also explore the mechanism of photobleaching under these conditions, in order to find out whether bleaching occurs through one of the known mechanisms (see above) or another, unknown one.

6.2 Results and discussion

To study the possibility of measuring fluorescence from individual fluorophores in the center of the trap and the influence of the trap laser light, we measured the fluorescence from the dye Cy3, attached with short linkers (about a nanometer) to trapped silica beads of 444 nm diameter. It proved to be rather difficult to measure signals from single fluorophores, due to (i) the residual movement and rotation of the trapped beads, which led to substantial fluctuations of the fluorescence intensity, and (ii) the rapid bleaching of the signal. The former problem was solved by reducing the mobility of the beads by working in an agarose gel (1% w/v). In most biophysical assays used for combined trapping and fluorescence experiments this problem does not exist because the bead is attached to the cover glass or largely immobilized via the molecule to be manipulated. An example of the fluorescence signal from a single Cy3 molecule attached to a trapped bead in an agarose gel is shown in Figure 6.1a. The signal bleached in two steps, indicating that two fluorophores were bound to the bead. From the time trace it is clear that fluorescence arising from a single fluorophore in an optical trap can be detected above the background signal, although the Cy3 molecules appeared considerably more susceptible to photobleaching than without the trap present.

To quantify the photostability we determined from traces like that shown in Figure 6.1a the time before bleaching for 36 single fluorophores, shown as a histogram in Figure 6.1b. The histogram can be fitted by a single exponential with a bleaching rate of $0.17 \pm 0.06\,s^{-1}$ (the accuracy of the fitted value is rather low due to the low number of data points). At higher power of the trapping laser (25 mW) the bleaching rate increased substantially to $0.32 \pm 0.09\,s^{-1}$ (data not shown).

To track down the origin of the increased bleaching rate in the presence of the trapping laser more statistics were needed. Since there is no necessity to do this experiment with single molecules we used beads coated with 10–100 fluorophores (as judged from fluorescence intensity). At this surface density the fluorophores were far enough apart on the beads to not interact and to not transfer excitations. The advantages of this approach are that (i) the bleaching rate could be determined from the intensity time trace of a single trapped bead, which is also expected to decay exponentially; (ii) the fluorescence intensities are about 10–100× higher, so that the experiments could be done in water and no gels were needed to improve the signals.

Figure 6.2a shows an example of such a time trace, fitted with a single exponential. Using this approach we determined that the bleaching increased substantially with trapping laser intensity (Figure 6.2b). The bleaching-rate dependence on trapping power was linear, indicating that the enhanced bleaching was caused by a pro-

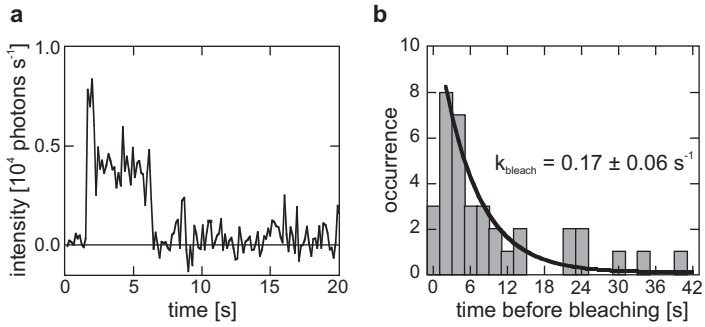

Figure 6.1 – Single-molecule photobleaching. [**a**] Time trace of the fluorescence intensity of two Cy3 molecules attached to a trapped bead. [**b**] Histogram of the times before bleaching of 32 such Cy3 molecules with an exponential fit with decay constant $0.17 \pm 0.06\,s^{-1}$. The power of the 850-nm trapping laser was 7.4 mW (in the sample), the intensity of the 532-nm fluorescence excitation laser was 350 W cm^{-2}.

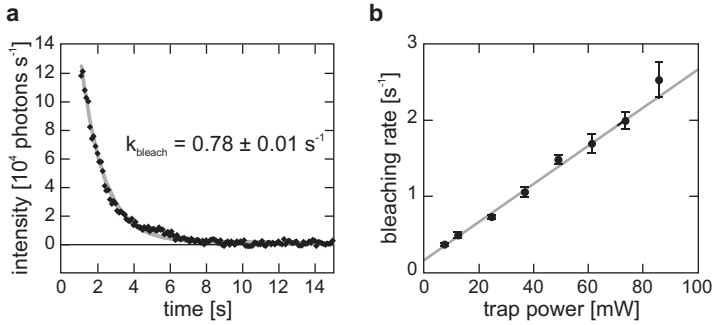

Figure 6.2 – Effect of the power of the trap laser on photobleaching. [**a**] Time trace of the fluorescence intensity of many Cy3 molecules attached to a trapped bead (diamonds) with an exponential fit with decay constant $0.78 \pm 0.01\,s^{-1}$ (gray line). The power of the 850-nm trapping laser was 25 mW, the intensity of the 532-nm fluorescence excitation laser was 350 W cm^{-2}. [**b**] Trap laser power dependence of the bleaching rate. Shown are the average bleaching rates from about ten beads per power (solid circles, the error bars represent the standard error of the mean), and a linear fit to the averaged data (solid line), with intercept $0.16 \pm 0.02\,s^{-1}$ and slope $25 \pm 1\,s^{-1}\,W^{-1}$. The intensity of the 532-nm fluorescence excitation laser was 350 W cm^{-2}.

cess involving one and not two 850-nm photons. Note that the straight line does not extrapolate to the origin, reflecting the fact that at zero trapping power, but with fluorescence excitation light present, bleaching still occurs. similar measurements performed with 1000-nm trapping light (data not shown), lower bleaching rates were

observed (70 ± 10% of that with 850-nm trapping light). This difference can be explained by the smaller area of the focal spot at 850 (about 70%) than at 1000 nm. We also measured the effect of the intensity of the fluorescence excitation light on photobleaching. Figure 6.3a shows that the bleaching rate again increased linearly with the excitation intensity. The data can be well fitted with a straight line through the origin, indicating that the absorption of a green photon is necessary for photobleaching to occur. To prove this point we performed an experiment with fluorescence excitation light that was repetitively switched on and off. The resulting time trace (Figure 6.3b) clearly shows that the fluorescence intensity was equal before and after a dark period during which only the trapping laser was present. These results indicate that the enhanced bleaching of fluorescence in the optical trap is a 2-photon process, involving the absorption of first a visible and then an NIR photon. In all our experiments we did not observe fluorescence arising from multiphoton excitation by the NIR trapping laser. Fluorescence was only detected when green excitation light was present (as can be seen in Figure 6.3b).

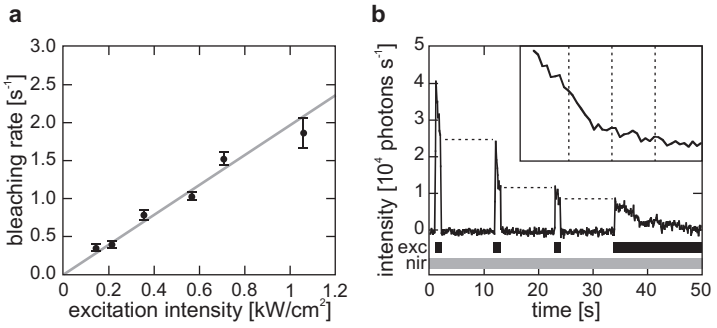

Figure 6.3 – Effect of the intensity of the fluorescence excitation light on photobleaching. [**a**] Fluorescence excitation intensity dependence of the bleaching rate of hundreds of Cy3 molecules attached to a trapped bead. Shown are the fitted rates, the average bleaching rates from about ten beads per power (solid circles, the error bars represent the standard error of the mean), and a linear fit to the averaged data (solid line), with slope 1.96 ± 0.05 cm^2 s^{-1} kW^{-1} and the origin as intercept. The power of the 850-nm trapping laser was 25 mW. [**b**] Time trace of the fluorescence intensity of many Cy3 molecules attached to a trapped bead with the fluorescence excitation laser chopped as indicated by the black bar in the bottom of the figure marked 'exc'. The three horizontal lines are drawn to indicate that no bleaching takes place when only the laser trap is present. The power of the trapping laser was kept constant at 25 mW, as indicated by the gray bar in the bottom of the figure marked 'nir'. In the inset the periods without fluorescence excitation light are cut out of the trace. The transitions between two periods with the green laser on are indicated by the vertical dashed lines.

condition	relative bleaching rate
untreated	1
degassed under argon	0.97 ± 0.03
oxygen scavenger	0.46 ± 0.03
ascorbic acid	0.25 ± 0.01

Table 6.1 – Effect of antioxidants and oxygen depletion on the bleaching rates. The data were measured with 89 mW trapping power and 350 W cm^{-2} fluorescence excitation intensity and are represented relative to the values for the untreated sample under the same optical conditions.

The 2-photon bleaching process could involve triplet and ionized states of the dye. In order to find out whether triplet states are involved we measured the bleaching rate in the presence of an oxygen scavenging mixture based on glucose oxidase, glucose, catalase and dithiothreitol (DTT). In Table 6.1, we show that the oxygen scavenger decreases the bleaching rate more than twofold. It should be noted that the DTT in the oxygen scavenger mixture is an antioxidant. It could well be that the decrease of the bleaching rate is caused in this case by the antioxidant and not the oxygen-free conditions. To confirm this, we measured the bleaching rate under oxygen-free conditions achieved by degassing the sample and found that the absence of oxygen does not influence the bleaching rate. However, in the presence of the antioxidant ascorbic acid the rate decreased fourfold (Table 6.1). From these results it can be concluded that triplet states are no intermediates in the enhanced bleaching process, since reduction of the oxygen concentration does not influence the bleaching rate. It has been shown that oxygen-free conditions can cause increased triplet state lifetimes [169] and prevention of the production of singlet oxygen—a well-documented cause for photobleaching [162]. Based on the strong effect of antioxidants we suggest a model for the photobleaching process consisting of the sequential absorption of two photons, ending up in a higher excited (singlet) state, from which the dye can readily ionize to a non-fluorescent state, forming a solvated electron and a dye cation (see Figure 6.5 and conclusion below). In the presence of antioxidants this cation can be reduced back to its neutral, fluorescent form [167].

To further characterize the process we studied the dependence of bleaching rates on the relative polarization of the fluorescence excitation and the trapping beams. In these experiments we measured a bleaching rate that was 1.7 ± 0.3 times higher with parallel polarizations of the two beams than with perpendicular polarizations (data not shown). Given our model for the bleaching process as the consecutive absorption of first a visible and then an NIR photon, this experiment is in some ways equivalent to a fluorescence anisotropy [170] or a pump-probe transient-absorption anisotropy

measurement [171]. The NIR photon plays the role of the fluorescence or the probe pulse in the respective cases. Any anisotropy measured by comparing parallel and perpendicular polarizations of visible and NIR beams reflects relative orientations of the transition dipoles of first and second absorption process. These transition dipoles can be intrinsically non-parallel, or they can become non-parallel due to rotation of the molecule during the two events (absorption-absorption or absorption-fluorescence).

Using the formula for anisotropy ($r = (k_{\parallel} - k_{\perp})/(k_{\parallel} + 2k_{\perp})$, with $k_{\parallel}$ the bleaching rate with parallel polarizations and $k_{\perp}$ the bleaching rate with perpendicular polarizations) the anisotropy in our experiments was calculated to be 0.19 ± 0.07. For perfectly aligned static transition dipoles the anisotropy would be 0.4 [170, 171]. The measured lower value indicates that the two absorption processes have transition dipole moments that are not exactly parallel and/or that some polarization is lost by rotational motion of the chromophores during the lifetime of the (first) excited state. To find out which of the two possibilities is the cause of the decreased anisotropy, we also determined the fluorescence anisotropy of the same bead/dye system, which was 0.15 ± 0.03. In Cy3 the transition dipole moments of absorption and emission are nearly parallel [172], so it can be assumed that the fluorescence depolarization is due to rotation of the dye within the excited state lifetime (due to their size the beads hardly rotate in this time). The relatively low value of the fluorescence anisotropy indicates that the linkage of the dye to the bead is rather flexible, even more so than in previous studies using similar chemistry for dye attachment to proteins, in which values of 0.25–0.32 were observed [172, 173]. The higher flexibility in our experiments could be caused by the longer linker we used than in those studies (the silane is flexible as well) and the absence of non-specific interactions between protein and dye [9]. The fluorescence anisotropy is nearly equal to the bleaching anisotropy. This provides additional evidence that the time scale of the two-photon bleaching process is set by the lifetime of the first excited singlet state. If this were not the case, the fluorophores would have more (or less) time to rotate, leading to a bleaching anisotropy substantially lower (or higher) than the fluorescence anisotropy. Within this model, the fact that the dye rotation already accounts for the observed bleaching anisotropy leads us to conclude that the dipole moments of the two transitions involved are approximately parallel.

In the measurements described so far we used the dye Cy3, a dye that is widely used in single-molecule fluorescence experiments because of its high photostability upon direct excitation with green light [9, 166]. When used in two-photon excitation microscopy (with NIR light) this dye bleaches rather fast [174]. In a last set of experiments we therefore compared the bleaching of Cy3 in combined trapping and fluorescence experiments with that of other frequently used dyes in the same

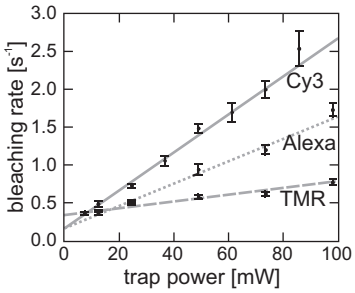

Figure 6.4 – Dependence of the bleaching rate on trapping laser power. Data is shown for beads with many dye molecules (either Cy3, Alexa-555, or TMR) attached. The solid circles represent average bleaching rates from about ten beads per power (error bars show the standard error of the mean). The three lines are linear fits to the averaged data are shown, with intercept $0.16 \pm 0.02\,s^{-1}$ and slope $25 \pm 1\,s^{-1}\,W^{-1}$ for Cy3 (solid line), intercept $0.17 \pm 0.02\,s^{-1}$ and slope $15 \pm 1\,s^{-1}\,W^{-1}$ for Alexa-555 (dotted line), and intercept $0.33 \pm 0.03\,s^{-1}$ and slope $4.5 \pm 0.5\,s^{-1}\,W^{-1}$ for TMR (dashed line). The intensity of the 532-nm fluorescence excitation laser was kept constant at $350\,W\,cm^{-2}$.

wavelength range, TMR and Alexa-555. The measured bleaching rates, shown in Figure 6.4, clearly show that Cy3 is much more sensitive to the enhanced bleaching effect than the other two dyes. In fact, the dye that is least photostable in one-photon experiments, TMR (which therefore also has the highest bleaching rate extrapolated to zero trapping power in Figure 6.4), is most resilient to the presence of the high-intensity trapping beam. The difference between the three dyes can be caused by three photophysical properties. One would expect that (i) the shorter the singlet excited state lifetime of the dye is, the lower the bleaching rate is, (ii) the lower the absorption cross sections of the excited state absorption from the first singlet excited state to higher singlet states is, the lower the bleaching rate is, and (iii) the lower the coupling between the higher singlet excited states and ionized states is, the lower the bleaching rate is. Unfortunately, to our knowledge, neither experimental data nor quantum-chemical calculations on excited state absorption spectra or on ionization potentials are available to compare the three dyes with respect to the latter two properties. However, there should be large differences between the dyes in these respects, since the lifetime (property (i)) of Cy3 (<0.3 ns, data from Amersham Biosciences) is substantially smaller than that of TMR (~ 2.5 ns [175]), while it nonetheless bleaches substantially faster in our experiments.

6.3 Conclusions

In experiments that combine single-molecule fluorescence spectroscopy with optical tweezers, attention has to be paid to limiting additional photobleaching of the fluorophores by the trapping laser. We have shown that an additional channel for photo destruction of the dyes is opened up in such experiments, causing, in general, a substantial increase of photobleaching. The bleaching mechanism we propose, which is consistent with all our results, is shown in Figure 6.5. The visible laser used for fluorescence excitation generates dye molecules in their (lowest) singlet excited state (S_1), from which fluorescence can take place. The intensity of the near-infrared trapping light is so high that even during the short lifetime (∼ns) of this state there is a considerable chance that a second photon is absorbed and higher excited states are generated (S_n). In general, these states couple efficiently to bleached, ionized states, in particular in polar solvents such as water [166], and as a consequence dye cations and solvated electrons are readily produced. We noticed that for Cy3 the bleaching is not much different when trapping light with a wavelength of 1000 is used instead of 850. The bleaching process we observed in the presence of a visible, resonant fluorescence excitation and a much stronger non-resonant, near-infrared trapping beam is related to enhanced photobleaching in 2-photon excited fluorescence experiments, which show a bleaching rate proportional to the third power of the excitation intensity [165, 167]. In those experiments, where only a non-resonant near-infrared laser beam is present at much higher power, bleaching takes place from higher excited states produced via a 3-photon process, either by direct 3-photon excitation, or by 2-photon excitation into the lowest singlet state immediately followed by an additional excitation by one photon into the higher excited states. In contrast, in our experiments the lowest singlet state is populated with 1-photon excitation and higher excited singlet states, from which photobleaching can occur, are populated via

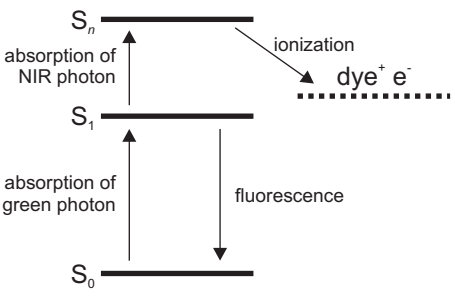

Figure 6.5 – Proposed model for the photobleaching process. Electronic energy level scheme indicating the states and transitions involved. S_0, S_1, and S_n are the singlet ground state, the lowest singlet excited state and higher excited singlet states, respectively. Dye^+ e^- is an ionized state consisting of a dye cation and a solvated electron.

excited-state absorption of one photon of different energy, from a different laser. In summary, we have shown that measuring fluorescence from a single fluorophore in an optical trap is challenging, but possible. Several measures can be taken to reduce the additional photobleaching in the combined fluorescence and trapping experiments: (i) choice of the right fluorophore (TMR is better than Alexa-555, which is better than Cy3); (ii) use of low trapping and fluorescence excitation powers; (iii) use of antioxidants such as ascorbic acid; (iv) use of perpendicular polarization of the fluorescence excitation and trapping laser beams.

6.4 Experimental methods

6.4.1 Setup

A custom-built instrument, capable of high-sensitivity fluorescence imaging and optical trapping, was used for the experiments (Figure 6.6). Trapping light was provided by a continuous-wave Ti:Sapphire laser (Coherent Mira 900F with a triple-plate birefringent filter, pumped by a Coherent Verdi V10 frequency-doubled Nd:YVO_4 laser (532 nm)), tunable from 730 to 1000 nm. The laser was used at 850 nm unless stated otherwise. The laser beam was expanded and coupled into an oil-immersion microscope objective (Nikon SFluor 100×, NA=1.3), using a 700-nm short-pass dichroic mirror (700dcsx, Chroma). Fluorescence excitation light was provided by the 532-nm laser. The beam was slightly decollimated for widefield epi-illumination and coupled into the objective with a 565-nm long-pass dichroic mirror (q565lp, Chroma). Fluorescence from the sample was collected with the same objective, filtered by the dichroic mirrors, a color-glass filter (Schott, BG39) or a short-pass filter (e750sp, Chroma), a 532-nm notch filter (Kaiser Optical Systems HPFN-532.0), and a bandpass filter (hq610/75m, Chroma) and detected with a back-illuminated, frame-transfer CCD camera (Roper Scientific, Micromax 512FTB).

In most experiments, the fluorescence excitation light was circularly polarized with a Berek's variable wave plate (New Focus, 5540) while the trapping light was vertically polarized. In the combined trapping / fluorescence experiments in which the effect of polarization was investigated, the polarization of the fluorescence excitation light was altered using the variable wave plate and converted into horizontal and vertical (linear) polarizations (see below).

Silica beads used for trapping were visualized using trans-illumination with a blue LED (470 nm). The light from the LED was coupled into the sample with a condenser (Nikon, Achromat Aplanat) and detected with a CCD camera (Watec 902B). The (green) laser intensity was calibrated by measuring the Gaussian fluorescence pro-

file from a sample of homogeneously spin-coated DiI (Fluka, dissolved in toluene). The intensity at the position of the laser trap (the maximum of the Gaussian) was determined from the width of the Gaussian. The half width at $1/e^2$ times the maximum (the waist) was 8.06 μm, leading to a peak intensity of 981 W cm^{-2} per mW (transmitted) power. As a measure for the intensity of the trapping laser we used the total transmitted power, P. The exact intensity the trapped bead is exposed to in the focus, I, is not very well defined, because the bead performs Brownian motion in an approximately Gaussian intensity profile, but is on the order of 600 kW cm^{-2} per mW transmitted power, as calculated from $I = P \cdot \mathrm{NA}^2/(0.61)^2$, with the numerical aperture NA = 1.3 and the wavelength $\lambda = 850$ nm [164].

Fluorescence anisotropy was measured with the same setup. In these experiments, the fluorescence excitation light was alternated between horizontal and vertical polarizations using an electro-optical modulator (Conoptics 350-80), driven by a D/A computer board (National Instruments PCI-6733), in synchronization with the readout of the camera. In these experiments the beads were non-specifically attached to the glass surface by adding NaCl (∼1 M).

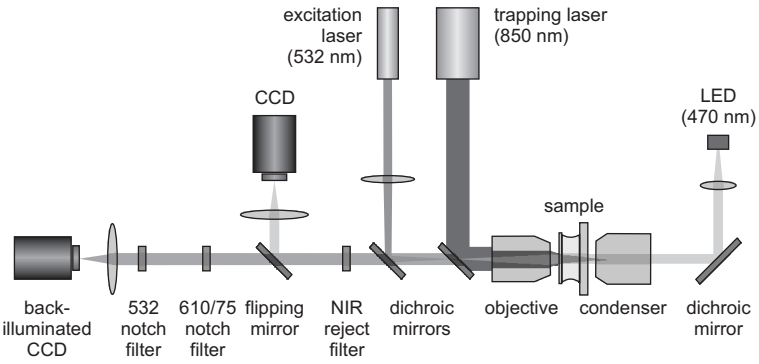

Figure 6.6 – Diagram of the instrument used for combined fluorescence. For details, see section 6.4.1.

6.4.2 Preparation of fluorescent beads

Silica beads with a diameter of 444 nm were a kind gift of the Colloid Synthesis Facility, Utrecht University. To attach fluorophores, beads were derivatized with reactive amine groups on the surface by incubation in a solution of 33% v/v aminopropyltriethoxysilane (Aldrich) in water for 15 minutes. After washing the beads in water (by several centrifugation/resuspension cycles), they were incubated for 90 minutes in a sodiumcarbonate buffer (100 mM, pH 8.3) with a small quantity of aminoreactive

fluorophores (Cy3 succinimidyl-ester (Amersham Biosciences), Alexa-555-maleimide or carboxytetramethylrhodamine-succinimidyl-ester (TMR, both Molecular Probes)) dissolved in dimethylformamide. Finally, the beads were washed twice to remove unreacted dye.

In some of the experiments oxygen-free conditions were created either (i) by vacuum degassing and flushing the sample with argon gas or (ii) by adding an oxygen scavenging system (0.02 mg ml^{-1} glucose oxydase, 25 mM glucose, 0.035 mg ml^{-1} catalase, and 4 mM dithiothreitol), and subsequently sealing the sample chamber with vacuum grease. In another experiment ascorbic acid (100 mM, dissolved in water, pH set to 7) was added.

6.5 Acknowledgments

We thank the Colloid Synthesis Facility, Utrecht University for kindly providing silica beads. This work was funded by a VIDI-grant from the Research Council for Earth and Life Sciences (ALW) and grants from the Foundation for Fundamental Research on Matter (FOM), both with financial support from the Netherlands Organization for Scientific Research (NWO).

7

Dissecting elastic heterogeneity along DNA molecules coated partly with RAD51

Abstract — Nucleoprotein filament formation by recombinases is central to homologous recombination. To follow this process, we used fluorescent human RAD51 recombinase to visualize the interactions with double-stranded DNA (dsDNA). Fluorescence imaging revealed that RAD51 filament formation on dsDNA initiates from multiple nucleation points, resulting in RAD51–dsDNA nucleoprotein filaments interspersed with regions of bare DNA. The elastic properties of such heterogeneously coated DNA molecules were assessed by combining force-extension measurements using optical traps with fluorescence microscopy. This combination of single-molecule techniques allows discrimination of segments within an individual DNA molecule and determination of their elastic properties. The non-fluorescent zones of DNA-RAD51 constructs showed the well-known (over)stretching behavior of bare DNA. In contrast, the fluorescent, RAD51-coated zones did not overstretch and RAD51 remained stably bound in a structure that was about 50% longer than bare DNA. These results illustrate the power of adding sensitive fluorescence imaging to optical tweezers instrumentation.

This chapter has been published in *Biophysical Journal* [93].

7.1 Introduction

Optical tweezers have proven to be versatile tools to mechanically probe DNA and the interactions with DNA-binding proteins [7,27,31,33,153]. Combining this technique with fluorescence microscopy is a powerful means to simultaneously observe proteins bound to the DNA and detect induced mechanical perturbations. However, only a few such applications have been reported [140, 142, 151]. Here, we image fluorescence during force-extension measurements on double-stranded DNA (dsDNA) coated with fluorescently labeled recombinase proteins. This approach allows detailed analysis of elasticity of different segments on the same DNA molecule, either coated with fluorescently labeled protein or uncoated, rather than an average analysis over the whole molecule. Therefore, we can directly identify different elements of a complex structure and coherently dissect their separate elastic behavior, without assuming uniform molecular characteristics.

Using this combined approach, we have studied the mechanical aspects of human recombinase protein RAD51 binding to dsDNA. RAD51 forms the catalytic core of eukaryotic homologous recombination, an essential mechanism for maintaining genome integrity [91,176,177]. Homologous recombination serves both as a cross-over mechanism for chromatids during meiosis and as a reliable repair pathway for dsDNA breaks or stalled replication forks [178]. Recombinase proteins drive DNA strand exchanges between homologous DNA molecules. RAD51 is structurally and functionally similar to the prokaryotic RecA and archaeal RadA recombinases [91, 176, 177]. Like other recombinases, RAD51 forms nucleoprotein filaments on both single-stranded (ssDNA) and dsDNA [176].

To study RAD51 nucleoprotein formation on DNA using the combined trapping and fluorescence approach, we have generated functional single-cysteine variants of human RAD51 recombinase and labeled them with Alexa-555 (Molecular Probes)—a detailed description of the variants and their biochemical functionality tests has been published [134]. Filaments assembled at multiple sites on dsDNA. Therefore, the dsDNA molecules become discontinuously coated with RAD51, reflected both in intermittent fluorescence emission along the DNA and heterogeneous elasticity (see below).

7.2 Experimental assay

For a quantitative analysis of the mechanical properties of RAD51 nucleoprotein filaments, we used a double optical trap setup to manipulate individual RAD51–dsDNA complexes. A description of this setup will be given in section 8.3. In order to

demonstrate the ability to extract features of an inhomogeneously coated single DNA molecule, filaments were assembled with Alexa-555 labeled RAD51 onto 48-kbp biotinylated λ phage dsDNA [33]. Assembly occurred in the presence of 1 mM ATP, 30 mM KCl, and with 2 mM $CaCl_2$ (instead of $MgCl_2$) in order to strongly reduce disassembly of the nucleoprotein filaments [179, 180]. By tuning the RAD51:bp stoichiometry during assembly, conditions were obtained resulting in incomplete coverage of the DNA molecules. Single filaments were tethered from both ends to two streptavidin-coated beads, optically trapped in a custom-built flow cell [33] using a 3-W 1064 nm laser. By moving one of the traps, tension can be applied on the filament in a controlled manner. Combining back-focal-plane interferometry [21] with wide-field epi-fluorescence imaging (532 nm laser excitation) onto a CCD camera (Cascade 512B, Princeton Instruments), both the force on the fixed bead and fluorescence images of the whole construct were recorded at 5 Hz. Moreover, the distance between the beads over time was tracked using transmitted brightfield video-microscopy. Together, this allows determination of the elastic properties of distinct segments in a DNA molecule.

7.3 Non-uniform elasticity

To dissect the force-extension data of the heterogeneous construct, kymographs were constructed from fluorescence images like those in Figure 7.1a [181]. The kymograph in Figure 7.1b shows that RAD51 remains stably bound even at forces that overstretch dsDNA. Moreover, it is locally anchored to the DNA: the relative position of the fluorescent zones did not change in several stretching cycles on the same construct. While it is still possible that the dsDNA held within the filament is dynamically melted, one or both strands must be tightly bound to RAD51. This behavior of RAD51, polymerized into ATP-coordinated nucleoprotein filaments, is thus very different from the one-dimensional sliding along dsDNA of RAD51 oligomers reported by Granéli *et al*. [133], a property that is ATP independent and presumably unrelated to nucleoprotein filament formation.

The force-extension curve of the entire construct in Figure 7.2a and comparison to the curve of bare DNA (shown in gray) immediately shows the qualitative effect of RAD51 binding. First, the steep tension increase commences at larger extension than for bare dsDNA, indicative of a longer contour length. Second, the length increase during the overstretching transition (induced at tensions exceeding 65 pN) is less than the factor 1.7 increase for bare dsDNA [7], suggesting reduced overstretching for RAD51-coated dsDNA.

The kymograph was subjected to edge detection with sub-pixel resolution to dis-

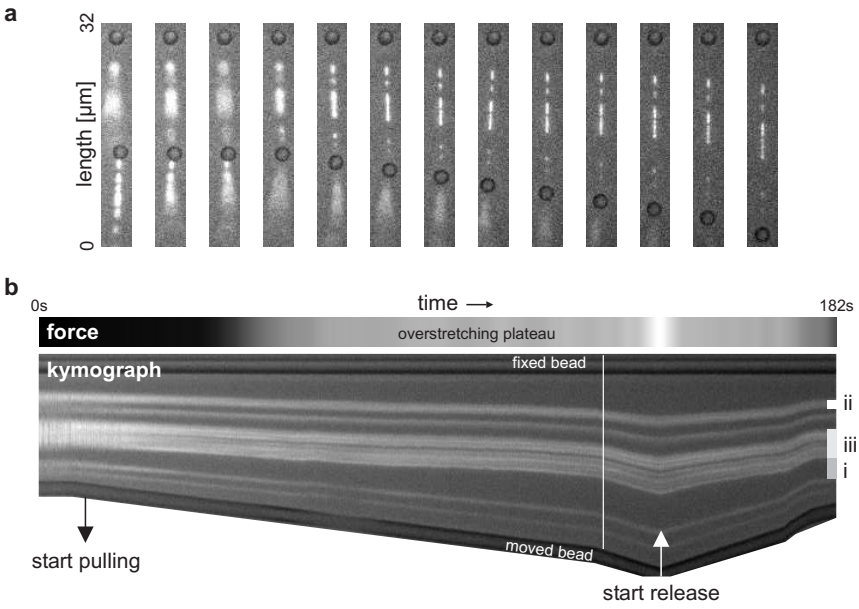

Figure 7.1 – Fluorescence stills and kymograph of a single 48 kbp λ-dsDNA molecule partly coated with fluorescent RAD51. [**a**] Fluorescence stills of such an assembly extracted from a movie, tethered between two streptavidin-coated polystyrene beads. [**b**] Kymograph generated from the successive frames (like those in panel a) of the movie recorded during extension of the construct. Fluorescence decay is due to photobleaching and not RAD51 dissociation, as tested by varying the laser power. The corresponding force time trace is depicted in grayscales (top bar; white corresponds to 90 pN); Figure 7.2b–d shows partial force-extension curves of the segments designated i, ii and iii.

criminate fluorescent from dark zones and monitor them in time during extension. Force-extension curves were then generated for specific parts of the construct (Figure 7.2b–d). The force-extension behavior of a non-fluorescent zone (bare zone (i), Figure 7.2b) was, as expected from the apparent absence of RAD51 on this part of the dsDNA, indiscernable from that of published curves of dsDNA [7]. It showed a steep increase of force when stretched up to a contour length of 2.8 µm. At forces exceeding 65 pN a clear overstretching plateau was reached that ended at a length of 4.8 µm, i.e., ∼170% of the contour length of this part of the dsDNA. In sharp contrast, the force-extension behavior of a continuously fluorescent zone, indicative of RAD51-coated DNA (continuous zone (ii), Figure 7.2c), showed that this zone did not overstretch under high tension (up to 90 pN). This has also been observed for RecA [153, 182, 183]. The force-extension behavior of a composite zone ((iii), Fig-

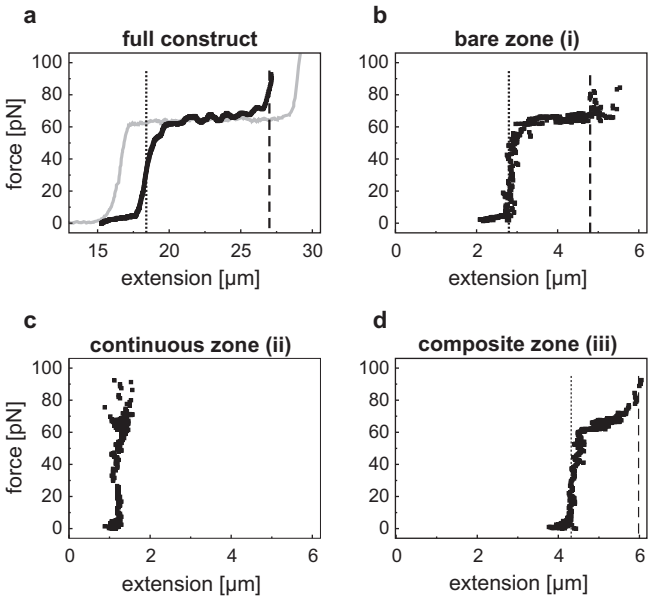

Figure 7.2 – Elasticity of segments of a RAD51–dsDNA assembly. [**a**] Force-extension curve corresponding to the construct in Figure 7.1b. The gray trace shows a bare λ DNA reference curve. [**b–d**] Force-extension curves of the bare zone (i), the continuous fluorescent zone (ii) and the composite fluorescent zone (iii) as indicated on the right of the kymograph in Figure 7.1b.

ure 7.2d), apparently including zones with and without bound RAD51, was more complex. An overstretching plateau was observed, but the dsDNA could only be stretched to 140% of its contour length. This composite behavior observed in the force-extension curve can be accounted for by a linear combination of coated, rigid parts (*cf.* Figure 7.2c), and bare, elastic parts (*cf.* Figure 7.2b). With this assumption, the fraction of the dsDNA coated by RAD51 (f) and the RAD51-induced elongation factor of the coated parts (e) were estimated from the force-extension curve of the full construct (Figure 7.2a) as follows. The measured contour length of the partially coated and extended filament (18.4 μm, fit to worm-like chain [7], see Figure 7.2a) was expressed as the sum of an uncoated part of length $L_0(1-f)$ and a coated (and extended) fraction of length $L_0 f e$, L_0 being the 16.4-μm contour length of relaxed uncoated λ-DNA. Similarly, assuming that only uncoated segments stretch under tension and knowing that bare dsDNA can be overstretched to 170% of its relaxed contour length [7], the overstretched length of the partially coated filament (27.0 μm, from inspection of Figure 7.2a) was expressed as the sum of $1.7 \cdot L_0(1-f)$ and $L_0 f e$. From

this set of equations, the values of f and e were solved, yielding a coated fraction f of 25% (for the DNA molecule in Figure 7.2) and a RAD51-induced extension e of 148%. This latter value was reproduced within 4% (standard deviation) with other RAD51–dsDNA assemblies and is comparable to those determined from scanning force and electron microscopy images [176, 180].

In this chapter, we have shown that RAD51 nucleates at multiple sites along ds-DNA, hence forming discrete segments. Moreover, the elasticity analysis showed that the DNA within the filament is stably bound to and held rigidly by RAD51. This information could only be obtained by combining fluorescence imaging with single-molecule manipulation with optical tweezers, hence avoiding the averaging over heterogeneous segments.

7.4 Acknowledgments

We thank Bram van den Broek for a critical reading of the manuscript. This work was supported by the Biomolecular Physics program of the Dutch organization for Fundamental Research of Matter (FOM), and grants from the Dutch Cancer Society (KWF), the Netherlands Organization for Scientific Research (NWO), the Association for International Cancer Research (AICR) and the European Commission.

8

Counting RAD51 proteins disassembling from nucleoprotein filaments under tension

Abstract — The central catalyst in eukaryotic ATP-dependent homologous recombination consists of RAD51 proteins, polymerized around single-stranded DNA. This nucleoprotein filament recognizes a homologous duplex DNA segment and invades it [184, 185]. After strand exchange, the nucleoprotein filament should disassemble in order for the recombination process to complete [186]. The molecular mechanism of RAD51 filament disassembly is poorly understood. Here, we have combined optical tweezers with single-molecule fluorescence microscopy and microfluidics [93, 142] to reveal that disassembly results from the interplay between ATP hydrolysis and release of the tension stored in the nucleoprotein filament. Applying external tension to the DNA, we found that disassembly slows down and can even be stalled. We quantified the fluorescence of RAD51 patches and found that disassembly occurs in bursts interspersed by long pauses. Upon relaxation of a stalled complex, pauses were suppressed resulting in a large burst. These results imply that tension-dependent disassembly takes place only from filament ends, after tension-independent ATP hydrolysis. Our integrative single-molecule approach elucidates the importance of both enzymatic turnover and mechanics in this key homologous recombination reaction step. In this sense, RAD51 filament dynamics bear remarkable resemblance to other polymeric protein assemblies, such as cytoskeletal filaments.

8.1 Introduction

Homologous recombination is a vital mechanism that helps to maintain genome integrity by repairing double-strand breaks in DNA, and generates genetic diversity by exchanging DNA between chromosomes in meiotic cell division. The central process in homologous recombination is the strand exchange between homologous segments of DNA. Recombinase proteins such as RecA and RAD51 catalyze this process by forming an ATP-dependent helical filament around single-stranded DNA (ssDNA) [184]. This filament finds a homologous segment of double-stranded DNA (dsDNA), invades it and catalyzes strand exchange to generate a joint molecule. This resulting structure is further processed in multiple steps by additional proteins, finally yielding two intact, homologous dsDNAs [184, 185]. In order for these steps to proceed properly, it is essential that RAD51 filaments disassemble. It has been shown that hydrolysis of ATP bound at the interface between adjacent monomers is a prerequisite for filament disassembly [176, 187, 188]. RecA and RAD51 not only form ATP-dependent filaments on ssDNA, but also on dsDNA [93, 138, 180, 183]. These dsDNA nucleoprotein filaments may have deleterious effects *in vivo*, e.g., by sequestering these recombinases in nonfunctional dsDNA complexes or by rendering it inaccessible to other DNA transactions. RAD51 filament disassembly can be aided by auxiliary proteins [186]. To understand recombinase removal, it is essential to elucidate the molecular mechanism of the intrinsic RAD51 disassembly reaction.

To follow this process under controlled conditions, we have developed an instrument that combines fluorescence microscopy with force-measuring dual optical traps and a custom-built multi-channel microfluidic flow cell (see section 8.3.1 and Chapter 4) [33, 90, 138]. This instrument enabled us to control and trigger biochemical reactions while mechanically manipulating individual DNA molecules. At the same time, it allowed us to image and quantify the fluorescence from functional human RAD51 variants with a single surface-exposed cysteine, labeled with Alexa-555 [93, 134].

8.2 Results

8.2.1 Triggering RAD51 disassembly

Figure 8.1a depicts our experimental assay, in which we moved single Ca^{2+}-stabilized RAD51–dsDNA complexes [93, 179, 189] to a Mg^{2+}-containing buffer by shifting the microscope stage between parallel flow channels within a second. This buffer exchange activates ATP hydrolysis. Figure 8.1b shows a kymograph [93] of fluorescently

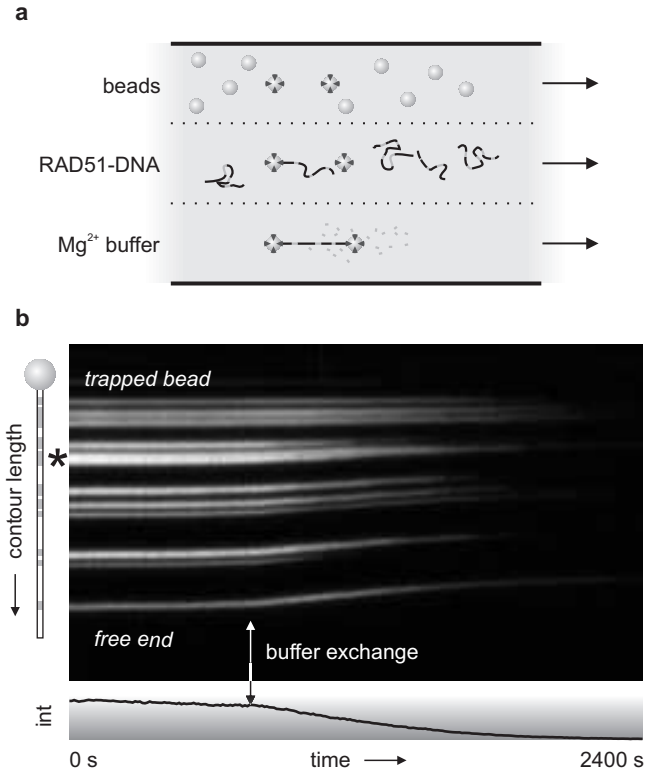

Figure 8.1 – Assay for real-time triggering of RAD51 disassembly. [**a**] Schematic of the multi-channel flow cell approach. A typical experiment is preceded by catching beads in optical traps and the capture of a dsDNA molecule, preincubated with fluorescently labeled RAD51 in stabilizing conditions using Ca^{2+}, by one or both ends. ATP hydrolysis is subsequently triggered by moving the trapped RAD51–DNA complex to a channel containing Mg^{2+}, setting off disassembly. [**b**] Kymograph of a RAD51-coated dsDNA molecule held from one end and stretched using buffer flow. After ∼900 seconds, the trap is moved to the Mg^{2+}-containing buffer channel, as indicated by the vertical double-headed arrow. The subsequent filament disassembly is recognized by the simultaneous contraction and the steady decrease in (integrated) fluorescence intensity (indicated in the graph at the bottom). Patches of RAD51 are marked gray in the cartoon on the left. The asterisk indicates a RAD51 patch that appears to disassemble from one or both ends. The time-lapse movie from which the kymograph was constructed was taken with a 0.5-s exposure time and a 10-s period.

labeled RAD51 polymerized onto a dsDNA molecule, held from one side by a single optically trapped bead and stretched by buffer flow. The triggered ATP hydrolysis results in filament disassembly, as evidenced by a steady decrease of fluorescence in-

tensity concurrent with a marked shrinkage of the complex. This shrinkage, due to relief of RAD51-induced DNA extension upon disassembly, immediately excludes photobleaching as the cause of intensity decrease [93]. Some patches appear to shrink from one or both ends (e.g., the patch marked with an asterisk, Figure 8.1b), suggesting that disassembly occurs from filament ends, as has been reported for RecA [190–192]. With a more sophisticated analysis, we will address this question in more detail below.

8.2.2 Effect of DNA tension

RAD51 forms helical filaments on dsDNA that extend the DNA by about 50% compared to its naked B-form [93, 134, 176, 180]. Could the tension thus stored be a driving force for the disassembly process [193]? To test this hypothesis, we captured RAD51–DNA complexes from both ends between two optically trapped beads [33,93]. Figure 8.2a shows the time course of fluorescence intensity and tension for a complex undergoing disassembly while being held at fixed end-to-end length. Due to the shrinking contour length, the DNA pulls itself taut, after which tension gradually builds up. We observed that disassembly slowed down with increasing tension and even stalled at a tension of $48 \pm 3\,\mathrm{pN}$ (s.e.m.; $n = 7$; obtained from exponential saturation fits). To test that this slowing down is an actual characteristic of RAD51 and not just due to the decreasing number of monomers left to dissociate, we examined the effect of a sudden tension release, induced by instantaneously moving the optical traps closer together. Indeed, Figure 8.2b shows that disassembly immediately reinitiates after tension release, confirming the stabilizing effect of tension on RAD51 filaments.

Figure 8.3 shows how the disassembly rate, calculated as the normalized time derivative of the fluorescence intensity, decreases with tension. This decrease is well fit by a single exponential, suggesting a rate dependence according to Arrhenius' law: $k(F) = k_0 \exp\left[x^\dagger F/k_\mathrm{B}T\right]$, where $k_\mathrm{B}T$ is the thermal energy, F the tension and $x^\dagger$ the distance to the transition state along the relevant reaction coordinate [104]. Apparently, the energy barrier of disassembly is raised by an increase of tension, stabilizing the RAD51-bound state. We determined $x^\dagger$ to be $0.27 \pm 0.04\,\mathrm{nm}$ (s.e.m., $n = 9$). One RAD51 monomer covers 3 base pairs and holds them in an extended conformation of about 1.5 nm in length (compared to 1 nm in canonical B-form DNA) [93, 176, 180, 189]. Therefore, upon disassembly of a single RAD51 the DNA length decreases at most half a nanometer from the bound to the unbound state. Hence, our value for the location of the transition state, $x^\dagger$ is consistent with RAD51 filaments disassembling one monomer at a time.

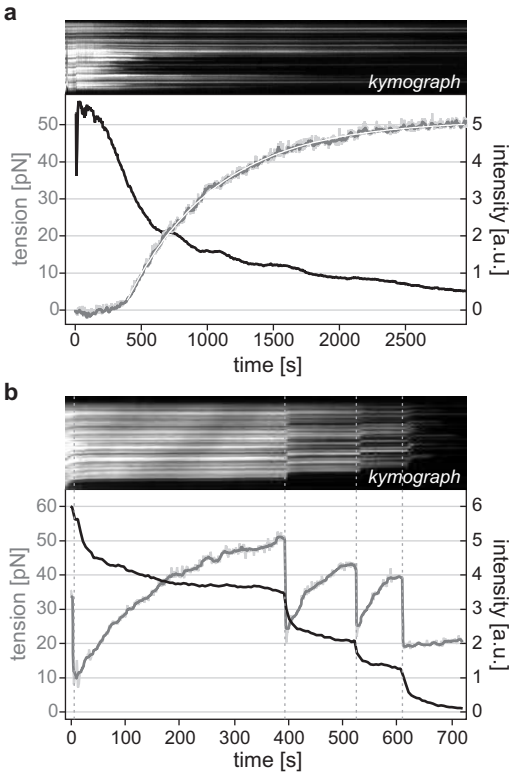

Figure 8.2 – The RAD51 disassembly rate is reversibly reduced by DNA tension. [**a**] Kymograph and integrated intensity trace (black line) of a RAD51–dsDNA complex, held at a fixed end-to-end distance, brought into disassembling conditions at $t = 0$. The tension (gray lines; dark line is a 5-second median filter) builds up as a result of the DNA contraction that accompanies RAD51 filament disassembly, but levels off to stall around 50 pN (white line is an exponential saturation fit). The rate of intensity decrease (slope of black trace) slows down accordingly. [**b**] Disassembly, stalled by tension, reinitiates by instantaneously lowering the tension (vertical dashed lines).

8.2.3 RAD51 disassembles in bursts

Can we demonstrate more directly that RAD51 filaments disassemble as monomers from filament ends and can we extract kinetic rates? To address these questions, we have calibrated the fluorescence intensity to numbers of RAD51 monomers (see section 8.3.4 and Figure 8.8). The calibration factor was determined from the labeling ratio of 1.3 fluorophores per monomer [134] and the average intensity of single Alexa-555 fluorophores. The latter was obtained from single-molecule photobleach-

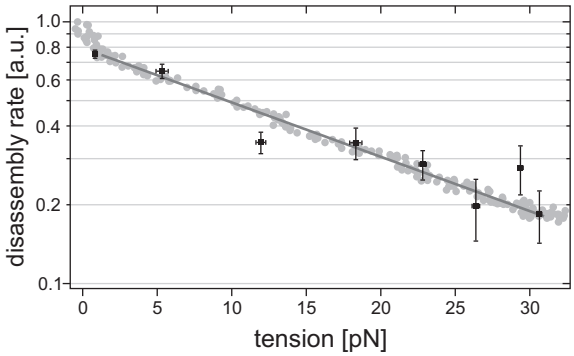

Figure 8.3 – Disassembly rate decreases exponentially with tension. The rate is measured as the time derivative of integrated intensity traces, divided by the instantaneous intensity to compensate for the decreasing number of proteins and filament ends available for disassembly. Black symbols correspond to directly differentiated intensity traces, box-averaged to reduce the scatter due to differentiation (error bars represent s.e.m.); gray circles are the analytical derivative of a phenomenological double-exponential fit to the raw intensity trace, normalized by this same raw trace. Both traces are well fit by an Arrhenius-like exponential function (dark gray line), yielding the same fit value ($x^{\dagger} = 0.20\,\mathrm{nm}$, for this RAD51–DNA complex).

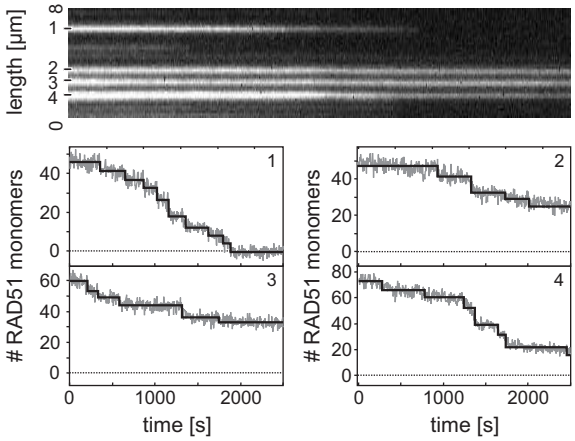

Figure 8.4 – RAD51 disassembly occurs in bursts interspersed with long pauses. Calibrated intensity traces of the isolated, short RAD51 patches indicated in the kymograph show a burst pattern of disassembly activity interspersed by pauses on the order of minutes. These staircases of intensity decrease are well fitted by a step-fitting routine [194].

ing steps in Ca^{2+}-stabilized, optically trapped RAD51–DNA complexes. Figure 8.4 shows a kymograph and corresponding disassembly traces of four isolated RAD51 patches. A striking feature emerged: the intensity decrease was not continuous, but occurred in bursts of varying size, interspersed with pauses on the order of minutes. We fitted many such isolated disassembling filaments using a step-fitting algorithm (black lines in Figure 8.4) [194]. Using the fitted steps, the kinetics of the disassembly can be analyzed from distributions of pause durations and burst sizes (Figure 8.5a and Figure 8.9). Pause durations are exponentially distributed, with a mean of 156 s, suggesting that the pauses were caused by a single Poisson waiting step in the reaction.

8.2.4 Model for RAD51 disassembly

This burst-wise disassembly can be understood with a model in which monomers dissociate exclusively from filament ends after ATP hydrolysis (graphically depicted

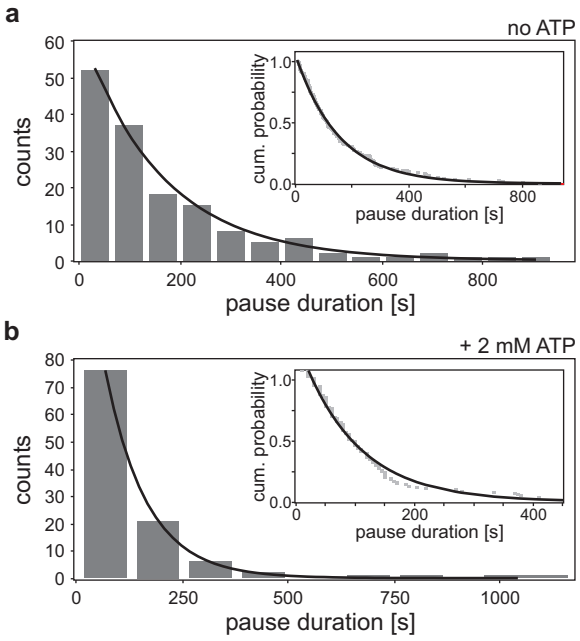

Figure 8.5 – Pause duration histograms. [**a**] Pause durations are exponentially distributed, both when binned into a histogram (decay constant 159 s) and when plotted as a cumulative probability distribution (inset, decay constant 154 s). [**b**] Pauses still occur in the presence of 2 mM ATP with an average duration of 97 s, implying that ATP renewal does not occur significantly.

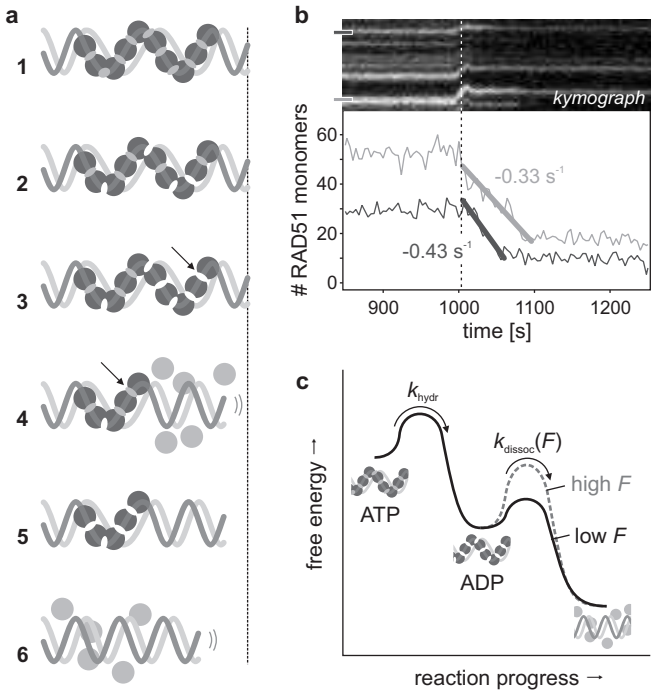

Figure 8.6 – RAD51 disassembly pathway. [**a**] Proposed reaction mechanism. (1) All RAD51 monomers start out having ATP bound and are thus fixed to the DNA. (2) ATP hydrolysis is triggered by exposing the nucleoprotein filament to a Mg^{2+}-containing buffer; filaments remain stable as long as the terminal RAD51 subunits have not yet hydrolyzed their ATP. (3) ATP at the terminal monomer (black arrow) is hydrolyzed. (4] Disassembly occurs in a burst until the next ATP-bound monomer (black arrow) is exposed on the end. (5) Disassembly is paused again until ATP at terminal RAD51 is hydrolyzed. (6) Disassembly is complete; DNA has returned to its relaxed, B-form state. [**b**] Stalled disassembly reactions that are reinitiated by a release of tension (dotted line) show long bursts of disassembly activity. The slopes of these bursts (linear fits) yield the intrinsic dissociation rate of RAD51 at low tension. [**c**] Free energy diagram depicting the reaction progress. Once the hydrolysis of ATP by a terminal RAD51 monomer (governed by a tension-independent rate k_{hydr}, [1–3] in panel a) is completed, the ADP-bound monomers dissociate with a rate $k_{\mathrm{dissoc}}(F)$ that exponentially reduces with DNA tension ([4] in panel a).

in Figure 8.6a). Assuming ATP hydrolysis to take place uniformly along the nucleoprotein filament (as is the case for RecA [195]), we interpret pauses as events in which filament disassembly transiently halts because the terminal monomer has ATP

bound. Once that ATP is hydrolyzed the terminal monomer dissociates, as do the neighbors that already have hydrolyzed their ATP. This burst of disassembly stops once an ATP-bound monomer is encountered. An inference of this model is that the ATPase rate of RAD51 bound to dsDNA is the reciprocal of the average pause duration. However, to accurately determine this rate we need to take into account that the fit residuals in the pause plateaus show a small but nonzero average slope (-0.01 monomers/s). This indicates that small steps (1–3 monomers) are hidden in the noise in our single-patch intensity traces (Figure 8.4) under the applied illumination conditions ($\sim$2.7 monomers s.d.). From this we could determine that on average one short disassembly event per fitted pause was not detected and that we thus overestimated the average pause duration by a factor 2. Taking this into account, we determined that the ATP hydrolysis rate, k_{hydr}, is 0.6–1.3 $\cdot$ $10^{-2}\,\mathrm{s}^{-1}$. This value is similar to that measured with bulk chemical kinetics assays [196], which confirms that the observed pauses are governed by ATP hydrolysis. Interestingly, burst-wise disassembly was still observed in the presence of 2 mM ATP ($k_{\mathrm{hydr}} = 1.0 \cdot 10^{-2}\,\mathrm{s}^{-1}$, Figure 8.5b). This implies that ATP renewal along the filaments takes place at a significantly lower rate than hydrolysis, if occurring at all, suggesting that ADP release is slower than disassembly. This is consistent with ATPase assays that showed that ADP release is the rate-limiting step in the ATPase cycle [196–198]. Our model also predicts the shape of the intensity curves such as shown in Figure 8.3a (see Figure 8.9 in the Appendix, page 119), yielding an estimate for the average filament length of 10–50 monomers, in agreement with earlier results [189]. Moreover, we can predict that on average 5–10 monomers are involved in a burst, which is in perfect agreement with our measurements (Figure 8.10 in the Appendix, page 121).

In our model, ATP hydrolysis precedes RAD51 dissociation. Which of these two causes the reaction to stall, when we apply tension to the DNA (Figures 8.2 and 8.3)? In case only dissociation would depend on tension, ATP hydrolysis would proceed even while disassembly is stalled with high tension. When such a stalled complex is relaxed, an extended disassembly burst without pauses is expected. Indeed, Figure 8.6b shows that isolated stalled patches exhibit such extended disassembly, confirming that ATP hydrolysis continues even at high DNA tension. Apparently, DNA tension changes the rate-limiting reaction step: ATP hydrolysis on the filament ends at no tension and monomer dissociation at high tension. The extended bursts in Figure 8.6b allowed us to directly determine the intrinsic dissociation rate of RAD51 monomers at low tension from the slope of the intensity decrease: $k_{\mathrm{dissoc}} = 0.51 \pm 0.14\,\mathrm{s}^{-1}$ (s.e.m., $n = 5$). Figure 8.6c summarizes the complete mechanokinetic model for ATP hydrolysis and tension-dependent RAD51 disassembly in a free-energy diagram. The extension of DNA that RAD51 imposes acts as a loaded spring that, in part, drives the disassembly

reaction. For this to occur, the RAD51–DNA complex needs to thermally shorten by $x^{\dagger}$ in order to reach the transition state. When external tension is applied, the complex stiffens and consequently the amplitude of thermal fluctuations is reduced, kinetically disfavoring disassembly. In contrast, ATP hydrolysis seems to be independent of DNA tension, suggesting that hydrolysis does not alter the extended configuration of the DNA by RAD51.

Previous reports have discussed the similarities between filament dynamics of RAD51-like recombinases and those of microtubules and actin filaments [199–201]. In all these, nucleotide triphosphate-bound subunits assemble on a filament end and dissociate after nucleotide hydrolysis. The results presented here indicate that the parallel goes even further. First, the burst-like disassembly of RAD51 filaments, triggered by ATP hydrolysis at the terminal subunit, resembles 'catastrophes' of microtubules, periods of shrinkage caused by nucleotide hydrolysis in the GTP-cap (at the tip of the microtubule). Second, the kinetics of RAD51 disassembly are altered by applying external forces, as is the case for microtubules [202]. Cells use the work generated by cytoskeletal filament assembly and disassembly to drive processes such as cell locomotion and chromosome separation. RAD51 filaments similarly store or release elastic energy by extending or relaxing their substrate DNA. It thus appears to be a recurring theme that protein filament (dis)assembly, nucleotide hydrolysis and mechanical work are tightly coupled. An integrative single-molecule approach as employed here allows concurrent visualization, quantification, manipulation and triggering of the dynamics of such complex biological assemblies.

8.3 Experimental methods

8.3.1 Dual trap and fluorescence microscope

The combined fluorescence and optical trapping instrument was built around an Eclipse TE2000-U inverted microscope (Nikon), equipped with a stage riser kit (T-BSUK, Nikon) that allows for stacking two dichroic filter turrets. The optical traps are generated by a Nd:YVO_4 laser (Ventus 1064 nm, 3 W cw, Laser Quantum, Cheshire, UK), isolated against back reflections by a Faraday isolator (IO-5-λ-HP, Optics For Research, Caldwell, NJ). This laser beam was split into two beams by a polarizing beam splitter cube (10BC16PC.9, Newport, Irvine, CA). In both beam paths, a 1 : 2.67 telescope system was implemented allowing for simultaneous beam expansion and beam steering in the sample. In one path, the first telescope lens could be displaced laterally using two computer-controlled actuators (T–LA28, Zaber Technologies Inc., Richmond, BC, Canada) to allow positioning of that trap with a joystick. The beams

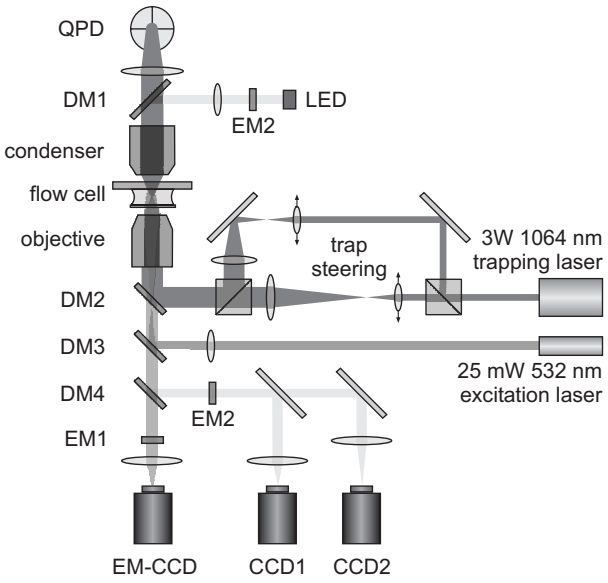

Figure 8.7 – Experimental apparatus. Schematic of the combined dual trap and fluorescence microscope. Abbreviations: DM – dichroic mirror; EM – emission filter; QPD – quadrant photodiode; LED – light emitting diode; (EM-)CCD – (electron-multiplied) charge coupled device. See text for details.

are recombined using a beam splitter cube and coupled via a dichroic mirror ('DM2': 950dcsp, Chroma Tech Corp., Rockingham, VT) into a water-immersion objective (Plan Apochromat 60×, NA = 1.2, Nikon) to generate the laser traps. For displacement detection of the static trap, the intensity profile in the back focal plane of the condenser (Achromat/Aplanat, NA = 1.4, Nikon) was imaged onto a quadrant photodiode ('QPD', SPOT-9DMI, UDT Sensors, Hawthorne, CA) [24]. The photocurrents from the quadrants were differentially amplified with custom electronics [24, 48] to yield x and y displacement signals that were recorded using a 24-bit A/D converter (NI-PCI-4474, National Instruments). Displacement signals were calibrated using power spectrum analysis [24].

For fluorescence excitation of Alexa-555-labeled RAD51, a 532 nm laser (GCL-025-L, 25 mW cw, Crystalaser, Reno, NV) was decollimated for widefield excitation and coupled into the second dichroic filter turret ('DM3': z532rdc, Chroma). Fluorescence emission was band-pass filtered ('EM1': hq575/50m, Chroma) and imaged onto a sensitive electron multiplying CCD camera ('EM-CCD': Cascade 512B, Princeton Instruments, Monmouth Junction, NJ) and read out using the WinView software package (Princeton Instruments). Camera readout could be externally triggered us-

ing a TTL signal for time lapsed data acquisition, reducing the dose illumination and consequently photobleaching of the dyes.

In addition, a bright-field image of the trapped beads, illuminated by a blue LED (LXHL-NB98 Luxeon Star/O, LumiLeds; using Chroma filters 'DM1': 520dcrx, 'DM4': z488rdc, and 'EM2': d440/20) was imaged onto a CCD camera (902K, Watec) that was read out by an image acquisition board (PCI-1407, National Instruments) for online measurement of bead separations.

The custom-built flow cell (Figure 8.1a) featuring multiple parallel, laminar channels with different buffers and reaction components that can be swiftly exchanged has been described in Chapter 4 and elsewhere [90].

8.3.2 DNA and RAD51 preparation

Terminally biotinylated λ-DNA was prepared as described in Chapter 4 and elsewhere [33, 90]. A description of the purification and labeling of functional RAD51 variants has been detailed before [134]. In short, functional human RAD51 variants with only a single surface-exposed cysteine (at residue 31; the cysteine at redidue 319 was replaced by a serine residue), were generated, labeled with Alexa-555, and tested positively for activity.

RAD51–dsDNA nucleoproteins were pre-assembled in Ca^{2+}-stabilized conditions as used before [93, 134]. All buffers were degassed and kept under nitrogen atmosphere to reduce photobleaching. As an additional measure against photobleaching, 1 mM of the reducing agent dithiotreitol (DTT) was present in all buffer solutions.

ATP hydrolysis was triggered in the flow cell by exposing the trapped RAD51–dsDNA complex to a buffer containing 10 mM Mg^{2+} and 10 mM EGTA.

8.3.3 Data analysis

Kymography

Time-lapse recorded fluorescence images were analyzed using kymographs [93], generated using custom-written LabVIEW software. This was done by (i) selecting a narrow box encompassing the DNA contour in all frames, (ii) integrating the pixel values across the DNA to obtain a single line of pixels per frame, (iii) subtracting a per-frame computed background value, and (iv) pasting these pixel lines into consecutive columns of a single image.

Step-fitting algorithm

The Matlab routine for the automated step-fitting algorithm [194], kindly shared by Jacob Kerssemakers, was adapted to suppress back steps. In our implementation, the routine is run with increasing numbers of fitted steps, until the first back step is detected. The optimal number of steps for each trace was obtained both by visual inspection of the fit results and by using the fit/counterfit analysis as used by Kerssemakers *et al.* [194], yielding equal results.

8.3.4 Fluorescence quantification

To calculate the number of RAD51 monomers from the CCD-recorded fluorescence intensity, we analyzed intensity traces of sparsely labeled RAD51–dsDNA constructs

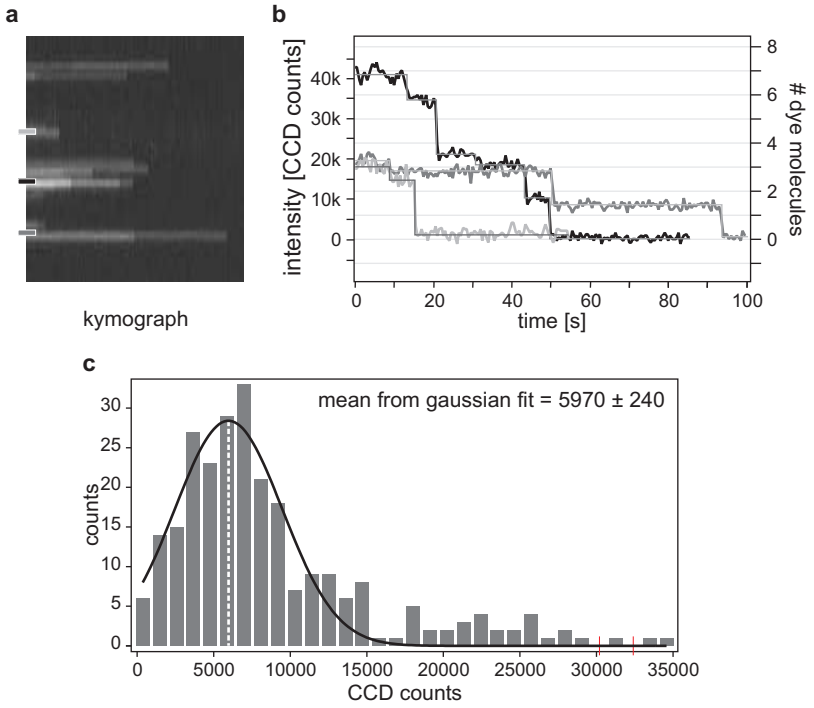

Figure 8.8 – Fluorescence quantification. [**a**] Kymograph of a trapped, sparsely RAD51-coated dsDNA molecule photobleached with ∼10–100× more intense excitation power than used in the disassembly studies. [**b**] Intensity traces of the RAD51 patches indicated in a, indicating the stepwise bleaching. [**c**] Step-size histogram of fitted bleaching steps. The Gaussian fit yields the intensity calibration.

at elevated excitation powers, when photobleaching is increased. Our instrument proved capable of identifying individual bleaching steps in these traces, the size of which corresponds to the fluorescence from a single Alexa-555 label (Figures 8.8a and b). We used an automated step-fitting algorithm [194] to extract these steps in an unbiased manner. The distribution of step sizes and a Gaussian fit are shown in Figure 8.8c. The thus obtained intensity calibration was used to generate the right axis in Figure 8.8b.

The labeling efficiency of our RAD51 variants was determined to be 1.3 dyes per monomer using mass spectrometry [134]. We can thus calibrate the recorded intensity to the number of RAD51 monomers, trivially correcting for differences in exposure time or excitation power.

8.4 Acknowledgments

We thank Bram van den Broek, Remus Dame and Marcel Janson for discussions and a critical reading of the manuscript, and Jacob Kerssemakers for kindly providing his step-fitting algorithm. This work was supported by the Biomolecular Physics program of the Dutch organization for Fundamental Research of Matter (FOM), and grants from the Dutch Cancer Society (KWF), the Netherlands Organization for Scientific Research (NWO), the Association for International Cancer Research and the European Commission Integrated Project.

Appendix: Filament length and burst size

The model depicted in Figure 8.6 was implemented in LabVIEW-based simulations. Filaments were generated with exponentially distributed lengths (filaments with generated with identical lengths yield only minute differences), initially with ATP bound to all monomers. In an iterative manner, ATP hydrolysis was then allowed to occur randomly along the filaments (typically with a 5‰ chance per iteration for each monomer), after which consecutive terminal monomers where ATP hydrolysis had taken place were removed. The shape of the thus obtained disassembly traces de-

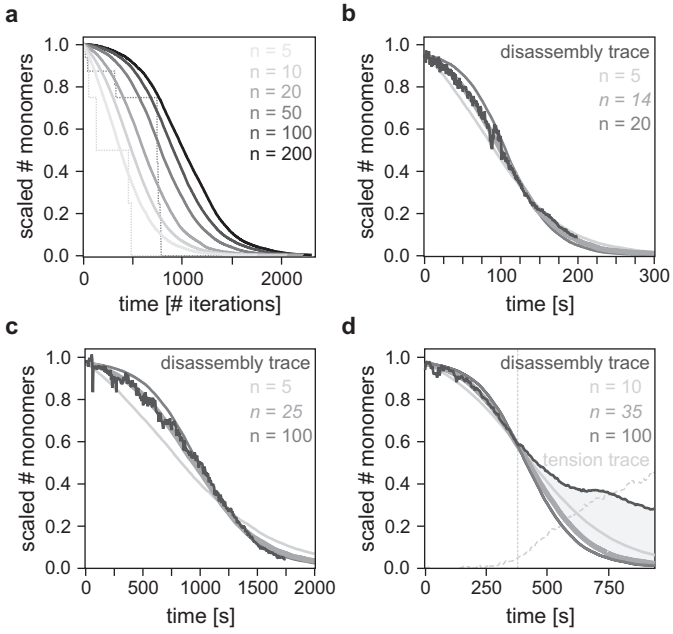

Figure 8.9 – Filament length. [**a**] Simulations of our RAD51 disassembly model reveal a dependence of the shape of disassembly traces on the average initial filament length. The solid, smooth lines are averaged traces (>1000 filaments) for 6 different initial filament lengths; the dotted lines represent individual traces with 10 and 50 monomers, showing pauses and bursts of disassembly. [**b–d**] This shape dependence can be exploited to estimate the average filament length in the measured disassembly traces. Filaments disassembling under negligible DNA tension follow model traces well (panels b and c). The disassembly trace from Figure 8.2a (panel d) indicates that once tension builds up (light gray trace), the trace deviates from the simulated line (shaded area), as expected. The simulated traces indicated in italic make the best fits; we obtained an average initial filament length of <50.

pends on the (average) number of monomers per filament (Figure 8.9a). For long filaments, disassembly is initially limited since it only occurs from filament ends. Disassembly gradually accelerates, because the reservoir of monomers with hydrolyzed ATP grows. This growth is limited by depletion of the reservoir when filaments start to disappear entirely (end effects). For short filaments, disassembly is initially less limited due to the large relative number of ends. In addition, end effects occur sooner. By comparing these simulated traces to experimental ones, we obtained an estimate for the initial filament length in our experiments of 10–50 monomers (Figures 8.9b-d). Disassembly traces recorded with constant DNA tension (using flow-induced drag) are well described by the model (Figures 8.9b and c). As expected, simulated traces start to deviate once DNA tension builds up (Figure 8.9d, shaded area). It is important to note that this relatively short filament length, similar to previous reports [134, 189], depends on the experimental conditions in which filaments were assembled.

As indicated in Figure 8.10a, simulations based on the proposed model yield exponentially distributed burst sizes, averaging to 5–10 monomers per burst for exponentially distributed initial filaments lengths between 10–50 monomers.

Using the step-fitting routine [194], the distribution of numbers of monomers in fitted disassembly bursts was obtained, shown as dark gray bins in Figure 8.10b. The cumulative probability distribution (inset) suggests an exponential distribution with a mean of 5 RAD51 monomers, yet the histogram lacks small bursts (1–3 monomers), which are hidden in the noise. From the remaining average slope in fitted pause plateaus (-0.01 monomers/s; see main text), we estimate that $\sim$1 small burst is missed per pause ($\sim$150 in total). The undetected small bursts are expected to be normally distributed with a standard deviation of 2.7 monomers (the noise in our intensity traces). The light gray bins represent the 150 missed bursts that, together with the measured bursts, recover the expected exponential distribution. This consistency further supports our model of uniform ATP hydrolysis combined with terminal RAD51 dissociation.

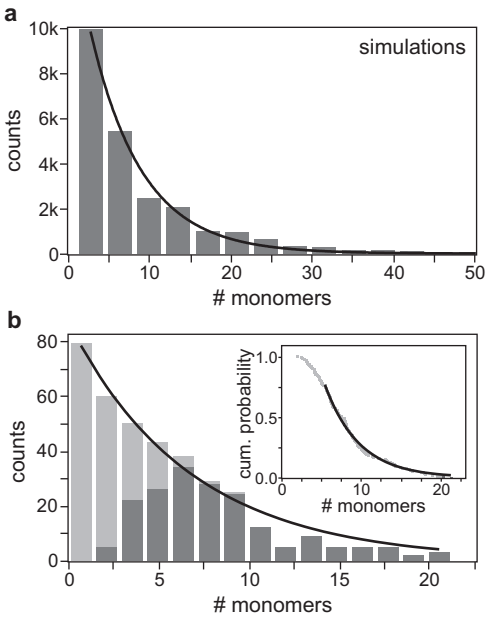

Figure 8.10 – Burst size distribution. [**a**] Simulations based on the proposed model yielded exponentially distributed burst sizes, averaging to 5–10 monomers per burst for exponentially distributed initial filament lengths between 10–50 monomers. [**b**] Experimentally observed burst sizes, obtained from step fits to disassembly traces, seem consistent with exponentially distributed bursts. See text for details.

9

DNA overstretching is a local melting transition

Abstract — Single-molecule manipulation techniques have provided a profound understanding of the elastic behavior of DNA. We now know that DNA can be viewed as an extensible worm-like chain. Interestingly, at stretching forces around 65 pN, DNA has been shown to undergo a phase transition, in which the polymer gains ∼70% in contour length over a very narrow force range. Over the past decade, several models have been put forward that unite many of the experimentally observed characteristics of this overstretching transition. Nevertheless, the basic structure of the overstretched DNA is still subject to debate. Different models do not agree over whether the two strands are melting their base pairs during the transition, or whether the DNA helix unwinds to form a new, base paired structure, named S-DNA. Here, we report experiments that combine the powers of single-DNA manipulation and fluorescence microscopy, to reveal that the overstretching transition is indeed a force-induced melting transition. We use the intercalating dye YOYO and fluorescent single-stranded DNA-binding proteins to specifically visualize double- and single-stranded segments in DNA molecules undergoing the transition. Our data unambiguously show that the overstretching transition comprises a gradual conversion from double-stranded to single-stranded DNA. Moreover, the processivity of the transition can be directly assessed, indicating that melting initiates preferentially on the extremities of the DNA or on a single-stranded nick. Our observation that at 65 pN of tension the DNA indeed reversibly melts, demonstrates that the effects of tension and temperature are similar. Therefore, DNA tension can be reliably used as a tool to investigate the thermodynamics of DNA-protein interaction.

9.1 Introduction

The elastic properties of DNA affect a wide variety of cellular processes in which DNA is involved, such as protein-induced DNA bending, twisting or looping but also, on a larger scale, genome compaction into chromatin or viral capsids, or recombination. Ever since the first single-molecule stretching experiments were performed on double-stranded DNA (dsDNA) [3], many efforts have been put in understanding its elastic behavior [203]. Using scanning force microscopes [204–206], magnetic

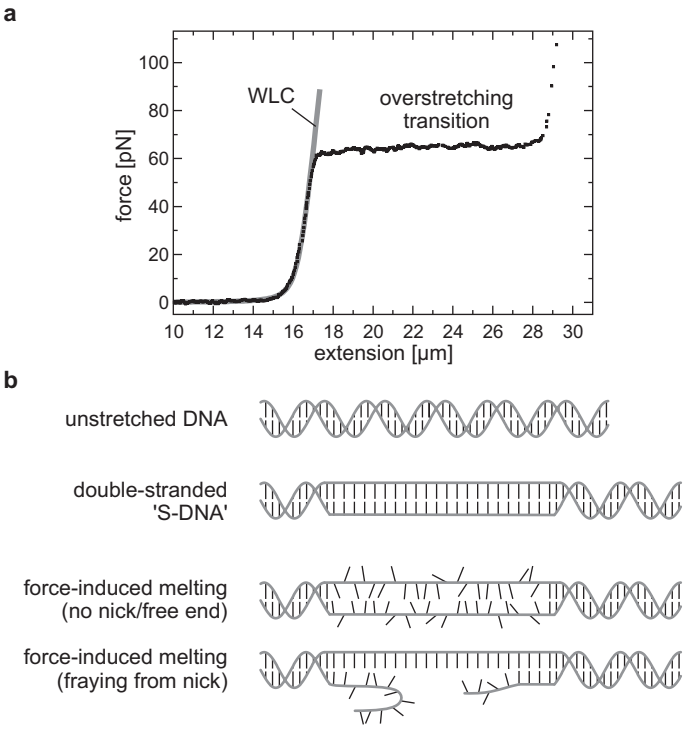

Figure 9.1 – DNA under high tension undergoes the overstretching transition. [**a**]. Typical force-extension curve of λ-DNA, with a contour length of 16.5 µm. The part before the overstretching is well-described by the model curve of an extensible worm-like chain (WLC, gray line). At 65 pN, the OS transition allows an extension of the DNA from 100% to about 170% its contour length. [**b**]. Two models exist that explain the molecular nature of the OS transition. The first one interprets the transition as a gradual unwinding of the DNA double helix, to obtain a parallel ladder which has its base pairing largely intact. Alternatively, the transition is explained as force-induced melting of the two strands. Experimental evidence exists for both models, leaving the interpretation enigmatic.

tweezers [156] or optical tweezers [6–8], different regimes of pulling speed, torsion, and force have been probed. As a consequence, the elastic behavior of dsDNA under moderate forces is now well understood in terms of an (extensible) worm-like chain (WLC) [5, 6]. At stretching forces over 65 pN, dsDNA undergoes a phase transition in which it gains about 70% of contour length with only minor increase in force (see Figure 9.1a) [7, 8]. This structural rearrangement of DNA has been speculated to resemble that in the stretched nucleoprotein filaments involved in homologous recombination [93, 184]. The narrow force range over which this so-called *overstretching* (OS) transition takes place indicated that it is a highly cooperative process. However, the molecular mechanism of the transition has been subject to debate.

Two qualitatively different models exist. The fist one assumes that the OS transition comprises a gradual conversion to a double-stranded conformation structurally different from Watson and Crick's B-DNA [2], named *S-DNA* [8], the structure of which is usually depicted as an unwound ladder with its base pairing largely intact as in Figure 9.1b. The second model assumes that the OS transition is a *force-induced melting* transition that gradually breaks the hydrogen bonds between the two strands to yield single-stranded DNA (ssDNA), similar to thermal melting [207–210]. This base pair melting can either occur between two parallel strands, or initiate from fraying ends or nicks, thus spatially separating the two strands (see Figure 9.1b). This interpretation is supported by a thorough thermodynamic analysis [207] that explains most reported data, including dependencies on solution conditions such as pH, salt and temperature [207, 209, 211, 212]. However, two major arguments against a melting interpretation have been put forward. First, it has been shown that DNA can remain stable beyond the OS transition even when pulled from opposite strands. One would expect that in that case the two strands would separate upon completion of a melting transition. Second, an additional transition at forces of 150-300 pN has been reported [204, 206], depending on the pulling rate and sequence. This transition results either in rupture when pulled from opposite strands, or in ssDNA when pulled from the same strand. Consequently, it was identified as the conversion from S-DNA to ssDNA. In response, it was argued [207] that the stability beyond the OS transition of opposite-strand pulled DNA is only transient and caused by the one-dimensional nature of the transition. Using helix-coil polymer theory [213], the authors calculated the average number of nucleotides in a double-stranded ('helix') or single-stranded ('coil') segment as a function of force [207]. Doing so, they show that the average number of nucleotides in a single-stranded fragment above the overstretching force remains finite. This implies that the average length of a melted segment can be smaller than the total length of the DNA even at forces well above the transition force, explaining that the two strands are still (transiently) stabilized beyond the

transition by short base-paired stretches. In addition to thermodynamic calculations, molecular dynamics simulations have also provided support for force-induced melting [214]. Nevertheless, all melting evidence is based on rather intricate thermodynamic or molecular modeling, and as such is indirect. Moreover, other studies based on different mechanical models claim to exclude the existence of single-stranded segments in the OS transition [215], primarily based on the observation that the elastic response beyond the OS transition differs from that of ssDNA.

To try and settle the disagreement over the nature of the OS transition, we took an approach that *directly* visualizes where and how the transition occurs, without the need for any modeling. We combined micromechanical DNA manipulation using optical traps with simultaneous fluorescence microscopy of dyes bound to the DNA [93] (see Figure 9.6 in section 9.4). Using both dsDNA- and ssDNA-specific fluorescent markers, we were able to assess the nucleation, processivity, and dependence on sequence composition of the OS transition. Moreover, we unambiguously demonstrate that DNA overstretching is in fact a force-induced melting transition. This validates the application of tension to the DNA as a tool to understand the thermodynamics of DNA-protein interactions [31, 210, 216–219].

9.2 Results

9.2.1 Overstretching transition initiates locally and is cooperative

To directly observe the local initiation and cooperativity of the OS transition, we sparsely coated λ-DNA molecules with fluorescently labeled RAD51 variants [93, 134]. These isolated RAD51 filaments serve as nonspecific location markers along the DNA contour. When polymerized into nucleoprotein filaments, RAD51 is locally anchored onto the DNA and does not participate in the OS transition [93]. Therefore, we do not anticipate its presence to alter the overstretching behavior of neighboring uncoated segments. Figure 9.2a shows a kymograph (see section 9.4) [93] of a thus labeled DNA molecule undergoing two overstretching cycles—the corresponding force-extension traces are shown in Figure 9.2b. The kymograph reveals that the two dark, uncoated segments of the DNA (labeled 1 and 2) do not undergo the transition simultaneously. The lengthening of the top patch (1) levels off when the OS plateau is reached (grayscale force bar in Figure 9.2a). Figure 9.2c shows how the two uncoated segments overstretch sequentially. The relative extensions of the two uncoated segments (obtained by applying edge-detection algorithms to the kymograph [93]) are plotted against the relative extension of the entire DNA molecule. During the first pull, the bottom patch 2 (dashed light gray line) goes significantly

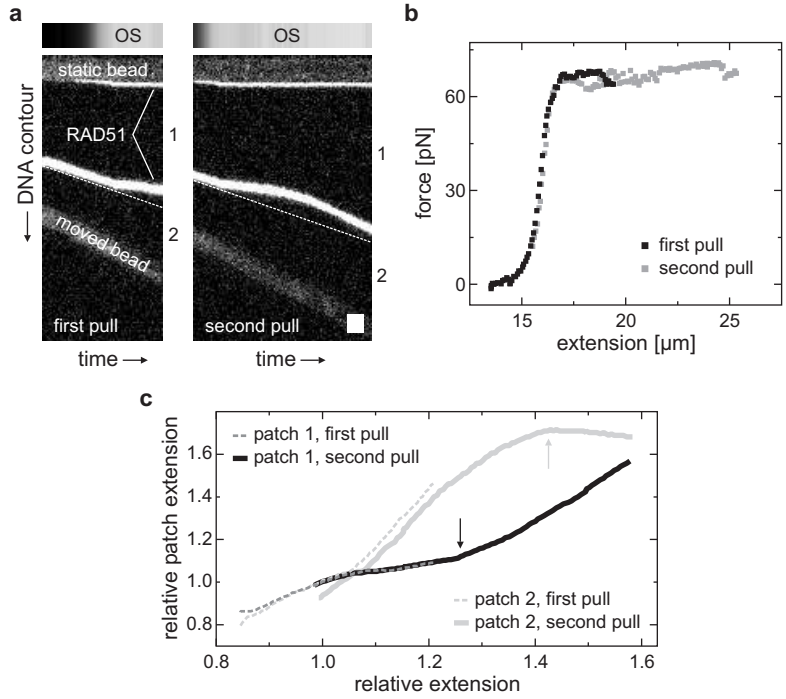

Figure 9.2 – Overstretching is locally nucleated and highly processive. [**a**]. Kymograph of the repeated overstretching of a DNA molecule, coated sparsely with isolated RAD51 filaments, reveals the transition to nucleate and proceed locally; the two uncoated segments do not grow simultaneously. Trapped beads and RAD51 patches are indicated. Time proceeds along the horizontal axis; the bar at the top displays the development of force, indicating where the transition occurs. The white scale bar is $10\,\mathrm{s} \times 2\,\mu\mathrm{m}$. [**b**]. Force-extension curve corresponding to the kymograph in panel a. Data is shown for the first forward pull (black squares), the relaxation (open black squares), and the second pull (gray squares). The second pull goes significantly deeper into the transition than the first one. [**c**]. By plotting the relative extensions L/L_0 of the two patches (1 and 2 in panel a) versus the relative extension of the full DNA molecule, the sequential overstretching is clearly revealed. Only at an extension where the bottom patch is almost entirely overstretched (light gray lines and upward arrow), the overstretching of the top patch initiates (black lines and downward arrow).

into the transition (150% relative extension), whereas patch 1 (dashed dark gray line) halts at the onset of the transition (<110% relative extension). This implies that the transition—irrespective of its structural nature—nucleates locally and proceeds cooperatively from there. In the second pull, both the bottom and the top

segments are pulled into overstretching (to relative extensions of 170% and 160%, respectively). This does not occur simultaneously, however: patch 2 reaches the end of the transition at a relative extension of the full molecule of ∼140%, where patch 1 has just started (vertical arrows). This underscores the local nature of the transition.

To try and understand what structural/chemical feature underlies the initiation of the OS transition in a DNA segment, we coated molecules more densely with RAD51 to have more markers. Figure 9.3a shows kymographs of two consecutive stretching cycles on the same molecule. As reported before [93], the RAD51-coated segments themselves do not stretch at all. As in Figure 9.2, it is clear that in both cases the uncoated segments do not stretch simultaneously, but rather one after another. In between the two stretching cycles, the DNA has been given ample time to return to its

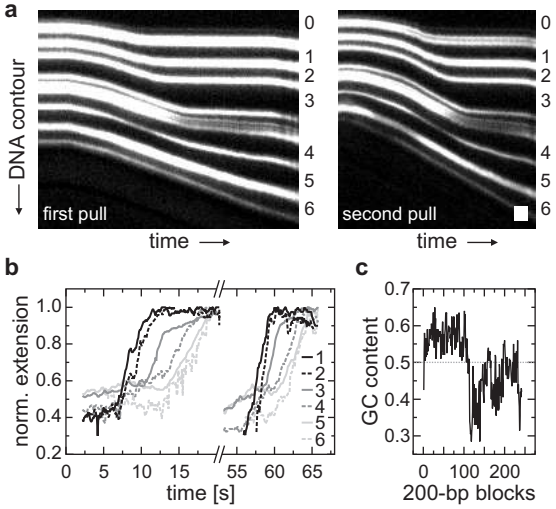

Figure 9.3 – Overstretching initiates reproducibly at 'weak spots'. [**a**]. Kymographs of two stretching cycles on the same, more densely RAD51-coated, DNA molecule. The various uncoated (dark) segments do not overstretch homogeneously but one after another. The order in which the segments overstretch is reproducible. The white scale bar is $1\,\mathrm{s} \times 2\,\mu\mathrm{m}$. [**b**]. Normalized extension traces of the uncoated segments in panel a confirm the reproducibility of the ordered overstretching. Numbers refer to the indicated segments in panel a. The transition proceeds through the molecule from top to bottom, suggesting the influence of structural characteristics like base pair composition and/or single-stranded nicking. [**c**]. Base pair composition of λ-DNA averaged over 200-bp blocks reveals a significant deviation from the dashed 50%-baseline, providing a structural basis for the inhomogeneity of the transition. Alternatively, stochastically occurring nicks could underlie this phenomenon.

B-DNA conformation. Strikingly, the order in which the segments overstretch is not only reproducible, but also appears to be subdivided in two halves along the molecule. This is clearly seen in Figure 9.3b, where the (normalized) length of the numbered segments is plotted versus time: the transition seems to first occur in the top half (patches 1–3) and then in the bottom half (patches 4–6). This behavior has been observed in most experiments with modest RAD51 coating. A possible explanation for this observation is that the initiation of the transition is affected by the inhomogeneous base composition of λ-DNA, which is relatively GC-rich in one half and AT-rich in the other (see Figure 9.3c). Although we do not know *a priori* what the orientation of a trapped DNA molecule is, this may thus be inferred from the overstretching pattern. Alternatively, single-stranded nicks could act as weak spots where the transition more easily nucleates. This suggestion is in line with the observation that the patch at the top of the kymograph in Figure 9.3a (tagged 0), closest to the trapped bead and thus to the free end of the DNA, reproducibly overstretches first. Also in the DNA molecule of Figure 9.2, the patch with a free end (2) overstretched before the other patch, which does not have a free end (1).

9.2.2 Overstretching is nucleation-limited at DNA extremities

Clearly, the OS transition is dominated by a nucleation event, yet the nature of the transition needs to be assessed with other methods. In order to elucidate the structural basis of the OS transition, we designed an experiment to distinctly visualize double-stranded segments along a partly overstretched λ-DNA molecule, by rapidly transferring them to a buffer containing the bis-intercalator YOYO. Figure 9.4a shows fluorescence images of six individual λ-DNA molecules, exposed to YOYO at increasing extensions (indicated on the right). At extensions L up to the contour length L_0 (i.e., relative extensions $L/L_0 \leq 1$) the molecule is stained along its full length (image 1). Interestingly, at extensions beyond the contour length (i.e., in the OS transition) only a discrete fraction of the molecule is stained (images 2–6). This occurs irrespective of the monovalent salt concentration (ranging from <5 mM to 150 mM NaCl). YOYO binds with strong preference to dsDNA, upon which its fluorescence quantum yield is greatly enhanced [220]. Apparently, the OS transition involves a gradual structural conversion to a DNA conformation into which YOYO cannot intercalate. Indeed, the fluorescence images indicate that the labeled fraction reduces with increasing extension. Another interesting observation is that in all the molecules we analyzed, the DNA segments at the extremities, close to both beads, remained unstained. Hence, we conclude that the free ends of dsDNA form favorable nucleation points for the transition. In a few cases, an additional unlabeled segment was

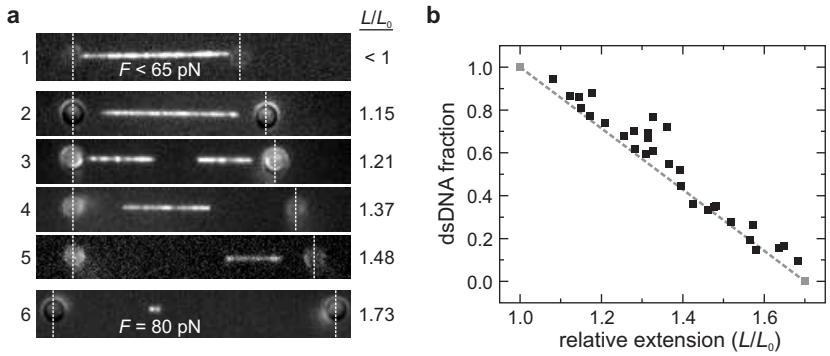

Figure 9.4 – DNA overstretching is a nucleation-limited, first-order phase transition. [**a**]. Fluorescence images of different λ-DNA molecules exposed to the intercalating dye YOYO at various stages of the OS transition show a binary subdivision in labeled and unlabeled segments. The locations of the optically trapped beads are indicated by the vertical dashed lines. The molecule in image 1 is exposed to YOYO prior to the OS transition and becomes labeled along its full length. When exposed to YOYO at higher extensions, discrete unlabeled segments appear and the labeled fraction decreases. The image in image 3 has an unlabeled segment halfway, suggesting an extra OS nucleation on a nick. Image 6 is taken beyond the OS transition at a force of 80 pN, yet still shows a short YOYO-labeled segment that holds the two strands together. The subdivision in large labeled and unlabeled segments reveals that the OS transition is nucleation-limited. [**b**]. The YOYO-labeled fractional contour lengths from images like those in panel a can be converted to the fraction of nucleotides that are still base paired, assuming the YOYO-bound segments to be B-form dsDNA with—at 65 pN—a length per base pair of 0.35 nm [207, 211]. When plot against the relative extension L/L_0, this yields a straight line, which implies that our fluorescence data indeed confirm the OS transition to be a first-order one-dimensional phase transition. The two gray points and the gray dashed line reflect the assumption that there is 100% dsDNA at the onset of the OS transition, and no dsDNA beyond it, at $L/L_0 \approx 1.7$, and were added to guide the eye.

observed in between two labeled segments (e.g., image 3), which may imply overstretching initiated from a single-stranded nick. Strikingly, image 6 is taken beyond the OS transition at a force of 80 pN, yet still contains a short segment that gets labeled by YOYO. Apparently, some dsDNA is still present beyond the transition. This observation explains why the DNA molecule—pulled from its two strands on opposite sides—can at least transiently remain intact beyond the OS transition, as qualitatively anticipated by Rouzina *et al.* [207].

Assuming the YOYO-intercalated segments to be B-form dsDNA, we can convert the apparent contour length fractions seen in the fluorescence images to the actual

fraction of nucleotides that are still base paired. Importantly, we measured the labeled fraction at negligible dye : base pair ratio, to avoid overestimation due to YOYO-induced DNA lengthening (see section 9.4). Figure 9.4b displays this dsDNA fraction versus the relative extension L/L_0. The observed linear dependence confirms that the transition is a first-order one-dimensional phase transition [221]. The two gray points reflect the assumption that there is 100% dsDNA at the onset of the OS transition, and no dsDNA beyond it, at $L/L_0 \approx 1.7$, and have been added to guide the eye. All data lie close to the dashed line connecting these points. This implies that the YOYO-labeled fraction is a largely continuous double-stranded segment with no significant overstretched segments that are too small to be resolved as gaps in the fluorescence images. Such local overstretching would lead to an overestimation of the dsDNA fraction and thus a shift to higher dsDNA fraction. From Figure 9.4b we estimate that such a shift can at most be ∼5%. These data reveal the substantial processivity of the transition when initiated from a free end (see discussion). The fact that the YOYO-labeled fraction for significantly converted molecules is consistently positioned asymmetrically along the molecule (rather than in the center), suggests that the GC-rich half of the molecule (Figure 9.3c) is more resistant to overstretching, which would be anticipated for a process that involves base pair melting.

9.2.3 Overstretching is a melting transition

What can be concluded about the structure of the DNA segments that are not intercalated by YOYO? The conversion to ssDNA cannot be inferred exclusively from the occurrence of the dark patches: the large unlabeled segments as seen in Figure 9.4a can also consist of an extended but base-paired DNA structure (S-DNA), into which YOYO cannot intercalate. To try and find independent evidence for the formation of ssDNA, we generated Alexa-555-labeled human mitochondrial single-stranded DNA-binding proteins (mtSSB, see section 9.4), which has a high binding specificity for ssDNA [222, 223]. Importantly, the dsDNA is not structurally destabilized by the presence of 50 nM mtSSB, as evidenced from (forward) force-extension curves being indistinguishable from those of naked DNA. This is similar to what has been reported for bacteriophage T4 gene 32 protein (gp32) [216, 224, 225]. Reverse stretching curves show very significant hysteresis, indicative of mtSSB binding and hence of the binding of ssDNA [216, 225] (data not shown). Figure 9.5a shows three fluorescence images of a DNA molecule that is overstretched in the presence of fluorescent mtSSB. Fluorescence appears as two isolated dots. We interpret this as mtSSB binding to the partially melted strand that is not under tension, as schematically depicted in Figure 9.5b. Indeed, the fluorescent spot on the left brightens and moves away from

the bead with increasing extension (Figures 9.5a and c). This implies that mtSSB binds to ssDNA that gradually accumulates as the transition proceeds inwards. No fluorescence was observed along extended segments like in the case of YOYO. We independently determined that mtSSB cannot bind to ssDNA under tensions exceeding

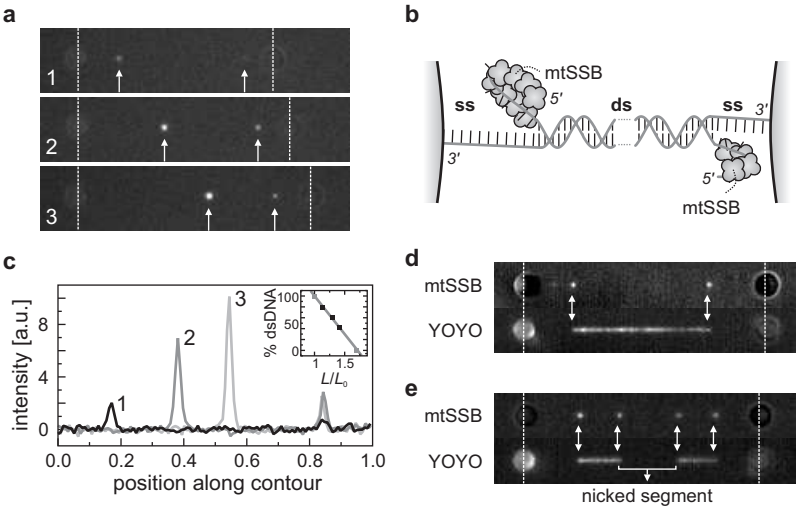

Figure 9.5 – DNA overstretching is a melting transition. [**a**]. Three consecutive fluorescence images of a DNA molecule being stretched in the presence of an Alexa-555-labeled variant of human mitochondrial single-stranded DNA-binding protein (mtSSB) show brightening and translocating spots (white arrows). [**b**]. Interpretation of the fluorescence images in panel a. Overstretching initiates on the fraying ends near the beads. One of the melted DNA strands is not under tension and can bind fluorescent mtSSB, appearing as a bright dot. More mtSSB can bind as soon as more dsDNA is melted. [**c**]. The intensity in the moving spot in panel a scales linearly with the distance it has moved away from the bead. This is consistent with the interpretation of ssDNA accumulating during overstretching. The right spot remains stationary and does not brighten. The inset shows the fraction of base-paired nucleotides (interpreting the segment between the dots as dsDNA; see section 9.4) versus the relative extension, L/L_0, which is consistent with a first-order phase transition (*cf*. Figure 9.4b). [**d–e**]. Two-color fluorescence experiments, in which Alexa-555-labeled mtSSB and YOYO are excited in an alternating manner, reveal that the mtSSB dots coincide with the edges of extended YOYO-labeled segments (white arrows). This corroborates both the interpretation of YOYO-labeled segments as dsDNA, and that of the Alexa-555 dots as mtSSB bound to a melted strand at the junction of the OS transition. The images in panel e show a molecule that, apart from at its extremities, also initiated the transition halfway the molecule, presumably on a nick.

~40 pN (data not shown), consistent with the reported wrapped binding mode of the tetrameric mtSSB [226,227]. The inset in Figure 9.5c shows the double-stranded fraction of the DNA contour for the three images in panel a versus the relative extension, which, analogous to Figure 9.4b, implies a first-order phase transition.

As a final piece of evidence for force-induced melting and the resulting conversion from dsDNA to ssDNA, we combined the mtSSB and YOYO approach by performing two-color fluorescence experiments. We partly overstretched DNA molecules in the presence of mtSSB (like in Figure 9.5a) and exposed them to YOYO at a fixed extension (*cf*. Figure 9.4a). Figure 9.5d shows two fluorescence images, obtained by exciting Alexa-555 or YOYO, respectively. The isolated dots caused by mtSSB binding to a partly melted ssDNA strand (like those in Figure 9.5a) perfectly coincide with the edges of a YOYO-labeled double-stranded segment (white arrows in Figure 9.5d). Figure 9.5e shows a molecule in which the OS transition nucleated not only at its extremities like in Figure 9.5d, but apparently also at a single-stranded nick in the center part. If the segment were to be nick-free, both strands would be under high tension and no ssDNA would accumulate at the transition interface. The corresponding YOYO image indisputably distinguishes double-stranded segments from single-stranded ones. These combined images indeed unequivocally show that the OS transition is a force-induced melting transition.

9.3 Discussion

The identification of the OS transition as force-induced base pair melting over a wide range of monovalent salt concentrations precludes the transition to a base paired S-DNA structure [215]. By specifically staining both ds- and ssDNA domains overstretching was directly observed to initiate at the extremities of the DNA. This can be explained by free ends of dsDNA forming the favorable nucleation point, potentially induced by 'fraying' [228]. Likewise, we occasionally observed transitions occurring halfway a DNA molecule (see Figure 9.4a, image 3 and Figure 9.5e), which can be interpreted as having initiated on a nick. The remarkable processivity of overstretching through a heterogeneous sequence landscape of thousands of base pairs, as seen directly in Figures 9.4 and 9.5, had not been anticipated in previous melting studies [207, 211]. Apparently, the energy penalty for melting even large numbers of GC base pairs is lower than that to nucleate a new melted bubble at an interior location other than a nick. Force-induced melting had been suggested to occur in small domains throughout the DNA molecule, in analogy to thermal DNA melting [207, 211, 229]. Our observations render a large-scale occurrence of such interior single-stranded bubbles improbable. The analogy with thermal DNA melting,

therefore, breaks down in the nucleation behavior. Whereas thermal melting initiates largely as interior (AT-rich) bubbles [230, 231], force-induced melting is shown here to favor nucleation at the DNA extremities. The different manner in which energy is supplied (homogeneously for the former vs. through backbone strain for the latter) presumably underlies this discrepancy. Nonetheless, the application of tension in a single DNA molecule assays has proven an excellent tool to investigate the thermodynamics of DNA-protein interactions [210, 216–219].

In our case of RAD51-coated DNA (Figures 9.2 and 9.3), the OS transition is still observed to occur even though no free end may be available. Every uncoated segment has to independently nucleate the transition at least once since the RAD51 filaments act as roadblocks to the transition [93]. It is unlikely that each naked segment in Figure 9.3a contains a nick. Therefore, we believe that the transition can also initiate internally. A similar situation probably occurs when the melting cooperativity is locally hindered by other DNA-binding ligands such as psoralen crosslinkers [7] or intercalators [217, 221]. The processivity is in this case limited by the distance (and base pair composition) between two such roadblocks.

The significant hysteresis that is often observed upon relaxation of a partially overstretched DNA molecule (e.g., open squares in Figure 9.2b) can be explained as delayed reannealing of the two melted strands [7, 207]. Such delay can be attributed to a few potential causes. First, electrostatic repulsion between the two strands, most prominent at low ionic strength when screening is minor, keeps the strands from restoring their base pairing. Indeed, hysteresis effects have been reported to occur predominantly in low salt conditions [7, 207]. Alternatively, the distant physical separation of the two complementary strands, which we have shown to occur in the case of mtSSB binding (Figure 9.5), may allow the formation of secondary structures (e.g., hairpins) in the slack melted strand. Reannealing of the base pairing will have to compete with this structure, causing hysteresis.

Apart from revealing a preference for initiation on fraying ends, our data are consistent with a dependence on sequence composition, as expected for a melting transition. The inhomogeneous sequence composition of λ-DNA, one half being GC-rich and the other AT-rich (Figure 9.3d), gives rise to enhanced stability in one half of the molecule. This is qualitatively seen in RAD51-, YOYO- as well as mtSSB-data. Interestingly, our observation of molecules with a small YOYO-labeled and thus double-stranded segment at forces beyond the overstretching transition (e.g., image 6 in Figure 9.4a) immediately provides a basis for explaining the (transient) stability of DNA molecules attached and pulled on from two opposite strands. As discussed in the introduction, the observation of this 'beyond-OS' stability has been a key argument against a melting interpretation. We argue that, with the melting

of the last GC base pairs pending, the steep increase of force observed beyond the OS plateau (see Figure 9.1a) indeed corresponds to the elastic stretching of the hybrid ds–ssDNA molecule, of which the (largely GC-paired) double-stranded region gradually degrades [215]. We thus attribute the reported second transition at 150–300 pN [204, 206] to these last base pairs yielding. Although qualitatively different from the equilibrium helix-coil model put forward by Rouzina *et al.* [207], our data support their inference that the DNA can be held together by local non-melted regions—albeit a single one.

In conclusion, we have unveiled the gradual conversion of ds- to ssDNA during the DNA overstretching transition using a combination of DNA manipulation and fluorescence microscopy. Our independent and combined observations of YOYO and mtSSB binding to ds- and ssDNA, respectively, were performed by direct fluorescence visualization and concurrent force-extension measurements. Our interpretation therefore does not rely on thermodynamic, mechano-chemical or other models and assumptions. Moreover, the insensitivity of the observed force-induced melting to ionic strength leads us to conclude that the generic process governing the OS transition is processive base pair melting; we found no indication for a base-paired 'S-DNA' intermediate. We anticipate that our results can provide a new starting point for theoretical investigations of the energetics involved in the transition.

9.4 Experimental methods

9.4.1 Experimental setup

The combined fluorescence and optical trapping instrument, schematically depicted in Figure 9.6, was built around an Eclipse TE2000-U inverted microscope (Nikon), equipped with a stage riser kit (T-BSUK, Nikon) that allows for stacking two dichroic filter turrets. The optical traps are generated by a Nd:YVO_4 laser (Ventus 1064 nm, 3 W cw, Laser Quantum, Cheshire, UK), isolated against back reflections by a Faraday isolator (IO-5-λ-HP, Optics For Research, Caldwell, NJ). The beam was split into two beams by a polarizing beam splitter cube (10BC16PC.9, Newport, Irvine, CA). In both beam paths, a 1 : 2.67 telescope system was implemented allowing for simultaneous beam expansion and beam steering in the sample. In one path, the first telescope lens could be displaced laterally using two computer-controlled actuators (T–LA28, Zaber Technologies Inc., Richmond, BC, Canada) to allow positioning of that trap with a joystick. The beams are recombined using a beam splitter cube and coupled via a dichroic mirror ('DM2': 950dcsp, Chroma Tech Corp., Rockingham, VT) into a water-immersion objective (Plan Apochromat 60×, NA = 1.20, Nikon) to generate the laser

traps. For displacement detection of the static trap, the intensity profile in the back focal plane of the condenser (Achromat/Aplanat, NA = 1.4, Nikon) was imaged onto a quadrant photodiode ('QPD', SPOT-9DMI, UDT Sensors, Hawthorne, CA) [21]. The photocurrents from the quadrants were differentially amplified with custom electronics [21, 48] to yield x and y displacement signals that were recorded using a 24-bit A/D converter (NI-PCI-4474, National Instruments). Displacement signals were calibrated using power spectrum analysis [21].

For fluorescence excitation of YOYO respectively Alexa-555, a linearly polarized 473 nm laser (Cobolt Blues™, 25 mW cw, Cobolt AB, Stockholm, Sweden) or 532 nm laser (GCL-025-L, 25 mW cw, Crystalaser, Reno, NV) was decollimated for widefield excitation and coupled into the second dichroic filter turret ('DM3': z473rdc (YOYO), z532rdc (Alexa-555), or z488/532/633rdc (triple-band), Chroma).

Fluorescence emission was band-pass filtered ('EM1': hq540/80m-2p (YOYO), hq575/50m (Alexa-555), or z488/532/633m (triple-band), Chroma) and imaged onto a sensitive electron multiplying CCD camera ('EM-CCD': Cascade 512B, Princeton Instruments, Monmouth Junction, NJ) and read out using the WinView software package (Princeton Instruments). Camera readout could be externally triggered using

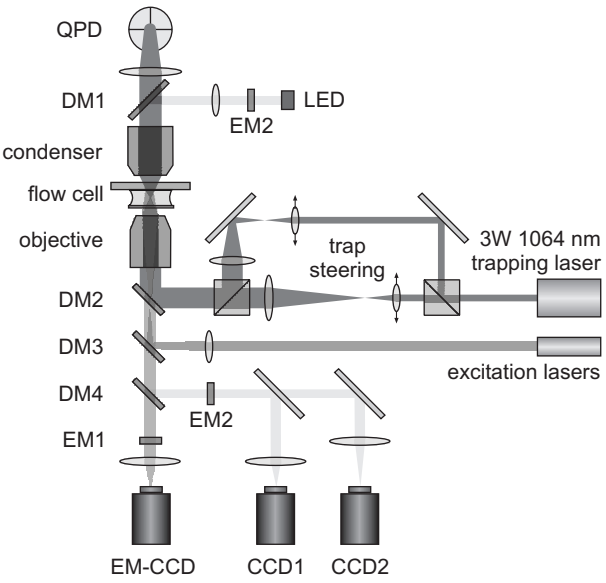

Figure 9.6 – Schematic of the combined dual trap and fluorescence microscope. Abbreviations: DM – dichroic mirror; EM – emission filter; QPD – quadrant photodiode; LED – light emitting diode; (EM-)CCD – (electron-multiplied) charge coupled device. See section 9.4 for details.

a TTL signal for time lapsed data acquisition.

In addition, a bright-field image of the trapped beads, illuminated by a blue LED (LXHL-NB98 Luxeon Star/O, LumiLeds; using Chroma filters 'DM1': 520dcrx, 'DM4': z488rdc, and 'EM2': d440/20) was imaged onto a CCD camera (902K, Watec) that was read out by an image acquisition board (PCI-1407, National Instruments) for online measurement of bead separations.

The custom-built flow cell with multiple parallel, laminar channels that can contain different buffers and reaction components that can be swiftly exchanged has been described elsewhere [90].

9.4.2 Preparation of DNA, RAD51, SSB, and YOYO

Terminally biotinylated (3'-end) λ-DNA and functional human RAD51 labeled with Alexa-555 were prepared as described elsewhere [33, 90, 134]. RAD51-dsDNA nucleoproteins were pre-assembled in Ca^{2+}-stabilized conditions as before [93, 134]. YOYO was purchased from Molecular Probes (trade name YOYO-1®).

For fluorescent labeling of human mitochondrial single-stranded DNA-binding proteins, a cysteine residue was introduced at the C-terminal end by PCR. The PCR fragment was cloned into pBacPAK9 and used to generate recombinant Autographa californica nuclear polyhedrosis virus (BacPAK, Clontech). The protein was expressed in Spodoptera frugiperda (Sf9) cells and purified as previously described [232], with an additional purification step (prior to the hydroxyapatite column) using a 1-ml Hi-Trap SP column (GE Healthcare). The purified mtSSB cysteine variant was stored in 10 mM KPO_4 pH 7.2, 0.1 M NaCl and 10% glycerol, and labeled with maleimide Alexa-555 dye (Molecular Probes). Unreacted dye was removed from the sample with size-exclusion spin-columns (Sephadex G-25, GE Healthcare).

9.4.3 Experimental procedures

DNA molecules were captured between two optically trapped beads (1.87 μm streptavidin-coated polystyrene beads, Spherotech) using the multi-channel laminar flow cell and stretched by increasing the distance between the optical traps. Fluorescence and force-extension data were recorded in a synchronized manner. For experiments involving YOYO labeling, partly overstretched DNA molecules were exposed to a 10-mM Tris buffer (pH 7.4–7.8) containing 10–50 nM YOYO and either 5, 50, or 150 mM NaCl, while fluorescence was recorded. Measurements of the labeled fraction were performed only on the first few frames where YOYO appeared, in order to avoid overestimation due to the YOYO-induced lengthening of dsDNA: we estimate that in this case the dye : base pair ratio does not exceed 1 : 500.

Stretching experiments with mtSSB were performed in a 10-mM Tris buffer (pH 7.4–7.8) containing 50 nM Alexa-555 labeled mtSSB and 50 mM NaCl. Fluorescence snapshots were taken in a flow channel without mtSSB to reduce background fluorescence. For two-color experiments, such mtSSB-labeled DNA molecules were exposed to a 10-nM YOYO buffer.

9.4.4 Kymograph analysis

Time-lapse recorded fluorescence images were analyzed using background-subtracted kymographs [93], generated using custom-written LabVIEW software (Figures 9.2a and 9.3a). To automatically extract partial extensions of RAD51-free segments, LabVIEW edge-detection routines were used on these kymographs to obtain sub-pixel resolution as before [93].

9.5 Acknowledgments

We thank Mauro Modesti for purification, labeling and testing of fluorescent RAD51. This work is part of the research program of the 'Stichting voor Fundamenteel Onderzoek der Materie (FOM)', which is financially supported by the 'Nederlandse Organisatie voor Wetenschappelijk Onderzoek (NWO)'.

10

A polarized view on DNA under tension

Abstract — In the past decades, sensitive fluorescence microscopy techniques have contributed significantly to our understanding of the dynamics of DNA. The specific labeling of DNA using intercalating dyes has allowed for quantitative measurement of thermal fluctuations the polymers undergo. On the other hand, recent advances in single-molecule manipulation techniques have unraveled the mechanical and elastic properties of this intricate polymer. Here, we have combined these two approaches to study the conformational dynamics of DNA under a wide range of tensions. Using polarized fluorescence microscopy in conjunction with optical-tweezers based manipulation of YOYO-intercalated DNA, we controllably align the YOYO dyes as a function using DNA tension, enabling us to disentangle the rapid dynamics of the dyes from that of the DNA itself. With unprecedented control of the DNA alignment, we resolve an inconsistency in reports about the tilted orientation of intercalated dyes. We find that intercalated dyes are on average oriented perpendicular to the DNA, yet undergo fast dynamics on the time scale of absorption and fluorescence emission. Moreover, we assess the structural changes occurring in and beyond the overstretching transition of double-stranded DNA, during which the base pairs gradually melt. Our combined approach thus contributes to the elucidation of unique features of DNA dynamics.

10.1 Introduction

With the advent of single-molecule observation techniques, DNA has become a model system for studying the dynamics of semi-flexible polymers [233–235]. The direct visualization of fluorescently labeled DNA undergoing Brownian motion using DNA-specific fluorescent dyes has allowed for a quantitative understanding of its thermal fluctuations [123, 150, 236]. Many dyes specific to double-stranded DNA (dsDNA) have been employed both in bulk and microscopic fluorescence applications. These dyes can be classified according to their mode of binding to DNA into two major categories: groove binding dyes (e.g., DAPI or Hoechst, binding in the minor groove) and intercalating dyes (e.g., ethidium bromide, SYBR dyes, or cyanine dyes like TOTO, YO, YOYO, etc.). The latter are planar organic structures that specifically bind dsDNA by sandwiching in between consecutive base pairs (see Figure 10.1 and inset), thereby lengthening the DNA upon binding [237]. Both groove binders and intercalators have a well-defined orientation with respect to the helix axis of the DNA. For intercalators, the absorption and emission dipole moments are roughly perpendicular to the DNA helix axis [238, 239].

This latter property makes intercalated dyes particularly suitable for polarized optical spectroscopy [240]. Such techniques, including linear or circular dichroism spectroscopy and fluorescence anisotropy, can be used to study the orientation and orientational dynamics in macro- or microscopic samples [240–242].

Fluorescence polarization anisotropy (FPA) measures the reorientation of a sample within the ultrashort time span between excitation and emission of a fluorescence photon. This is achieved by exciting the sample with linearly polarized light and probing how much fluorescence signal is emitted with its polarization parallel and

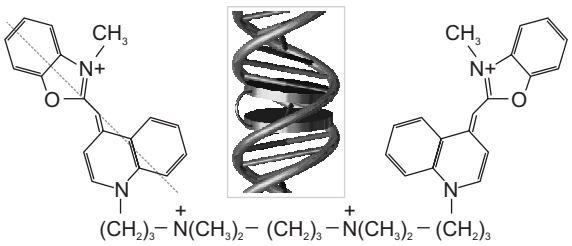

Figure 10.1 – Intercalating dyes have a defined orientation when bound to ds-DNA. Chemical structure of the bis-intercalator YOYO. The dashed line across the chromophore on the left depicts the orientation of the absorption and emission dipole moment [238]. The inset shows schematically how its two chromophores intercalate in between the base pairs of dsDNA.

perpendicular to the excitation polarization. The anisotropy r is defined as:

$$r = \frac{I_{\parallel} - I_{\perp}}{I_{\parallel} + 2I_{\perp}}, \tag{10.1}$$

where the I terms correspond to the fluorescence intensities with polarization parallel and perpendicular to the excitation polarization, indicated by the suffixes. This quantity has been used to study reorientations of DNA conformations both in steady state [243, 244], and in a time-resolved manner [245], for quantitation of rotational diffusion.

Linear dichroism (LD) measurements, on the other hand, probe the anisotropic *absorption* of linearly polarized light. LD measurements require sample orientation: for unordered, isotropic samples, the absorbing molecules on average assume every orientation, rendering LD zero. LD is defined as $\mathrm{LD} = {}_{\parallel}A - {}_{\perp}A$, where the prefixes indicate the incident light polarization with respect to the sample orientation axis. To avoid the comparison of absolute sample absorptions, one uses the *reduced* linear dichroism $\mathrm{LD_r}$, i.e., the LD normalized by the isotropic absorption A_{iso}. For a sample with cylindrical symmetry around the sample axis, this can be estimated as $A_{\mathrm{iso}} = \frac{1}{3}\left({}_{\parallel}A + 2\,{}_{\perp}A\right)$ [241]. For fluorescent samples, $\mathrm{LD_r}$ can also be measured by probing the fluorescence emission upon polarized excitation:

$$\mathrm{LD_r} = \frac{{}_{\parallel}I - {}_{\perp}I}{I_{\mathrm{iso}}} = \frac{{}_{\parallel}I - {}_{\perp}I}{\frac{1}{3}\left({}_{\parallel}I + 2\,{}_{\perp}I\right)}. \tag{10.2}$$

Several techniques exist to obtain the macroscopic preferred sample orientation required for $\mathrm{LD_r}$ measurements, including the use of flow fields, electrophoresis, compressed gels or stretched films [241]. Values for $\mathrm{LD_r}$ yield a measure for the average orientation of the absorbing (and, for fluorescence-detected $\mathrm{LD_r}$, also emitting) dipole:

$$\mathrm{LD_r} = \tfrac{3}{2}S\left(3\cos^2\theta - 1\right), \tag{10.3}$$

with θ the average angle between the absorbing dipole moment and the sample orientation, and S the orientation factor, equal to 1 for a perfectly aligned sample and 0 for an isotropic one [241]. In practice, sample alignment is imperfect, such that $\mathrm{LD_r}$ measurements yield a measure for $\left\langle \cos^2\theta \right\rangle$, i.e., an average effective dipole orientation angle. This makes the quantitative interpretation of $\mathrm{LD_r}$ measurements problematic: imperfect sample alignment always yields an underestimated θ if no independent assessment of S is at hand.

$\mathrm{LD_r}$ measurements have been widely applied to DNA and DNA-binding (intercalating) dyes in bulk spectrometric assays [238,239,241,246–248]. Due to the aforementioned difficulties, some reports do not agree on the orientation of base pairing plane

of dsDNA, assessed using LD_r spectroscopy in the UV, where nucleic acids strongly absorb. Inclination angles of up to 25° have been reported [239,241,246,247], whereas structural studies reported the base-pairing plane to make only a small (<10°) angle with respect to the B-form helix [2,241,249]. A similar disagreement exists about the orientation of fluorescent dyes intercalated in dsDNA [238,239,241,246,248,250]. In addition to spectrometric assays, polarized fluorescence microscopy has been applied to the study of intercalated dye orientation [153, 251–253]. In these cases, samples were oriented using hydrodynamic flow. However, the discrepancy about intercalator orientation remained unresolved.

Fluorescence anisotropy and linear dichroism measurements can also be united, by combining polarization-selective excitation with polarization-sensitive detection of the fluorescence of oriented samples. This yields four intensity measurements, ${}_{\mathrm{ex}}I_{\mathrm{em}}$, where the prefix 'ex' indicates the excitation polarization and the suffix 'em' the fluorescence polarization. To allow a quantitative comparison of the (most often uncalibrated) intensities ${}_{\mathrm{ex}}I_{\mathrm{em}}$, the following emission (P) and absorption (Q) polarization *ratios* are often considered instead [254–256]:

$$P_{\parallel} = \frac{{}_{\parallel}I_{\parallel} - {}_{\parallel}I_{\perp}}{{}_{\parallel}I_{\parallel} + {}_{\parallel}I_{\perp}}, \qquad P_{\perp} = \frac{{}_{\perp}I_{\perp} - {}_{\perp}I_{\parallel}}{{}_{\perp}I_{\perp} + {}_{\perp}I_{\parallel}}, \tag{10.4}$$

$$Q_{\parallel} = \frac{{}_{\parallel}I_{\parallel} - {}_{\perp}I_{\parallel}}{{}_{\parallel}I_{\parallel} + {}_{\perp}I_{\parallel}}, \qquad Q_{\perp} = \frac{{}_{\perp}I_{\perp} - {}_{\parallel}I_{\perp}}{{}_{\perp}I_{\perp} + {}_{\parallel}I_{\perp}}. \tag{10.5}$$

These P and Q ratios are related to FPA and LD_r, respectively (*cf.* Eqs 10.1 and 10.2 [240, 241].

The application of single-molecule manipulation techniques to DNA provides fine control over its extension, while allowing measurements of the piconewton forces involved in stretching it. Using such techniques, the mechanical and elastic properties of DNA have been assessed and are now well understood [5–7, 203, 207]. Here, we have taken an approach combining optical tweezers and polarized fluorescence microscopy, to investigate the dynamics of intercalated DNA under increasing levels of tension. We directly measured the alignment of the transition dipoles of the dyes when the DNA is pulled taut. We performed Monte Carlo simulations of partially extended polymers. Moreover, we extended the analysis of Irving [254] to express the polarization ratios P and Q in terms of the orientation of individual dyes with respect to a laboratory symmetry axis, originally developed for the study of the orientation of myosin light chains in muscle fibers [255, 256]. Doing so, we are able to discern between fluorescence depolarization due to either statically tilted intercalation, or fast diffusional dynamics of DNA and dyes. Moreover, by pulling with forces at which the DNA undergoes the famous overstretching transition (see Chapter 9) [7], we study

the dynamics of DNA undergoing force-induced base pair melting. We show that intercalating dyes stay bound to even largely melted DNA.

10.2 Results and discussion

10.2.1 Force-extension before and after labeling

Unlabeled DNA molecules were suspended between two optically trapped beads in the experimental setup depicted in Figure 10.12a on page 161. Force-extension analysis was used to reveal whether a single molecule was captured, upon which the DNA was moved to a buffer containing 100–200 nM YOYO (see section 10.4.6). For DNA molecules under tension, YOYO binding could be observed as a decrease of tension, caused by the lengthening of the DNA upon intercalation [237]. The extent of labeling could be controlled simply by changing the duration of exposure to dye. Figure 10.2 shows force-extension graphs for DNA molecules before and after labeling. The extent of labeling could be calculated for each DNA molecule from the ratio of contour length before and after labeling (see section 10.4.6). Typically, the ratio of dyes to base pairs was 1 : 40. At higher labeling ratios (up to 1 : 10), the DNA overstretching transition,

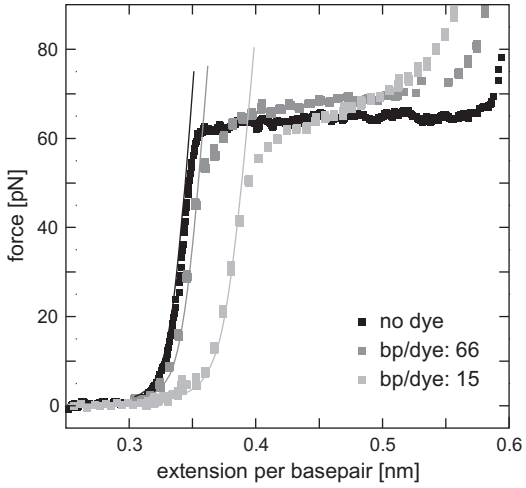

Figure 10.2 – Intercalation of dsDNA by YOYO extends DNA. Force-extension plots of three molecules with different levels of labeling show the DNA lengthening induced by YOYO intercalation. The solid lines are curve fits to the extensible worm-like chain [5]. The corresponding labeling ratios indicated in the legend are estimated by comparison of the fitted contour lengths before and after labeling.

occurring as a force plateau at 65 pN, picks up a slope (*cf*. gray traces in Figure 10.2). This is most likely caused by the intercalating dyes interfering with the transition, rendering it less cooperative [217, 221] and rendering the end of the transition less sharp, as is discussed below. In all cases, the labeling ratio was low enough to preclude YOYO binding modes other than intercalation [239].

10.2.2 Polarized fluorescence

Next, the DNA was moved to a buffer channel without YOYO. Here, the concurrent polarized fluorescence and DNA extension experiments were performed by recording fluorescence images with polarization of the excitation light alternating between perpendicular and parallel to the DNA, respectively. These orthogonal axes are graphically depicted in Figure 10.3. A Wollaston prism in front of the camera (see Figure 10.12a and section 10.4.4) was used to spatially separate the emitted fluorescence into two orthogonal polarizations [257] to generate four intensity signals for every DNA extension, ${}_{\mathrm{ex}}I_{\mathrm{em}}$, with excitation polarization 'ex' and emission polarization 'em' being either parallel (‖) or perpendicular (⊥) to the DNA. After recording images

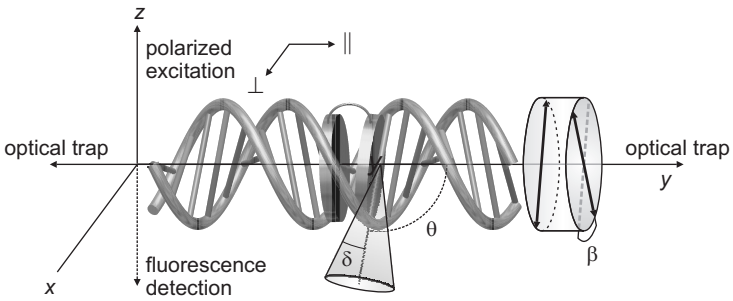

Figure 10.3 – Coordinate system for polarized fluorescence of DNA under controlled tension. The DNA is pulled taut using two optical traps on the y–axis. The fluorescence excitation propagates in the positive z–direction with its polarization alternately aligned with the x– and y–axis (⊥ and ‖ respectively); emission is collected in epi-fluorescence mode, i.e., in the negative z–direction. The absorption and emission dipole moments of the intercalated dyes (depicted as cylindrical disks) make an angle θ with respect to the local DNA helix axis. In the 'fast wobble' model (see text), the dye undergoes rapid reorientations at the timescale between absorption and emission of a photon within a cone of semi-angle δ. The two intercalated chromophores of a YOYO dimer make an azimuthal angle β with respect to each other, as indicated by the cylinder on the right. The latter becomes relevant when energy transfer between these chromophores is accounted for—see section 10.4.8.

for both polarizations 'ex', the DNA extension was stepwise increased. Figure 10.4a shows a sequence of images of the four intensity channels ${}_{\mathrm{ex}}I_{\mathrm{em}}$ at different DNA extensions and forces. It appears that the dyes gradually align their emission dipoles in the direction orthogonal to the DNA, as qualitatively evidenced by the fading of channels of those with a parallel component, in favor of ${}_{\perp}I_{\perp}$. This effect is more readily seen when the fluorescence in each frame is integrated and background corrected (see section 10.4.5). Figure 10.4b displays the intensities ${}_{\parallel}I_{\parallel}$ and ${}_{\perp}I_{\perp}$ (normalized to the maximum of ${}_{\perp}I_{\perp}$) as a function of the relative extension L/L_0. The graph shows the data of 22 DNA molecules (gray symbols), as well as the same data after applying a median filter (solid gray lines) and a box average (white symbols; error bars

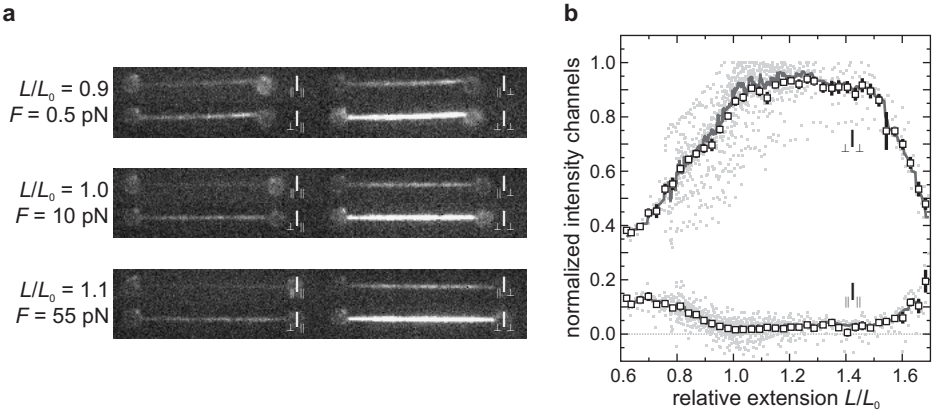

Figure 10.4 – Polarized fluorescence of DNA at increasing extensions. [**a**] Consecutive polarized fluorescence images of a DNA molecule at the three extensions and forces indicated on the left. For every extension and force, the corresponding four polarized fluorescence images ${}_{\mathrm{ex}}I_{\mathrm{em}}$ are shown. The intensities with a parallel component are decreasing with tension, in favor of ${}_{\perp}I_{\perp}$. [**b**] Integrated intensities ${}_{\parallel}I_{\parallel}$ and ${}_{\perp}I_{\perp}$ (normalized to the maximum of ${}_{\perp}I_{\perp}$) versus the relative extension L/L_0. The data of 22 separate experiments on individual DNA molecules is shown (gray symbols), as well as the same data after applying a median filter (solid gray lines) and a box average (white symbols; error bars represent s.e.m.). The other two channels, ${}_{\perp}I_{\parallel}$ and ${}_{\parallel}I_{\perp}$, follow qualitatively the same trend as ${}_{\parallel}I_{\parallel}$ (not shown). The intensity in the ${}_{\perp}I_{\perp}$ channel increases up to an extension of $L/L_0 = 1$, whereas ${}_{\parallel}I_{\parallel}$ falls off, indicating the gradual alignment of transition dipoles perpendicular to the DNA. When the DNA is pulled taut, both ${}_{\perp}I_{\perp}$ and ${}_{\parallel}I_{\parallel}$ plateau for the duration of the DNA overstretching transition. Beyond the transition, a sharp decline of ${}_{\perp}I_{\perp}$ is observed, while the intensity channels with a parallel component slightly recover. This latter fact precludes the drop in ${}_{\perp}I_{\perp}$ as being (exclusively) due to dye dissociation.

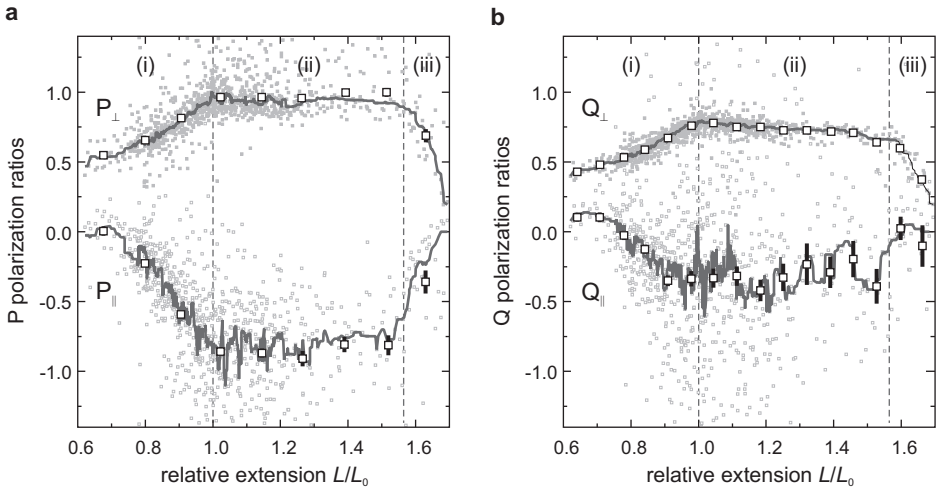

Figure 10.5 – Absorption and emission polarization ratios. [**a**] Emission polarization ratios $P_\perp$ (filled gray squares) and $P_\parallel$ (open gray squares) plotted versus DNA extension for 22 individual DNA molecules. Also shown is median-filtered (solid gray lines) and box-averaged data (white symbols; error bars represent s.e.m.). [**b**] Absorption polarization ratios $Q_\perp$ (filled gray squares) and $Q_\parallel$ (open gray squares) plotted against extension like in panel a. In both panels, the vertical dashed lines divide the graphs into three regimes of stretching, described in the text.

represent s.e.m.). The other two channels, ${}_\perp I_\parallel$ and ${}_\parallel I_\perp$, follow the same trend as ${}_\parallel I_\parallel$ (not shown). For quantitative analysis, the obtained intensities were corrected for the unequal transmission of the microscope optics for the two polarizations. In addition, the emission depolarization resulting from the collection of off-axis rays by the high numerical aperture (NA) objective was compensated for (see section 10.4.7).

For a quantitative interpretation of the intensities ${}_{\mathrm{ex}}I_{\mathrm{em}}$, we used the emission and absorption polarization ratios P and Q of Eq. 10.4 and 10.5. Figure 10.5 shows these polarization ratios, calculated from the four polarized intensity channels ${}_{\mathrm{ex}}I_{\mathrm{em}}$ after applying the above corrections, versus the relative extension L/L_0, as well as median and box averaged data. (The enhanced scatter in $Q_\parallel$ at larger extensions is caused by values of ${}_\parallel I_\parallel$ and ${}_\perp I_\parallel$ being close to zero.)

Three regimes can be distinguished (separated by the vertical dashed lines in Figures 10.5a and b): the ratios incline at extensions at which the DNA is slack ($L/L_0 < 1$; regime [i]), display a plateau in the DNA overstretching transition ($1 < L/L_0 \lesssim 1.55$; regime [ii]), and show a sharp depolarization at extensions beyond this transition (regime [iii]). These three regimes are assessed in more detail below.

10.2.3 Regime [i]: slack DNA

At extensions ranging down from $L/L_0 = 1$, i.e., before the DNA is pulled taut and therefore at negligible DNA tension, the polarization ratios display an increasing depolarization. This observation underscores the necessity for proper sample alignment in polarized absorption measurements like linear dichroism [241]. For a quantitative interpretation of LD_r measurements, one often has to assume a 'perfect' sample alignment ($S = 1$, see Eq. 10.3). The behavior of the polarization ratios up to $L/L_0 = 1$ immediately exposes the vulnerability of this quantitation for imperfect sample alignment, as will be discussed below. The origin of this depolarization is an increase in (thermally excited) DNA diffusion on the millisecond time scale: the lower the end-to-end length, the more conformational states the DNA can explore. Hence, at lower extensions, the dipole moments of the intercalated dyes will undergo larger thermal fluctuations around the symmetry axis connecting the two beads.

In addition to this depolarization caused by the relatively slow DNA fluctuations ('slow wobble'), the dyes may perform rapid, intrinsic dynamics on the nanosecond timescales between fluorescence excitation and emission [242]. Such 'fast wobble' also has a depolarizing effect. However, most polarization-based techniques cannot discriminate properly between such slow and fast wobble depolarization.

Irving developed a framework to express the polarization ratios P and Q in terms of the orientation of individual dyes with respect to a laboratory symmetry axis [254]. He derived expressions for two cases: (1) the absorption and emission dipole vectors of the dye making a static inclination angle θ_a and θ_e to the symmetry axis (i.e., no fast wobble), and (2) the dye undergoing rapid dynamics within a cone of semi-angle δ on the timescale between absorption and emission of a photon (cone-restricted fast wobble). The angles θ and δ are shown in Figure 10.3. Both a static inclination angle of the dye's dipole moments with respect to the symmetry axis and cone mobility have a depolarizing effect on the measured P and Q ratios. Note that for intercalating chromophores, the absorption and emission dipole moments have been reported to be parallel [238]: $\theta_a = \theta_e$.

The P and Q values attained at the extrema (at $L/L_0 = 1$, where the DNA alignment is near-perfect) can be used to estimate the average dye orientation within both the static inclination model and the cone dynamics model. For the extremum values, the static inclination model corresponds best to an angle θ of $\sim$75° with respect to the DNA axis. Likewise, in the cone dynamics model a cone angle δ ranging between 0° and 35° can be found for an inclination angle θ ranging from 75° to 90°. However, as with other methods, there is no way to discriminate between these models based only on single polarization ratio values.

In order to quantitatively interpret the dependence of the polarization ratios on DNA extension, and exploit our controlled experiments of increasing slow-wobble depolarization at $L/L_0 < 1$, we performed Monte Carlo simulations of DNA conformations with fixed ends (see Figure 10.9 and section 10.4.1 for a description). Together with a generalization of Irving's model to allow for a local symmetry axis other than a global laboratory axis (see sections 10.4.2 and 10.4.3), these allowed us to calculate the expected dependencies for Irving's orientational dynamics models discussed above.

Figure 10.6 shows a zoom-in on regime [i] of the polarization ratios, along with four such model traces. The thick, light gray lines correspond to static inclination angles (i.e., no fast wobble; $\delta = 0°$) of 75° (dashed line) and 90° (solid line), both of which have been reported for YOYO and other intercalators [238, 250, 251]. Both these curves show a significant deviation from both our $P_{\|}$ and $Q_{\|}$ data. We infer that the additional depolarization induced by DNA dynamics is inconsistent with a model based on a static dipole inclination alone.

The thick, dark gray lines in Figure 10.6 correspond to actual least-squares fits of the data to a model including fast wobble in a cone with semi-angle δ (see section 10.4.3). The fits were performed globally, i.e., to all four traces simultaneously. The inclination angle θ is in both cases found to be 90°; the cone angle $\delta \approx 25°$. The difference between the dashed and solid lines is a third relevant angle: the azimuthal angle β between the two consecutive chromophores of a bis-intercalating YOYO dimer (see Figure 10.3). This angle can be used to account for the energy transfer between these chromophores [244], which depolarizes P and Q as well. In this case, an effective angle of 25° can be assumed between the absorbing and emitting dipole (see section 10.4.8). The solid line represents a curve fit where we have set $\beta = 25°$.

The significant improvement of the fit (both with and without accounting for energy transfer) indicates that there is no static inclination of the intercalated dipole moments (i.e., $\theta = 90°$) and that, even when slow wobble is suppressed by pulling the DNA taut, the dyes still undergo fast reorientations, which can be described as diffusion in a cone with a semi-angle of $\sim 25°$. Again, the decline of the polarization ratios for extensions below $L/L_0 = 1$ emphasizes the importance of proper sample alignment in linear dichroism measurements [241], as discussed below.

Although these conclusions hold for the internal motion of the intercalated dyes, it seems reasonable to assume that the base pairs of the DNA undergo similar dynamics themselves, permitting the dyes to wobble in their binding pockets. We will address this in more detail later.

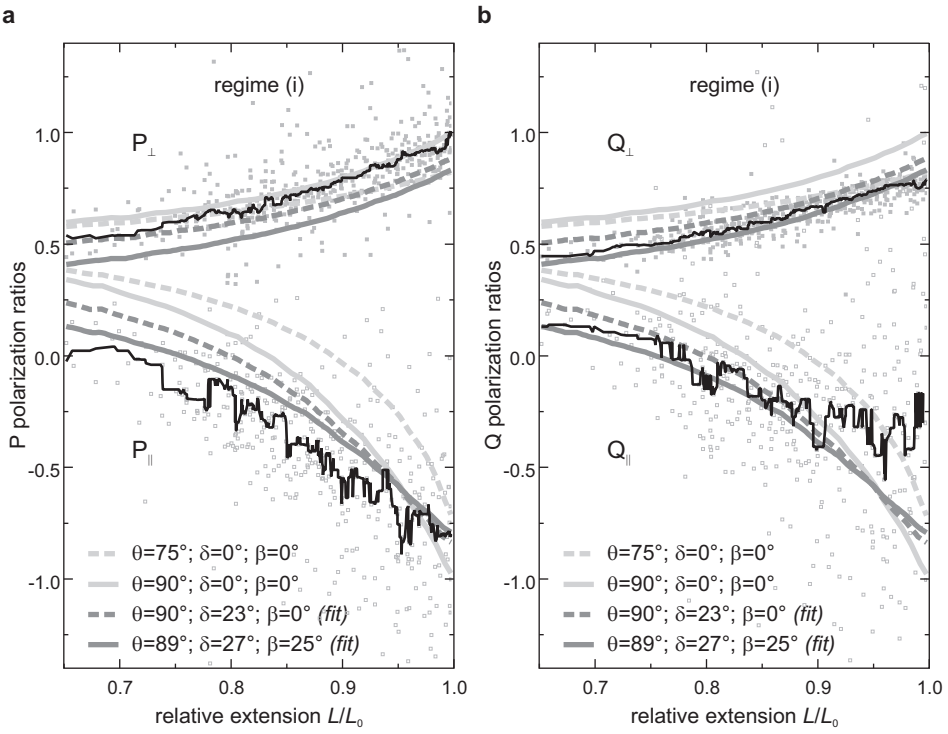

Figure 10.6 – Fits of the polarization ratios in regime [i] to Monte Carlo simulated model traces. [**a–b**] Simulated traces and least-squares fits to $P_{\parallel}$ and $P_{\perp}$ (panel a) and $Q_{\parallel}$ and $Q_{\perp}$ (panel b). The gray symbols and the black lines represent the raw data and the same data after a rank-10 median filter, respectively. The light gray lines are simulated traces of a static inclination model with $\theta = 75°$ (dashed line) and $\theta = 90°$ (solid line), both systematically deviating from the data. The dark gray lines are global fits to the data (i.e., simultaneously to P and Q data) and correspond to simulated curves including fast dye dynamics within a cone of angle δ. Fits are performed both with and without taking energy transfer between the two chromophores in account, as discussed in the text.

10.2.4 Regime [ii]: partially overstretched DNA

In regime [ii], the four polarization ratios stay approximately constant at the level attained at $L/L_0 = 1$. This range of extensions coincides with the overstretching (OS) transition, in which dsDNA is progressively melted to yield two essentially single-stranded DNA (ssDNA) molecules [207] (see also Chapter 9). What does our observation of constant polarization ratios during this force-induced melting imply? Firstly, it shows that in the OS transition, no significant base pair tilting occurs at or around

the intercalated base pairs. This had been suggested as one of the possible structures of (partially) overstretched DNA [7]. Note that the presence of intercalating moieties influences the cooperativity of the OS transition [217, 221]. The otherwise extensive processivity of the melting, as reported in Chapter 9, will presumably be limited to domains between two YOYO dyes. Nonetheless, the dyes do not appreciably start to exhibit more ('fast' or 'slow') orientational dynamics during overstretching, which would induce a steady depolarization. Surprisingly, despite the significant change in local structure and mechanics that accompanies the force-induced melting of DNA, no static reorientation of intercalated dyes, nor any alteration of their rotational dynamics is observed.

Another interesting observation is that YOYO is not forced to dissociate during the OS transition, as evidenced from the constant intensity in the ${}_{\perp}I_{\perp}$ channel (Figure 10.4b). Possibly, intercalated YOYO dimers locally reinforce the DNA, preventing the transition from progressing processively. Since YOYO binds with high specificity to dsDNA compared to ssDNA [220] (see Chapter 9), the stable binding of YOYO in the OS transition suggests that at least the local DNA structure around the dyes resembles that of dsDNA.

10.2.5 Regime [iii]: DNA beyond overstretching

Unlike in the OS transition itself, the dyes do show a significant depolarization beyond the force-induced melting (regime [iii] with $L/L_0 \gtrsim 1.55$, see Figure 10.5). This implies, not unexpectedly, that a considerable conformational change occurs. Surprisingly, only moderate dye dissociation occurs even in the regime where the force on the DNA ramps up steeply. For example, the molecule in Figure 10.7a, first pulled to 115 pN and then relaxed, displays a decrease in ${}_{\perp}I_{\perp}$ intensity of only 20% in the OS plateau before and after the pull. Figure 10.7a shows how in the molecule, which was contiguously labeled before the pull (top image), YOYO dissociates at high force only from a confined patch close to the right bead (middle image), whereas the fluorescence intensity along the rest of the molecule is retained (*cf*. bottom and top images). Unfortunately, most DNA molecules were photocleaved due to bleaching YOYO dyes [139, 258], before getting to this stage. However, the molecules that did survive the OS transition (3 out of 22) indeed show that no massive, homogeneous YOYO dissociation occurs. This is corroborated by the observation that the three intensity channels with a 'parallel' component gain intensity in the regime beyond the OS transition (e.g., ${}_{\parallel}I_{\parallel}$ in Figure 10.4b).

What could be the nature of the orientational change that causes the depolarization beyond the OS transition? Two possibilities exist, schematically depicted in

Figure 10.7b. Firstly, the dyes may undergo enhanced (fast or slow) dynamics within their binding pockets, rendering their orientation distribution virtually isotropic (Figure 10.7b: 'wobbling bases'). Such enhanced dynamics causes the polarization ratios to vanish, as observed. Secondly, the dyes may display an overall quasi-static conformational change. For example, the bases may tilt with respect to their initially orthogonal orientation as suggested before [7], due to shear forces propagating through the largely melted DNA as it is pulled from its two opposite 3' ends. Such 'static' tilt would similarly cause the observed depolarization (Figure 10.7b: 'tilting bases'). It is difficult to decisively conclude which of these two modes underlies the observed

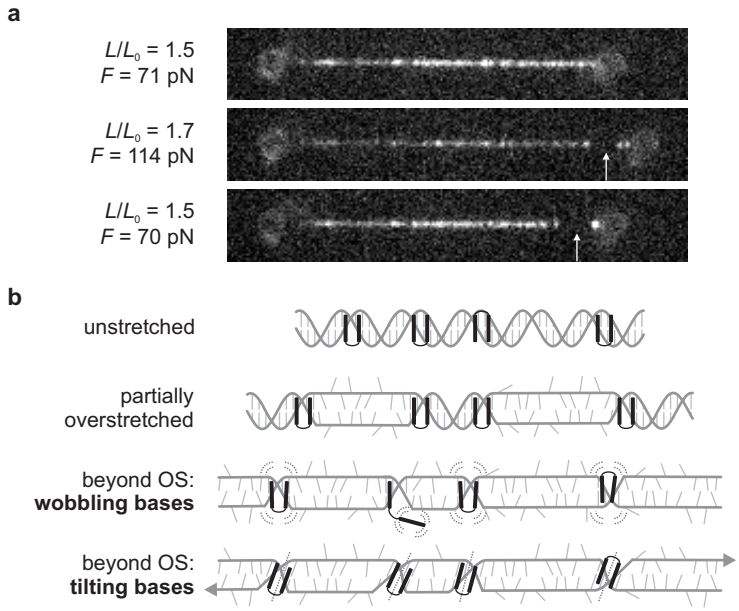

Figure 10.7 – YOYO stays bound beyond the overstretching transition. [**a**] Three snapshots of a molecule ($_{\perp}I_{\perp}$ channel) before, during and after the steep force-increase phase beyond the OS transition. The white arrow marks a short segment where YOYO disappears beyond the transition. However, the overall fluorescence intensity, which is reduced in the middle image, is regained in the bottom one, showing that YOYO is not forced to dissociate from the largely melted DNA apart from the marked segment. [**b**] Models explaining fluorescence depolarization beyond the OS transition. As was shown in Chapter 9, partially overstretched DNA still contains large base-paired segments. Presumably, only isolated domains surrounding intercalated dyes are still base paired beyond overstretching. This may either allow the dyes to perform larger-amplitude dynamics ('wobbling bases'), or induce a net shear force on the DNA, tilting the bases and the dyes.

depolarization. We would, however, expect a condition of enhanced dynamics to quench fluorescence emission, similar to what is observed for intercalating dyes free in solution, which has been attributed to efficient quenching due to internal motion of the chromophores [259, 260]. Since the fluorescence pathways seem not considerably quenched overall (*cf*. the brightening of the three parallel intensity channels), we argue that a static tilting model is more plausible.

A final interesting observation is that for intercalated DNA the end of the overstretching transition is less sharp, and that it occurs at lower extension than without intercalating dyes. For non-intercalated dsDNA, the OS transition ends at $L/L_0 = 1.7$, whereas the force for intercalated DNA starts to deviate from the overstretching plateau around $L/L_0 \approx 1.55$–1.6, depending on the labeling ratio (Figure 10.2). We argue that the melting transition is less cooperative for intercalated DNA and confined to domains between intercalators, leading to the observed more gradual switch to the enthalpic stretching phase beyond the transition, before the molecule is melted throughout.

10.2.6 Comparison to LD_r-based studies

As mentioned before, most previous studies on the orientation of intercalating dyes, both in photospectrometric [238, 239, 241, 246, 250] and in microscopy assays [153, 242, 251–253], rely on measurements of the (reduced) linear dichroism (LD_r). Our unprecedented control over the DNA alignment directly reveals the vulnerability of such approaches for imperfect alignment. Nonetheless, according to Eq. 10.3, precise knowledge of the orientation factor S is a prerequisite for a quantitative interpretation of LD_r values. To underscore this importance, we show in Figure 10.8 the dependence of LD_r on the extension of our DNA molecules. Again, data for 22 molecules is merged. The (fluorescence-detected) LD_r values were calculated from the four intensity channels according to

$$\mathrm{LD_r} = \frac{{}_{\parallel}I_{\mathrm{em}} - {}_{\perp}I_{\mathrm{em}}}{{}_{\mathrm{iso}}I_{\mathrm{em}}} = \frac{{}_{\parallel}I_{\mathrm{em}} - {}_{\perp}I_{\mathrm{em}}}{\frac{1}{3}\left({}_{\parallel}I_{\mathrm{em}} + 2\,{}_{\perp}I_{\mathrm{em}}\right)}, \tag{10.6}$$

adding the emissions 'em' in the parallel and the perpendicular channels (*cf*. Eq. 10.2). The (static) inclination angle θ, calculated from LD_r according to Eq. 10.3 assuming $S = 1$, is plotted in the bottom graph. Obviously, the value of LD_r or θ strongly depends on the extension of the DNA, as addressed before: Figure 10.8 shows how an underestimated value is obtained at extensions $L/L_0 < 1$. This may well be the cause of the reported orientation angles deviating significantly from 90° [153, 238, 250–253].

Moreover, steady-state linear-dichroism measurements do not allow for distinguishing between static dye inclination and depolarization due to fast wobble, like we do in Figure 10.6. The light gray, thick lines in Figure 10.8 correspond to Monte Carlo simulations using a static tilted inclination of $\theta = 75°$ (gray dotted line), and a fast-wobble cone of $\delta = 25°$ around an essentially perpendicular inclination angle $\theta = 89°$ (gray solid line) as we obtained from our fits. The largely overlapping curves show that these qualitatively different models yield indistinguishable LD_r results. In contrast, our approach of polarized excitation in combination with polarization-selective fluorescence detection on micromanipulated, individual DNA molecules is indeed able to tell these models apart (see Figure 10.6), without the need for time-resolved fluorescence measurements [171, 245].

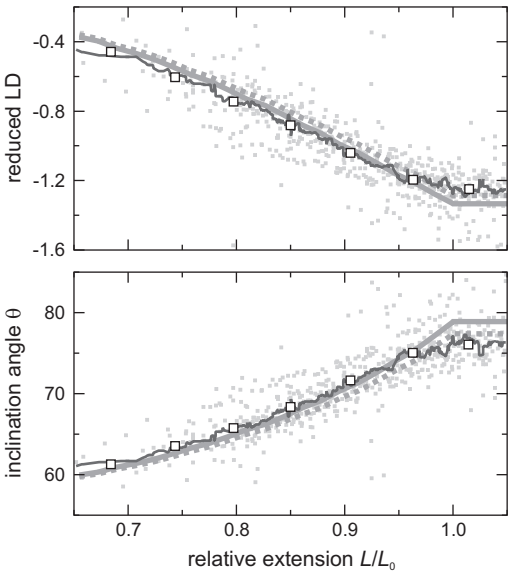

Figure 10.8 – Measured reduced LD and estimation of inclination angle depend strongly on sample alignment. The top graph shows the reduced linear dichroism, calculated from our data using Eq. 10.2 as a function of extension. Clearly, the value for LD_r depends strongly on how far one stretches the DNA out. The bottom graph shows the inclination angle calculated from LD_r according to Eq. 10.3 assuming $S = 1$. The light gray simulated traces show that steady-state LD_r measurements are not capable of discriminating between fast-wobble and tilted-inclination depolarization: a static inclination of $\theta = 75°$ almost entirely coincides with the fast-wobble model with the parameters obtained from our fits ($\theta = 89°, \delta = \beta = 25°$).

The observed fast dye reorientation dynamics may also be the cause of reported tilted inclination angles of the DNA base pairs themselves within the helix, as discussed in section 10.1. Our present study may help and identify the source of this discrepancy.

10.3 Conclusions

In summary, we have demonstrated the application of single-molecule manipulation techniques to polarized fluorescence microscopy of individual DNA molecules. By extending DNA molecules in a controlled manner, we increasingly suppress Brownian dynamics, pulling the DNA taut. In combination with Monte Carlo simulations, this allowed us to dissect the sources of fluorescence depolarization due to the dynamics of the DNA itself, and the rapid reorientation of the dyes within their binding pockets. We can now exclude such depolarization, reported before both from bulk spectroscopic and microscopic studies, to be due to a tilted intercalation mode: the transition moments of the YOYO chromophores are on average oriented perpendicular to the DNA helix.

The observed behavior in the overstretching transition reveals that no dye dissociates or even reorients measurably. This is unexpected, since the dsDNA into which it is intercalated is gradually converted to ssDNA, which cannot be intercalated. Only beyond the overstretching transition, where the DNA is held together only by isolated base pairs (see Chapter 9), a considerable depolarization is observed, presumably caused by an average tilting of the DNA base pairs. These unique observations on DNA dynamics could only be made thanks to our combined polarized fluorescence and DNA manipulation assay.

10.4 Experimental methods

10.4.1 Monte Carlo simulations of DNA with fixed ends

To interpret the shape of fluorescence intensity traces at DNA extensions up to the overstretching regime (i.e., $L/L_0 < 1$) we set out to simulate DNA conformations undergoing Brownian dynamics, while keeping the end points fixed: $L/L_0 = \text{constant}$. We employed the Metropolis scheme for Monte Carlo (MC) simulations [261, 262]. Using this algorithm, average values for observables of a system can be calculated by randomly sampling the phase space of those quantities. The efficiency of the algorithm relies on a smart selection for generating a next state to be sampled. Typically, a new state is generated by making a random change to the current state, a Monte Carlo 'move'. For this new state, the energy difference ΔE with the previous one is

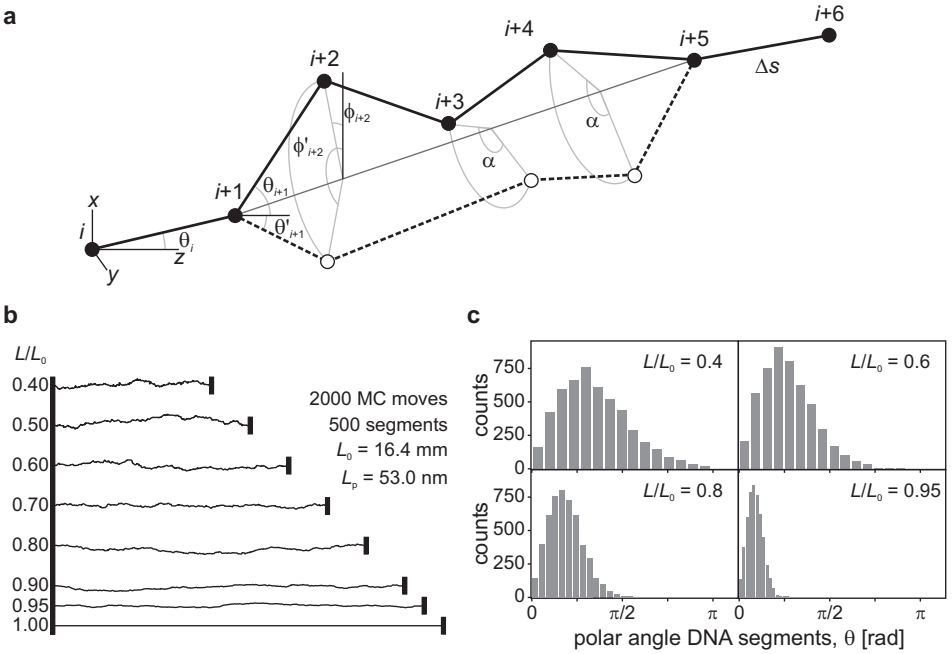

Figure 10.9 – Monte Carlo simulations of extended DNA with fixed end points. [**a**] Parametrization of a DNA molecule in segments with polar angles (θ_i, ϕ_i). The end points of the DNA lie along the z–axis. The Monte Carlo 'moves' are made by randomly selecting two nodes along the molecule, and rotating all segments in between these nodes around the line connecting them with a randomly selected angle α. [**b**] Simulated molecules for the fractional extensions L/L_0 indicated on the left. [**c**] Distributions of axial angles θ for four values of L/L_0, indicating the straightening out of the DNA. Azimuthal angles ϕ are uniformly distributed in all cases.

calculated. Any new state with $\Delta E < 0$, i.e., with lower energy than the previous state, is 'accepted'. If $\Delta E > 0$, the new state is accepted with a probability equal to the Boltzmann factor: $\exp\left(-\Delta E/k_{\mathrm{B}}T\right)$, where $k_{\mathrm{B}}T$ is the thermal energy [262]. For accepted states, the relevant parameters are calculated to obtain an expectation value.

We simulated DNA molecules with a contour length L_0 as chains of N rigid segments of length $\Delta s = L_0/N$, with axial angle θ_i with respect to the laboratory z–axis and an azimuthal axis ϕ_i around it (see Figure 10.9a). For a given contour length L_0, a starting configuration with end-to-end length L was generated by setting $\phi_i = 0$, and $\theta_i = \arccos\left(L/L_0\right)$ for $0 < i < N/2-1$ and $\theta_i = -\arccos\left(L/L_0\right)$ for $N/2 < i < N-1$, i.e., a triangle. Alternatively, the starting configuration could be set to alternating pos-

itive and negative angles $|\theta_i| = \arccos\left(L/L_0\right)$, i.e., a zig-zag pattern. The Monte Carlo moves were performed as follows. Two nodes along the molecule's contour were randomly selected (e.g., $i+1$ and $i+5$ in Figure 10.9a). All segments in between these nodes where then rotated around the line connecting the nodes by a random angle $\alpha \in [0, 2\pi]$ (see Figure 10.9a). The energy of both states was calculated from the bending energy:

$$E \;=\; \frac{L_\mathrm{p} k_\mathrm{B} T}{2} \int_0^L \left(\frac{\mathrm{d}\xi}{\mathrm{d}s}\right)^2 \mathrm{d}s \;=\; \frac{L_\mathrm{p} k_\mathrm{B} T}{2\Delta s} \sum_{i=0}^{N-1} \Delta\xi_i^2, \tag{10.7}$$

where L_p is the persistence length of the DNA, Δs the length of a segment and $\Delta\xi_i$ the angle between segments i and $i+1$, obtained using the inner product. In practice, only the energy change at the (randomly) selected nodes was calculated to reduce computational costs.

This choice of MC moves—albeit highly unphysical—ensures an efficient sampling of phase space because of its delocalized nature, while keeping the end-to-end distance unchanged. Typically, the number of MC moves required to avoid 'memory' of the artificial starting configuration was ∼3–5N. This equilibration was seen as the total energy of the molecule leveling off to reach a steady state. This was found to be independent of which starting configuration was used: the low-energy triangle state with a single bend or the high-energy zig-zag state.

Figure 10.9b shows molecules at the indicated end-to-end distances L/L_0, simulated using the parameters indicated on the right. Using the simulations, distributions of polar coordinates θ and ϕ were obtained as a function of L/L_0. For all values of L/L_0, distributions of azimuthal angles ϕ are uniform between 0 and 2π. Figure 10.9c shows the distributions of axial angles θ for four values of L/L_0, and how the distributions narrow when the molecules are stretched. The vanishing of θ near 0 is due to the fact that the density of polar coordinate states vanishes at $\theta = 0$: $\mathrm{d}\Omega = \sin\theta \; \mathrm{d}\theta \; \mathrm{d}\phi$.

The simulations were used to calculate expectation values for the polarized fluorescence intensities in the DNA stretching experiments, as discussed in the next sections.

10.4.2 Dye mobility induced by DNA dynamics: 'slow wobble'

Irving[1] developed a framework to calculate the observable quantities, ${}_{\parallel}I_{\parallel}$, ${}_{\perp}I_{\parallel}$, ${}_{\parallel}I_{\perp}$ and ${}_{\perp}I_{\perp}$, in terms of the polar orientation angles of a fluorescent dye with its absorption and emission dipoles cylindrically distributed around the z–axis. To this end, he

[1]This section is based on and expands the work of dr. Malcolm Irving [254]. Here, we repeat those equations from his work that are required for a proper understanding of our approach.

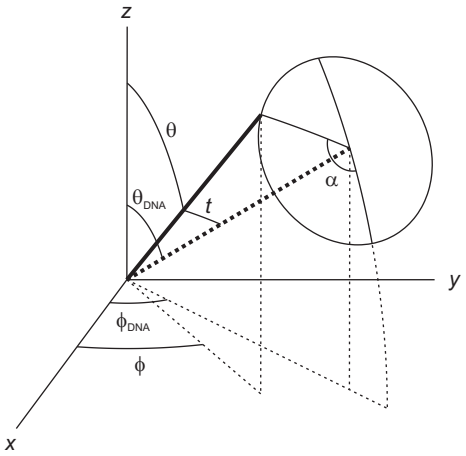

Figure 10.10 – Angular coordinates for a dye with static inclination with respect to a symmetry axis. The (absorption or emission) dipole moment of a dye (thick solid line) makes axial and azimuthal angles t and α with its symmetry axis with polar coordinates $(\theta_{\mathrm{DNA}}, \phi_{\mathrm{DNA}})$ (thick dashed line). The dipole's coordinates (θ, ϕ) can be expressed in terms of the parametric coordinates (t, α) and the symmetry axis coordinates using the spherical law of cosines (eq. 10.9).

calculated the probabilities $\left(p_{\parallel}, p_{\perp}\right)_{\mathrm{a,e}}$ of absorbing and emitting light with its polarization parallel or perpendicular to the z–axis. These probabilities being equal to the squared projection of the dipole vector onto the respective axes, this yields [254]:

$$\text{fixed dye} \quad \begin{cases} {}_{\parallel}I_{\parallel} = k \cos^2\theta_{\mathrm{a}}\ \cos^2\theta_{\mathrm{e}}, \\ {}_{\parallel}I_{\perp} = k \cos^2\theta_{\mathrm{a}}\ \sin^2\theta_{\mathrm{e}}\ \cos^2\phi_{\mathrm{e}}, \\ {}_{\perp}I_{\parallel} = k \sin^2\theta_{\mathrm{a}}\ \cos^2\theta_{\mathrm{e}}\ \cos^2\phi_{\mathrm{a}}, \\ {}_{\perp}I_{\perp} = k \sin^2\theta_{\mathrm{a}}\ \sin^2\theta_{\mathrm{e}}\ \cos^2\phi_{\mathrm{a}}\ \cos^2\phi_{\mathrm{e}}, \end{cases} \tag{10.8}$$

with θ_{a} and θ_{e} the polar angles of respectively the absorption and emission dipole moments with respect to the z–axis, ϕ_{a} and ϕ_{e} the corresponding azimuthal angles and k a normalization constant. In practice, absorption and emission dipoles intercalating dyes chromophores [238].

To interpret the measured polarized fluorescence intensities at DNA extensions below the overstretching regime ($L/L_0 < 1$) and account for 'slow wobble' dynamics, we set out to calculate expectation values for ${}_{\mathrm{ex}}I_{\mathrm{em}}$ from the simulated molecules described in section 10.4.1, for a dye with cylindrical symmetry not around one of the laboratory axes, but around the axis of a simulated DNA segment with polar angles $(\theta_{\mathrm{DNA}}, \phi_{\mathrm{DNA}})$. The dipole axis makes an angle t with this DNA segment; its

azimuthal angle α is measured with respect to the plane defined by the z–axis and that of the DNA. Figure 10.10 gives a graphical definition of these parameters. We rewrite equations 10.8 in terms of these new parameters, making use of the spherical law of cosines and a derivative of it [254]:

$$\begin{aligned} \cos\theta &= \cos t\ \cos\theta_{\mathrm{DNA}} - \sin t\ \sin\theta_{\mathrm{DNA}}\ \cos\alpha, \\ \sin\theta\ \cos\phi &= \cos t\ \sin\theta_{\mathrm{DNA}}\ \cos\phi_{\mathrm{DNA}} \\ &\quad + \sin t\ \cos\alpha\ \cos\theta_{\mathrm{DNA}}\ \cos\phi_{\mathrm{DNA}} \\ &\quad - \sin t\ \sin\alpha\ \sin\phi_{\mathrm{DNA}}. \end{aligned} \tag{10.9}$$

Substituting equations 10.9 into equations 10.8 and integrating over α around the symmetry axis, we find for ${}_{\parallel}I_{\parallel}$ (assuming parallel absorption and emission dipoles):

$$\begin{aligned} {}_{\parallel}I_{\parallel} &= 4\,(44\cos 2t + 5\,(\cos 4t + 3))\cos 2\theta_{\mathrm{DNA}} \\ &\quad + (20\cos 2t + 35\cos 4t + 9)\cos 4\theta_{\mathrm{DNA}} \\ &\quad + 60\cos 2t + 9\cos 4t + 123. \end{aligned} \tag{10.10}$$

Similar (but significantly more complex) equations are obtained for ${}_{\perp}I_{\parallel}$, ${}_{\parallel}I_{\perp}$ and ${}_{\perp}I_{\perp}$. Using these equations, the observable quantities ${}_{\mathrm{ex}}I_{\mathrm{em}}$ and the P and Q polarization ratios can be analytically calculated for Monte Carlo simulated DNA molecules at any fractional extension. By averaging these quantities over large numbers of simulated DNA conformations, we calculate the effect of slow-wobble dynamics.

10.4.3 Dye mobility on the fluorescence time scale: 'fast wobble'

Irving expanded his calculations to account for rapid motion of the dye on the time scale of fluorescence absorption and emission, 'fast wobble' [254]. Assuming the dye to diffuse freely in a cone of semi-angle δ, the general polarized intensity ${}_{\mathrm{ex}}I_{\mathrm{em}}$ is given by:

$${}_{\mathrm{ex}}I_{\mathrm{em}} = \frac{\iint p_{\mathrm{am}}(\theta_{\mathrm{a}},\phi_{\mathrm{a}})\,\mathrm{d}\Omega \iint p_{\mathrm{en}}(\theta_{\mathrm{e}},\phi_{\mathrm{e}})\,\mathrm{d}\Omega}{\left(\iint \mathrm{d}\Omega\right)^2}, \tag{10.11}$$

where the integrals are taken over the solid angle of the cone:

$$\iint \mathrm{d}\Omega = \int_{\gamma=0}^{2\pi}\int_{\beta=0}^{\delta} \sin t\ \mathrm{d}\beta\ \mathrm{d}\gamma = 2\pi\,(1-\cos\delta), \tag{10.12}$$

with γ and β the parametric coordinates of a dipole vector in the cone (see Figure 10.11a). Using equations 10.9, the integrals of the absorption probabilities p_{am}

and p_{an} in equation 10.11 can be explicitly calculated, yielding [254]:

$$\iint p_{\mathrm{a}_\parallel}(\theta_{\mathrm{a}},\phi_{\mathrm{a}})\,\mathrm{d}\Omega = 2\pi(1-\cos\delta)(k/2) \times\left[\omega+(2-3\omega)\cos^2\theta_{\mathrm{cone,a}}\right], \tag{10.13}$$

$$\iint p_{\mathrm{a}_\perp}(\theta_{\mathrm{a}},\phi_{\mathrm{a}})\,\mathrm{d}\Omega = 2\pi(1-\cos\delta)(k/2) \times\left[\omega+(2-3\omega)\sin^2\theta_{\mathrm{cone,a}}\cos^2\phi_{\mathrm{cone,a}}\right], \tag{10.14}$$

$$\text{with } \omega = 1-(1+\cos\delta+\cos^2\delta)/3. \tag{10.15}$$

The emission probabilities are obtained simply by substituting suffixes 'a' by 'e'. In Irving's derivation, the result of the above integrations was integrated over the azimuthal angle ϕ to account for the rotational symmetry around the z–axis. In our case of rotational symmetry around a DNA segment with coordinates $(\theta_{\mathrm{DNA}},\phi_{\mathrm{DNA}})$, we need to integrate around this segment's axis. We therefore parametrize our coordinates again in terms of this axis with the quantities introduced in Figure 10.10b using the

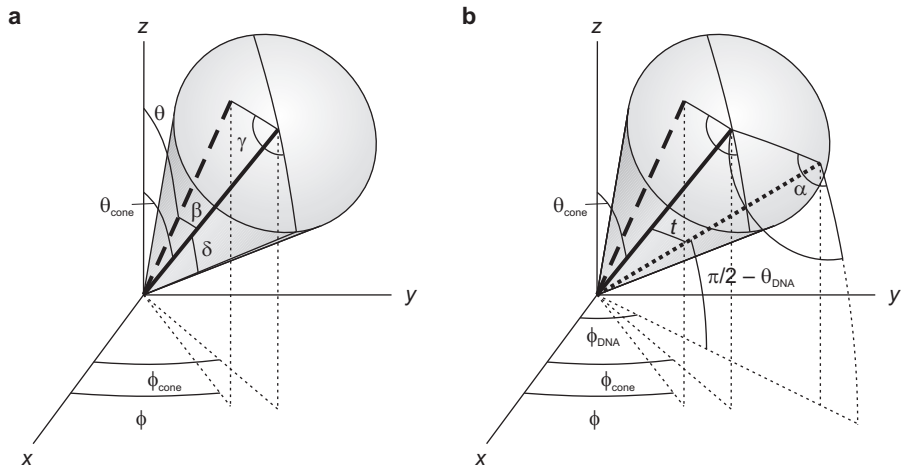

Figure 10.11 – Angular coordinates for a dye undergoing rapid motion in a cone. [**a**] The cone axis (thick solid line) is defined by polar angles $(\theta_{\mathrm{cone}},\phi_{\mathrm{cone}})$. A dipole vector in the cone (thick dashed line), defined by polar angles (θ,ϕ) is parametrized by azimuthal angle γ and axial angle β (running from 0 to δ, the semi-angle of the cone). [**b**] Like in Figure 10.10, the cone axis coordinates can be expressed in terms of the angular distance to a DNA segment axis with coordinates $(\theta_{\mathrm{DNA}},\phi_{\mathrm{DNA}})$ (thick dotted line).

spherical cosine law once more (Eq. 10.9). The resulting polarized intensities read:

$$
\begin{aligned}
{}_{\parallel}I_{\parallel} &= k\int_0^{2\pi} \mathrm{d}\alpha \left[\omega + (2-3\omega)\left[\cos t\cos\theta_{\mathrm{DNA}} - \cos\alpha\sin t\sin\theta_{\mathrm{DNA}}\right]^2\right] \\
&\quad \times \left[\omega + (2-3\omega)\left[\cos t\cos\theta_{\mathrm{DNA}} - \cos(\alpha-\beta)\sin t\sin\theta_{\mathrm{DNA}}\right]^2\right], \qquad (10.16)\\
{}_{\parallel}I_{\perp} &= k\int_0^{2\pi} \mathrm{d}\alpha \left[\omega + (2-3\omega)\left[\cos t\cos\theta_{\mathrm{DNA}} - \cos\alpha\sin t\sin\theta_{\mathrm{DNA}}\right]^2\right] \\
&\quad \times \left[\omega + (2-3\omega)\left[\cos\phi_{\mathrm{DNA}}\left(\cos(\alpha-\beta)\cos\theta_{\mathrm{DNA}}\sin t\right.\right.\right. \\
&\quad \left.\left.\left. + \cos t\sin\theta_{\mathrm{DNA}}\right) - \sin t\sin(\alpha-\beta)\sin\phi_{\mathrm{DNA}}\right]^2\right], \qquad (10.17)\\
{}_{\perp}I_{\parallel} &= k\int_0^{2\pi} \mathrm{d}\alpha \left[\omega + (2-3\omega)\left[\cos t\cos\theta_{\mathrm{DNA}} - \cos(\alpha-\beta)\sin t\sin\theta_{\mathrm{DNA}}\right]^2\right] \\
&\quad \times \left[\omega + (2-3\omega)\left[\cos\phi_{\mathrm{DNA}}\left(\cos\alpha\cos\theta_{\mathrm{DNA}}\sin t + \cos t\sin\theta_{\mathrm{DNA}}\right)\right.\right. \\
&\quad \left.\left. - \sin t\sin\alpha\sin\phi_{\mathrm{DNA}}\right]^2\right], \qquad (10.18)\\
{}_{\perp}I_{\perp} &= k\int_0^{2\pi} \mathrm{d}\alpha \left[\omega + (2-3\omega)\left[\cos\phi_{\mathrm{DNA}}\left(\cos\alpha\cos\theta_{\mathrm{DNA}}\sin t + \cos t\sin\theta_{\mathrm{DNA}}\right)\right.\right. \\
&\quad \left.\left. - \sin t\sin\alpha\sin\phi_{\mathrm{DNA}}\right]^2\right] \times \left[\omega + (2-3\omega)\left[\cos\phi_{\mathrm{DNA}}\right.\right. \\
&\quad \times \left(\cos(\alpha-\beta)\cos\theta_{\mathrm{DNA}}\sin t + \cos t\sin\theta_{\mathrm{DNA}}\right) \\
&\quad \left.\left. - \sin t\sin(\alpha-\beta)\sin\phi_{\mathrm{DNA}}\right]^2\right]. \qquad (10.19)
\end{aligned}
$$

Here we have assumed that $\theta_{\mathrm{a}} = \theta_{\mathrm{e}}$. We have written $\beta = \phi_{\mathrm{a}} - \phi_{\mathrm{e}}$ for the azimuthal angle difference between absorption and emission dipoles. This parameter can be used to account for energy transfer between the two dye moieties of a bis-intercalating dye. In that case, the azimuthal angle difference between the dyes, depending on their axial distance and the helical pitch of DNA [244], will set the angle difference between the absorbing and emitting dipole, as will be discussed in section 10.4.8.

The integrals over α can in principle be calculated analytically. However, the mathematical complexity is such that numerical evaluation is more efficient. Doing so, we can simultaneously take into account the depolarizing effects of slow-wobble and fast-wobble dynamics.

10.4.4 Optical trapping and polarized fluorescence microscopy

The optical-trapping instrument was adapted from that described in Chapters 8 and 9, and is depicted in Figure 10.12a. For polarized fluorescence excitation, a linearly polarized 473-nm laser (Cobolt Blues™, 25 mW cw, Cobolt AB, Stockholm, Sweden) was led through an electro-optic modulator (EOM, model 350-80, Conoptics, Danbury, CT). The polarization state of the excitation laser was modulated by applying

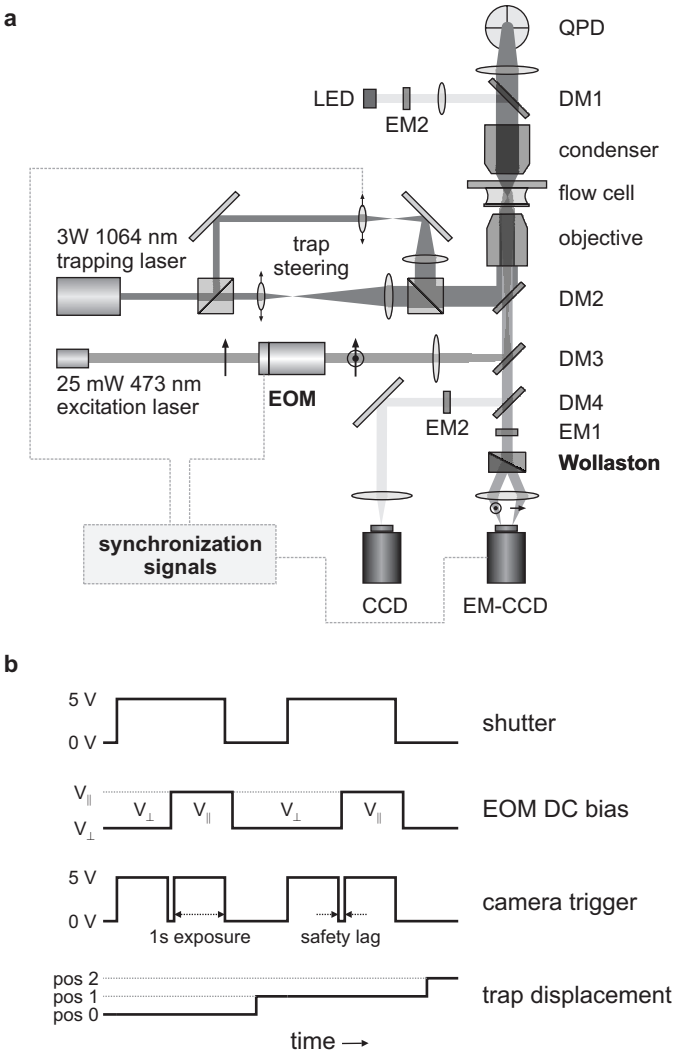

Figure 10.12 – Experimental setup. [**a**] Schematic of the combined dual trap and polarized fluorescence microscope. Abbreviations: EOM – electro-optic modulator; DM – dichroic mirror; EM – emission filter; QPD – quadrant photodiode; LED – light emitting diode; (EM-)CCD – (electron-multiplied) charge coupled device. See section 10.4.4 for details. [**b**] Synchronization signals (dashed lines in panel a) used for coordinated camera exposure, adjustment of excitation polarization, and trap displacement. The excitation polarization is alternated using a 2-step block signal supplied to the DC bias input of an electro-optic modulator. The polarization change occurs during the safety lag in between two camera exposures to avoid fluorescence recording with mixed polarizations. See section 10.4.5 for details.

different sequential DC voltages to the EOM synchronized with camera readout (see section 10.4.5). A Berek variable wave plate (model 5540, New Focus) was used for fine-tuning of the polarization state after the EOM. The polarized light was decollimated for widefield excitation, and coupled into the microscope objective using a dichroic mirror ('DM3': z473rdc, Chroma).

Fluorescence emission was band-pass filtered ('EM1': hq540/80m-2p, Chroma) and imaged onto a sensitive electron-multiplying CCD camera ('EM-CCD': Cascade 512B, Princeton Instruments, Monmouth Junction, NJ). In front of the camera, a Wollaston prism (WSP9015, FOCtek Photonics, Fujian, China) was placed to spatially decompose the fluorescent light upon polarization onto different segments of the CCD sensor.

The custom-built flow cell featuring multiple parallel, laminar channels with different buffers that can be swiftly exchanged has been described in Chapter 4 [90].

10.4.5 Procedures for polarized fluorescence measurements

To measure the four polarized intensities ${}_{\mathrm{ex}}I_{\mathrm{em}}$, like indicated in Figure 10.4a, the excitation polarization was alternated using the EOM, while the emission signal was split into two perpendicular emission polarizations using the Wollaston prism, imaged simultaneously onto the camera. (see Figure 10.12a). Camera readout, excitation shutter and polarization, and trap movement were synchronized using computer-generated signals (PCI-6229 multifunction DAQ-board, National Instruments) as follows (see Figure 10.12b). The 473-nm laser shutter was opened with a TTL signal. Concurrently, the camera was triggered for 1-sec exposure of one frame by the rising flank of a TTL pulse. Next, the excitation polarization was rotated by 90° by changing the bias voltage ($V_{\perp} \rightarrow V_{\parallel}$) on the EOM and exposure of a second frame was started by another TTL pulse to the camera. After the second frame, the shutter was closed and the polarization state was changed back. In the interval to the next exposure cycle the DNA molecule was stretched or released by stepwise displacement of one of the traps using a linear actuator (T–LA28, Zaber Technologies Inc., Richmond, BC, Canada). The emission splitting using the Wollaston prism allowed for simultaneous imaging of the two polarizations onto separate segments of the CCD sensor.

The camera synchronization signal was recorded in conjunction with the force on the DNA and the bead-bead distance. Hence, all fluorescence images could be linked to the corresponding DNA tension and extension. Fluorescence intensities were obtained from the images as follows. In every frame, the total fluorescence intensity in both polarizations was extracted by integrating the light intensity in a rectangle, with a fixed width of typically 8 pixels (corresponding to $\sim$1.4 μm) perpendicular to

the DNA long axis and a length scaling with the corresponding DNA extension, to enclose the entire DNA molecule. For background correction, the average intensity in a dark region shifted several pixels with respect to the DNA was subtracted from each pixel. As a consistency check, we repeated the above procedure for segments of the imaged DNA molecules (by changing the length of the rectangular box), which yielded the same (normalized) intensities.

10.4.6 Sample preparation of DNA and dyes

Biotinylation of λ-DNA was performed as described in Chapter 4 and elsewhere [33]. Unlabeled DNA molecules were captured between a set of trapped beads and stretched to measure the contour length. Next, the bead-DNA-bead complex was moved to a 10-mM Tris buffer containing 100–200 nM YOYO (trade name YOYO-1®, Molecular Probes) and 5–10 mM NaCl for intercalation. We have found this relatively low salt concentration to enhance the binding stability of YOYO. The final labeling ratio was set both by the time duration the molecule was exposed to YOYO, and by the DNA tension at which the labeling took place [217]. For each molecule, this ratio was determined by comparing its contour length after intercalation with that before it, assuming every dye moiety to add 0.34 nm to the DNA contour length [237]. The labeling ratio in our experiments was typically 1 YOYO dimer per 40 bp. The actual experiments were performed in a YOYO-free Tris buffer containing 5 mM NaCl. All buffers were degassed and kept under nitrogen atmosphere to reduce photobleaching.

10.4.7 Transmission and high-NA corrections

The transmission of the microscope optics for the two orthogonal polarizations need not be equal *a priori*. Particularly dichroic mirrors, placed under 45°, display unequal polarized transmissions [263]. Therefore, we measured the transmission of the excitation laser after the microscope objective using a power meter—found as a ratio of 1.12—and corrected for the consequent difference in excitation power. Likewise, we determined the transmission ratio M of the two fluorescence polarizations from the sample to the camera. We hereto measured the anisotropy of a homogeneous sample of YOYO-labeled DNA molecules with two orthogonal excitation polarizations:

$$r_1 = \frac{{}_{\parallel}I_{\parallel} - M_{\parallel}I_{\perp}}{{}_{\parallel}I_{\parallel} + 2M_{\parallel}I_{\perp}}, \tag{10.20}$$

$$r_2 = \frac{M_{\perp}I_{\perp} - {}_{\perp}I_{\parallel}}{M_{\perp}I_{\perp} + 2{}_{\perp}I_{\parallel}}. \tag{10.21}$$

Since the anisotropy is a property of the sample, independent of the microscope optics, r_1 and r_2 should be equal, and can thus be used to find the ratio M—0.68.

A last correction was required to compensate for the high numerical aperture (NA) of the water-immersion objective of NA = 1.2. This high NA results in partial depolarization of high-angle (i.e., off-axis) emitted fluorescence, causing mixing between the observed intensities ${}_{\mathrm{ex}}I_{\mathrm{em}}$. Axelrod derived expressions for this correction [264,265]. An emitting dipole in the sample which would have intensity components ($I_x = I_\perp, I_y = I_\parallel, I_z = I_\perp$) (see Figure 10.3) when observed at low NA, will be observed as:

$$\left(I_\perp\right)_{\mathrm{observed}} = c_1 I_x + c_3 I_y + c_2 I_z, \tag{10.22}$$

$$\left(I_\parallel\right)_{\mathrm{observed}} = c_1 I_x + c_2 I_y + c_3 I_z. \tag{10.23}$$

Axelrod analytically derived the coefficients c_1, c_2 and c_3 to be [264,265]:

$$c_1 = \frac{2 - 3\cos\sigma + \cos^3\sigma}{6(1-\cos\sigma)}, \tag{10.24}$$

$$c_2 = \frac{1 - 3\cos\sigma + 3\cos^2\sigma - \cos^3\sigma}{24(1-\cos\sigma)}, \tag{10.25}$$

$$c_3 = \frac{5 - 3\cos\sigma - \cos^2\sigma - \cos^3\sigma}{8(1-\cos\sigma)}. \tag{10.26}$$

Here, σ is the maximum viewing angle of the objective: $\sigma = \arcsin(\mathrm{NA}/n)$, with n being the refractive index of the immersion medium. For our water-immersion objective ($n = 1.33$) of NA = 1.2, these coefficients take on the values 0.23, 0.013, and 0.76, respectively. The polarized intensities ${}_{\mathrm{ex}}I_{\mathrm{em}}$ were corrected for this mixing.

10.4.8 Data fitting and analysis

The dependence of the P and Q polarization ratios on relative DNA extension, shown in Figure 10.5, was fitted to the different models described above as follows. For a range of angles, P/Q vs L/L_0 values were tabulated. The fit function, used for Levenberg-Marquardt least-squares fitting, calculated function values by linearly interpolating these tabulated values. The angle β was used to account for energy transfer between the two YOYO chromophores [244]. This angle was determined to be 51° [244], based on one bis-intercalating dye dimer sandwiching two base pairs, and every chromophore unwinding the DNA helix by ∼20° [237, 239, 244, 266]. In the case of energy transfer between the chromophores, the emitted photon is equally likely emitted by either of the two [244]. Therefore, such energy transfer can be emulated in the simulations by setting $\beta = 51°/2 = 25°$ as the effective azimuthal angle

between the absorbing and emitting dipole. In fact, the two chromophores of a YOYO dimer are indeed close enough such as to allow efficient transfer.

In the least-squares fits, β was kept fixed at either 0° or 25°, whereas the inclination angle θ and the cone angle δ were fit parameters. Fits were performed 'globally', i.e., on all four polarization ratios $P_{\parallel}$, $P_{\perp}$, $Q_{\parallel}$, and $Q_{\perp}$ simultaneously.

10.5 Acknowledgments

We thank Pleuni Hooijman for assistance with the experiments. This work is part of the research program of the 'Stichting voor Fundamenteel Onderzoek der Materie (FOM)', which is financially supported by the 'Nederlandse Organisatie voor Wetenschappelijk Onderzoek (NWO)'.

References

[1] P. C. Nelson, M. Radosavljevic, and S. Bromberg. *Biological physics: energy, information, life*. W.H. Freeman and Co., New York, 2004.

[2] J. D. Watson and F. H. C. Crick. Molecular Structure of Nucleic Acids - a Structure for Deoxyribose Nucleic Acid. *Nature*, 171(4356):737–738, 1953.

[3] S. B. Smith, L. Finzi, and C. Bustamante. Direct mechanical measurements of the elasticity of single DNA molecules by using magnetic beads. *Science*, 258(5085):1122–1126, 1992.

[4] C. Bustamante, J. F. Marko, E. D. Siggia, and S. Smith. Entropic elasticity of lambda-phage DNA. *Science*, 265(5178):1599–1600, 1994.

[5] J. F. Marko and E. D. Siggia. Stretching DNA. *Macromolecules*, 28(26):8759–8770, 1995.

[6] M. D. Wang, H. Yin, R. Landick, J. Gelles, and S. M. Block. Stretching DNA with optical tweezers. *Biophysical Journal*, 72(3):1335–1346, 1997.

[7] S. B. Smith, Y. Cui, and C. Bustamante. Overstretching B-DNA: the elastic response of individual double-stranded and single-stranded DNA molecules. *Science*, 271(5250):795–799, 1996.

[8] P. Cluzel, A. Lebrun, C. Heller, R. Lavery, J. L. Viovy, D. Chatenay, and F. Caron. DNA: An extensible molecule. *Science*, 271(5250):792–794, 1996.

[9] A. N. Kapanidis and S. Weiss. Fluorescent probes and bioconjugation chemistries for single-molecule fluorescence analysis of biomolecules. *Journal of Chemical Physics*, 117(24):10953–10964, 2002.

[10] G. Binnig, C. F. Quate, and C. Gerber. Atomic force microscope. *Physical Review Letters*, 56(9):930–933, 1986.

[11] P. J. de Pablo, I. A. T. Schaap, F. C. MacKintosh, and C. F. Schmidt. Deformation and Collapse of Microtubules on the Nanometer Scale. *Physical Review Letters*, 91(9):098101, 2003.

[12] I. L. Ivanovska, P. J. de Pablo, B. Ibarra, G. Sgalari, F. C. MacKintosh, J. L. Carrascosa, C. F. Schmidt, and G. J. L. Wuite. Bacteriophage capsids: Tough nanoshells with complex elastic properties. *Proceedings of the National Academy of Sciences of the USA*, 101(20):7600–7605, 2004.

[13] A. Ashkin. Acceleration and Trapping of Particles by Radiation Pressure. *Physical Review Letters*, 24(4):156–159, 1970.

[14] A. Ashkin, J. M. Dziedzic, J. E. Bjorkholm, and S. Chu. Observation of a single-beam gradient force optical trap for dielectric particles. *Optics Letters*, 11(5):288–290, 1986.

[15] A. Ashkin. Forces of a Single-Beam Gradient Laser Trap on a Dielectric Sphere in the Ray Optics Regime. *Biophysical Journal*, 61(2):569–582, 1992.

[16] K. Svoboda and S. M. Block. Biological Applications of Optical Forces. *Annual Review of Biophysics & Biomolecular Structure*, 23:247–285, 1994.

[17] K. C. Neuman and S. M. Block. Optical trapping. *Review of Scientific Instruments*, 75(9):2787–2809, 2004.

[18] J. R. Moffitt, Y. R. Chemla, S. B. Smith, and C. Bustamante. Recent Advances in Optical Tweezers. *Annual Review of Biochemistry*, In press, 2008.

[19] E. J. G. Peterman, F. Gittes, and C. F. Schmidt. Laser-induced heating in optical traps. *Biophysical Journal*, 84(2):1308–1316, 2003.

[20] K. C. Vermeulen, G. J. L. Wuite, G. J. M. Stienen, and C. F. Schmidt. Optical trap stiffness in the presence and absence of spherical aberrations. *Applied Optics*, 45(8):1812–1819, 2006.

[21] F. Gittes and C. F. Schmidt. Interference model for back-focal-plane displacement detection in optical tweezers. *Optics Letters*, 23(1):7–9, 1998.

[22] R. Brown. A brief account of microscopical observations : made in the months of June, July, and August, 1827, on the particles contained in the pollen of plants and on the general existence of active molecules in organic and inorganic bodies. *Philosophical Journal*, 4:358–371, 1828.

[23] F. Reif. *Fundamentals of statistical and thermal physics*. McGraw-Hill series in fundamentals of physics. McGraw Hill, New York, 1965.

[24] F. Gittes and C. F. Schmidt. Signals and noise in micromechanical measurements. In *Methods in Cell Biology*, volume 55, pages 129–156. Academic Press, London, 1998.

[25] M. W. Allersma, F. Gittes, M. J. deCastro, R. J. Stewart, and C. F. Schmidt. Two-dimensional tracking of ncd motility by back focal plane interferometry. *Biophysical Journal*, 74(2 Pt 1):1074–1085, 1998.

[26] K. C. Vermeulen, J. van Mameren, G. J. M. Stienen, E. J. G. Peterman, G. J. L. Wuite, and C. F. Schmidt. Calibrating bead displacements in optical tweezers using acousto-optic deflectors. *Review of Scientific Instruments*, 77(1):013704, 2006.

[27] C. Bustamante, J. C. Macosko, and G. J. L. Wuite. Grabbing the cat by the tail: Manipulating molecules one by one. *Nature Reviews Molecular Cell Biology*, 1(2):130–136, 2000.

[28] J. T. Finer, R. M. Simmons, and J. A. Spudich. Single myosin molecule mechanics - piconewton forces and nanometer steps. *Nature*, 368(6467):113–119, 1994.

[29] D. E. Smith, S. J. Tans, S. B. Smith, S. Grimes, D. L. Anderson, and C. Bustamante. The bacteriophage phi 29 portal motor can package DNA against a large internal force. *Nature*, 413(6857):748–752, 2001.

[30] M. D. Wang, M. J. Schnitzer, H. Yin, R. Landick, J. Gelles, and S. M. Block. Force and velocity measured for single molecules of RNA polymerase. *Science*, 282(5390):902–907, 1998.

[31] G. J. L. Wuite, S. B. Smith, M. Young, D. Keller, and C. Bustamante. Single-molecule studies of the effect of template tension on T7 DNA polymerase activity. *Nature*, 404(6773):103–106, 2000.

[32] K. Svoboda, C. F. Schmidt, B. J. Schnapp, and S. M. Block. Direct Observation of Kinesin Stepping by Optical Trapping Interferometry. *Nature*, 365(6448):721–727, 1993.

[33] B. van den Broek, M. C. Noom, and G. J. L. Wuite. DNA-tension dependence of restriction enzyme activity reveals mechanochemical properties of the reaction pathway. *Nucleic Acids Research*, 33(8):2676–2684, 2005.

[34] B. Schnurr, F. Gittes, F. C. MacKintosh, and C. F. Schmidt. Determining microscopic viscoelasticity in flexible and semiflexible polymer networks from thermal fluctuations. *Macromolecules*, 30(25):7781–7792, 1997.

[35] K. M. Addas, C. F. Schmidt, and J. X. Tang. Microrheology of solutions of semiflexible biopolymer filaments using laser tweezers interferometry. *Physical Review E*, 70(2):021503, 2004.

[36] I. M. Tolic-Norrelykke, E. L. Munteanu, G. Thon, L. Oddershede, and K. Berg-Sorensen. Anomalous diffusion in living yeast cells. *Physical Review Letters*, 93(7):078102, 2004.

[37] F. Gittes and C. F. Schmidt. Microscopic approaches to dynamics and structure of biological motors. *Current Opinion in Solid State & Materials Science*, 1(3):412–424, 1996.

[38] F. C. MacKintosh and C. F. Schmidt. Microrheology. *Current Opinion in Colloid & Interface Science*, 4(4):300–307, 1999.

[39] A. Buosciolo, G. Pesce, and A. Sasso. New calibration method for position detector for simultaneous measurements of force constants and local viscosity in optical tweezers. *Optics Communications*, 230(4-6):357–368, 2004.

[40] E. L. Florin, A. Pralle, E. H. K. Stelzer, and J. K. H. Horber. Photonic force microscope calibration by thermal noise analysis. *Applied Physics A*, 66:S75–S78, 1998.

[41] L. P. Ghislain, N. A. Switz, and W. W. Webb. Measurement of Small Forces Using an Optical Trap. *Review of Scientific Instruments*, 65(9):2762–2768, 1994.

[42] G. J. L. Wuite, R. J. Davenport, A. Rappaport, and C. Bustamante. An integrated laser trap/flow control video microscope for the study of single biomolecules. *Biophysical Journal*, 79(2):1155–1167, 2000.

[43] K. Berg-Sorensen and H. Flyvbjerg. Power spectrum analysis for optical tweezers. *Review of Scientific Instruments*, 75(3):594–612, 2004.

[44] M. J. Lang, C. L. Asbury, J. W. Shaevitz, and S. M. Block. An automated two-dimensional optical force clamp for single molecule studies. *Biophysical Journal*, 83(1):491–501, 2002.

[45] R. Nambiar, A. Gajraj, and J. C. Meiners. All-optical constant-force laser tweezers. *Biophysical Journal*, 87(3):1972–1980, 2004.

[46] W. H. Wright, G. J. Sonek, and M. W. Berns. Parametric study of the forces on microspheres held by optical tweezers. *Applied Optics*, 33(9):1735–1748, 1994.

[47] H. Felgner, O. Muller, and M. Schliwa. Calibration of light forces in optical tweezers. *Applied Optics*, 34(6):977–982, 1995.

[48] E. J. G. Peterman, M. A. van Dijk, L. C. Kapitein, and C. F. Schmidt. Extending the bandwidth of optical-tweezers interferometry. *Review of Scientific Instruments*, 74(7):3246–3249, 2003.

[49] F. Gittes and C. F. Schmidt. Thermal noise limitations on micromechanical experiments. *European Biophysics Journal With Biophysics Letters*, 27(1):75–81, 1998.

[50] R. T. Dame, J. van Mameren, M. S. Luijsterburg, M. E. Mysiak, A. Janicijevic, G. Pazdzior, P. C. van der Vliet, C. Wyman, and G. J. L. Wuite. Analysis of scanning force microscopy images of protein-induced DNA bending using simulations. *Nucleic Acids Research*, 33(7):e68, 2005.

[51] R. E. Harrington. DNA curving and bending in protein-DNA recognition. *Molecular Microbiology*, 6(18):2549–2555, 1992.

[52] P. C. van der Vliet and C. P. Verrijzer. Bending of DNA by transcription factors. *Bioessays*, 15(1):25–32, 1993.

[53] J. van Noort, S. Verbrugge, N. Goosen, C. Dekker, and R. T. Dame. Dual architectural roles of HU: Formation of flexible hinges and rigid filaments. *Proceedings of the National Academy of Sciences of the USA*, 101(18):6969–6974, 2004.

[54] B. M. Ali, R. Amit, I. Braslavsky, A. B. Oppenheim, O. Gileadi, and J. Stavans. Compaction of single DNA molecules induced by binding of integration host factor (IHF). *Proceedings of the National Academy of Sciences of the USA*, 98(19):10658–10663, 2001.

[55] R. T. Dame. The role of nucleoid-associated proteins in the organization and compaction of bacterial chromatin. *Molecular Microbiology*, 56(4):858–870, 2005.

[56] J. F. Thompson and A. Landy. Empirical estimation of protein-induced DNA bending angles: applications to lambda site-specific recombination complexes. *Nucleic Acids Research*, 16(20):9687–9705, 1988.

[57] D. Sun, L. H. Hurley, and R. M. Harshey. Structural distortions induced by integration host factor (IHF) at the H' site of phage lambda probed by (+)-CC-1065, pluramycin, and KMnO4 and by DNA cyclization studies. *Biochemistry*, 35(33):10815–10827, 1996.

[58] K. K. Swinger, K. M. Lemberg, Y. Zhang, and P. A. Rice. Flexible DNA bending in HU-DNA cocrystal structures. *EMBO Journal*, 22(14):3749–3760, 2003.

[59] F. V. Murphy, R. M. Sweet, and M. E. Churchill. The structure of a chromosomal high mobility group protein-DNA complex reveals sequence-neutral mechanisms important for non-sequence-specific DNA recognition. *EMBO Journal*, 18(23):6610–6618, 1999.

[60] P. A. Rice, S. Yang, K. Mizuuchi, and H. A. Nash. Crystal structure of an IHF-DNA complex: a protein-induced DNA U-turn. *Cell*, 87(7):1295–1306, 1996.

[61] E. R. Jamieson, M. P. Jacobson, C. M. Barnes, C. S. Chow, and S. J. Lippard. Structural and kinetic studies of a cisplatin-modified DNA icosamer binding to HMG1 domain B. *Journal of Biological Chemistry*, 274(18):12346–12354, 1999.

[62] K. Wojtuszewski and I. Mukerji. HU binding to bent DNA: a fluorescence resonance energy transfer and anisotropy study. *Biochemistry*, 42(10):3096–3104, 2003.

[63] M. Lorenz, A. Hillisch, S. D. Goodman, and S. Diekmann. Global structure similarities of intact and nicked DNA complexed with IHF measured in solution by fluorescence resonance energy transfer. *Nucleic Acids Research*, 27(23):4619–4625, 1999.

[64] M. Lorenz, A. Hillisch, D. Payet, M. Buttinelli, A. Travers, and S. Diekmann. DNA bending induced by high mobility group proteins studied by fluorescence resonance energy transfer. *Biochemistry*, 38(37):12150–12158, 1999.

[65] R. T. Dame, C. Wyman, and N. Goosen. Insights into the regulation of transcription by scanning force microscopy. *Journal of Microscopy*, 212(3):244–253, 2003.

[66] C. Bustamante and C. Rivetti. Visualizing protein-nucleic acid interactions on a large scale with the scanning force microscope. *Annual Review of Biophysics & Biomolecular Structure*, 25:395–429, 1996.

[67] C. Rivetti, C. Walker, and C. Bustamante. Polymer chain statistics and conformational analysis of DNA molecules with bends or sections of different flexibility. *Journal of Molecular Biology*, 280(1):41–59, 1998.

[68] D. A. Erie, G. Yang, H. C. Schultz, and C. Bustamante. DNA bending by Cro protein in specific and nonspecific complexes: implications for protein site recognition and specificity. *Science*, 266(5190):1562–1566, 1994.

[69] G. H. Seong, E. Kobatake, K. Miura, A. Nakazawa, and M. Aizawa. Direct atomic force microscopy visualization of integration host factor-induced DNA bending structure of the promoter regulatory region on the Pseudomonas TOL plasmid. *Biochemical and Biophysical Research Communications*, 291(2):361–366, 2002.

[70] R. Sieira, D. J. Comerci, L. I. Pietrasanta, and R. A. Ugalde. Integration host factor is involved in transcriptional regulation of the Brucella abortus virB operon. *Molecular Microbiology*, 54(3):808–822, 2004.

[71] O. Kratky and G. Porod. Röntgenuntersuchung aufgelöster fademolekule. *Recueil*, 68:1106–1122, 1949.

[72] J. A. Schellman. Flexibility of DNA. *Biopolymers*, 13(1):217–226, 1974.

[73] Y. Lu, B. D. Weers, and N. C. Stellwagen. Analysis of the intrinsic bend in the M13 origin of replication by atomic force microscopy. *Biophysical Journal*, 85(1):409–415, 2003.

[74] C. Rivetti, M. Guthold, and C. Bustamante. Wrapping of DNA around the E.coli RNA polymerase open promoter complex. *EMBO Journal*, 18(16):4464–4475, 1999.

[75] J. Wilhelm and E. Frey. Radial distribution function of semiflexible polymers. *Physical Review Letters*, 77(12):2581–2584, 1996.

[76] M. E. Mysiak, M. H. Bleijenberg, C. Wyman, P. E. Holthuizen, and P. C. van der Vliet. Bending of adenovirus origin DNA by nuclear factor I as shown by scanning force microscopy is required for optimal DNA replication. *Journal of Virology*, 78(4):1928–1935, 2004.

[77] M. E. Mysiak, C. Wyman, P. E. Holthuizen, and P. C. van der Vliet. NFI anc Oct-1 bend the Ad5 origin in the same direction leading to optimal DNA replication. *Nucleic Acids Research*, 32(21):6218–6225, 2004.

[78] A. Janicijevic, K. Sugasawa, Y. Shimizu, F. Hanaoka, N. Wijgers, M. Djurica, J. H. Hoeijmakers, and C. Wyman. DNA bending by the human damage recognition complex XPC-HR23B. *DNA Repair*, 2(3):325–336, 2003.

[79] C. P. Verrijzer, J. A. van Oosterhout, W. W. van Weperen, and P. C. van der Vliet. POU proteins bend DNA via the POU-specific domain. *EMBO Journal*, 10(10):3007–3014, 1991.

[80] C. Rivetti, M. Guthold, and C. Bustamante. Scanning force microscopy of DNA deposited onto mica: equilibration versus kinetic trapping studied by statistical polymer chain analysis. *Journal of Molecular Biology*, 264(5):919–932, 1996.

[81] C. Rivetti and S. Codeluppi. Accurate length determination of DNA molecules visualized by atomic force microscopy: evidence for a partial B- to A-form transition on mica. *Ultramicroscopy*, 87(1-2):55–66, 2001.

[82] M. E. Mysiak. *Molecular architecture of the preinitiation complex in adenovirus DNA replication*. PhD thesis, Utrecht University, 2004.

[83] P. R. Bevington and D. K. Robinson. *Data reduction and error analysis for the physical sciences*. McGraw-Hill, Boston, 3rd edition, 2003.

[84] R. T. Dame. *Architectural roles of H-NS and HU in DNA compaction and transcription regulation*. PhD thesis, Leiden University, 2003.

[85] N. Goosen. *Regulation of transposition of bacteriophage Mu*. PhD thesis, Leiden University, 1984.

[86] R. T. Dame, C. Wyman, and N. Goosen. Structural basis for preferential binding of H-NS to curved DNA. *Biochimie*, 83(2):231–234, 2001.

[87] F. M. L. Almeida, M. Barbi, and M. A. B. do Vale. A proposal for a different chi-square function for Poisson distributions. *Nuclear Instruments & Methods in Physics Research A*, 449(1-2):383–395, 2000.

[88] E. Peeters, R. Willaert, D. Maes, and D. Charlier. Ss-LrpB from Sulfolobus solfataricus condenses about 100 base pairs of its own operator DNA into globular nucleoprotein complexes. *Journal of Biological Chemistry*, 281(17):11721–11728, 2006.

[89] J. F. Graveland-Bikker, I. A. T. Schaap, C. F. Schmidt, and C. G. deKruif. Structural and Mechanical Study of a Self-Assembling Protein Nanotube. *Nano Letters*, 6(4):616–621, 2006.

[90] M. C. Noom, B. van den Broek, J. van Mameren, and G. J. L. Wuite. Visualizing single DNA-bound proteins using DNA as a scanning probe. *Nature Methods*, 4(12):1031–1036, 2007.

[91] S. C. West. Molecular views of recombination proteins and their control. *Nature Reviews Molecular Cell Biology*, 4(6):435–445, 2003.

[92] M. van den Bosch, P. H. Lohman, and A. Pastink. DNA double-strand break repair by homologous recombination. *Biological Chemistry*, 383(6):873–892, 2002.

[93] J. van Mameren, M. Modesti, R. Kanaar, C. Wyman, G. J. L. Wuite, and E. J. G. Peterman. Dissecting elastic heterogeneity along DNA molecules coated partly with Rad51 using concurrent fluorescence microscopy and optical tweezers. *Biophysical Journal*, 91(8):L78–L80, 2006.

[94] B. van den Broek, F. Vanzi, D. Normanno, F. S. Pavone, and G. J. L. Wuite. Real-time observation of DNA looping dynamics of Type IIE restriction enzymes NaeI and NarI. *Nucleic Acids Research*, 34(1):167–174, 2006.

[95] M. S. Luijsterburg, M. C. Noom, G. J. L. Wuite, and R. T. Dame. The architectural role of nucleoid-associated proteins in the organization of bacterial chromatin: a molecular perspective. *Journal of Structural Biology*, 156(2):262–272, 2006.

[96] R. T. Dame, M. C. Noom, and G. J. L. Wuite. Bacterial chromatin organization by H-NS protein unravelled using dual DNA manipulation. *Nature*, 444(7117):387–390, 2006.

[97] O. G. Berg, R. B. Winter, and P. H. von Hippel. Diffusion-driven mechanisms of protein translocation on nucleic acids. 1. Models and theory. *Biochemistry*, 20(24):6929–6948, 1981.

[98] D. M. Gowers and S. E. Halford. Protein motion from non-specific to specific DNA by three-dimensional routes aided by supercoiling. *EMBO Journal*, 22(6):1410–1418, 2003.

[99] P. H. von Hippel and O. G. Berg. Facilitated target location in biological systems. *Journal of Biological Chemistry*, 264(2):675–678, 1989.

[100] V. Epshtein, F. Toulme, A. R. Rahmouni, S. Borukhov, and E. Nudler. Transcription through the roadblocks: the role of RNA polymerase cooperation. *EMBO Journal*, 22(18):4719–4727, 2003.

[101] L. R. Brewer, M. Corzett, and R. Balhorn. Protamine-induced condensation and decondensation of the same DNA molecule. *Science*, 286(5437):120–123, 1999.

[102] Y. Arai, R. Yasuda, K. Akashi, Y. Harada, H. Miyata, Jr. Kinosita, K., and H. Itoh. Tying a molecular knot with optical tweezers. *Nature*, 399(6735):446–448, 1999.

[103] L. C. Gosule and J. A. Schellman. Compact form of DNA induced by spermidine. *Nature*, 259(5541):333–335, 1976.

[104] E. Evans. Probing the relation between force - lifetime - and chemistry in single molecular bonds. *Annual Review of Biophysics & Biomolecular Structure*, 30:105–128, 2001.

[105] N. Shimamoto. One-dimensional diffusion of proteins along DNA - Its biological and chemical significance revealed by single-molecule measurements. *Journal of Biological Chemistry*, 274(22):15293–15296, 1999.

[106] W. Trabesinger, G. J. Schutz, H. J. Gruber, H. Schindler, and T. Schmidt. Detection of individual oligonucleotide pairing by single-molecule microscopy. *Analytical Chemistry*, 71(1):279–283, 1999.

[107] D. A. Hiller, J. M. Fogg, A. M. Martin, J. M. Beechem, N. O. Reich, and J. J. Perona. Simultaneous DNA binding and bending by EcoRV endonuclease observed by real-time fluorescence. *Biochemistry*, 42(49):14375–14385, 2003.

[108] G. Charvin, A. Vologodskii, D. Bensimon, and V. Croquette. Braiding DNA: experiments, simulations, and models. *Biophysical Journal*, 88(6):4124–4136, 2005.

[109] S. M. Lindsay, L. A. Nagahara, T. Thundat, U. Knipping, R. L. Rill, B. Drake, C. B. Prater, A. L. Weisenhorn, S. A. Gould, and P. K. Hansma. STM and AFM images of nucleosome DNA under water. *Journal of Biomolecular Structure and Dynamics*, 7(2):279–287, 1989.

[110] W. Fritzsche, L. Takac, and E. Henderson. Application of atomic force microscopy to visualization of DNA, chromatin, and chromosomes. *Critical Reviews in Eukaryotic Gene Expression*, 7(3):231–240, 1997.

[111] S. Kasas, N. H. Thomson, B. L. Smith, H. G. Hansma, X. Zhu, M. Guthold, C. Bustamante, E. T. Kool, M. Kashlev, and P. K. Hansma. Escherichia coli RNA polymerase activity observed using atomic force microscopy. *Biochemistry*, 36(3):461–468, 1997.

[112] J. van Noort, K. O. van der Werf, A. P. Eker, C. Wyman, B. G. de Grooth, N. F. van Hulst, and J. Greve. Direct visualization of dynamic protein-DNA interactions with a dedicated atomic force microscope. *Biophysical Journal*, 74(6):2840–2849, 1998.

[113] J. H. G. Huisstede, K. O. van der Werf, M. L. Bennink, and V. Subramaniam. Force detection in optical tweezers using backscattered light. *Optics Express*, 13(4):1113–1123, 2005.

[114] S. J. Koch, A. Shundrovsky, B. C. Jantzen, and M. D. Wang. Probing protein-DNA interactions by unzipping a single DNA double helix. *Biophysical Journal*, 83(2):1098–1105, 2002.

[115] S. C. Kowalczykowski, D. A. Dixon, A. K. Eggleston, S. D. Lauder, and W. M. Rehrauer. Biochemistry of homologous recombination in Escherichia coli. *Microbiological Reviews*, 58(3):401–465, 1994.

[116] S. E. Halford, A. J. Welsh, and M. D. Szczelkun. Enzyme-mediated DNA looping. *Annual Review of Biophysics & Biomolecular Structure*, 33:1–24, 2004.

[117] P. V. Cornish and T. Ha. A Survey of Single-Molecule Techniques in Chemical Biology. *ACS Chemical Biology*, 2(1):53–61, 2007.

[118] J. H. Kim and R. G. Larson. Single-molecule analysis of 1D diffusion and transcription elongation of T7 RNA polymerase along individual stretched DNA molecules. *Nucleic Acids Research*, 35(11):3848–3858, 2007.

[119] A. Bensimon, A. Simon, A. Chiffaudel, V. Croquette, F. Heslot, and D. Bensimon. Alignment and Sensitive Detection of DNA by a Moving Interface. *Science*, 265(5181):2096–2098, 1994.

[120] R. Lebofsky and A. Bensimon. Single DNA molecule analysis: applications of molecular combing. *Briefings in Functional Genomics and Proteomics*, 1(4):385–96, 2003.

[121] D. Bensimon, A. J. Simon, V. Croquette, and A. Bensimon. Stretching DNA with a Receding Meniscus - Experiments and Models. *Physical Review Letters*, 74(23):4754–4757, 1995.

[122] Z. Gueroui, C. Place, E. Freyssingeas, and B. Berge. Observation by fluorescence microscopy of transcription on single combed DNA. *Proceedings of the National Academy of Sciences of the USA*, 99(9):6005–6010, 2002.

[123] A. Crut, D. Lasne, J. F. Allemand, M. Dahan, and P. Desbiolles. Transverse fluctuations of single DNA molecules attached at both extremities to a surface. *Physical Review E*, 67(5):051910, 2003.

[124] T. F. Chan, C. Ha, A. Phong, D. M. Cai, E. Wan, L. Leung, P. Y. Kwok, and M. Xiao. A simple DNA stretching method for fluorescence imaging of single DNA molecules. *Nucleic Acids Research*, 34(17):–, 2006.

[125] A. Crut, B. Geron-Landre, I. Bonnet, S. Bonneau, P. Desbiolles, and C. Escude. Detection of single DNA molecules by multicolor quantum-dot end-labeling. *Nucleic Acids Research*, 33(11):–, 2005.

[126] D. Axelrod. Total Internal Reflection Fluorescence Microscopy in Cell Biology. *Traffic*, 2(11):764–774, 2001.

[127] R. E. Thompson, D. R. Larson, and W. W. Webb. Precise Nanometer Localization Analysis for Individual Fluorescent Probes. *Biophysical Journal*, 82(5):2775–2783, 2002.

[128] A. Granéli, C. C. Yeykal, T. K. Prasad, and E. C. Greene. Organized arrays of individual DIVA molecules tethered to supported lipid bilayers. *Langmuir*, 22(1):292–299, 2006.

[129] P. C. Blainey, A. M. van Oijen, A. Banerjee, G. L. Verdine, and X. S. Xie. A base-excision DNA-repair protein finds intrahelical lesion bases by fast sliding in contact with DNA. *Proceedings of the National Academy of Sciences of the USA*, 103(15):5752–5757, 2006.

[130] P. S. Doyle, B. Ladoux, and J. L. Viovy. Dynamics of a tethered polymer in shear flow. *Physical Review Letters*, 84(20):4769–4772, 2000.

[131] A. M. van Oijen, P. C. Blainey, D. J. Crampton, C. C. Richardson, T. Ellenberger, and X. S. Xie. Single-molecule kinetics of lambda exonuclease reveal base dependence and dynamic disorder. *Science*, 301(5637):1235–1238, 2003.

[132] J. B. Lee, R. K. Hite, S. M. Hamdan, X. S. Xie, C. C. Richardson, and A. M. van Oijen. DNA primase acts as a molecular brake in DNA replication. *Nature*, 439(7076):621–624, 2006.

[133] A. Granéli, C. C. Yeykal, R. B. Robertson, and E. C. Greene. Long-distance lateral diffusion of human Rad51 on double-stranded DNA. *Proceedings of the National Academy of Sciences of the USA*, 103(5):1221–1226, 2006.

[134] M. Modesti, D. Ristic, T. van der Heijden, C. Dekker, J. van Mameren, E. J. G. Peterman, G. J. L. Wuite, R. Kanaar, and C. Wyman. Fluorescent human RAD51 reveals multiple nucleation sites and filament segments tightly associated along a single DNA molecule. *Structure*, 15(5):599–609, 2007.

[135] T. K. Prasad, C. C. Yeykal, and E. C. Greene. Visualizing the assembly of human Rad51 filaments on double-stranded DNA. *Journal of Molecular Biology*, 363(3):713–728, 2006.

[136] S. Mangenot, M. Hochrein, J. Radler, and L. Letellier. Real-time imaging of DNA ejection from single phage particles. *Current Biology*, 15(5):430–435, 2005.

[137] P. Grayson, L. Han, T. Winther, and R. Phillips. Real-time observations of single bacteriophage lambda DNA ejections in vitro. *Proceedings of the National Academy of Sciences of the USA*, 104(37):14652–14657, 2007.

[138] R. Galletto, I. Amitani, R. J. Baskin, and S. C. Kowalczykowski. Direct observation of individual RecA filaments assembling on single DNA molecules. *Nature*, 443(7113):875–878, 2006.

[139] M. A. van Dijk, L. C. Kapitein, J. van Mameren, C. F. Schmidt, and E. J. G. Peterman. Combining optical trapping and single-molecule fluorescence spectroscopy: Enhanced photobleaching of fluorophores. *Journal of Physical Chemistry B*, 108(20):6479–6484, 2004.

[140] M. J. Lang, P. M. Fordyce, and S. M. Block. Combined optical trapping and single-molecule fluorescence. *Journal of Biology*, 2(1):6, 2003.

[141] M. J. Lang, P. M. Fordyce, A. M. Engh, K. C. Neuman, and S. M. Block. Simultaneous, coincident optical trapping and single-molecule fluorescence. *Nature Methods*, 1(2):133–139, 2004.

[142] R. R. Brau, P. B. Tarsa, J. M. Ferrer, P. Lee, and M. J. Lang. Interlaced Optical Force-Fluorescence Measurements for Single Molecule Biophysics. *Biophysical Journal*, 91(3):1069–1077, 2006.

[143] T. T. Perkins, S. R. Quake, D. E. Smith, and S. Chu. Relaxation of a Single DNA Molecule Observed by Optical Microscopy. *Science*, 264(5160):822–826, 1994.

[144] T. T. Perkins, D. E. Smith, and S. Chu. Direct Observation of Tube-Like Motion of a Single Polymer-Chain. *Science*, 264(5160):819–822, 1994.

[145] T. T. Perkins, D. E. Smith, R. G. Larson, and S. Chu. Stretching of a Single Tethered Polymer in a Uniform-Flow. *Science*, 268(5207):83–87, 1995.

[146] P. R. Bianco, L. R. Brewer, M. Corzett, R. Balhorn, Y. Yeh, S. C. Kowalczykowski, and R. J. Baskin. Processive translocation and DNA unwinding by individual RecBCD enzyme molecules. *Nature*, 409(6818):374–378, 2001.

[147] N. Handa, P. R. Bianco, R. J. Baskin, and S. C. Kowalczykowski. Direct visualization of RecBCD movement reveals cotranslocation of the RecD motor after Chi recognition. *Molecular Cell*, 17(5):745–750, 2005.

[148] M. Spies, I. Amitani, R. J. Baskin, and S. C. Kowalczykowski. RecBCD enzyme switches lead motor Subunits in response to chi recognition. *Cell*, 131(4):694–705, 2007.

[149] M. Spies, P. R. Bianco, M. S. Dillingham, N. Handa, R. J. Baskin, and S. C. Kowalczykowski. A molecular throttle: The recombination hotspot chi controls DNA translocation by the RecBCD helicase. *Cell*, 114(5):647–654, 2003.

[150] S. R. Quake, H. Babcock, and S. Chu. The dynamics of partially extended single molecules of DNA. *Nature*, 388(6638):151–154, 1997.

[151] Y. Harada, T. Funatsu, K. Murakami, Y. Nonoyama, A. Ishihama, and T. Yanagida. Single-molecule imaging of RNA polymerase-DNA interactions in real time. *Biophysical Journal*, 76(2):709–715, 1999.

[152] A. Ishijima, H. Kojima, T. Funatsu, M. Tokunaga, H. Higuchi, H. Tanaka, and T. Yanagida. Simultaneous observation of individual ATPase and mechanical events by a single myosin molecule during interaction with actin. *Cell*, 92(2):161–171, 1998.

[153] M. L. Bennink, O. D. Scharer, R. Kanaar, K. Sakata-Sogawa, J. M. Schins, J. S. Kanger, B. G. de Grooth, and J. Greve. Single-molecule manipulation of double-stranded DNA using optical tweezers: interaction studies of DNA with RecA and YOYO-1. *Cytometry*, 36(3):200–208, 1999.

[154] E. A. Abbondanzieri, W. J. Greenleaf, J. W. Shaevitz, R. Landick, and S. M. Block. Direct observation of base-pair stepping by RNA polymerase. *Nature*, 438(7067):460–465, 2005.

[155] M. Capitanio, D. Maggi, F. Vanzi, and F. S. Pavone. FIONA in the trap: the advantages of combining optical tweezers and fluorescence. *Journal of Optics A*, 9(8):S157–S163, 2007.

[156] T. R. Strick, J. F. Allemand, D. Bensimon, A. Bensimon, and V. Croquette. The elasticity of a single supercoiled DNA molecule. *Science*, 271(5257):1835–1837, 1996.

[157] A. M. van Oijen. Honey, I shrunk the DNA: DNA length as a probe for nucleic-acid enzyme activity. *Biopolymers*, 85(2):144–153, 2007.

[158] W. E. Moerner and M. Orrit. Illuminating single molecules in condensed matter. *Science*, 283(5408):1670–1676, 1999.

[159] S. Weiss. Fluorescence spectroscopy of single biomolecules. *Science*, 283(5408):1676–1683, 1999.

[160] A. Ashkin. Optical trapping and manipulation of neutral particles using lasers. *Proceedings of the National Academy of Sciences of the USA*, 94(10):4853–4860, 1997.

[161] K. C. Neuman, E. H. Chadd, G. F. Liou, K. Bergman, and S. M. Block. Characterization of photodamage to escherichia coli in optical traps. *Biophysical Journal*, 77(5):2856–2863, 1999.

[162] F. Wilkinson, D. J. McGarvey, and A. F. Olea. Excited Triplet-State Interactions with Molecular-Oxygen - Influence of Charge-Transfer on the Bimolecular Quenching Rate Constants and the Yields of Singlet Oxygen (O- 2(Asterisk),(1)Delta(G)) for Substituted Naphthalenes in Various Solvents. *Journal of Physical Chemistry*, 98(14):3762–3769, 1994.

[163] Y. Harada, K. Sakurada, T. Aoki, D. D. Thomas, and T. Yanagida. Mechanochemical coupling in actomyosin energy transduction studied by in vitro movement assay. *Journal of Molecular Biology*, 216(1):49–68, 1990.

[164] C. Xu, W. Zipfel, J. B. Shear, R. M. Williams, and W. W. Webb. Multiphoton fluorescence excitation: new spectral windows for biological nonlinear microscopy. *Proceedings of the National Academy of Sciences of the USA*, 93(20):10763–10768, 1996.

[165] G. H. Patterson and D. W. Piston. Photobleaching in two-photon excitation microscopy. *Biophysical Journal*, 78(4):2159–2162, 2000.

[166] C. Eggeling, J. Widengren, R. Rigler, and C. A. M. Seidel. Photobleaching of fluorescent dyes under conditions used for single-molecule detection: Evidence of two-step photolysis. *Analytical Chemistry*, 70(13):2651–2659, 1998.

[167] P. S. Dittrich and P. Schwille. Photobleaching and stabilization of fluorophores used for single-molecule analysis with one- and two-photon excitation. *Applied Physics B*, 73(8):829–837, 2001.

[168] S. Hohng and T. Ha. Near-complete suppression of quantum dot blinking in ambient conditions. *Journal of the American Chemical Society*, 126(5):1324–1325, 2004.

[169] J. A. Veerman, M. F. Garcia-Parajo, L. Kuipers, and N. F. van Hulst. Time-varying triplet state lifetimes of single molecules. *Physical Review Letters*, 83(11):2155–2158, 1999.

[170] C. R. Cantor and P. R. Schimmel. *Techniques for the study of biological structure and function*. W. H. Freeman, San Francisco, 1980.

[171] H. van Amerongen and W. S. Struve. Polarized Optical Spectroscopy of Chromoproteins. In *Biochemical Spectroscopy*, volume 246 of *Methods in Enzymology*, pages 259–283. Academic Press, San Diego, 1995.

[172] K. Adachi, R. Yasuda, H. Noji, H. Itoh, Y. Harada, M. Yoshida, and Jr. Kinosita, K. Stepping rotation of F1-ATPase visualized through angle-resolved single-fluorophore imaging. *Proceedings of the National Academy of Sciences of the USA*, 97(13):7243–7247, 2000.

[173] E. J. G. Peterman, H. Sosa, L. S. Goldstein, and W. E. Moerner. Polarized fluorescence microscopy of individual and many kinesin motors bound to axonemal microtubules. *Biophysical Journal*, 81(5):2851–2863, 2001.

[174] A. Jenei, A. K. Kirsch, V. Subramaniam, D. J. Arndt-Jovin, and T. M. Jovin. Picosecond multiphoton scanning near-field optical microscopy. *Biophysical Journal*, 76(2):1092–1100, 1999.

[175] R. Kuhnemuth and C. A. M. Seidel. Principles of single molecule multiparameter fluorescence spectroscopy. *Single Molecules*, 2(4):251–254, 2001.

[176] F. E. Benson, A. Stasiak, and S. C. West. Purification and characterization of the human Rad51 protein, an analogue of E. coli RecA. *EMBO Journal*, 13(23):5764–5771, 1994.

[177] C. Wyman and R. Kanaar. Homologous recombination: down to the wire. *Current Biology*, 14(15):R629–R631, 2004.

[178] B. Michel, M. J. Flores, E. Viguera, G. Grompone, M. Seigneur, and V. Bidnenko. Rescue of arrested replication forks by homologous recombination. *Proceedings of the National Academy of Sciences of the USA*, 98(15):8181–8188, 2001.

[179] D. V. Bugreev and A. V. Mazin. Ca2+ activates human homologous recombination protein Rad51 by modulating its ATPase activity. *Proceedings of the National Academy of Sciences of the USA*, 101(27):9988–9993, 2004.

[180] D. Ristic, M. Modesti, T. van der Heijden, J. van Noort, C. Dekker, R. Kanaar, and C. Wyman. Human Rad51 filaments on double- and single-stranded DNA: correlating regular and irregular forms with recombination function. *Nucleic Acids Research.*, 33(10):3292–3302, 2005.

[181] C. M. Waterman-Storer, A. Desai, J. C. Bulinski, and E. D. Salmon. Fluorescent speckle microscopy, a method to visualize the dynamics of protein assemblies in living cells. *Current Biology*, 8(22):1227–1230, 1998.

[182] J. F. Leger, J. Robert, L. Bourdieu, D. Chatenay, and J. F. Marko. RecA binding to a single double-stranded DNA molecule: A possible role of DNA conformational fluctuations. *Proceedings of the National Academy of Sciences of the USA*, 95(21):12295–12299, 1998.

[183] M. Hegner, S. B. Smith, and C. Bustamante. Polymerization and mechanical properties of single RecA-DNA filaments. *Proceedings of the National Academy of Sciences of the USA*, 96(18):10109–10114, 1999.

[184] P. R. Bianco, R. B. Tracy, and S. C. Kowalczykowski. DNA strand exchange proteins: a biochemical and physical comparison. *Frontiers in Bioscience*, 3:D570–603, 1998.

[185] P. Sung, L. Krejci, S. Van Komen, and M. G. Sehorn. Rad51 Recombinase and Recombination Mediators. *Journal of Biological Chemistry*, 278(44):42729–42732, 2003.

[186] L. S. Symington and W. D. Heyer. Some disassembly required: role of DNA translocases in the disruption of recombination intermediates and dead-end complexes. *Genes & Development*, 20(18):2479–2486, 2006.

[187] S. C. Kowalczykowski and A. K. Eggleston. Homologous Pairing and DNA Strand-Exchange Proteins. *Annual Review of Biochemistry*, 63:991–1043, 1994.

[188] P. Chi, S. Van Komen, M. G. Sehorn, S. Sigurdsson, and P. Sung. Roles of ATP binding and ATP hydrolysis in human Rad51 recombinase function. *DNA Repair*, 5(3):381–391, 2006.

[189] T. van der Heijden, R. Seidel, M. Modesti, R. Kanaar, C. Wyman, and C. Dekker. Real-time assembly and disassembly of human RAD51 filaments on individual DNA molecules. *Nucleic Acids Research*, 35(17):5646–5657, 2007.

[190] J. E. Lindsley and M. M. Cox. Assembly and disassembly of RecA protein filaments occur at opposite filament ends. Relationship to DNA strand exchange. *Journal of Biological Chemistry*, 265(16):9043–9054, 1990.

[191] T. A. Arenson, O. V. Tsodikov, and M. M. Cox. Quantitative analysis of the kinetics of end-dependent disassembly of RecA filaments from ssDNA. *Journal of Molecular Biology*, 288(3):391–401, 1999.

[192] C. Joo, S. A. McKinney, M. Nakamura, I. Rasnik, S. Myong, and T. Ha. Real-time observation of RecA filament dynamics with single monomer resolution. *Cell*, 126(3):515–527, 2006.

[193] C. Wyman. Monomer networking activates recombinases. *Structure*, 14(6):949–950, 2006.

[194] J. W. J. Kerssemakers, E. L. Munteanu, L. Laan, T. L. Noetzel, M. E. Janson, and M. Dogterom. Assembly dynamics of microtubules at molecular resolution. *Nature*, 442(7103):709–712, 2006.

[195] S. L. Brenner, R. S. Mitchell, S. W. Morrical, S. K. Neuendorf, B. C. Schutte, and M. M. Cox. RecA protein-promoted ATP hydrolysis occurs throughout recA nucleoprotein filaments. *Journal of Biological Chemistry*, 262(9):4011–4016, 1987.

[196] G. Tombline and R. Fishel. Biochemical characterization of the human RAD51 protein. I. ATP hydrolysis. *Journal of Biological Chemistry*, 277(17):14417–14425, 2002.

[197] G. Tombline, C. D. Heinen, K. S. Shim, and R. Fishel. Biochemical characterization of the human RAD51 protein. III. Modulation of DNA binding by adenosine nucleotides. *Journal of Biological Chemistry*, 277(17):14434–14442, 2002.

[198] K. S. Shim, G. Tombline, C. D. Heinen, N. Charbonneau, C. Schmutte, and R. Fishel. Magnesium influences the discrimination and release of ADP by human RAD51. *DNA Repair*, 5(6):704–717, 2006.

[199] S. C. Kowalczykowski. Biochemistry of Genetic-Recombination - Energetics and Mechanism of DNA Strand Exchange. *Annual Review of Biophysics & Biophysical Chemistry*, 20:539–575, 1991.

[200] X. Li, X. P. Zhang, J. A. Solinger, K. Kiianitsa, X. Yu, E. H. Egelman, and W. D. Heyer. Rad51 and Rad54 ATPase activities are both required to modulate Rad51-dsDNA filament dynamics. *Nucleic Acids Research*, pages 4124–4140, 2007.

[201] J. Howard. *Mechanics of motor proteins and the cytoskeleton*. Sinauer Associates Publishers, Sunderland, Mass., 2001.

[202] M. E. Janson, M. E. de Dood, and M. Dogterom. Dynamic instability of microtubules is regulated by force. *Journal of Cell Biology*, 161(6):1029–1034, 2003.

[203] C. Bustamante, Z. Bryant, and S. B. Smith. Ten years of tension: single-molecule DNA mechanics. *Nature*, 421(6921):423–427, 2003.

[204] M. Rief, H. Clausen-Schaumann, and H. E. Gaub. Sequence-dependent mechanics of single DNA molecules. *Nature Structural Biology*, 6(4):346–349, 1999.

[205] T. Strunz, K. Oroszlan, R. Schäfer, and H.-J. Guntherodt. Dynamic force spectroscopy of single DNA molecules. *Proceedings of the National Academy of Sciences of the USA*, 96(20):11277–11282, 1999.

[206] H. Clausen-Schaumann, M. Rief, C. Tolksdorf, and H. E. Gaub. Mechanical Stability of Single DNA Molecules. *Biophysical Journal*, 78(4):1997–2007, 2000.

[207] I. Rouzina and V. A. Bloomfield. Force-induced melting of the DNA double helix. 1. Thermodynamic analysis. *Biophysical Journal*, 80(2):882–893, 2001.

[208] I. Rouzina and V. A. Bloomfield. Force-induced melting of the DNA double helix. 2. Effect of solution conditions. *Biophysical Journal*, 80(2):894–900, 2001.

[209] M. C. Williams, J. R. Wenner, L. Rouzina, and V. A. Bloomfield. Effect of pH on the overstretching transition of double-stranded DNA: Evidence of force-induced DNA melting. *Biophysical Journal*, 80(2):874–881, 2001.

[210] M. C. Williams, I. Rouzina, and V. A. Bloomfield. Thermodynamics of DNA interactions from single molecule stretching experiments. *Accounts of Chemical Research*, 35(3):159–166, 2002.

[211] J. R. Wenner, M. C. Williams, I. Rouzina, and V. A. Bloomfield. Salt dependence of the elasticity and overstretching transition of single DNA molecules. *Biophysical Journal*, 82(6):3160–3169, 2002.

[212] M. C. Williams, J. R. Wenner, I. Rouzina, and V. A. Bloomfield. Entropy and Heat Capacity of DNA Melting from Temperature Dependence of Single Molecule Stretching. *Biophysical Journal*, 80(4):1932–1939, 2001.

[213] A. I. U. Grosberg and A. R. Khokhlov. *Statistical physics of macromolecules*. AIP series in polymers and complex materials. AIP Press, New York, 1994.

[214] S. Piana. Structure and energy of a DNA dodecamer under tensile load. *Nucleic Acids Research*, 33(22):7029–7038, 2005.

[215] S. Cocco, J. Yan, J. F. Leger, D. Chatenay, and J. F. Marko. Overstretching and force-driven strand separation of double-helix DNA. *Physical Review E*, 70(1):011910, 2004.

[216] K. Pant, R. L. Karpel, and M. C. Williams. Kinetic Regulation of Single DNA Molecule Denaturation by T4 Gene 32 Protein Structural Domains. *Journal of Molecular Biology*, 327(3):571–578, 2003.

[217] I. D. Vladescu, M. J. McCauley, M. E. Nunez, I. Rouzina, and M. C. Williams. Quantifying force-dependent and zero-force DNA intercalation by single-molecule stretching. *Nature Methods*, 4(6):517–522, 2007.

[218] M. J. McCauley, J. Zimmerman, L. J. Maher III, and M. C. Williams. HMGB Binding to DNA: Single and Double Box Motifs. *Journal of Molecular Biology*, 374(4):993–1004, 2007.

[219] M. C. Williams, I. Rouzina, and R. L. Karpel. Quantifying DNA-Protein Interactions by Single Molecule Stretching. In *Methods in Cell Biology*, volume Volume 84, pages 517–540. Academic Press, 2008.

[220] H. S. Rye, S. Yue, D. E. Wemmer, M. A. Quesada, R. P. Haugland, R. A. Mathies, and A. N. Glazer. Stable Fluorescent Complexes of Double-Stranded DNA with Bis-Intercalating Asymmetric Cyanine Dyes - Properties and Applications. *Nucleic Acids Research*, 20(11):2803–2812, 1992.

[221] I. D. Vladescu, M. J. McCauley, I. Rouzina, and M. C. Williams. Mapping the phase diagram of single DNA molecule force-induced melting in the presence of ethidium. *Physical Review Letters*, 95(15):158102, 2005.

[222] B. Mignotte, M. Barat, and J. C. Mounolou. Characterization of a Mitochondrial Protein-Binding to Single-Stranded-DNA. *Nucleic Acids Research*, 13(5):1703–1716, 1985.

[223] K. Li and R. Sanders Williams. Tetramerization and Single-stranded DNA Binding Properties of Native and Mutated Forms of Murine Mitochondrial Single-stranded DNA-binding Proteins. *Journal of Biological Chemistry*, 272(13):8686–8694, 1997.

[224] B. M. Alberts and L. Frey. T4 Bacteriophage Gene 32: a Structural Protein in Replication and Recombination of DNA. *Nature*, 227(5265):1313–1318, 1970.

[225] K. Pant, R. L. Karpel, I. Rouzina, and M. C. Williams. Mechanical Measurement of Single-molecule Binding Rates: Kinetics of DNA Helix-destabilization by T4 Gene 32 Protein. *Journal of Molecular Biology*, 336(4):851–870, 2004.

[226] U. Curth, C. Urbanke, J. Greipel, H. Gerberding, V. Tiranti, and M. Zeviani. Single-Stranded-DNA-Binding Proteins from Human Mitochondria and Escherichia-Coli Have Analogous Physicochemical Properties. *European Journal of Biochemistry*, 221(1):435–443, 1994.

[227] C. Yang, U. Curth, C. Urbanke, and C. H. Kang. Crystal structure of human mitochondrial single stranded DNA binding protein at 2.4 angstrom resolution. *Nature Structural Biology*, 4(2):153–157, 1997.

[228] J. L. Leroy, M. Kochoyan, T. Huynhdinh, and M. Gueron. Characterization of base-pair opening in deoxynucleotide duplexes using catalyzed exchange of the imino proton. *Journal of Molecular Biology*, 200(2):223–238, 1988.

[229] D. Stigter. An electrostatic model of B-DNA for its stability against unwinding. *Biophysical Chemistry*, 75(3):229–233, 1998.

[230] Y. Zeng, A. Montrichok, and G. Zocchi. Length and Statistical Weight of Bubbles in DNA Melting. *Physical Review Letters*, 91(14):148101, 2003.

[231] Y. Zeng, A. Montrichok, and G. Zocchi. Bubble Nucleation and Cooperativity in DNA Melting. *Journal of Molecular Biology*, 339(1):67–75, 2004.

[232] J. A. Korhonen, M. Gaspari, and M. Falkenberg. TWINKLE has 5 '-> 3 ' DNA helicase activity and is specifically stimulated by mitochondrial single-stranded DNA-binding protein. *Journal of Biological Chemistry*, 278(49):48627–48632, 2003.

[233] C. Bustamante. Direct Observation and Manipulation of Single DNA Molecules using Fluorescence Microscopy. *Annual Review of Biophysics & Biophysical Chemistry*, 20(1):415–446, 1991.

[234] E. S. Yeung. Dynamics of Single Biomolecules in Free Solution. *Annual Review of Physical Chemistry*, 55(1):97–126, 2004.

[235] E. S. G. Shaqfeh. The dynamics of single-molecule DNA in flow. *Journal of Non-Newtonian Fluid Mechanics*, 130(1):1–28, 2005.

[236] T. T. Perkins, D. E. Smith, and S. Chu. Single Polymer Dynamics in an Elongational Flow. *Science*, 276(5321):2016–2021, 1997.

[237] H. M. Berman and P. R. Young. The Interaction of Intercalating Drugs with Nucleic-Acids. *Annual Review of Biophysics & Bioengineering*, 10:87–114, 1981.

[238] C. Carlsson, A. Larsson, M. Jonsson, B. Albinsson, and B. Norden. Optical and Photophysical Properties of the Oxazole Yellow DNA Probes YO and YOYO. *Journal of Physical Chemistry*, 98(40):10313–10321, 1994.

[239] A. Larsson, C. Carlsson, M. Jonsson, and N. Albinsson. Characterization of the Binding of the Fluorescent Dyes YO and YOYO to DNA by Polarized-Light Spectroscopy. *Journal of the American Chemical Society*, 116(19):8459–8465, 1994.

[240] J. R. Lakowicz. *Principles of fluorescence spectroscopy*. Springer, New York ; Berlin, 3rd edition, 2006.

[241] B. Nordén, M. Kubista, and T. Kurucsev. Linear Dichroism Spectroscopy of Nucleic Acids. *Quarterly Reviews of Biophysics*, 25(1):51–170, 1992.

[242] J. N. Forkey, M. E. Quinlan, and Y. E. Goldman. Protein structural dynamics by single-molecule fluorescence polarization. *Progress in Biophysics & Molecular Biology*, 74(1-2):1–35, 2000.

[243] D. Genest, P. A. Mirau, and D. R. Kearns. Investigation of DNA dynamics and drug-DNA interaction by steady state fluorescence anisotropy. *Nucleic Acids Research*, 13(7):2603–2615, 1985.

[244] C. Carlsson, A. Larsson, M. Bjorkman, M. Jonsson, and B. Albinsson. Experimental and simulated fluorescence depolarization due to energy transfer as tools to study DNA-dye interactions. *Biopolymers*, 41(5):481–494, 1997.

[245] S. Georghiou, T. D. Bradrick, A. Philippetis, and J. M. Beechem. Large-amplitude picosecond anisotropy decay of the intrinsic fluorescence of double-stranded DNA. *Biophysical Journal*, 70(4):1909–1922, 1996.

[246] M. Eriksson, B. Norden, and S. Eriksson. Anthracycline-DNA Interactions Studied with Linear Dichroism and Fluorescence Spectroscopy. *Biochemistry*, 27(21):8144–8151, 1988.

[247] P.-J. Chou and W. C. Johnson. Base inclinations in natural and synthetic DNAs. *Journal of the American Chemical Society*, 115(4):1205–1214, 1993.

[248] E. Tuite and B. Norden. Sequence-Specific Interactions of Methylene-Blue with Polynucleotides and DNA - A Spectroscopic Study. *Journal of the American Chemical Society*, 116(17):7548–7556, 1994.

[249] H. P. Spielmann, D. E. Wemmer, and J. P. Jacobsen. Solution Structure of a DNA Complex with the Fluorescent Bis-Intercalator TOTO Determined by Nmr-Spectroscopy. *Biochemistry*, 34(27):8542–8553, 1995.

[250] J. M. Schurr and B. S. Fujimoto. The Amplitude of Local Angular Motions of Intercalated Dyes and Bases in DNA. *Biopolymers*, 27(10):1543–1569, 1988.

[251] A. Agronskaia, J. M. Schins, B. G. de Grooth, and J. Greve. Polarization effects in flow cytometric DNA sizing. *Applied Optics*, 38(4):714–719, 1999.

[252] J. M. Schins, A. Agronskaia, B. G. de Grooth, and J. Greve. Orientation of the chromophore dipoles in the TOTO-DNA system. *Cytometry*, 37(3):230–237, 1999.

[253] J. H. Werner, E. J. Larson, P. M. Goodwin, W. P. Ambrose, and R. A. Keller. Effects of fluorescence excitation geometry on the accuracy of DNA fragment sizing by flow cytometry. *Applied Optics*, 39(16):2831–2839, 2000.

[254] M. Irving. Steady-state polarization from cylindrically symmetric fluorophores undergoing rapid restricted motion. *Biophysical Journal*, 70(4):1830–1835, 1996.

[255] T. S. Allen, N. Ling, M. Irving, and Y. E. Goldman. Orientation changes in myosin regulatory light chains following photorelease of ATP in skinned muscle fibers. *Biophysical Journal*, 70(4):1847–1862, 1996.

[256] N. Ling, C. Shrimpton, J. Sleep, J. Kendrick-Jones, and M. Irving. Fluorescent probes of the orientation of myosin regulatory light chains in relaxed, rigor, and contracting muscle. *Biophysical Journal*, 70(4):1836–1846, 1996.

[257] Jr. Kinosita, K., H. Itoh, S. Ishiwata, K. Hirano, T. Nishizaka, and T. Hayakawa. Dual-view microscopy with a single camera: real-time imaging of molecular orientations and calcium. *Journal of Cell Biology*, 115(1):67–73, 1991.

[258] B. Åkerman and E. Tuite. Single- and double-strand photocleavage of DNA by YO, YOYO and TOTO. *Nucleic Acids Research*, 24(6):1080–1090, 1996.

[259] V. Sundström and T. Gillbro. Viscosity dependent radiationless relaxation rate of cyanine dyes. A picosecond laser spectroscopy study. *Chemical Physics*, 61(3):257–269, 1981.

[260] T. L. Netzel, K. Nafisi, M. Zhao, J. R. Lenhard, and I. Johnson. Base-content dependence of emission enhancements, quantum yields, and lifetimes for cyanine dyes bound to double-strand DNA: Photophysical properties of monomeric and bichromophoric DNA stains. *Journal of Physical Chemistry*, 99(51):17936–17947, 1995.

[261] N. Metropolis, A. W. Rosenbluth, M. N. Rosenbluth, A. H. Teller, and E. Teller. Equation of state calculations by fast computing machines. *Journal of Chemical Physics*, 21(6):1087–1092, 1953.

[262] D. Frenkel and B. Smit. *Understanding Molecular Simulation*. Academic Press, Boston, 2002.

[263] E. Hecht. *Optics*. Addison-Wesley, Reading, Mass., 3rd edition, 1998.

[264] D. Axelrod. Carbocyanine Dye Orientation in Red-Cell Membrane Studied by Microscopic Fluorescence Polarization. *Biophysical Journal*, 26(3):557–573, 1979.

[265] D. Axelrod. Fluorescence Polarization Microscopy. *Methods in Cell Biology*, 30:333–352, 1989.

[266] M. Hayashi and Y. Harada. Direct observation of the reversible unwinding of a single DNA molecule caused by the intercalation of ethidium bromide. *Nucleic Acids Research*, 35(19):e125, 2007.

List of publications

1. Meindert A. van Dijk, Lukas C. Kapitein, Joost van Mameren, Christoph F. Schmidt, and Erwin J. G. Peterman.
   Combining optical trapping and single-molecule fluorescence spectroscopy: Enhanced photobleaching of fluorophores.
   Journal of Physical Chemistry B, 108(20):6479–6484, 2004 — **Chapter 6**.

2. Remus T. Dame*, Joost van Mameren*, Martijn S. Luijsterburg, Monika E. Mysiak, Ana Janićijević, Grzegorz Pazdzior, Peter C. van der Vliet, Claire Wyman, and Gijs J. L. Wuite.
   Analysis of scanning force microscopy images of protein-induced DNA bending using simulations.
   Nucleic Acids Research, 33(7):e68, 2005 — **Chapter 3**.

3. Karen C. Vermeulen*, Joost van Mameren*, Ger J. M. Stienen, Erwin J. G. Peterman, Gijs J. L. Wuite, and Christoph F. Schmidt.
   Calibrating bead displacements in optical tweezers using acousto-optic deflectors.
   Review of Scientific Instruments, 77(1):013704, 2006 — **Chapter 2**.

4. Joost van Mameren, Mauro Modesti, Roland Kanaar, Claire Wyman, Gijs J. L. Wuite, and Erwin J. G. Peterman.
   Dissecting elastic heterogeneity along DNA molecules coated partly with Rad51 using concurrent fluorescence microscopy and optical tweezers.
   Biophysical Journal, 91(8):L78–L80, 2006 — **Chapter 7**.

5. Mauro Modesti, Dejan Ristić, Thijn van der Heijden, Cees Dekker, Joost van Mameren, Erwin J. G. Peterman, Gijs J. L. Wuite, Roland Kanaar, and Claire Wyman.
   Fluorescent human RAD51 reveals multiple nucleation sites and filament segments tightly associated along a single DNA molecule.
   Structure, 15(5):599–609, 2007.

6. Maarten C. Noom*, Bram van den Broek*, Joost van Mameren, and Gijs J. L. Wuite.
   Visualizing single DNA-bound proteins using DNA as a scanning probe.
   Nature Methods, 4(12):1031–1036, 2007 — **Chapter 4**.

* Joint first authors.

7. Joost van Mameren, Mauro Modesti, Roland Kanaar, Claire Wyman, Erwin J. G. Peterman, and Gijs J. L. Wuite.
   Counting RAD51 proteins disassembling from nucleoprotein filaments under tension.
   Under revision with Nature — **Chapter 8**.
8. Joost van Mameren, Erwin J. G. Peterman, and Gijs J. L. Wuite.
   See me, feel me: Methods to concurrently manipulate and visualize single DNA molecules.
   Under review with Nucleic Acids Research — **Chapter 5**.
9. Joost van Mameren, Peter Gross, Géraldine Farge, Maria Falkenberg, Pleuni Hooijman, Erwin J. G. Peterman, and Gijs J. L. Wuite.
   DNA overstretching is a local melting transition.
   In preparation — **Chapter 9**.
10. Joost van Mameren, Karen C. Vermeulen, Gijs J. L. Wuite, and Erwin J. G. Peterman.
    A polarized view on DNA under tension.
    In preparation — **Chapter 10**.
11. Bram van den Broek*, Maarten C. Noom*, Joost van Mameren, and Gijs J. L. Wuite.
    Visualizing the formation and collapse of DNA toroids.
    In preparation.

* Joint first authors.

Samenvatting

Biofysica

De titel van dit proefschrift luidt, vertaald naar hedendaags Nederlands: 'het integreren van *single-molecule* visualisatie en DNA-micromanipulatie'. Met vertalen alleen komen we dus vermoedelijk voor de gemiddelde 'leek' niet zo heel veel verder... Het wetenschappelijk onderzoek dat in dit proefschrift beschreven staat valt in de categorie **'biofysica'**—een samentrekking van 'bio(logie)' en 'fysica' (natuurkunde). Dit deel van de natuurkunde houdt zich bezig met het bestuderen van biologische systemen. De gedachte "daar hebben we toch al biologen voor", is legitiem: biologisch en later moleculair biologisch onderzoek heeft ons de afgelopen eeuwen al ontzettend veel geleerd over de werking van het leven tot op het kleinste niveau. Wat kunnen fysici daaraan toevoegen?

Fysici hebben de neiging om vragen te stellen die, zoals te verwachten valt, fysisch van aard zijn. Dit gaat dan vaak over begrippen als energie of kracht. Van dergelijke vragen zijn er ontzettend veel te stellen in het kader van de biologie. Hoe zijn spieren bijvoorbeeld in staat kracht te genereren? Wat zorgt daarbij voor de omzetting van chemische energie in mechanische of bewegingsenergie? Gelukkig stellen biofysici niet alleen vragen, maar doen ze ook verwoede pogingen die te beantwoorden. Ze gebruiken daarbij veelal geavanceerde technieken en theorieën, die in de biologie (nog) niet veel gebruikt worden: biofysica is de bestudering van de biologie met natuurkundige technieken.

Deze samenvatting is bedoeld om uiteen te zetten wat voor biofysisch onderzoek er zoal in dit proefschrift beschreven staat. Het duiden van de titel lijkt daarbij een aardig startpunt. We hakken de titel daarbij op in onderdelen.

Het integreren van *single-molecule* visualisatie en **DNA**-micromanipulatie

Laten we beginnen met **DNA**. Iedereen heeft wel op zijn minst een vaag idee van wat DNA is. De media staan bol van DNA-ouderschapstests, DNA-bewijs in forensisch onderzoek, enzovoort. In deze context wordt DNA gebruikt als een unieke 'vingerafdruk'

van een levend wezen (meestal een mens), die met enkel een minuscule hoeveelheid biologisch materiaal (zoals een haar) eenduidig de eigenaar daarvan kan identificeren. Twee kenmerken van DNA zijn daarbij cruciaal: [1] DNA is aanwezig in alle biologische bouwstenen van een organisme (cellen), en [2] dit DNA is uniek voor elk individueel organisme. Dit laatste komt doordat bij het ontstaan van een nieuw organisme het DNA van de ouders gemengd wordt. Het feit dat in alle cellen het volledige DNA van het organisme aanwezig is, is van levensbelang: op het DNA is in feite de ingrediëntenlijst voor de cel vastgelegd. Even een korte introductie in de moleculaire biologie. De DNA-code bestaat uit vier 'letters' A, T, C en G, *basen* genaamd. De volgorde, of *sequentie*, waarin deze letters in het DNA worden aaneengeschakeld is de genetische blauwdruk van een organisme. Het DNA van de simpelste virussen bestaat al uit duizenden basen, terwijl dat van mensen er wel rond de drie miljard bevat. Andere belangrijke bouwstenen van de cel, **eiwitten** (Engels: *proteins*), worden geproduceerd aan de hand van de code op het DNA.

Een ander bekend aspect van DNA is de tot de verbeelding sprekende structuur: een **dubbele helix** ('wenteltrap'). Een plaatje van deze structuur is te zien in Figuur 1.1 op pagina 4. De dubbele helix bestaat uit twee om elkaar heen gedraaide DNA-strengen die elk een aaneenschakeling van bovengenoemde basen is. De helix van dubbelstrengs DNA wordt bij elkaar gehouden doordat de basen in de twee strengen aan elkaar binden: A paart met T; C paart met G. Door deze specifieke paring bepaalt de basesequentie van de ene streng die van de andere volledig. Anders dan de statische figuur op pagina 4 doet vermoeden, is DNA een dynamisch molecuul. Tijdens diverse cellulaire processen wordt de helix lokaal ontrafeld, zodat de DNA-code kan worden 'afgelezen' en gebruikt om bijvoorbeeld eiwitten te produceren, of om het DNA te kopiëren. Dit laatste is benodigd voordat celdeling kan plaatsvinden: beide cellen moeten immers over het gehele DNA beschikken. Voor vele van dit soort dynamische DNA-processen is de interactie van DNA met gespecialiseerde eiwitten cruciaal. Deze eiwitten doen daarbij het eigenlijke werk.

In dit proefschrift komt een aantal DNA-bindende eiwitten aan bod. We komen eiwitten tegen die dubbelstrengs DNA buigen (Hoofdstuk 3), DNA in tweeën knippen bij een specifieke sequentie van baseparen (Hoofdstuk 4), of helpen bij de reparatie van ongewenste breuken (Hoofdstukken 7 en 8); we komen hier verderop nog op terug.

Het integreren van *single-molecule* visualisatie en DNA-micromanipulatie

Zoals hierboven gezegd, worden in de biofysica vaak natuurkundige methoden gebruikt. Sinds begin jaren negentig zijn er technieken beschikbaar, waarmee men

individuele moleculen (oftewel *single molecules*) kan *manipuleren*. Met zulke manipulatietechnieken kunnen we niet alleen duwen of trekken aan een individueel molecuul, maar we kunnen daarbij tegelijkertijd ook heel precies *meten* wat voor krachten daarbij worden uitgeoefend. Deze technologie is in de afgelopen decennia zodanig verfijnd, dat we er krachten zoals die in de biologie op de moleculaire schaal een rol spelen, mee kunnen uitoefenen en meten. Deze krachten zijn in de orde van **piconewtons**, oftewel 0,000000000001 newton. Ter vergelijking: het gewicht van 1 rijstkorrel (gemiddelde massa: 25 mg) is ongeveer tweehonderdvijftig miljoen piconewton. Deze minuscule krachten zijn ongeveer de krachten die zogeheten *motoreiwitten* uitoefenen, bijvoorbeeld voor actief transport in de cel of voor het helpen samentrekken van spieren. Juist voor de bestudering van dit soort processen in actie is een nauwkeurige meting van de krachten van groot belang.

Eén van de technieken die daarbij veel gebruikt worden is het **optisch pincet** (in het Engels: *optical tweezers* of *optical trap*); de meeste metingen in dit proefschrift zijn gedaan met één of meerdere optische pincetten. Zoals de naam al doet vermoeden, wordt voor een optisch pincet licht gebruikt om mee te manipuleren. In paragraaf 1.3.3 van de introductie wordt in detail de werking van het optisch pincet uiteengezet. In het kort komt het op het volgende neer. Wanneer een laserstraal met een sterke lens (bijvoorbeeld de objectieflens van een microscoop) gefocusseerd wordt, kan het brandpunt dat daarmee ontstaat gaan werken als een 'aanzuigpunt': kleine objecten die het licht breken worden naar het brandpunt toegetrokken en kunnen niet meer uit deze 'optische val' ontsnappen. Het fysische principe hierachter is dat licht druk op materie uitoefent. In de dagelijkse praktijk merken we daar (gelukkig) niks van als we bijvoorbeeld in de zon zitten, aangezien deze stralingsdruk erg zwak is. Voor heel sterke lichtbronnen in combinatie met kleine objecten kan de stralingsdruk echter wel degelijk verschil maken. Een object in een optisch pincet, dat het licht middels breking van richting verandert, krijgt daarbij zoveel 'duwtjes', dat het in het brandpunt opgesloten blijft. Een belangrijk aspect van een optisch pincet is dat het gevangen object zelf als een soort lens functioneert, die het licht 'verstrooit'. Door deze verstrooiing kunnen we heel nauwkeurig meten in hoeverre het deeltje zich nog in het pincet beweegt onder invloed van externe krachten.

In een aantal hoofdstukken van dit proefschrift wordt een enkel DNA-molecuul opgespannen tussen twee balletjes die elk met een optisch pincet vastgehouden en gemanipuleerd worden (zie het schematische plaatje hiernaast en kijk ook nog eens naar de omslag). We kunnen daarbij het DNA in plaats van als 'drager van gene-

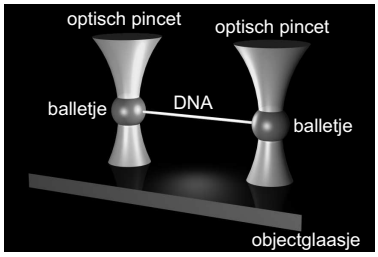

tisch materiaal', ook gewoon als een elastiekje beschouwen: door aan het DNA te trekken, kunnen we de **elastische eigenschappen** ervan onderzoeken. Het is gebleken dat DNA zich tot op zekere hoogte als een heel gewoon elastiekje gedraagt. Als we er twee keer zo hard aan trekken, rekt het ook twee keer zo ver uit. Als we er echter relatief hard aan trekken (wel 65 piconewton!...), gebeurt er iets interessants: we kunnen het DNA tot bijna twee keer de lengte oprekken zonder dat we daarbij extra kracht hoeven uit te oefenen. Deze *faseovergang*, die we **overstrekking** (Engels: *overstretching*) noemen, is omkeerbaar: het DNA raakt er (meestal) niet bij beschadigd. Wat er precies gebeurt, wordt in Hoofdstuk 9 (en deels hieronder) ontrafeld.

Het trekken aan een enkel DNA-molecuul klinkt obscuurder dan het is. Het kan namelijk goed worden gebruikt als uniek gereedschap om de binding van eiwitten aan DNA te bestuderen. Veel eiwitten veranderen de structuur van DNA wanneer ze eraan binden door het bijvoorbeeld te buigen, strekken of ontwinden. Eiwitbinding kan in die gevallen gemakkelijk gedetecteerd worden als een verandering van de elastische eigenschappen—zie Hoofdstuk 7. Daarnaast kunnen we het binden of loslaten van het DNA door eiwitten ook actief beïnvloeden door aan het DNA te trekken. In Hoofdstuk 8 maken we hiervan direct gebruik. Tenslotte is DNA ook een interessant modelsysteem als een relatief stijf *polymeer*. We kunnen de 'bewegingsdynamica' van DNA goed bestuderen met de hier beschreven methoden voor micromanipulatie—het onderwerp van Hoofdstuk 10.

Het integreren van *single-molecule* visualisatie en DNA-micromanipulatie

Tot nu toe hebben we het over manipulatie van en krachtmetingen aan individuele moleculen gehad. Het is echter ook mogelijk om individuele moleculen te **visualiseren**. Voor wie niet zo bekend is met de mogelijkheden en vooral onmogelijkheden van microscopie klinkt dat wellicht niet als een bijzonderheid. Algemeen bekend is immers dat microscopie gebruikt wordt om objecten sterk vergroot te kunnen bestuderen. Een principiële beperking schuilt echter in het licht, waarmee het object beschenen (en dus zichtbaar gemaakt) wordt: de *golflengte* ervan bepaalt hoe ver we maximaal op de details kunnen inzoomen (de **resolutie** van de microscoop). Deze golflengte ligt voor zichtbaar licht rond de halve micrometer (dus 0,0005 mm). Alhoewel dat erg klein lijkt, is dat toch nog een paar honderd maal groter dan bijvoorbeeld DNA dik is. Met 'normale' microscopie kunnen we dus DNA niet zien; we moeten trucs uithalen om het te visualiseren. Eén van de trucs is om niet met licht een afbeelding te maken, maar met een ultrascherp naaldje. Zo'n naaldje kan over een oppervlak bewogen worden en zo kleine hoogteverschillen registreren, min of meer zoals een ouderwetse platenspeler dat ook doet (maar dan een flink stuk

gevoeliger). Deze techniek wordt **atoomkrachtmicroscopie** (Engels: *atomic force microscopy* (AFM) of *scanning force microscopy* (SFM)) genoemd. Figuur 1.5 op pagina 11 geeft een schematische weergave van zo'n AFM, waarmee DNA tegenwoordig vrij gemakkelijk zichtbaar kan worden gemaakt. In Hoofdstuk 3 analyseren we met AFM-technologie gemaakte afbeeldingen van DNA met daarop eiwitten die het DNA buigen, om te bestuderen hoe scherp die buigingshoek is.

Een heel andere manier om de beperkte resolutie van de microscoop te 'overwinnen' is door **fluorescentie** te gebruiken. Fluorescentie is het fysische verschijnsel waarbij een molecuul licht absorbeert ('geëxciteerd wordt') en vervolgens licht van een iets 'rodere' kleur (langere golflengte of lagere energie) uitzendt. Doordat het een andere kleur heeft, kan fluorescentielicht met gebruik van de juiste filters goed van het exciterende licht gescheiden worden. Door dit met microscopie te combineren (**fluorescentiemicroscopie**), kan men de fluorescente moleculen feitelijk als kleine 'lampjes' inzetten: door ze met het juiste licht te beschijnen, gaan ze zelf licht uitzenden, wat specifiek gedetecteerd kan worden. De resolutiebeperking van de 'gewone' microscopie gaat hiervoor niet (of maar in beperkte mate) op. De fluorescente moleculen zijn immers vele malen kleiner dan de golflengte van het licht dat ze uitzenden, maar toch zichtbaar.

Lang niet alle moleculen zijn fluorescent. Om niet-fluorescente moleculen toch met fluorescentiemicroscopie zichtbaar te kunnen maken, kan men er in veel gevallen een fluorescent molecuul aan bevestigen ('fluorescent labelen'). In de biologie, biochemie en biofysica doet men dit vaak voor de bestudering van DNA en eiwitten. Inmiddels zijn de detectietechnieken zo gevoelig geworden, dat de fluorescentie van een enkel fluorescent of fluorescent gelabeld molecuul kan worden gemeten. Zulke **single-molecule fluorescentie** wordt gebruikt om individuele eiwitten te visualiseren terwijl ze 'aan het werk' zijn. Dat betekent dat ze niet, zoals bij electronenmicroscopie, bevroren of anderszins gefixeerd hoeven te worden: een groot voordeel. De eerder genoemde motoreiwitten zijn bijvoorbeeld op deze manier onder de microscoop direct te bestuderen als kleine bewegende stipjes, waarvan onder meer de snelheid onder diverse omstandigheden gemeten kan worden. Ook kunnen eiwitten die helpen DNA af te lezen of te dupliceren in actie gezien worden. Single-molecule fluorescentie heeft de afgelopen decennia een ware vlucht genomen en heeft de ontrafeling van een groot aantal biologische en biofysische vragen helpen beantwoorden. Verbeterde detectietechnieken hebben daaraan sterk bijgedragen, en zullen dat voorlopig nog blijven doen.

Het integreren van *single-molecule* visualisatie en DNA-micromanipulatie

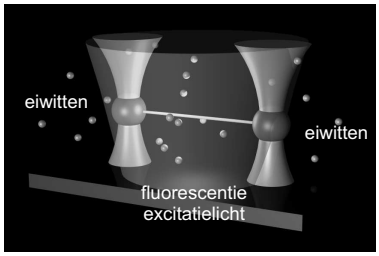

We komen daarmee bij het laatste aspect van de titel, te weten het woord **integreren**. Het grootste deel van dit proefschrift gaat over de gelijktijdige toepassing van manipulatie (met optische pincetten) en visualisatie (met fluorescentiemicroscopie) van DNA en DNA-bindende eiwitten. Naast de laser die tot een optisch pincet gefocusseerd wordt, voegt men een extra lichtbron toe (vaak ook een laser) waarmee de fluorescente moleculen geëxciteerd worden, zoals in de figuur schematisch is weergegeven. Fluorescente moleculen in dit proefschrift zijn òf gelabelde eiwitten, òf kleurstoffen die specifiek aan DNA binden. Ik heb voor mijn onderzoek een experimentele opstelling gebouwd, die speciaal voor die geïntegreerde experimenten uitgerust is. Dat betekent dat er nu in Amsterdam een microscoop staat die niet alleen voorzien is van een sterke laser voor de optische pincetten, maar ook van een extreem gevoelige camera, die de fluorescentie van individuele moleculen kan waarnemen. Daarnaast staan er om de microscoop heen nog een paar iets minder sterke lasers voor de excitatie van verschillende soorten fluorescente moleculen.

Gecombineerde manipulatie- en visualisatie-experimenten hebben een belangrijke toegevoegde waarde ten opzichte van experimenten met één van beide technieken. Ik licht dit toe aan de hand van een voorbeeld. In Hoofdstuk 7 bestuderen we, zoals hierboven al even genoemd, de veranderde elastische eigenschappen van DNA onder invloed van het binden van een speciaal eiwit. Dit eiwit, **RAD51** genaamd, is erg belangrijk bij het herstel van breuken in het DNA. Zulke breuken kunnen bijvoorbeeld, indien niet tijdig gerepareerd, aanleiding zijn voor bepaalde vormen van kanker, waaronder borstkanker. Ook is RAD51 actief bij het 'mengen' van het DNA van beide ouders tijdens de productie van voortplantingscellen, waardoor iedere voortplantingscel uniek DNA verkrijgt. Het eiwit klaart zijn klus door een **filament** (een soort 'eiwitjasje') om DNA te vormen. Het DNA wordt daarbij bijna 50% uitgerekt, en wordt aanmerkelijk stijver. Het zal inmiddels geen verrassing meer zijn dat optische pincetten deze effecten goed detecteerbaar maken. Tijdens manipulatie met optische pincetten ziet men echter niet direct waar, op welke manier en met hoeveel tegelijk de RAD51 eiwitten gebonden zijn. De gelijktijdige visualisatie, mogelijk door het gebruik van fluorescent gelabelde RAD51 eiwitten, maakt het mogelijk om te ontrafelen hoe de eigenschappen van een *onvolledig* bedekt DNA-molecuul ook inhomogeen veranderen. Zonder de directe visualisatie kan men enkel op een indirecte manier deze eigenschappen bestuderen.

Een ander voorbeeld van de toegevoegde waarde van de integratie van *single-molecule* visualisatie- en manipulatietechnieken is te vinden in Hoofdstuk 9. Daar onderzoeken we de overstrekking-faseovergang van DNA. Sinds de eerste ontdekking van dit verschijnsel in 1996 is er veel gespeculeerd en gemodelleerd wat er precies met de structuur van het DNA gebeurt. De helix-structuur van DNA deed vermoeden dat deze wenteltrap wellicht 'ontwond' tijdens de overgang, waarvoor gaandeweg verschillende modellen verschenen. Deze modellen deden onderling deels strijdige voorspellingen over de vraag of daarbij de bindingen tussen de baseparen al of niet verbroken worden. Als dat wel het geval is, wordt er dus tijdens het overstrekken langzaam maar zeker steeds meer enkelstrengs DNA gevormd. Alle experimenten die tot nu toe echter het overstrekken van DNA bestudeerden, waren gebaseerd op single-molecule *manipulatie*—men kon het DNA *voelen*, maar niet *zien*. Daarom gebruiken wij in Hoofdstuk 9 fluorescente labels die specifiek aan dubbelstrengs of enkelstrengs DNA binden. Daarmee kunnen we *direct* (dus zonder ingewikkelde modellen) zien of, waar en in welke mate enkelstrengs DNA wordt gevormd. We verhelderen daarmee de onduidelijkheid tussen de diverse modellen, waarbij we ook nog op zeer directe wijze kunnen aantonen dat de overstrekking eigenlijk nogal anders verloopt dan gedacht. Zonder gelijktijdige visualisatie hadden we dat niet kunnen doen.

Ik wil benadrukken dat bovenstaande voorbeelden slechts het 'topje van de ijsberg' blootgeleggen van wat er met dit soort geïntegreerde *single-molecule* technieken bereikt kan worden. Mijn verwachting is dan ook dat vergelijkbare experimenten in de toekomst de werking van een breed scala aan biologische systemen zullen ontrafelen. Dit proefschrift bevat een aantal voorbeelden die de voordelen van geïntegreerde *single-molecule* visualisatie en manipulatie tonen.

Opbouw van dit proefschrift

In het voorgaande is het onderwerp van een aantal hoofdstukken van dit proefschrift al even kort aan bod gekomen. Duidelijk is, zeker nu we de titel ontleed hebben, dat de geïntegreerde aanpak van gelijktijdige manipulatie en visualisatie van DNA en DNA-bindende eiwitten het hoofdthema is. In dit proefschrift staat een aantal verschillende onderzoeksprojecten beschreven, waarvan enkele inmiddels als op zichzelf staand geheel gepubliceerd zijn in een wetenschappelijke tijdschriften (zie pagina 183). Daarom wil ik tot slot van deze samenvatting nog even kort de inhoud en de onderlinge samenhang van de opeenvolgende hoofdstukken bespreken.

Hoofdstuk 1 geeft een algemene inleiding tot de biologische systemen en de biofysische technieken die in de latere hoofdstukken gebruikt worden. *Hoofdstuk 2* is een technisch hoofdstuk, waarin een nieuwe manier om met optische pincetten kwanti-

tatieve metingen te doen wordt beschreven. DNA wordt voor het eerst bestudeerd in *Hoofdstuk 3*, waar we, zoals hierboven beschreven, de buiging van DNA door diverse eiwitten analyseren aan de hand van AFM-afbeeldingen. In *Hoofdstuk 4* gebruiken we optische pincetten om DNA te manipuleren. We doen dit zelfs met twee DNA-moleculen tegelijk, die we om elkaar heen winden. Door nu het ene molecuul in een lusje langs het andere te schuiven, kunnen we onderzoeken of, waar en hoe sterk bepaalde eiwitten op het DNA gebonden zitten. Zo'n gelijktijdige manipulatie van twee DNA-moleculen is 'single-molecule acrobatiek' die niet eerder vertoond was.

Om de in de titel van het proefschrift aangekondigde combinatie van manipulatie en visualisatie van DNA in te leiden, bevat *Hoofdstuk 5* een overzicht van zulke technieken tot dusver. In *Hoofdstuk 6* bestuderen we het effect op de levensduur van fluorescente moleculen wanneer we ze aan de hoge laserintensiteit van optische pincetten blootstellen. Het blijkt dat fluorescente moleculen eerder kapotgaan ('bleken') door die intensiteit. We geven gelukkig ook een aantal manieren om dit ongewenste bij-effect te verminderen. In *Hoofdstuk 7* laten we de gebouwde experimentele opstelling 'los' op de bestudering van de elastische eigenschappen van DNA omhuld met RAD51 filamenten, zoals hierboven besproken. In *Hoofdstuk 8* kijken we vervolgens hoe deze filamenten stapsgewijs uit elkaar vallen. Dit is een belangrijk biologisch proces, aangezien de biochemische reactie waaraan RAD51 meewerkt niet kan verlopen zonder dat de eiwitmantel eerst van het DNA verwijderd wordt. Door onder meer te analyseren hoe dit uit elkaar vallen beïnvloed wordt door spanning in het DNA, kunnen we een gedetailleerd moleculair model opstellen van hoe deze reactie precies in zijn werk gaat. In dit hoofdstuk komt de gecombineerde techniek maximaal tot zijn recht: weglaten van manipulatie òf visualisatie had de metingen en het opstellen van het daaruit voortvloeiende moleculaire model onmogelijk gemaakt. In het eerder besproken *Hoofdstuk 9* wordt opgehelderd hoe tijdens het overstrekken van DNA de twee strengen langzaam maar zeker van elkaar loskomen. *Hoofdstuk 10*, tenslotte, beschrijft de resultaten van experimenten waar we DNA-manipulatie met optische pincetten combineren met *gepolariseerde* fluorescentiemicroscopie. Met deze experimenten zijn we in staat om de oriëntatie van bepaalde fluorescente moleculen gebonden aan het DNA, en daarmee ook die van het DNA zelf, te bestuderen bij verschillende spanningen in het DNA. Deze experimenten leren ons iets over de bewegingsdynamica van DNA in een vloeistof, waar ik hier niet verder op in zal gaan.

Hopelijk heeft de lezer nu een goed beeld van de inhoud en de context van het in dit proefschrift beschreven onderzoek. Mogelijk houdt deze samenvatting de lezer nog even in zijn 'greep' en brengt ze 'licht' bij het lezen van mijn proefschrift.

Dankwoord

Toch grappig, promoveren. Je werkt jarenlang aan een boekje, dat je probeert te vullen met wetenschappelijk onderzoek dat door vakgenoten gewaardeerd wordt. Daarbij ben je er nochtans bij voorbaat al zeker van dat 95% van de mensen die dat doorwrochte boekje uiteindelijk in handen krijgen, direct beginnen (en vaak ook eindigen) met dat wat je als schrijver als àllerlaatste doet... Toch (of misschien wel juist daarom) is het een groot genoegen om een dankwoord te schrijven!

Ik begin daarbij met de twee heren die mij de mogelijkheid hebben geboden mijn promotieonderzoek bij ze te doen: Erwin en Gijs. Ik was het eerste gezamenlijke 'kindje' in een samenwerking die volgens mij uiterst vruchtbaar genoemd mag worden. Dat moge ook blijken uit het feit dat verschillende promovendi ná mij onder een vergelijkbare duo-begeleiding aan hun promotieonderzoek zijn begonnen. Ik kan zeggen: voor mij was dat duidelijk een voorrecht! En niet alleen omdat je met twee begeleiders ook ongeveer twee keer zoveel kans hebt er minimaal één op de VU aan te treffen natuurlijk. Wat het zo vruchtbaar maakt is dat jullie elkaar in meerdere opzichten complementeren. Erwin als trouwe rots in de branding, met begrip voor (want vaak herkenning van?) frustraties van een onderzoeker-in-opleiding, maar tevens een creatief experimentator met oog voor detail, en kennis van de catalogi van welke laser-, optica-, camera-, ...-leverancier ook. Aan de andere kant ook als prettige reisgenoot door Utah en naar Berlijn! En als cruciale gesprekspartner in discussies die het niet van nuance moeten hebben. Hoeveel standrechtelijke executies mogen we nog verwachten? Daarnaast Gijs als onderzoeker die opbloeit als er onbegrepen data op zijn bureau wordt gelegd (waarbij 'op' ook gelijk aangeeft in welke richting hij daarbij gaandeweg de discussie beweegt vanaf het zitvlak van zijn stoel...), die kan motiveren en kan laten geloven in eigen data/kunnen zoals ik nog niet vaak heb meegemaakt. "Even mijn data door Gijs heen halen", zegt genoeg. Heren copromotoren: hartelijk dank! Ik heb veel geleerd en het erg bij en met jullie naar mijn zin gehad.

Dat naar de zin hebben is natuurlijk ook in belangrijke mate te danken aan de collega's uit Uk11 en later U030. Hoewel ik in de 'eindfase' de dierentuin die het af en toe was maar nauwelijks met mijn koptelefoon kon overstemmen, heeft dat alles

me toch aanzienlijk meer gebracht dan gekost! En (gelukkig) niet alléén maar lol, maar ook vruchtbare discussies over wetenschap en goede gesprekken over menselijke zaken. Dus Bram, Maarten, Sander, Peter, Niels, Siet, Lukas, Irena, Iwan, Andrea, maar natuurlijk ook de promovendi in de aanpalende kamer Karen, Maryam, Mikhail, Steph, Ienas, de postdocs Remus, Wouter, Catherine, Zdeněk, Marcel, Daisuke, Stefan, Pedro, Gijsje, Mattijs en de analisten Els en Iris: bedankt, danke, blagodarya, grazie, mamnuun, spaseeba, merci, dêkuji, arigatou, gracias, thanks, voor de toffe en inspirerende tijd! Ik wens ieder van jullie alle goeds voor de toekomst. Bram en Maarten, het opereren als drie-eenheid zal ik missen. Ben benieuwd of we het ieder voor zich óók kunnen redden! En, niet onbelangrijk: is *ons* flow-systeem wel in goede handen?...

Christoph wil ik graag bedanken voor het starten en uitbouwen van de vakgroep waar dit alles heeft plaatsgevonden. Hoewel al enige tijd uit het zicht verdwenen, staat toch tenminste de befaamde espressomachine nog altijd als een fier aandenken aan goede tijden overeind! Fred, mijn promotor, dank ik natuurlijk ten eerste voor het zich willen kwijten van deze zware en verantwoordelijke taak, maar niet minder om zijn samenbindende rol in het levend houden van Het CoSy-Gevoel (inclusief zijn 'eigen' groepje theoreten)—met de jaarlijkse slemppartijen in diverse Amsterdamse grachtenpanden als mooiste voorbeeld.

Een universitaire onderzoeksgroep draait natuurlijk niet alleen op mensen die ook daadwerkelijk betaald worden voor wat ze doen. Leuk was het om er zoveel studenten bij te hebben! Leve dan ook de medische natuurwetenschappers, die de winkel de afgelopen jaren bijna overnamen. De studenten die ik de afgelopen jaren tijdens hun bachelorstage heb begeleid, Guus, Boy, Bram P en Pleuni, dank ik voor de plezierige samenwerking en natuurlijk voor hun noeste pogingen om meetresultaten voor (onder andere) mijn proefschrift te vergaren (gelukt Pleuni!).

Bij experimenteel onderzoek en vooral bij het daartoe bouwen van een experimentele opstelling is het heel prettig om op de deskundige ondersteuning van een goede fijnmechanische instrumentatiegroep te kunnen rekenen. Met name Pierre en Bart wil ik danken voor hun inzet de afgelopen jaren! Voor de secretariële ondersteuning was Gerrie natuurlijk jarenlang de continue factor, met als herhaald succesnummer de befaamde CoSy summerschools samen met de Amolf gang. Haar opvolgster Kiokkie dank ik voor haar praktische hulp in het staartje van mijn VU-tijd.

For the RAD51 project we fruitfully collaborated with Mauro, Claire and Roland from the Erasmus Medical Center in Rotterdam. Mauro taught me a great deal about homologous recombination, and I think our scientific complementarity provided a solid basis for writing some nice stories together. Let's cross our fingers for Chapter 8!...

Als promovendus in dienst van FOM heb ik een aantal aangename privileges ge-

noten. Ten eerste is daar het vermaarde FOM-cursusaanbod. Dank, Harry, voor de nuttige cursus 'loopbaanzelfsturing'. Ik hoop dat ik 'mijn vuur' in Berlijn gevonden heb! Huib, bedankt voor de inspirerende week in Nyenrode. Natuurlijk ook dank aan alle medecursisten voor alle openhartige feedback en niet te vergeten de gezelligheid! Daarnaast heb ik binnen de FOM-gelederen ook veel plezier gehad als lid van de centrale ondernemingsraad (COR). Het COR-werk vormde een prettige afwisseling met het doen van onderzoek, en bovendien een leerzame ervaring. COR-leden 2005-2006 en mensen op het FOM-bureau: bedankt daarvoor!

Het is erg fijn om, naast het academische gebeuren, met vrienden over 'normale zaken' te praten en leuke dingen te doen. Ook al is een goed deel zelf ook gepromoveerd of daar nog mee bezig (c.q. heeft een relatie met zo'n type), het zijn wat mij betreft juist de normale zaken die vrienden vrienden maken. Agnes, Bram, Hylke, Inge, Jeroen, Laura, Liselot, Maarten, Meindert, Nathalie, Paul B, Paul N, Rutger, Ruth, Sandra, Theo, Tom, Wilm, dank voor jullie vriendschap. Ook alle andere belangstellenden ben ik dankbaar!

Een aantal mensen heeft op iets directere wijze aan de totstandkoming van het voorliggende boekje bijgedragen. Uiteraard de coauteurs van de verschillende hoofdstukken/artikelen (zie pagina 183), maar ook mensen die zich belangeloos door delen van dit proefschrift heengewerkt hebben. Bram, Rutger, Tom, bedankt daarvoor! Rutger, de inhoud van dit boekje is niet jouw fysische stiel, maar je oprechte interesse, ook op afstand, maakt je een logische paranimf. Bram, jij hebt bijna alle hoofdstukken al eens gelezen en van uitzonderlijk gedetailleerd (beter bekend als Bram-esque) commentaar voorzien, dat je het paranimfschap eenvoudigweg afdwingt... Ik ben erg blij met jullie als pinguïns aan mijn zijde.

Familie! Voor de meesten zijn mijn onderzoeksbeslommeringen altijd een beetje ongrijpbaar geweest. Als jullie ná het lezen van de samenvatting nog vragen hebben, hoor ik het graag... Piet en Trudy, de afgelopen jaren officieel 'gepromoveerd' tot schoonouders, jullie wil ik bedanken voor de immer warme belangstelling (en uiteraard voor jullie dochter). Ook de interesse van mijn zus Annemieke, en zwager Martijn was erg fijn! Pap en mam, jullie dank ik voor jullie onvoorwaardelijke steun tijdens de afgelopen jaren, maar ook daarvóór en hopelijk nog ver in de toekomst. Ook op iets grotere afstand blijkt dat tot dusver te lukken!

Als laatste mag ik dan mijn VROUW bedanken. Yvonne, van alle mensen in dit dankwoord ben jij met stip het meest gebukt gegaan onder mijn schrijverij aan dit proefschrift. Tijdens de beruchte laatste loodjes, fijn gepland tijdens de opbouw van ons nieuwe leven in Berlijn, heb ik voor mijn gevoel meer van je gevraagd dan volgens de wet aan de huwelijkse staat verbonden is... Je hebt me daarbij doorlopend en niet-

aflatend ge- en ondersteund. Danke schön! Nu is het eindelijk af. Kunnen we goed genieten van ons leven in Berlijn! Ik heb er veel zin in om dat samen met jou te doen.

Joost van Mameren–Schotvanger
Berlijn, mei 2008

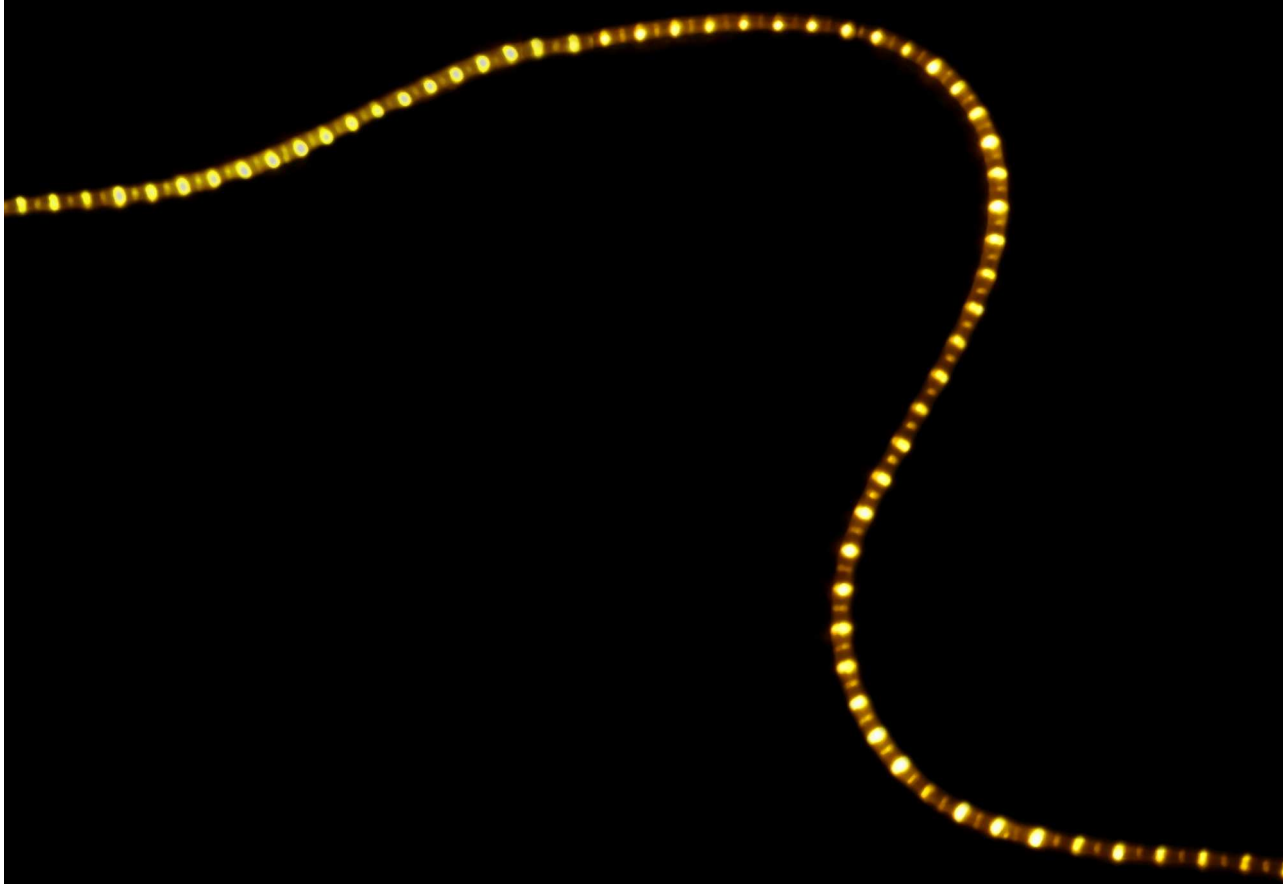

ISBN 978-90-8659-225-8